



HAL
open science

Planar slot photonic crystal cavities for on-chip hybrid integration

Thi Hong Cam Hoang

► **To cite this version:**

Thi Hong Cam Hoang. Planar slot photonic crystal cavities for on-chip hybrid integration. Optics [physics.optics]. Université Paris Saclay (COMUE), 2017. English. NNT : 2017SACLS063 . tel-01529759

HAL Id: tel-01529759

<https://theses.hal.science/tel-01529759>

Submitted on 31 May 2017

HAL is a multi-disciplinary open access archive for the deposit and dissemination of scientific research documents, whether they are published or not. The documents may come from teaching and research institutions in France or abroad, or from public or private research centers.

L'archive ouverte pluridisciplinaire **HAL**, est destinée au dépôt et à la diffusion de documents scientifiques de niveau recherche, publiés ou non, émanant des établissements d'enseignement et de recherche français ou étrangers, des laboratoires publics ou privés.

NNT : 2017SACLS063

THESE DE DOCTORAT
DE
L'UNIVERSITE PARIS-SACLAY
PREPAREE A
L'UNIVERSITE PARIS-SUD

ECOLE DOCTORALE N°575
Physique et ingénierie : Electrons, Photons, Sciences du vivant

Spécialité de doctorat : Physique

Par

Thi Hong Cam HOANG

Planar slot photonic crystal cavities
for on-chip hybrid integration

Thèse soutenue à Orsay, le 29 mars 2017

Composition du Jury :

M. Abderrahim Ramdane	Centre de Nanosciences et de Nanotechnologies	Président
M. Emmanuel Centeno	Institut Pascal	Rapporteur
M. Boris Gralak	Institut Fresnel	Rapporteur
M ^{me} Cécile Jamois	Institut des Nanotechnologies de Lyon	Examinatrice
M. Eric Cassan	Centre de Nanosciences et de Nanotechnologies	Directeur de thèse

Acknowledgements

I would like to give my foremost deep appreciation to Prof. Eric CASSAN, who gave me an opportunity to be enrolled in the field of silicon photonics, starting with this interesting Ph.D. project. His patience since my very beginning period with little background of this field, and his fruitful discussions as well as his passion inspiration have encouraged me and helped me to enrich my knowledge in this domain. It is my great pleasure to study and work in such a friendly team full of scientific supports. I would like to thank Dr. Laurent VIVIEN for training me on the optical bench when I characterized my first samples and letting me participate his CARTOON project. I would be thankful to Prof. Delphine MARRIS-MORRINI for our fruitful discussions. Moreover, my Ph.D. project would haven't been achieved operating devices without big efforts of Xavier LEROUX, who is specialized in clean-room work. I honestly thank him for our discussion, for explaining to me related techniques and especially for making our designs become real. I would like also to thank the Vietnamese government for their funding.

Doing research in our group, I have had the chance to collaborate with our great colleagues. I would thank Dr. Weiwei ZHANG, Dr. Samuel SERNA, Dr. Pierre COLMAN and Dr. Charles CAER who have helped me so much at the beginning and throughout my Ph.D. I am very happy to work with Elena DURAN and Dr. Carlos RAMOS for the CARTOON project. I would also thank Dr. Diego PEREZ-GALACHO, Nhung VU, Dr. Pedro DAMAS, Vladislav VAKARIN, Dr. Papichaya CHAISAKUL, Guillaume MARCAUD, Dorian OSER, Xin CUI for our nice conversations while having lunch together. I want to thank Dr. Adrien NOURY, Huy TRINH, Dr. Nicolas IZARD, Marthias BERCIANO, Dr. Daniel BENEDIKOVIC, Dr. Joan MANEL, Phuong DO and Qiankun LIU for sharing our office together. I would like to thank my Vietnamese friends in Orsay who supported me a lot during my very first days in France and shared with me my happy as well as my tough periods.

Finally, last not least, I would like to use this occasion to thank my beloved family for their endless love, encouragement and belief. This manuscript is devoted to them.

Orsay, April 2017

Thi Hong Cam HOANG

Introduction

Silicon photonics has become in the last years a mainstream in photonic technology and is promising to achieve monolithically integrated circuits on large silicon silicon on insulator (SOI) wafers in an approach based on a co-integration of electronic and optical functions on the same chips. In the wide range of passive and active components already available in silicon photonics, the development of integrated optical sources has not been carried out with the same dynamics due to indirect bandgap of silicon. Si is also known to suffer from strong two-photon absorption at telecom wavelengths, thus hindering the use of third-order nonlinearities for fast switching. To circumvent these intrinsic drawbacks and open the silicon platform to other applications such as on-chip (bio-) sensors, one approach is to introduce active materials (*e.g.* soft materials like polymers, graphene, carbon nanotubes, III/V compounds, functional oxides, *ect.*) in/on silicon platform. In this context, the current Ph.D. project has been carried out to pursue **hybrid integration in silicon**, *i.e.* by relying on approaches based on cladding or sandwiched active materials integrated with silicon photonic structures. The potential advantages of such hybrid on silicon approaches include low cost, easy processing and the possible use of various active materials. In such hybrid on silicon approaches, silicon is mainly used for the qualities of the SOI waveguide platform, *e.g.* for the low loss and strong index contrast of SOI optical waveguides. Active materials integrated on silicon through growth, spin-coating or other deposition techniques, bring on their side nonlinearities, modulation or luminescence properties that silicon cannot exhibit alone. With respect to such a scheme, a key point is to ensure that propagating or resonance optical modes are characterized by a sufficient overlap with the incorporated active materials that usually have lower refractive index values than Si.

In this thesis, the focus has been made on the design, fabrication, and characterization of hollow core silicon resonators based on two-dimensional photonic crystal cavities. We have studied slot photonic crystal cavities characterized by their high quality factors (*i.e.* Q of several tens of thousands) associated with small mode volumes (*i.e.* V of cubic wavelength, or less). The studies carried out have been oriented towards two types of proof-of-concept studies: the

realization of index sensors and that of cavities designed for the integration of light emitting active materials.

This manuscript is organized as follows:

Chapter 1 focuses on the context of silicon photonics as well as on the demand for integration in/on silicon. Then, strategies to integrate diverse active materials in silicon as well as the ability and prospects of hybrid integration in the silicon photonic platform are discussed. After that, different silicon-based building blocks are presented to implement this integration process in order to introduce **slot photonic crystal cavities**, which are the focus of this Ph.D. work.

Chapter 2 presents the design of slot photonic crystal cavities possessing high Q s and small mode volumes of the order of a fraction of cubic wavelength for optical resonances occurring in the telecom ranges, *i.e.* between 1.3 μm –1.6 μm wavelengths. In addition, the feasibility to excite photonic crystal slot cavity modes from an external waveguide is explored. Last, coupled slot photonic crystal cavities are investigated as a first step towards the exploitation of their modes as an engineering tool for light-matter enhancement in hybrid on-silicon photonic structures.

Chapter 3 is devoted to the experimental results of the Ph.D. work regarding the fabrication of the designed slot photonic crystal cavities, the refractive index sensing properties of these slot photonic crystal cavities around $\lambda = 1.58 \mu\text{m}$, as well as the integration of semiconducting single-walled carbon nanotubes in slot photonic crystal cavities for light emission near $\lambda = 1.28 \mu\text{m}$.

Finally, a **summary** and a **conclusion** to draw all main results of this Ph.D. are given, as well as the perspectives.

Contents

INTRODUCTION	ii
ACRONYM GLOSSARY	vii
Chapter 1. INTRODUCTION, CONTEXT AND MOTIVATIONS	1
1.1 Context and recent realizations in hybrid silicon photonics.....	2
1.1.1 Short description of the recent progress in silicon photonics	2
1.1.2 Need for hybrid integration on silicon	5
1.2 Integration in/on silicon photonics	6
1.2.1 Overview of the material families.....	6
1.2.1.1 Class of III-V semiconductor materials.....	6
1.2.1.2 Class of polymers	8
1.2.1.3 Class of quantum dots	9
1.2.1.4 Graphene	10
1.2.2 Special focus on carbon nanotubes (CNTs).....	12
1.2.2.1 Structure of CNTs	13
1.2.2.2 Optoelectronic properties of semiconducting single-walled carbon nanotubes.....	14
1.2.2.2.1 Optical bands and excitonic effects	14
1.2.2.2.2 Photoluminescence	15
1.2.2.2.3 State-of-the-art regarding optical gain.....	16
1.2.3 Integration in silicon photonics for sensing	17
1.3 Silicon photonic devices.....	20
1.3.1 Strip waveguides	20
1.3.2 Slot waveguides	21
1.3.3 Microring resonators	22
1.3.4 2D planar photonic crystals.....	24
1.3.4.1 W1 photonic crystal waveguides.....	26
1.3.4.2 Slot photonic crystal waveguides	27
1.3.4.3 Planar photonic crystal cavities	31
1.3.4.4 Slot photonic crystal cavities.....	34
1.4 Conclusion: motivations and manuscript outline	36

Chapter 2. DESIGN OF SLOT PHOTONIC CRYSTAL CAVITIES FOR SILICON HYBRID INTEGRATION	38
2.1 Design of slot photonic crystal cavities	38
2.1.1 Figures of merit of a photonic crystal cavity	38
2.1.1.1 Quality factor (Q)	39
2.1.1.2 Mode volume.....	42
2.1.2 Numerical simulations allowed to design slot photonic crystal cavities	43
2.1.2.1 Plane Wave Expansion (PWE).....	45
2.1.2.2 Finite-difference time-domain (FDTD).....	46
2.1.3 Design slot photonic crystal heterostructure cavities.....	46
2.1.4. Conclusion of section 2.1	50
2.2 Coupling slot photonic crystal cavities and waveguides.....	50
2.2.1 Design of a true-slot mode cavity	53
2.2.2 Coupling between a true-slot mode photonic crystal L3 cavity and a true-slot mode photonic crystal waveguide.....	55
2.2.3 Conclusion of section 2.2.....	59
2.3 Coupled slot photonic crystal cavities.....	59
2.3.1 Photonic molecules in planar guided wave optics	59
2.3.2 Tight-binding approximation applied to slot photonic crystal cavities.....	62
2.3.2.1 Principle of the tight-binding approximation	62
2.3.2.2 Bonding and antibonding photonic molecule supermodes seen by the tight-binding approach	64
2.3.2.3 Coupled photonic crystal L3 cavities	67
2.3.2.3.1 Design of a photonic crystal L3 cavity	67
2.3.2.3.2 Coupled photonic crystal L3 cavities	69
2.3.2.4 Investigation of coupled slot photonic crystal L3 cavities by FDTD simulation and tight-binding approach	73
2.3.2.4.1 Coupled true-slot mode photonic crystal L3 cavities ($W_{\text{slot}} = 200 \text{ nm}$).....	73
2.3.2.4.2 Coupled W1-like mode photonic crystal L3 cavities ($W_{\text{slot}} = 100 \text{ nm}$).....	76
2.3.3 Conclusion of section 2.3.....	79
2.4. Conclusion of chapter 2.....	80
Chapter 3. HYBRID SILICON PHOTONIC CRYSTAL CAVITIES: EXPERIMENTAL RESULTS	82
3.1 Fabrication of SOI slot photonic crystal waveguide cavities operating in the 1.3 - 1.6 μm range	83

3.1.1 Mask preparation for electron-beam lithography.....	83
3.1.2 Fabrication process	88
3.1.3 SEM images and analysis of the fabricated devices	92
3.1.4 Characterization	94
3.1.5 Conclusion of section 3.1	100
3.2 Slot photonic crystal cavities for index-sensing	101
3.2.1 Slot photonic crystal waveguide cavities for index sensing	101
3.2.1.1 Index variation process.....	101
3.2.1.2 Shift of cavity resonance wavelengths by cladding index variation	101
3.2.2 Conclusion of section 3.2.....	104
3.3 Integration of single-walled carbon nanotubes in slot photonic crystal cavities.....	105
3.3.1 Slot photonic crystal cavity at 1.28 μm resonance	106
3.3.2 Preparation of single-walled carbon nanotube solutions	107
3.3.3 Integration of single-walled carbon nanotubes in slot photonic crystal cavities	111
3.3.3.1 Linear transmission of slot photonic crystal cavity filled with s-SWNTS.....	111
3.3.3.2 Time of Flight measurement.....	112
3.3.3.3 Photoluminescence set-up	113
3.3.3.4 Photoluminescence spectra	114
3.3.4 Conclusion of section 3.3.....	118
3.4 Conclusion of chapter 3.....	118
CONCLUSION AND PERSPECTIVES.....	120
APPENDIX A	123
Coupled slot photonic crystal cavity and slot photonic crystal waveguide by the time-domain coupled mode theory (CMT).....	123
APPENDIX B	131
Supermodes of coupled slot photonic crystal cavities calculated by tight-binding approximation.....	131
PUBLICATIONS.....	138
LIST OF FIGURES.....	139
LIST OF TABLES.....	146
BIBLIOGRAPHY.....	147

Acronym Glossary

SOI = Silicon on Insulator
BOX = Buried Oxide
CMOS = Complementary Metal Oxide Semiconductor
NIR = Near-infrared
PIC = Photonic integrated circuit
TPA = Two-photon absorption
CNT = Carbon nanotube
QW = Quantum well
SOH = Silicon-organic hybrid
DDMEBT = 2-[4-(dimethylamino)phenyl]-3-[[4-(dimethylamino)phenyl]ethynyl]buta-1,3-diene-1,1,4,4-tetracarbonitrile
QD = Quantum dot
HSQDL = Hybrid silicon quantum dot lasers
EBL = E-beam lithography
hBN = hexagonal Boron Nitride
CARTOON = CARBON nanoTube phOtONic devices on silicon
s-SWNT = Semiconducting single-walled carbon nanotubes
MWNT = Multi-walled CNTs
PL = Photoluminescence
PLE = Photoluminescence excitation
PFO = Polyfluorene
VSL = Variable strip length
ASE = Amplified spontaneous emission
LOC = Lab-on-a-Chip
PDMS = Polydimethylsiloxane
FOM = Figure of Merit
 Q = Quality factor
 V = Mode volume
PhC = Photonic crystal
WG = Waveguide
SPCW = Slot photonic crystal waveguide
QED = Quantum electrodynamic
SEM = Scanning electron microscope
RMS = Root-mean-square roughness
ER = Extinction Ratio
IL = Insertion loss
PMMA = Polymethylmethacrylate ($C_5O_2H_8$)_n
TIR = Total Internal Reflection
TM = Transverse magnetic
TE = Transverse electric
FT = Fourier transform
ICP = Inductively coupled plasma

Chapter 1. Introduction, context and motivations

This chapter brings the **context of silicon photonics** and the need for integration in/on silicon in order to compensate some drawbacks of silicon and enrich the functionalities of the silicon-based platform. Based on this, strategies to integrate diverse active materials in silicon are introduced, as well as the ability and **prospects of hybrid integration in the silicon photonic platform**. Building blocks in silicon photonics are presented to implement this integration process. Starting from simple structures as strip waveguides and slot waveguides, photonic crystal (PhC) structures are described in order to introduce later **slot photonic crystal cavities**, a typical resonator which can confine light in an extremely small mode volume with an order of a fraction of cubic wavelength. These resonators will be primarily considered for hybrid integration purpose in this Ph.D. work for their particular versatile properties. The design of these hollow core cavities as well as optical configurations based on these cavities will be presented in chapter 2. The obtained experimental results regarding the targeted hybrid integration direction will be discussed in chapter 3.

This chapter is constructed as follows. Section 1.1 presents the context and some recent realizations in silicon photonics and in hybrid silicon photonics. In section 1.2, strategies for the integration in silicon photonics of active materials are discussed. A specific focus is made on carbon nanotubes in section 1.2.2 due to their interesting optoelectronic properties and to the use that was made of them in the present work. In section 1.3, we list some main components in silicon photonics: strip waveguides, slot waveguides, microring resonators, PhC cavities and slot PhC cavities and explain our motivations to study slot PhC cavities for hybrid on-chip integration.

1.1 Context and recent realizations in hybrid silicon photonics

1.1.1 Short description of the recent progress in silicon photonics

Silicon photonics research began from around 2000 and has now become a mainstream photonic technology. Silicon-on-insulator (SOI) platform in which a thin crystalline silicon film on top of a buried silicon oxide layer resides on a silicon substrate, is the foundation of silicon photonics. The functional optical elements are realized in the thin top silicon layer. The high index contrast between silicon ($n_{Si} \approx 3.48$ at $\lambda = 1.55 \mu\text{m}$) and the bottom ($n_{SiO_2} \approx 1.44$ at $\lambda = 1.55 \mu\text{m}$) and top cladding materials guarantees light to be strongly guided (including in bended optical waveguides). Moreover, the bandgap of silicon is around 1.1 eV at room temperature, high quality crystalline large SOI wafers with a good SiO₂/Si interface are commercially available, and mature and well controlled clean room fabrication processes have been developed for the CMOS technology. All these reasons explain why silicon is used for low-loss optical waveguiding at telecommunication wavelengths, *i.e.* from 1.3 μm to 1.6 μm and why it has been extensively considered in the last years for the realization of both passive and active (optoelectronic) integrated components [1].

Silicon photonics can offer almost complete suite of photonic components, such as passive devices (waveguides [2], bends [3], multiplexers and demultiplexers [4]), and active devices (modulators in which the refractive index of silicon can be modified through carrier injection or depletion [5]–[8] and amplifiers [9]). **Silicon based modulators** are commonly achieved by exploiting the plasma dispersion effect instead of the Pockels one [10]. Depending on the desired applications, different optical structures can be employed, which will either favor the compactness, the bandwidth, or else the extinction ratio of the modulating structures. An example of an electro-optic carrier injection based modulator PIN junction is shown in Fig. 1.1.1(a) [11]. This small footprint 1D photonic crystal modulator (600 nm wide) possesses a high extinction ratio, *i.e.* 8 dB with only 0.5 V driving voltage and low insertion loss of 1 dB but operates at a quite low modulation speed (3 Gbps). In another work, a Mach-Zehnder PIN junction modulator was shown to provide a high-speed operation up to 50 Gbps with 4.3 dB extinction ratio and a driving voltage of 4.35 V with an insertion loss level of 7.2 dB [12]. In another typical high-level work, a ring resonator integrated into a PINIP structure based modulator was reported to operate

at 40 Gbps with a high extinction ratio of 12 dB, an insertion loss of 3 dB and a driving voltage of 5 V [13].

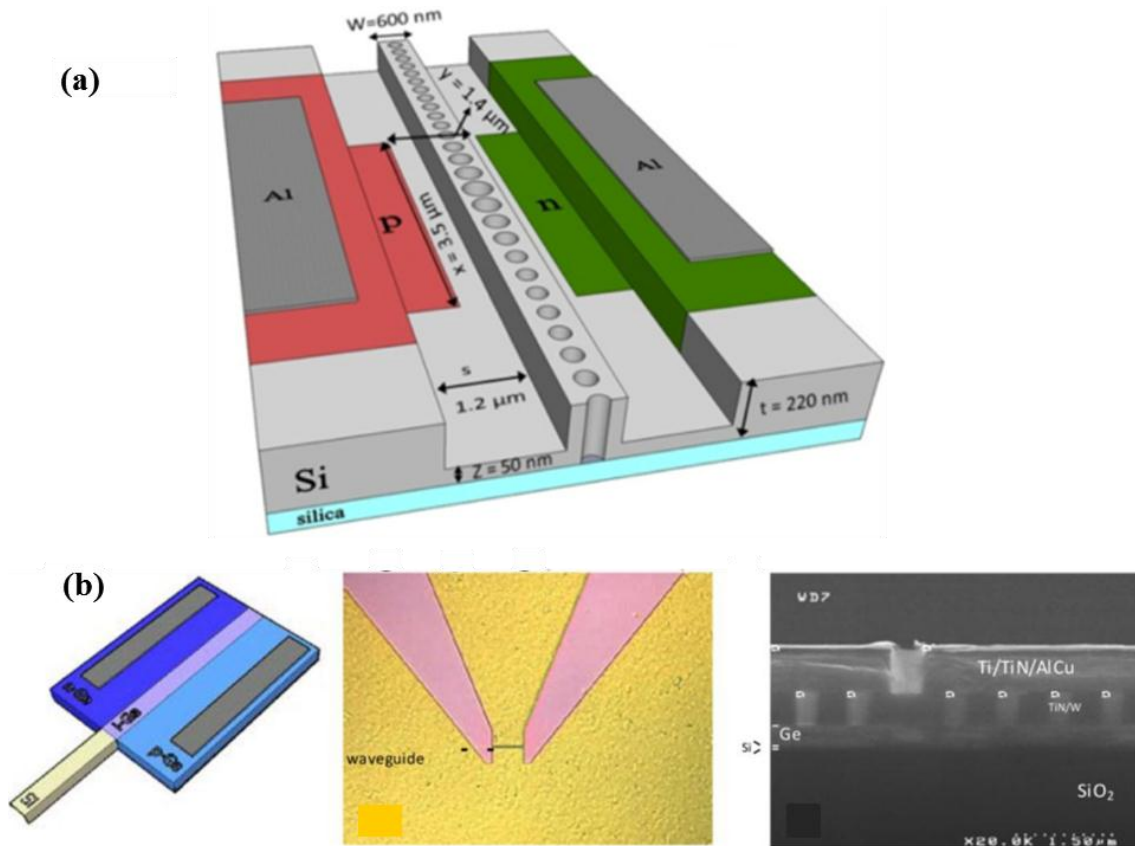


Fig. 1.1.1(a) 1D-silicon photonic crystal electro-optic modulator with Insertion Loss $IL = 1$ dB, Extinction ratio $ER = 8$ dB at a modulation speed of 3 Gbps [11] **(b)** Schematic view of a lateral pin Ge photodetector integrated at the end of a Si waveguide with responsivity of 0.8 A/W at 0.1 V bias, and a dark-current density of 80 A/cm² bandwidth up to 120 GHz at $\lambda = 1550$ nm, an open eye diagrams at 40 Gb/s were obtained under zero-bias [14].

For photodetectors, which are essential components of optical communication systems in the near-infrared (NIR) wavelength range, silicon exhibits some disadvantage, *i.e.* it is rather a poor absorber in the infrared because it is nearly transparent for $\lambda > 1.1 \mu\text{m}$. The absorption can be pushed up to 1.55 μm by the introduction of lattice damage through selective ion implantation. However, such structures still need high reverse biases (>10 V) and have limited responsivity, *i.e.* 0.14 A/W at -10 V bias [15]. On the contrary, Ge, which presents a strong absorption in the NIR wavelength range (up to 1.55 μm), can be considered for infrared optical detection. The hetero-epitaxy of Ge onto Si offers a simple, low-cost and high-throughput integration scheme that is compatible with the CMOS (Complementary Metal Oxide Semiconductor) technology. With recent efforts to overcome the lattice mismatch between Si and Ge (4.2%), Ge-on-Si

SOI platform covers different kinds of photonic components consisting of passive devices and active devices. PICs are pursued for optical communications to overcome the disadvantages of a discrete architecture, namely size, cost, power consumption and reliability. In this picture, integrated silicon photonics provides all the needed building blocks to establish on-chip optical links at high-data bit rates ($\gg 10$ Gbps) excepting an integrated monolithic silicon light source that is impeded by the silicon indirect bandgap.

This reason, added with the need for the realization of optical sensors as well as the need for an integrated nonlinear platform minimizing the effects of free carriers, make that integrating other active materials in/on silicon is in need.

1.1.2 Need for hybrid integration on silicon

In this manuscript, we define **hybrid integration on silicon** as bringing additional functionalities to Si by introducing “active” materials, *e.g.* soft materials like polymers, graphene, carbon nanotubes (CNTs), III/V compounds, functional oxides in/on silicon in the purpose of enriching the range of available physical effects (*e.g.* luminescence, $\chi^{(2)}$ and $\chi^{(3)}$ effects, etc.) for the realization of optical integrated functions.

The main purposes are: i) firstly benefit from this approach to achieve an optical source in silicon photonics, ii) minimize the effect of carriers on third-order nonlinearities, and lastly, iii) accomplish on-chip (bio-) sensing.

In the two first directions, integration on Si-based platform contributes to on-chip communications (either based on optoelectronic properties or all-optical ones by the use of nonlinear effects) by enabling important device building blocks such as rare-earth-doped Si/SiO₂ light-emitting devices [20], [21], or hybrid silicon lasers [22]–[32]. In the optical sensing applications, integrating materials on top of Si chips is intrinsically needed as the sensing material is deposited on top of the chips. Single/few molecules are grafted on top of photonic waveguiding structures (after the Si surface functionalization) and the role of the top covering solutions is to activate the chemical reactions between entities, *e.g.* antigen/antibody entities [33], [34].

There are various kinds of active materials to be integrated in silicon-based platform. In the next section, different related schemes are presented.

1.2 Integration in/on silicon photonics

1.2.1 Overview of the material families

Here, in this section we briefly review various material approaches to proceed to hybrid silicon integration. We will first discuss the direct band-gap material made of III-V compound semiconductors.

1.2.1.1 Class of III-V semiconductor materials

Owing to its indirect bandgap, silicon is prevented from becoming an ideal material for light emission while III-V materials (GaAs, InP...) with direct band-gap make efficient stimulated emission possible. Bonding III-V semiconductors onto SOI waveguides has succeeded in the realization of laser sources [25], [35], [36] (Fig. 1.2.1(a)) and amplifiers (Fig. 1.2.1(b)) [37]. In addition, high-speed III-V compound Si-based modulators can also be achieved due to the fact that III-V compounds can provide strong electro-optic (EO) effects [38].

Fig. 1.2.1(a) presents integrated hybrid InP/SOI lasers based on wafer bonding between a 200 mm SOI wafer with 400 nm silicon thickness and a 2'' InP wafer in which an optical cavity is defined by a III-V gain section of 400 μm length with two distributed Bragg Reflectors spaced 600 μm apart. In order to accomplish index matching between III-V and silicon waveguides, an adiabatic coupling taper is used from the 400 nm thick silicon waveguide to a 0.4 μm III-V tip. The laser performs with low threshold, *i.e.* 20 mA and high output power, *i.e.* >15 mW.

Fig. 1.2.1(b) illustrates a silicon amplifier comprising an offset multiple quantum well (QW) III-V region bonded to a SOI silicon waveguide. In this structure, the optical mode can see an electrically pumped gain from the III-V region while being guided by the underlying Si waveguide region. The fabricated device shows a maximum of 13 dB chip gain. The 3 dB output saturation power of the device is 11 dBm.

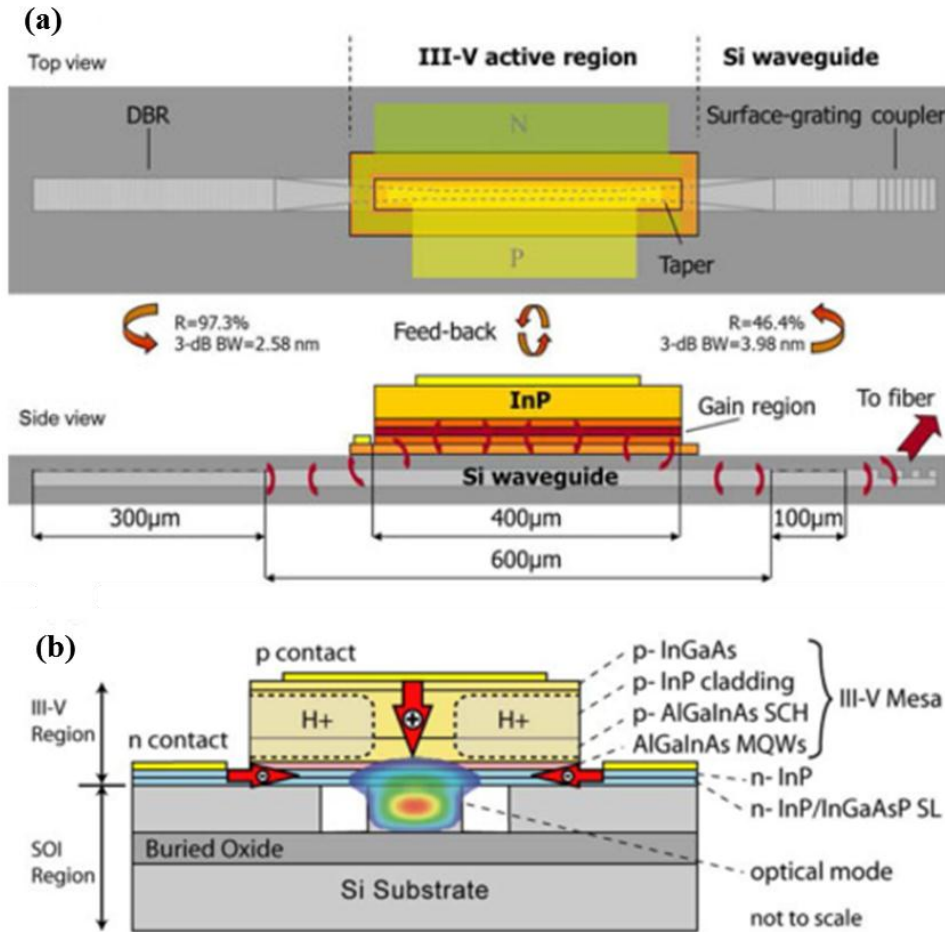


Fig. 1.2.1(a) Scheme of the hybrid III-V/Si laser in top and side views [36] **(b)** Integration of AlGaInAs-silicon evanescent amplifier, the optical mode can obtain electrically pumped gain from the III-V region why being guided by the underlying silicon waveguide region [37].

Regarding the fabrication flow of the structure, the Si waveguide was first fabricated in a CMOS fabrication process, then the III-V epitaxial structure grown on an InP substrate was transferred to the pattern silicon wafer through low-temperature oxygen plasma assisted wafer bonding with 300°C annealing temperature. It is noticeable that to inhibit the propagation of defects from the bonded layer into the QW regions, a superlattice region was used at the bonding interface.

The integration of III-V semiconductors in silicon photonics exploits the unique optical-electronic functionality of III-V technology and advanced low-cost volume production techniques associated with silicon. Overall, III/V diodes on Si are possible but bring additional complexity to the system integration schemes, either through bonding (wafer or chip bondings) or even through heteroepitaxy.

1.2.1.2 Class of polymers

Low optical loss polymers are of interest for photonic applications due to the potentials of these materials for low cost, ease of fabrication, and capability of their integration by simple techniques (*e.g.* spin-coating). For EO modulation, EO polymers can be engineered to obtain considerably large EO coefficients, γ_{33} , in order to reduce the half-way switching voltage. A CDL1/PMMA polymer with $\gamma_{33} = 60$ pm/V was for example prepared in Ref. [39] and served to the design of a device operating at the wavelength of 1318 nm and having a 0.8 V switching voltage, while even higher EO coefficients could be achieved, as $\gamma_{33} = 306$ pm/V at $\lambda = 1310$ nm [40]. In another complementary direction, the combination of silicon with active polymers was considered to minimize the effect of two-photon absorption (TPA) in silicon. Fig. 1.2.2(a) illustrates a silicon-organic hybrid (SOH) approach in which a silicon slotted waveguide was filled and surrounded by a high $\chi^{(3)}$ -nonlinear low TPA material nonlinear organic cladding processed by vapour deposition[41].

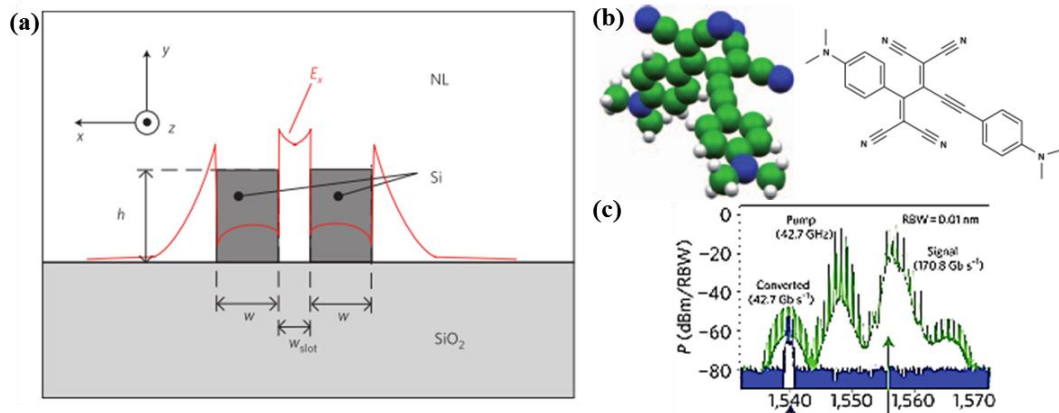


Fig. 1.2.2(a) Cross-section of a slotted SOI silicon waveguide covered by a nonlinear optical organic material (NL), w , h are the width and height of the ribs, respectively and w_{slot} is the width of the slot. The E_x component of the fundamental quasi-TE mode is confined in the slot and strongly enhanced within the low-index material filling in the slot. **(b)** Molecular structure of the organic material DDMEBT **(c)** Transmission spectra of SOH waveguide (green) and after band-pass filtering (blue) [41].

The geometry of the slot waveguide was chosen to provide a maximum electric field magnitude inside the slot while the organic material was developed by molecular beam deposition to obtain optimum nonlinear optical properties. This structure supported a nonlinear coefficient γ of around $100 \text{ W}^{-1}\text{m}^{-1}$, *i.e.* much higher than in optical fibers. In addition, as shown in Fig. 1.2.2(c), this SOH waveguide could demultiplex a 170.8 Gbs^{-1} telecommunication signal to 42.7 Gbs^{-1}

one by four wave mixing, demonstrating the viability of the proposed hybrid-on-silicon approach for all optical processing. The DDMEBT developed material(2-[4-(dimethylamino)phenyl]-3-[[4-(dimethylamino)phenyl]ethynyl]buta-1,3-diene-1,1,4,4-tetracarbonitrile) proved to have an off-resonant Kerr coefficient $n_2 \approx (1.7 \pm 0.8) \times 10^{-17} \text{ m}^2\text{W}^{-1}$ at $\lambda = 1.5 \text{ }\mu\text{m}$, a linear refractive index $n_0 = 1.8 \pm 0.1$, and a bulk material TPA figure-of-merit FOM_{TPA}^{Bulk} of 5.0 [42], to be compared with the 0.38 value of silicon around $\lambda = 1.5 \text{ }\mu\text{m}$.

1.2.1.3 Class of quantum dots

Quantum dots (QDs) are nanocrystals of a semiconductor material with a core (*e.g.* CdSe, CdS, InAs, InP, PbSe) –shell (ZnS) structure and a diameter that typically ranges from 2 nm to 10 nm. Direct bandgap semiconducting QDs own three dimensional confinement of carriers and exhibit a strong potential for light emission. They have been thus considered for the realization of QD lasers in silicon photonics [43], [44]. QD lasers support higher temperature stability and lower threshold current densities compared with quantum well lasers, *e.g.* QD lasers have negligible threshold variation between -40 and 100°C [45] and have threshold current densities as low as 19 Acm^{-2} in GaAs based QD lasers [46]. Various integration schemes have been employed such as external coupling via flip-chip bonding and butt coupling, wafer bonding and epitaxial growth [43]. Moreover, the integration of such a QD laser source directly on silicon can bring some practical benefits. It not only would allow high-volume, low-cost integrated III-V lasers with high-quality and reliable silicon photonics from CMOS foundries but also would reduce packaging costs. A typical work going into that direction was for example, to integrate an InAs QD laser on a silicon substrate by wafer-bonding in order to exploit the low loss properties of silicon waveguides [44], hybrid silicon quantum dot lasers (HSQDL) as depicted in Fig. 1.2.3(a)-(b).

It consisted of an SOI wafer with etched air trenches to form a silicon rib waveguide. A p-i-n GaAs-based diode laser structure with an InAs QD active region and a 320 nm thick 8 layers of QDs was transferred to a SOI substrate using an O₂ plasma-assisted direct bonding process. This device proved to work properly up to high temperature operation of $\sim 100^\circ\text{C}$, with a low threshold current density of $\sim 271 \text{ Acm}^{-2}$.

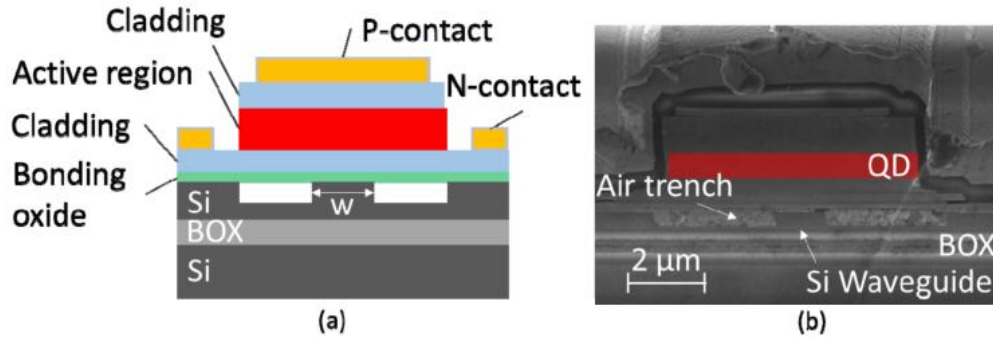


Fig. 1.2.3(a) Cross-sectional diagram of HSQDL device **(b)** Scanning electron micrograph of a polished cross section. The tapers were polished off in order to show the gain region. The air trench between the rib waveguide and the silicon cladding is filled with polishing residue [44].

Other kinds of materials which have attracted increasing attention in photonic applications thanks to their unusual optical and electrical properties are the carbon-based materials. In the following sub-section (1.2.1.4), we will discuss on graphene.

1.2.1.4 Graphene

Graphene is one kind of allotropes of carbon in the form of a 2D, atomic scale, honey-comb lattice in which one atom forms each vertex. It is known as the single layer of graphite, in which carbon atoms are bonded in sheets of a hexagonal lattice. It is of great interest because of its exceptional electrical and optical properties, *i.e.* graphene optical transitions can be controlled by shifting the electronic Fermi level, E_F , of graphene with electrostatic gating thanks to its extremely high carrier mobility (exceeding $200\,000\text{ cm}^2\text{V}^{-1}\text{s}^{-1}$ at room temperature [47]). A strong electro-absorption effect presents in graphene, also implies its strong potential for being used as an active medium in high speed optical electro-absorption modulator schemes. However, one of the challenges involved in a direct graphene modulator is the limited absorption of a monolayer. This can be overcome by integrating graphene with optical waveguides, which greatly increases the light/graphene interaction length through the coupling between the evanescent waves and graphene [48], or with optical cavities in which graphene can strongly interact with the cavity resonant field resulting in strong modulation with a few micrometers device footprints instead of several tens micrometers long active graphene channels [49]. Recently, integration of graphene into silicon-based photonic devices has been intensively researched and has brought a lot of high-performance optoelectronic integrated devices: modulators (high speeds with low power consumption and relatively small footprint [50]),

polarizers and photodetectors, and operating at extremely broad spectral range extending from the ultraviolet, visible and near-infrared to the mid-infrared, far-infrared and even to the terahertz and microwave regions due to its unique linear energy–momentum dispersion relation [51]. For example, a graphene-on-graphene based modulator (consisting of two separated graphene layers located on a silicon waveguide surrounded by silica) could spend power consumption as low as the best Si-based modulator, *i.e.* <0.5 fJ/bit [52], and a small footprint photodetector down to $50 \mu\text{m}^2$ due to graphene’s high optical absorption was demonstrated in Ref. [47].

An example of a high-speed electro-absorption modulator based on a graphene-boron nitride (BN) heterostructure integrated on silicon cavity is illustrated, as in Fig. 1.2.4 [49].

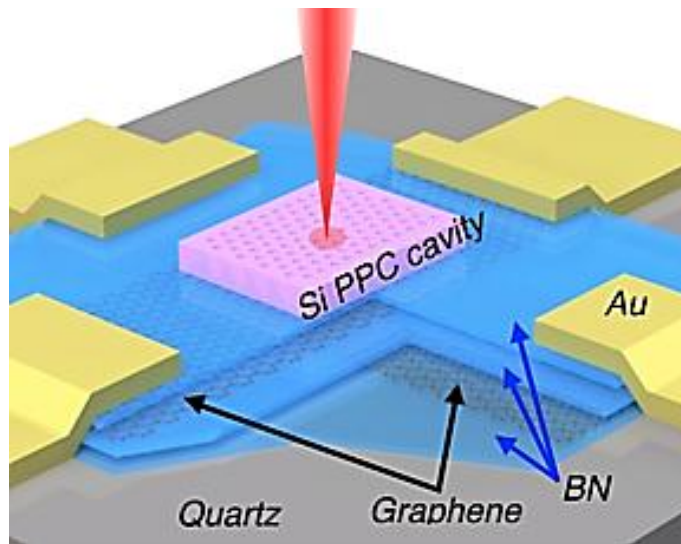


Fig. 1.2.4 Schematic of a graphene–hexagonal Boron Nitride (hBN) heterostructure-based planar electro-optic modulator. The dual-layer graphene capacitor on quartz substrate is optically coupled to the photonic crystal cavity [49].

In this modulator, a BN/graphene/BN/ graphene/BN five-layer stack was built by the van der Waals (vdW) assembly technique and then transferred to a quartz substrate. The two graphene sheets were positioned as crossed stripes in order to be contacted individually. The graphene edges were exposed by plasma etching the five-layer stack using a hydrogen-silsesquioxane (HSQ) resist mask patterned by electron beam lithography (EBL). Metal contacts of Cr/Pd/Au (1/20/50 nm) were deposited by electron beam evaporation, making edge-contact to the two graphene sheets. In this encapsulated dual-layer graphene structure, each one of the graphene sheets can be viewed as a gate and supplies gate voltage to the other.

The graphene-BN heterostructures made by the vdW technique demonstrated extremely high room-temperature mobility up to $140\,000\text{ cm}^2\text{V}^{-1}\text{s}^{-1}$, which is comparable to the theoretical acoustic phonon-scattering limit. The photonic crystal cavity (see Fig. 1.2.4) was fabricated on a SOI wafer by the combination of EBL, dry etching, and wet etching, then transferred onto the top surface of the prefabricated five-layer-stack device by the same technique. This electro-absorption modulator possessed a maximum modulation depth at 3.2 dB with a swing voltage of only 2.5 V, and high operation speed with a 3 dB cut-off frequency $f_c = 1.2\text{ GHz}$, switching energy approximately 1 pJ/bit, and a small footprint of several micrometers square. However, in the first demonstration, the modulation speed was limited to several kHz because the modulator required electrolyte doping to change Fermi level.

To sum up this section, with strong electro-absorption properties, graphene exhibits the prospects to bring complementary added values to the silicon platform while being compatible with the CMOS technology, allowing for monolithic integration with silicon through CVD growth techniques. However, one of the challenges to integrate graphene as an active medium in silicon photonic devices is raised by its ultra-small thinness which limits the light-matter interaction [53].

In this thesis, we have pursued another approach consisting of using **carbon nanotubes (CNTs)**, which also present very interesting optoelectronic properties, in view of their integration with silicon photonic structures (see chapter 3). For this reason, a **specific focus** is put on them hereafter in section 1.2.2.

1.2.2 Special focus on carbon nanotubes (CNTs)

In the carbon-based material family, carbon nanotubes (CNTs), especially single-walled carbon nanotubes (SWNTs) provide interesting physical properties for applications in optoelectronics. Recently, great efforts have been devoted in integrating single or few CNTs in photonic devices in order to achieve an integrated electroactive light source. Ring resonators [54], [55], photonic crystal cavities [56], or photonic crystal nanobeam cavities [57], [58] have been considered. In the same time, CNTs have been of great interest in the last years in our group. Dr. Laurent Vivien has led the **FP7-ICT CARTOON project** (2013–2016/December): “CARbon nanoTube

phOtONic devices on silicon”, with the primary goal of the development of a novel strategy for hybridizing silicon with CNTs for the realization of active integrated functions. I have participated in this project, and, in the scheme of my Ph.D. work, **I have exploited semiconducting single-walled carbon nanotubes (s-SWNTs) integrated in slot photonic crystal cavities in view of the enhancement of their light emission and of the coupling of their photoluminescence into mm-long integrated optical waveguides.**

1.2.2.1 Structure of CNTs

CNTs, discovered in 1991, are formed by **rolling-up a graphene sheet into a tube**. CNTs are nearly ideal one-dimensional (1D) systems, with diameters of only 1-3nm and lengths that can be on the scale of centimeters [59].

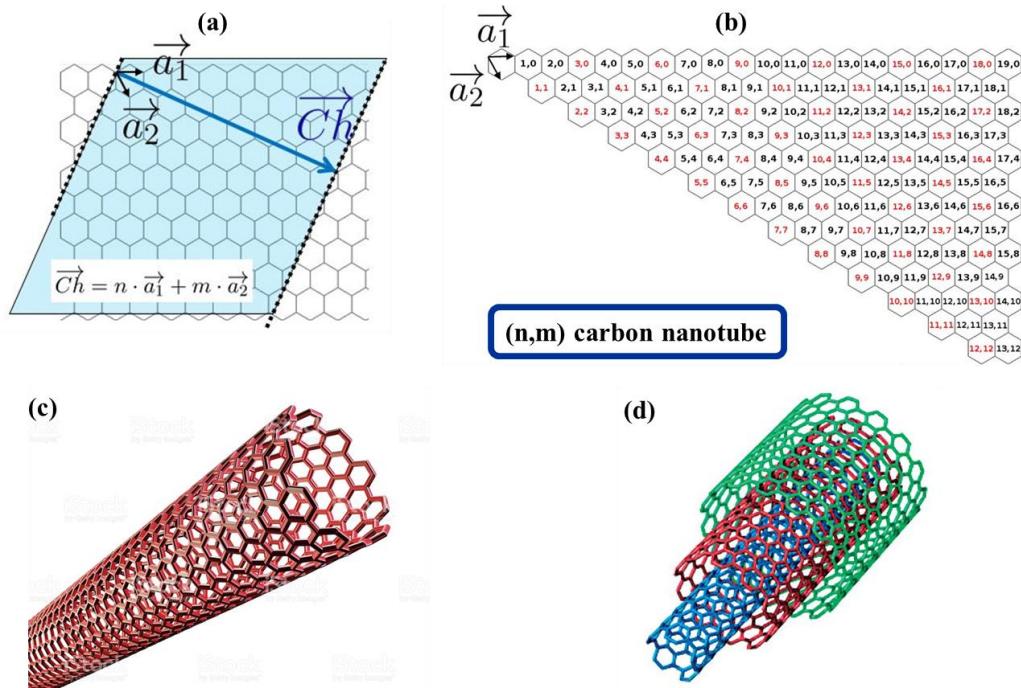


Fig. 1.2.5(a) Chiral vector indicates the rolling up direction **(b)** Different morphologies of CNTs **(c)** Single-walled CNTs (SWNTs), and **(d)** Multi-walled CNTs (MWNTs).

The chiral vector \vec{C}_h , which indicates the CNT rolling up direction, is defined as $\vec{C}_h = n\vec{a}_1 + m\vec{a}_2$ (Fig. 1.2.5(a)) where \vec{a}_1 and \vec{a}_2 are basis vectors of graphene lattice ($a_1 = a_2 = a$) and (n,m) are integers, called the chiral index or “chirality”. Fig. 1.2.5(b) shows different morphologies of CNTs for different values of (n,m) . The diameter of SWNTs is expressed as

$d = \frac{|\vec{C}_h|}{\pi} = \frac{a}{\pi} \sqrt{n^2 + nm + m^2}$. Depending on the chirality (n,m) , CNTs can be divided into zigzag

(where n or $m=0$), armchair (where $n=m$) or chiral structures (other cases of n, m). The armchair tubes are metallic-like. If $n-m=3i$, where i is a nonzero integer, the tubes are small-gap ($\approx 1-100$ meV) semiconductors, and all others are medium-gap ($\approx 0.5-1$ eV) semiconductors. **Statistically, a mix of CNTs contains 1/3 metallic and 2/3 semiconducting chiralities.** Based on the number of concentrically rolled-up graphene sheets, CNTs are classified into SWNTs (Fig. 1.2.5(c)) and multi-walled CNTs (MWNT) (Fig. 1.2.5(d)).

SWNTs are of interest for photonics because they possess outstanding electrical and thermal conductivities and enormous tensile strength, *i.e.* individual SWNTs have current carrying capacities of 10^9 Acm⁻², higher than copper or gold. Semiconducting species also exhibit higher electron mobility than silicon. Room temperature thermal conductivity of a single nanotube can be compared with that of diamond or in-plane graphite, and individual SWNTs are significantly stronger than steel: the tensile strengths of SWNTs are ~ 100 times greater than steel at 1/16th the weight [60]. **More interestingly, in the context of the present Ph.D. manuscript, they present interesting optoelectronic properties.**

1.2.2.2 Optoelectronic properties of semiconducting single-walled carbon nanotubes

1.2.2.2.1 Optical bands and excitonic effects

Electronic and optical properties of semiconducting SWNTs (s-SWNTs) are illustrated in Fig. 1.2.6 [61]. Band structure of s-SWNTs is made of a series of subbands as depicted in Fig. 1.2.6(a). Direct bandgap longitudinal transitions only occur between two optical bands with same indices (E_{ii} , $i = 1, 2, 3 \dots$). In addition, CNTs are characterized by the strong influence of excitons. Electron and hole interactions in CNTs indeed allow the formation of electron-hole pairs giving rise to a series of bound states. Moreover, the exciton binding energy in CNTs have been estimated and were proved to be large as great as few hundreds of meV [59].

Fig. 1.2.6(a)-(b) depict the simplest physical picture of PL. Light absorption occurs at the E_{22} exciton energy while recombination appears at E_{11} exciton one. Absorption and emission energies are naturally dependent on the nanotube diameter and chirality. From these key features,

we will understand the behaviour of the absorption spectrum of our prepared SWNTs solutions (see section 3.3.2).

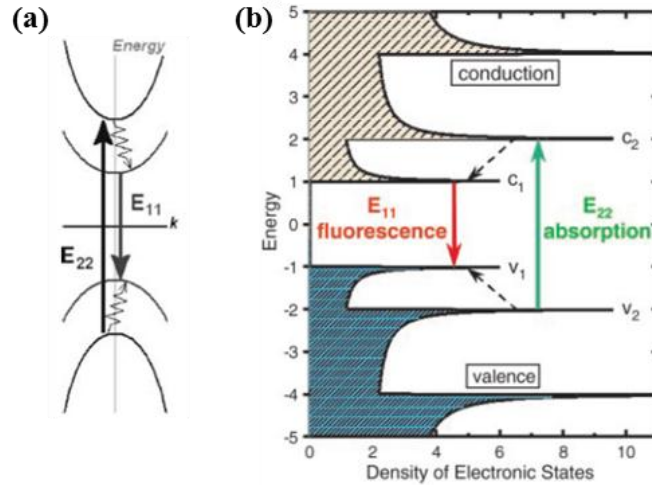


Fig. 1.2.6(a) The electronic dispersion relation of SWNTs (comprising the excitonic correction) [61] **(b)** Associated with each subband is a density of states that exhibit a singularity called a van Hove singularity of the semiconducting SWNTs. Solid line arrows depict the optical excitation and emission transitions of interest, while the dashed arrows denote non-radiative relaxation of the electron (in the conduction band) and hole (in the valence band) before emission [62].

1.2.2.2 Photoluminescence

s-SWNTs emit near-infrared light upon excitation, including photoluminescence (PL). They exhibit near-infrared E_{11} PL via E_{22} excitation [62]. The E_{11} energy is inversely proportional to the diameter of the SWNTs [61]. As a result, the absorption and emission properties of s-SWNTs can be studied by photoluminescence excitation (PLE) maps, which then produce information on the composition of the nanotube sample [62]. Fig. 1.2.7 shows an example of a PL map of SWNTs produced by the HiPCO process dispersed in the toluene solvent and selectively solubilized by PFO-P polymers [63].

Because of the unique emission properties of semiconducting SWNTs (s-SWNTs), they are interesting nanoscale infrared light emitters, which exhibit room temperature photo- and electroluminescence [64]–[67], and can be considered for the realization of optical sources in addition to their potentials for the realization of photodetectors [68] and optical modulators relying on intrinsically fast non-linear (Stark and Kerr) effects [69]. One possibility for enhancing their optoelectronic properties is to place them in or close to hollow core optical resonators in order to benefit from an increased optical density of states [54], [70]–[73].

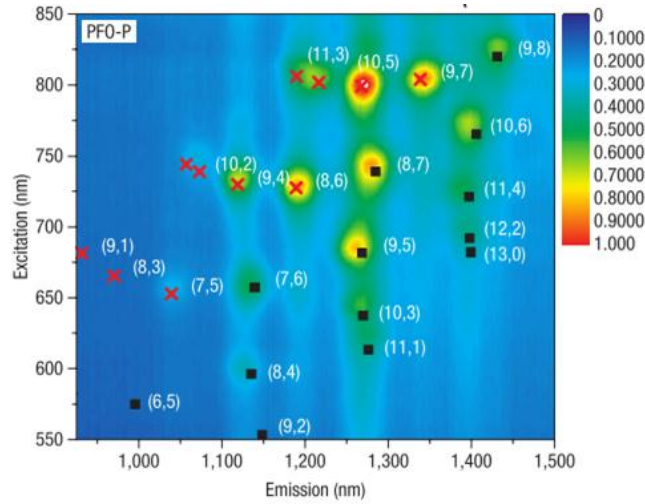


Fig. 1.2.7 Photoluminescence excitation maps of SWNTs in toluene solution prepared using nanotubes grown by the HiPCO process as starting material, and selectively solubilized by polymer poly(9,9-dioctylfluorenyl2,7-divinyl) PFO-P. The red crosses correspond to the family of tubes with $n-m = 3q-1$ and the black squares to those for $n-m = 3q+1$ [63].

1.2.2.2.3 State-of-the-art regarding optical gain

One challenge to exploit the emission properties of CNTs in view of optical gain originates from the need to circumvent the existing nonradiative des-excitation mechanisms, such as the Auger recombination or the energy transfer to m-SWNTs. Optical gain of s-SWNTs extracted by polyfluorene (PFO) method [74] was observed by our group [70] by the variable strip length (VSL) method. Fig. 1.2.8(a) illustrates the employed VSL method. In that work, a PFO wrapped SWNTs thin film was optically excited by an optical parametric oscillator laser emitting at a wavelength of 740 nm while the amplified spontaneous emission (ASE) of CNTs was collected at the edge of the strip pump beam. The ASE intensity (I_{ASE}) was described by this following equation:

$$I_{ASE}(l) \sim \frac{I_{Spont}}{g_{int} - \alpha} \left(e^{g_{int} l} - 1 \right) \quad (1.2.1)$$

with I_{Spont} the spontaneous emission intensity per length unit, α the overall loss coefficient, l the excitation length, and g_{int} the intrinsic gain.

A linewidth narrowing of 29% was observed for the (8, 7) nanotube at 1300 nm as well as similar linewidth narrowing feature in (8, 6) nanotubes at 1200 nm, as presented in Fig. 1.2.8(b).

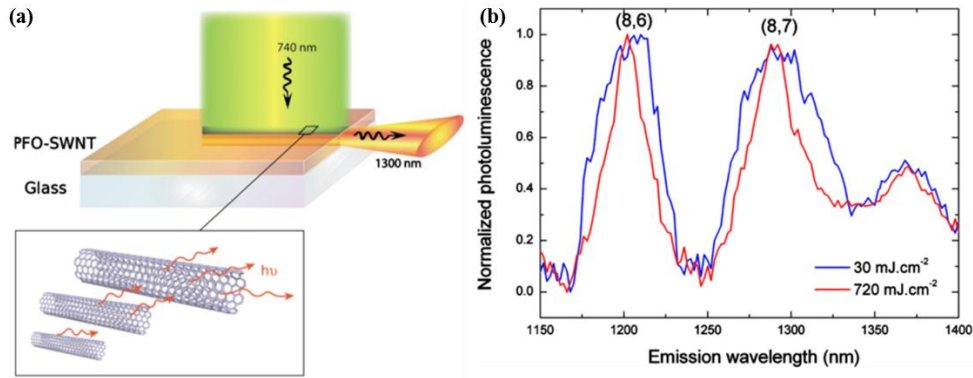


Fig. 1.2.8(a) Schematic representation of a variable strip length experiment to estimate optical gain of s-SWNTs **(b)** High resolution normalized spectra of the amplified spontaneous emission fluences with an excitation wavelength of 740 nm. A 29% linewidth narrowing (FWHM) from 63 to 45 nm was observed on the photoluminescence of (8, 7) nanotube at 1300 nm and linewidth narrowing of 28% (FWHM) from 44 to 32 nm was also observed for the (8, 6) nanotube at 1200 nm [70].

Then, optical gain could be estimated to around 190 cm^{-1} at the wavelength of 1300 nm from equation (1.2.1). This high value of intrinsic gain in CNTs showed the potentials of integrating s-SWNTs with photonic structures for on-chip light emission. This early demonstration was achieved by using planar optical waveguides only, and it was among the motivations of the CARTOON FP7 project to push the integration of CNTs in more advanced devices, including high- Q resonators. In this view, our contribution was the study of CNTs integration into slot silicon on insulator photonic crystal cavities.

1.2.3 Integration in silicon photonics for sensing

In another direction, one of the applications where silicon photonic devices have recently gained considerable attention is the field of integrated optical bio-chemical and gas sensing. Biosensors are devices able to detect a specific substance by converting the recognition from a biological entity (*i.e.* DNA, antibody, enzyme) into an physicochemical transduction signal that can be further processed and related to the concentration of the substance under analysis [75]. Taking advantage of a high index contrast material system and the well-established CMOS fabrication technology, highly compact and sensitive sensors as well as sensor arrays have been proposed and fabricated with low cost, leading to Lab-on-a-Chip (LOC) platform in which all functionalities are integrated in the same wafer, from sample preparation (filtration, homogenization and dilution), analyte detection, transducer readout to signal delivery [76].

Fig. 1.2.9(a) illustrates the evanescent field detection principle used in optical label-free biosensors.

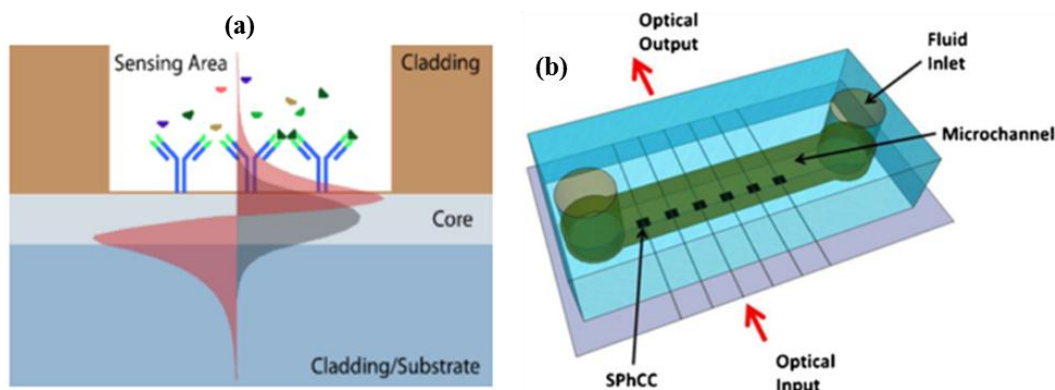


Fig. 1.2.9(a) Evanescent wave detection principle [77] **(b)** Schematic of slotted photonic crystal sensors with integrated PDMS microfluidics [78].

In a waveguide, due to total internal reflection at the interfaces, light propagates through the core producing an evanescent wave at the substrate and cladding boundaries [79]. In this scheme, if a sensing window is etched in the cladding, opening an access to the core surface, the behavior of the guided light in the core is directly related to any perturbation taking place in the evanescent area over the surface [77]. In resonators, there is a high field enhancement, *i.e.* the recirculating field is much larger than the incident field. Light traveling in a cavity interacts many times with objects inside or in the vicinity of the cavity before escaping from it. This enhanced light-matter interaction often makes optical resonators important parts of optical sensors.

The diversity of silicon photonic based sensing systems playing the role of optical transducers is large: Mach-Zehnder Interferometers, microdisks, microrings, photonic crystal cavities can be the base of biosensors, as summarized in Table 1.1. One of the challenges in silicon-based biosensors is functionalizing the surface in order to attach targeted biomolecules which are responsible for a local change of the optical index. The selection of an appropriate procedure to immobilize the biological elements on the sensor surface has become a critical step in the biosensor area as it guarantees the sensitivity, selectivity, stability and longevity of the biosensor, and enormous efforts are continuously made in order to optimize novel strategies according to the applications [80]. The immobilization process should not only guarantee an efficient coverage of the transducer surface with the biomolecules, while keeping intact their properties

(*e.g.* functionality, structure, biological activity, affinity, specificity), but it should also ensure their stability for storage and regeneration. A wide variety of biomolecules can be used as bioreceptors, *i.e.* antibodies, nucleic acid sequences, peptides, enzymes, cell receptors and many others. The selected biomolecule is dictated by the application and must be chosen to be highly specific for the target molecule and stable enough to be immobilized without losing functionality [75]. For example, silanization of the microring surface by condensation of surface silanols with functionalized silanes was used to provide a suitable biointerface between the transducer element and the biological medium[81], and in a similar sense surface of a photonic crystal cavity in Fig. 1.2.8(b) was functionalized to attach biotin molecules to the oxidized SOI [78].

In order to realize LOC devices, microfluidics must be taken into account (*i.e.* flow-cell volume, means of sample injection, diffusion, dispersion). Micro-fluidic channels should be fabricated and positioned with respect to silicon photonic devices and structures and various tested solutions with refractive index $n \approx 1.33$ can be injected through these microfluidic channels, such as polydimethylsiloxane (PDMS) microfluidic channels depicted in Fig. 1.2.9(b) [78]. Adapting to various kinds of silicon-based structures, fluidics can be ranged between micro and to nano sizes [75].

It is worth noticing that at least two parameters are generally necessary to define the properties of resonance sensors. First, the bulk sensitivity S of a refractive index sensor is defined as $S = \frac{d\lambda}{dn}$, *i.e.* magnitude in shift of the resonance wavelength versus the change in refractive index in case of introducing different cladding index materials. Second, the detection limit is defined as $DL = \frac{R}{S}$ [82], where S is the sensitivity and R is the sensor resolution - the smallest spectral shift that can be accurately measured. For label-free sensors in which spectral minimum wavelength detuning is dominated by the optical resonators, $R \sim \frac{\lambda_0}{Q}$, so that $DL \sim \frac{\lambda_0}{SQ}$. The Figure of Merit (*FOM*) then directly deduced from DL can be defined as $FOM = \frac{SQ}{\lambda_0}$, in which λ_0 is resonance wavelength and Q is the quality factor of the resonator [83].

Table 1.1 summarizes some sensing properties of optical sensing schemes in silicon photonics.

Table 1.1 Sensitivity, Quality factor (Q), FOM of various optical sensing systems

Sensing system		Q -factor in water (at telecom range)	Size	Sensitivity (nm/RIU)	FOM
	Mach-Zehnder interferometer (MZI) [84]	500	5 mm long	2000	645
	Microring [85]	2×10^3	50 μm radius	1300	1800
PhC based	1D nanobeam cavity [86]	2×10^4	Several	600	9500
	PhC slab [87]	3×10^3	tens μm long	644	1250
	Slot PhC cavity [78]	4×10^3		1538	3850
Plasmonic based	Metal–Insulator–Metal	105	744 nm	1160	80
	Plasmonic Disk Cavities [88]		radius		

As discussed in detail in chapter 3, our slot 2D photonic crystal cavities based on a non-free standing approach and covered by water present a Q around 25 000 with a sensitivity around 235 nm/RIU, *i.e.* a FOM of around 3790 with foot print of several tens μm^2 , close to the state-of-the-art in optical index sensing with Si structures.

In all this context related to hybrid integration, we have seen that important metrics in all situations is the **overlap factor between light and matter**. Hence, optical components with **small footprint and mode confinement in low-index materials** are needed. This demand can be met by using slot waveguide based resonators. Before presenting the behaviours of these structures, we will introduce step by step the main silicon photonic devices from strip waveguides, *i.e.* from simple components to the slotted photonic crystal cavities under interest in this Ph.D. work.

1.3 Silicon photonic devices

1.3.1 Strip waveguides

Strip waveguides are the basic building blocks in silicon photonic integrated circuits to connect different blocks by light propagation, as schematically depicted in Fig. 1.3.1(a). Under CMOS processes, strip waveguides are fabricated by lithography and etching, so that the shapes of waveguide cross-sections are preferentially rectangular. Optical modes are found by solving the Maxwell equations. Strip waveguides support TE-like and TM-like modes, as illustrated in Fig. 1.3.1(b). As visible, the modes are well confined in the core region thanks to the high index contrast between silicon ($n_{\text{Si}} \approx 3.48$) and silica ($n_{\text{SiO}_2} \approx 1.44$) at $\lambda = 1.55 \mu\text{m}$ and the thickness of

silicon core can be shrunk down to submicron sizes. In silicon waveguides, propagation losses are mainly due to interaction of the waveguiding mode with the sidewall surface roughness at the core-cladding interfaces [3], [89].

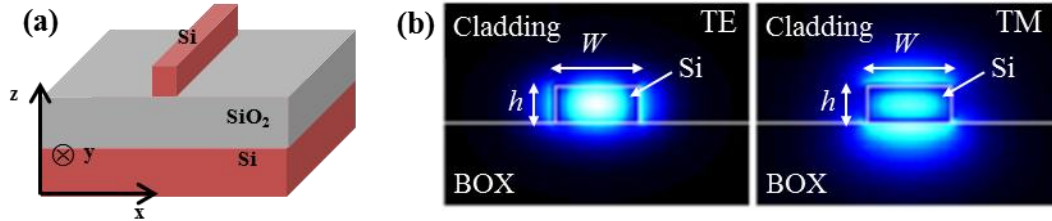


Fig. 1.3.1(a) Schematic of a strip waveguide **(b)** TE and TM modes in a silicon on insulator strip waveguide with an $h = 220$ nm wafer thickness and a waveguide width $W = 450$ nm. The upper cladding has the same refractive index as silica at the wavelength of 1550 nm [89].

TE modes have a large overlap with the sidewalls, while TM modes have a larger overlap with the top and bottom interfaces, as shown in Fig. 1.3.1 [89], which makes the two modes families behave differently with respect to optical losses. For commonly used SOI wafers, the silicon surface is flat with a root-mean-square roughness (RMS) of less than 0.1 nm thanks to the SOI wafer fabrication technology. Waveguide side-wall roughness level is determined by the lithography and etching processes and is typically on the order of few nanometers, much larger than the top/bottom surface roughness [90]. Scattering thus remains the dominant cause of loss in silicon waveguides. In spite of these technical constraints, optical losses of SOI waveguides have been reduced to typically $\sim 0.45 \pm 0.12$ dB/cm at $\lambda = 1.55$ μm in TE-like polarization [91], making them an efficient basis for the realization of various passive on-chip optical function. In typical SOI waveguides designed for telecom wavelengths, *e.g.* with ~ 400 nm \times ~ 220 nm dimensions, TM modes possess typically $\sim 35\%$ of light power confined in the top cladding material but it is only $\sim 15\%$ for TE modes, which are yet the preferred configuration for many on-chip applications. One of the motivations for introducing slot waveguides was precisely to increase the light power confinement out-of the waveguide core of TE-like modes.

1.3.2 Slot waveguides

Slot waveguides (see Fig. 1.3.2(a)), first introduced by Almeida *et al.*[92] by inserting a slot within the central part of a Si wire typically consist of two strips of high-index material that

enclose a sub-wavelength low-index slot region. Discontinuities of the normal components of the electric field at the high-index-contrast interfaces between silicon area and the material filling the slot lead to a partial mode confinement effect within the slot, *i.e.* within the low-index material (Fig. 1.3.2(b) and (c)):

$$\vec{D}_{Si}^n = \vec{D}_{Clad}^n \Rightarrow \epsilon_{Si} \vec{E}_{Si}^n = \epsilon_{Clad} \vec{E}_{Clad}^n \Rightarrow \vec{E}_{Clad}^n = \frac{\epsilon_{Si}}{\epsilon_{Clad}} \vec{E}_{Si}^n \quad (1.3.1)$$

The power confinement ratio in the low-index void is around 30% of the total power in typical slot SOI waveguides configurations [92].

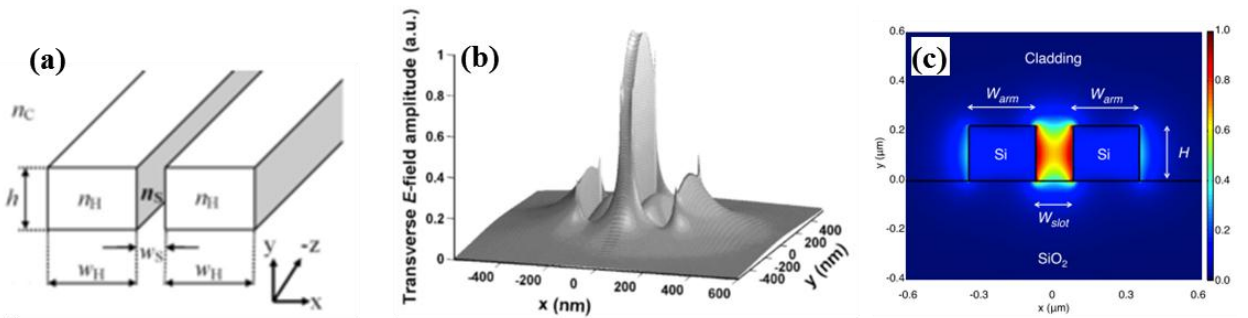


Fig. 1.3.2(a) Schematic of a slot waveguide **(b)** 3D surface plot of transverse E -field profile of the quasi-TE mode in a SOI-based slot waveguide at $\lambda_0 = 1.55 \mu\text{m}$, with $n_H = 3.48$, $n_S = n_C = 1.44$, $w_H = 180 \text{ nm}$, $w_S = 50 \text{ nm}$ and $h = 300 \text{ nm}$. The origin of the coordinate system is located at the center of the waveguide, with a horizontal x axis and a vertical y axis [92] **(c)** Simulated mode profile for the fundamental quasi-TE mode. $W_{arm} = 270 \text{ nm}$, $W_{slot} = 150 \text{ nm}$, $H = 220 \text{ nm}$, and the top cladding material is silicon oxide [93].

However the extreme confinement of light in the slot results in enhanced propagation losses due to the increased interaction of the waveguiding mode with the silicon rails sidewall roughness [91]. Previous works have yet shown that optimization of the fabrication processes can allow minimizing them down to around 1 dB/cm [94].

1.3.3 Microring resonators

Apart from (simple) strip waveguides, photon recycling inside optical resonators is of special interest for various applications including filtering, switching/modulation, and, to some of extent, to all situations requiring enhanced light-matter interactions. In the class of dielectric resonators, microring resonators, which are based on bended and closed on themselves waveguides, have been considered for years in silicon photonics. Basically, ring resonators can be deployed from

strip or slot waveguides. In any case, tight waveguide bends with low radiation losses are needed for achieving compact and high quality factor devices. Early work showed that 90° bending strip SOI waveguides can provide losses at 0.086 dB/turn for bending radii as small as $R = 1 \mu\text{m}$ or even down to 0.013 dB/turn for $R = 2 \mu\text{m}$ at the wavelength of 1500 nm [3]. On their side, bending losses of slot SOI waveguides are intrinsically larger than those of strip guides but can yet be controlled and minimized down to 0.02 dB/ μm for radius values larger around $5 \mu\text{m}$ (and are lower for larger radius values) [95].

To enter a little bit more into details, a ring resonator consists of an optical waveguide which is looped back on itself and a coupling mechanism to access the loop, as shown in Fig. 1.3.3. When the waves in the loop build up a round trip phase shift that equals an integer times 2π , the waves interfere constructively, and the cavity is in resonance. There are several configurations to form a ring resonator, which can be *all-pass* or *add-drop* (see Fig. 1.3.3).

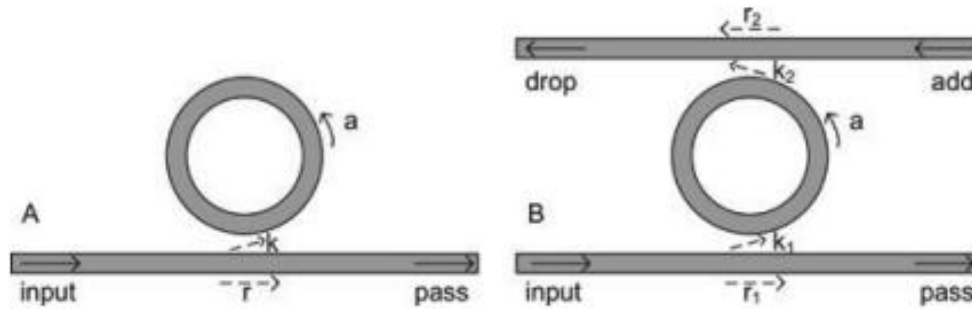


Fig. 1.3.3(A) All-pass and (B) add-drop ring resonator [96].

These devices have received a considerable interest in the literature and we will only quote here few typical results.

A SOI microring resonators based on a silicon strip waveguide as the one shown in Fig. 1.3.4(a), can possess a loaded Q -factor of 139 000 with a radius of $20 \mu\text{m}$ and propagation losses of 1.9 dB/cm [97]. In case of larger radius ring, a loaded Q -factor of 280 000 was obtained in a $50 \mu\text{m}$ -radius etchless silicon photonic ring resonators with losses of 0.8 dB/cm at the wavelength of 1550 nm [98]. In slot waveguide ring resonators, add-drop SOI-based slot microring resonators could achieve Q -factor of 23 400 with a radius of $50 \mu\text{m}$, with an extinction ratio of 14.7 dB [99]. A Q -factor of 30 600 was also achieved for the slot μ -ring racetrack add-drop resonator in Fig. 1.3.4(b) and having a radius of $50 \mu\text{m}$ [94].

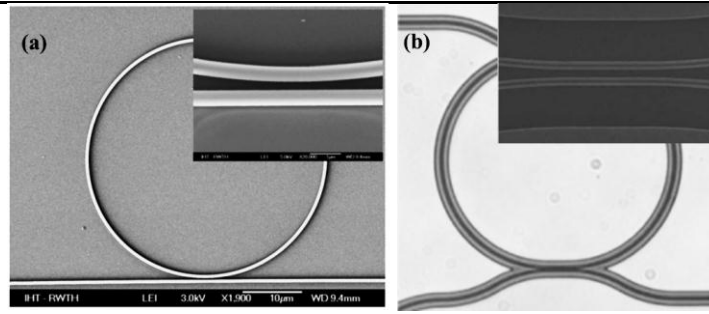


Fig. 1.3.4(a) μ -ring resonators [97] and (b) Slot μ -ring racetrack add-drop resonator [94].

Ring-resonators have been widely used in sensing applications. The sensitivity and limit of detection of refractive index sensor based on two ring resonators can be further improved by employing the Vernier effect in slightly different free-spectral range rings. This kind of sensors relies on the mechanism in which two ring resonators with different optical roundtrip lengths are cascaded. The drop signal of the first ring resonator serves as the input of the second then the transmission spectrum of the cascade of the two ring resonators is the product of the transmission spectra of the individual resonators. It exhibits peaks at wavelengths for which two resonance peaks of the respective ring resonators (partially) overlap, and the height of each of these peaks is determined by the amount of the overlap [100]–[102].

1.3.4 2D planar photonic crystals

Photonic crystals (PhCs) are artificial media realized by a periodic modulation of the refractive index. They can offer strong light confinement at the wavelength scale. Their dispersion relation is defined as the dependence of the frequency of a Bloch state versus the photon momentum: $\omega(\mathbf{k})$,

where the frequency is normalized according to $\omega_{normalized} = \frac{a}{2\pi c} \omega = \frac{a}{\lambda}$ and \mathbf{k} is normalized as

$\mathbf{k}_{normalized} = \frac{a}{2\pi} \mathbf{k}$. The band diagram is a plot of the dispersion of all of the allowed states for \mathbf{k}

within the Brillouin zone. The spatial periodicity comparable to the optical wavelength in photonic crystals can give rise to the so-called photonic band-gap (PBG), the forbidden frequency range in a certain direction for a certain polarization.

A typical SOI 2D planar PhC structure is shown in Fig. 1.3.5(a).

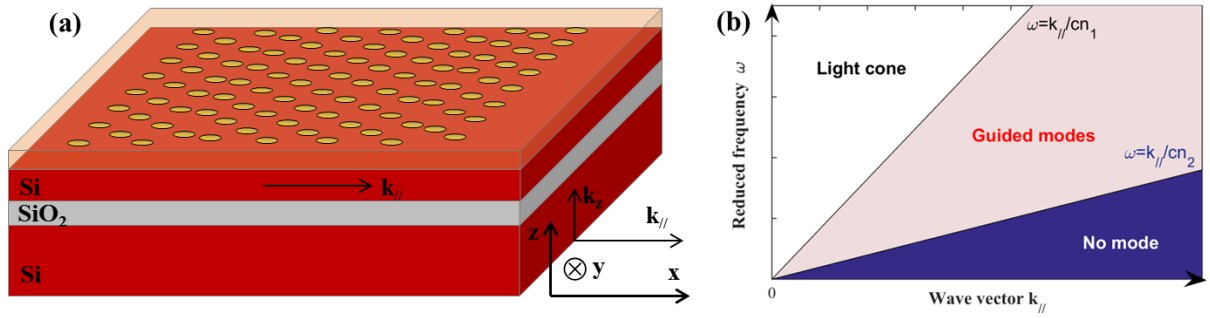


Fig. 1.3.5(a) SOI PhC slab and **(b)** the concept of light cone in SOI slab where n_1, n_2 corresponds to n_{SiO_2} and n_{Si} , respectively.

As we can see in Fig. 1.3.5(a), a buried silica and a top cladding material with refractive index n_{clad} can be considered in addition with the silicon planar waveguide ($n_{Si} \approx 3.48, n_{SiO_2} \approx 1.44$, at $\lambda = 1.55 \mu\text{m}$). This structure supports total internal reflection due to the higher refractive index in the slab waveguide core than the two above and below claddings. This defines the concept of *light cone* (Fig. 1.3.5(b)), *i.e.* all the modes are not confined inside the slab but those localized above this line can escape vertically and lead to intrinsic losses. On the contrary, below the *light line* $\omega = ck_{\parallel}/n_1$ -modes are truly guided inside the slab and are exponentially decaying (evanescent) above and below it.

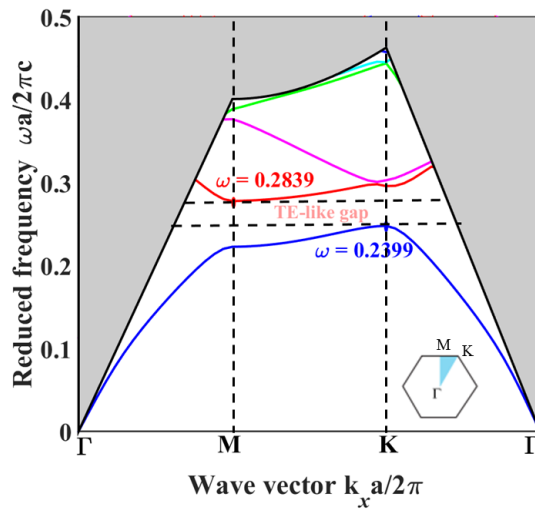


Fig. 1.3.6 Band diagram for SOI PhC of Fig. 1.3.5(a) in which hole radius $r = 0.276a$, slab thickness $h = 0.684a$. The grey shaded area is the light cone, corresponding to the extended modes. Below it are the TE-like guided bands localized to the slab: a TE-like gap is present from $\omega = 0.2399$ to 0.2839 (a/c).

Taking a typical example of a SOI PhC with hole radius $r = 0.276a$, slab thickness $h = 0.684a$, a cover cladding of refractive index 1.46, a photonic band-gap appears for the TE-polarization

between $a/\lambda \approx 0.24$ and $a/\lambda \approx 0.28$ (Fig. 1.3.6). This photonic band-gap was calculated by the Plane wave expansion method using the MIT Photonic-Bands (MPB) package (to be detailed in Chapter 2). Such a large TE-like band gap is necessary to exploit the in-plane gap guided modes while an r/a ratio around or slightly smaller than 0.3 can be achieved using lithography and etching fabrication techniques [103].

Starting from the photonic band-gap property of planar PhCs, defects can be introduced in their 2D bulk lattice in order to create waveguides or cavities presenting specific physical properties including slow light and tight photon confinement, respectively.

1.3.4.1 W1 photonic crystal waveguides

A W1 Photonic crystal waveguide, as schematically sketched in Fig. 1.3.7(a), is created by removing one row of holes in the 2D lattice of a planar PhC. Light can then be guided along the defect line thanks to the defect states located in the photonic band-gap. This structure has a higher index line defects when low-index holes are drilled in a high-index membranes, then supporting light confinement within a mixture of the TIR and photonic band-gap mechanisms [104]–[107]. SOI W1 PhC waveguide structures have been designed and fabricated for years, for example by Lončar *et al.* [108] and Jamois *et al.* [109], and have now entered some extent the toolbox of classical Si photonic structures. Fig. 1.3.7(b) shows a typical band structure of a SOI W1 PhC waveguide, calculated using the MPB package. This W1 PhC waveguide is based on a SOI PhC slab, as discussed previously.

In Fig. 1.3.7(b), the upper region corresponds to the light cone (black line). The modes in the package are the slab modes, while the two upper modes in the gap above this package are the W1 waveguide even and odd modes, respectively, named from their symmetry [103]. Fig. 1.3.7(c) focuses on the two TE-like modes with the profiles of the E_y field component shown in the insets. These two gap-guided modes indeed lie within the bandgap of the PhC as shown in Fig. 1.3.5. One mode is y -even (blue curve) and the other one is y -odd (red curve). Importantly, at the Brillouin zone edge, light group velocity vanishes to zero. In this kind of waveguides, light can in fact be slowed down with a group velocity v_g much smaller than the velocity c in vacuum thanks to the geometry degrees of freedom for engineering flat dispersion ($v_g = (d\omega/dk)$). The

slow down factor of v_g against c is usually evaluated by the group index n_g , given by

$$n_g \equiv \frac{c}{v_g} = c(d\omega/dk). \text{ This kind of structures is thus interesting for slow light investigation [110]}$$

or dispersion engineering [107], [111], [112].

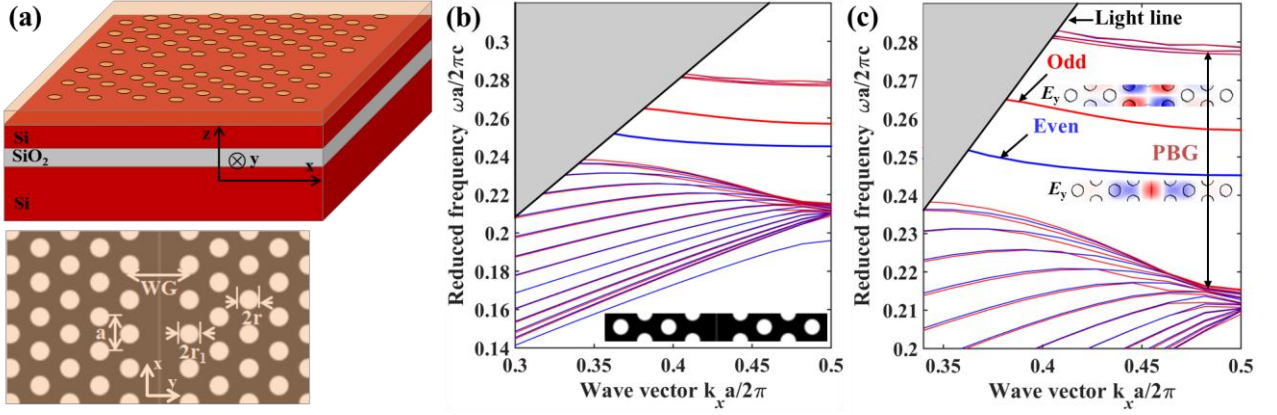


Fig. 1.3.7(a) Scheme of SOI W1 PhC waveguide and its horizontal view (b) Dispersion diagram of W1 PhC WG with the silicon core slab thickness $h = 0.684a$ and the hole radius $r = 0.276a$ with top cladding material of 1.46 refractive index (c) Zoom in of the dispersion diagram in (b) with two W1 TE-like even (blue curve) and odd (red curve) modes (insets correspond to the E_y field profiles).

For SOI photonic hybrid purpose, y -even modes are of interest. In this view, photonic crystal waveguides bring a good benefit for light-matter interactions (that scales as n_g or n_g^2 , etc.). However, as seen in Fig. 1.3.7(c) from the E_y field profile, most of the field energy still remains in the silicon material. Slot photonic crystal waveguides (SPCW), which supports E_y -even modes partially confined in the low-index material, can be considered to circumvent this drawback.

1.3.4.2 Slot photonic crystal waveguides

Slot photonic crystal waveguides (SPCWs), firstly proposed by Di Falco *et al.* [113], are constructed by introducing a slot cut along the length of a standard PhC planar waveguide. These structures allow the confinement and guiding of light when it is polarized with the electrical field perpendicular to the slot. They are of interest for hybrid integration as they can enhance the light-matter interaction due to the combined slot and slow light effects [114], [115] with a low-index material filling the slot. A schematic view of a SOI SPCW infiltrated with a cladding material is illustrated in Fig. 1.3.8(a) and the horizontal view is presented in Fig. 1.3.8(b).

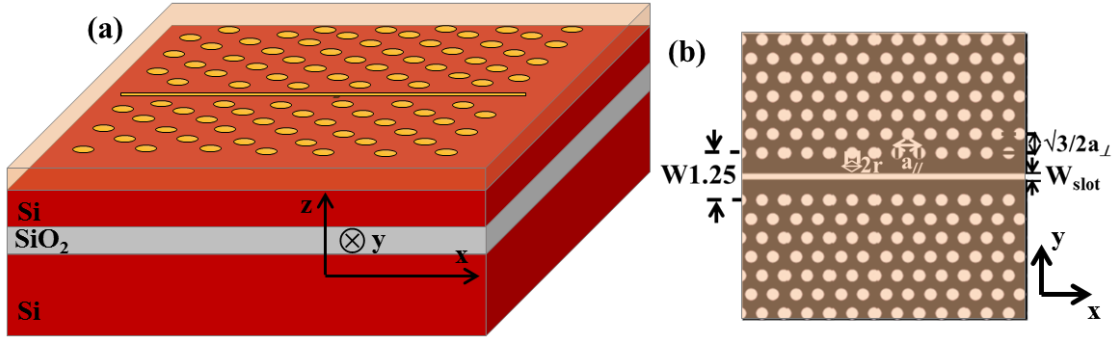


Fig. 1.3.8(a) Scheme of SOI SPCW and (b) Horizontal view of SOI SPCW infiltrated with a cladding material.

To show the modes that can be used, we calculated dispersion diagram of a SPCW as presented in Fig. 1.3.9(a). Typical dimensions for a SPCW have been chosen to achieve proper fraction of electric-field energy density in the cladding region (see Fig. 1.3.10). The dispersion diagram of this SPCW is shown in Fig. 1.3.9(a). The grey region is the light cone. There are three modes guided in band gap, with the E_y field profiles are depicted in Fig. 1.3.9(b).

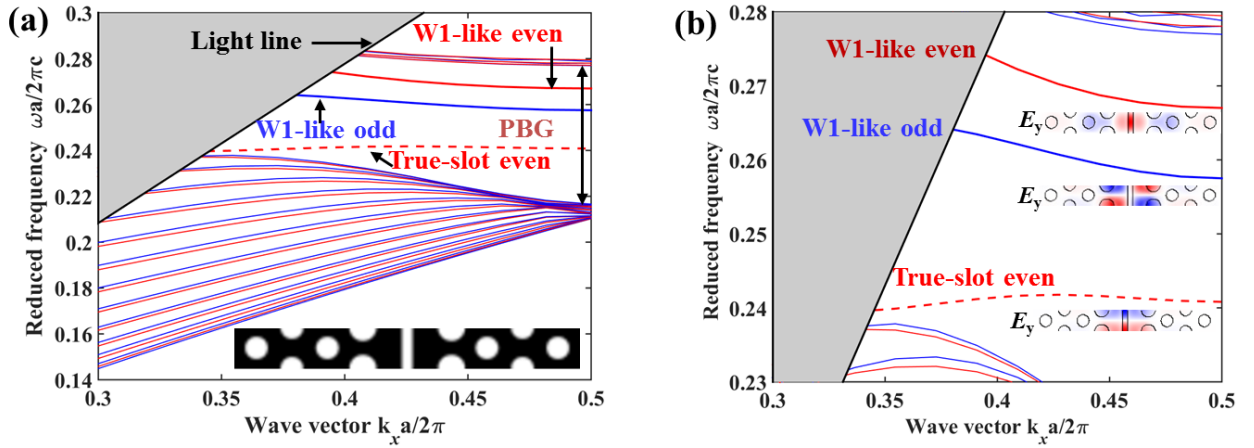


Fig. 1.3.9 (a) Dispersion diagram of SPCW with lattice constant $a = 380$ nm, slab thickness $h = 260$ nm, slot width $W_{\text{slot}} = 100$ nm and waveguide width $W1.25$ (i.e. $1.25 \sqrt[3]{a}$), hole radius $r = 105$ nm radius of the holes in the first two rows closet to the slot is $r_1 = 125$ nm and inset is its schematic view of the unit cell (b) Zoom of dispersion diagram focusing on three TE -like gap-guided modes: y -even true-slot mode (dash-red curve), y -odd $W1$ -like mode (blue curve), y -even $W1$ -like mode (red curve) and their field profiles of E_y components.

When the slot is inserted in the PhC waveguide, a slot mode occurs in addition to the $W1$ mode in standard PhC waveguide due to the reduction of the refractive index of the structure. As can be seen in Fig. 1.3.7(b) for the dispersion diagram of PhC waveguide compared with the one shown in Fig. 1.3.9(a), the true-slot mode is created from pulling the one below the package of slab modes. In the described $W1$ PhC waveguide, there are one odd and one even modes. In the

SPCW, the larger the slot width the smaller the effective index of the structure, so the **W1-LIKEEVEN** mode (red-curve) can be removed from the bandgap towards the upper mode continuum while the W1-like odd is not affected too much. The **TRUE-SLOTEVEN MODE** corresponds to the fundamental slot mode projected into the bandgap [113]. Inversely, a decrease in the slot width corresponds to smaller eigenfrequencies for the true-slot mode reaching the limit of the (bottom frequency) slab mode continuum. We notice that the slope of the dispersion curve of true-slot mode is positive and is opposite to those of W1-like modes. As shown in Fig. 1.3.9(b), the profile of E_y components of three gap-guided modes display the following symmetries: the true-slot mode is y-even and one of the two W1-like modes is y-odd, while the other one is y-even.

These properties, illustrated here in a specific situation, represent general properties of **silicon slotted photonic crystal waveguides**. This is the reason why further investigations performed in his manuscript on SPCW geometries will rely on the **True-slot mode** and/or **W1-like mode** presented here, respectively (see Fig. 1.3.9(b)).

In term of **integration purpose**, using the W1-like even and true-slot even modes is important because light is strongly confined in the slot area which is filled with an active material. Approaches to modifying the geometry of SPCW depend on which modes are to be employed. For example, if we want to maintain only the true-slot mode, we can increase the slot width instead of using a small one while keeping the two kinds of modes. For hybrid integration, y-even modes are under interest because the amount of fraction of electric field energy density in the cladding region (which partially/mainly corresponds to the slot) will decide the interaction between light and matter. That is the reason why **choosing the dimensions of the SPCW suitable to achieve proper fraction and also fitting with the fabrication constraints** is necessary. Some prominent factors in this purpose are: the value of the hole radius, especially the radius of holes in the first row (r_1) and the value of the slot width (W_{slot}). These parameters mainly affect the position of the modes and also the fraction of the dielectric energy distributed in the slot area infiltrated by active materials.

Accordingly, we have studied the fraction of the electric field energy density of guided modes confined in the cladding region as a function of the r_1 and W_{slot} parameters for they-even true-slot

mode and the W1-like mode, respectively. Simultaneously, a top cladding index $n_{clad} = 1.52$ was considered to match with the index value of standard soft-matter materials (*e.g.* polymers). The corresponding result is shown in Fig. 1.3.10(a) for the true-slot mode and in Fig. 1.3.10(b) for the W1-like mode, respectively.

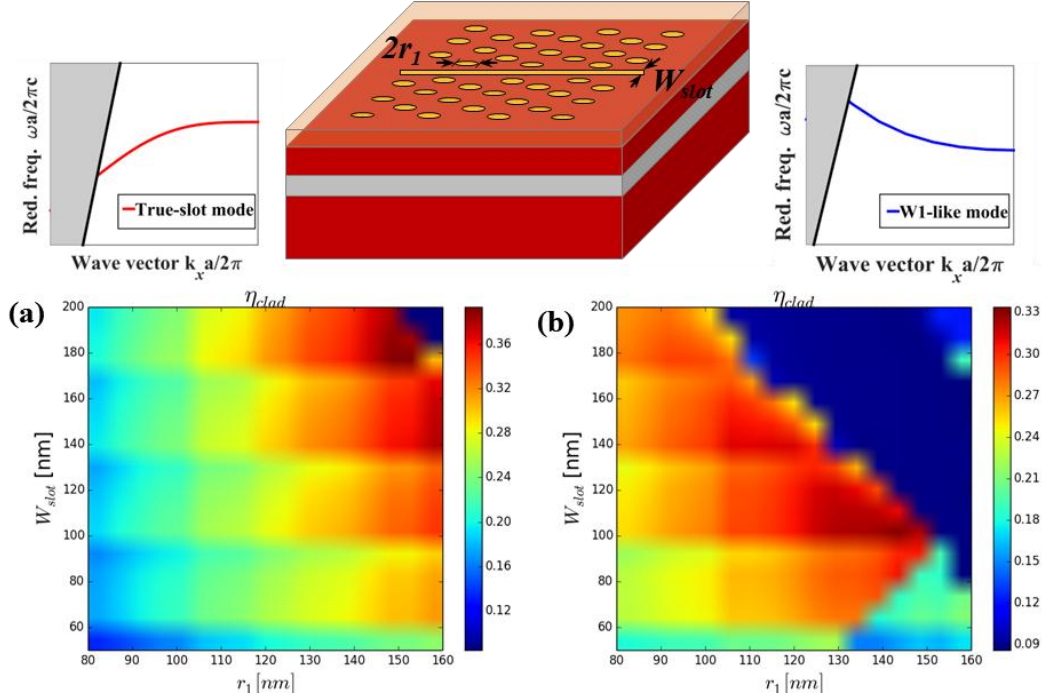


Fig. 1.3.10 Fraction of electric field energy density of cladding region as a function of slot width and radius of the holes in the first two rows and width of the slot of (a) True-slot mode and (b) W1-like mode in different SPCWs with hole radius r of 105 nm, lattice constant a of 400 nm, slab thickness h of 260 nm and a cover cladding material of 1.52 refractive index as a function of r_1 and W_{slot} , insets are two kinds of modes.

- From Fig. 1.3.10, we see that in order to exploit the true-slot mode, r_1 should be around 135 nm and slot width of around 190 nm, which both provides fraction of around 33% in the cladding area, which does not raise strong challenges for fabrication. As seen in Fig. 1.3.10(a), if r_1 is around 150 nm and the slot width is chosen as 190 nm, the fraction of the slot mode is highest (38%), however, choosing these parameters raises the risk of fabrication parameter uncertainties that may push the dielectric energy confinement factor to low values (see the blue area of Fig. 1.3.10(a)).
- Similarly, for the W1 like mode, r_1 should be in the range of 105 nm–130 nm with a slot width of ~ 100 nm. In this situation, the field confinement in the cladding material is around 30% which is suitable for hybrid integration purpose and also suited for fabrication.

Based on these simulation results, in order to manipulate the two kinds of modes simultaneously:

- We chose the value of $W_{\text{slot}} = 100$ nm and $r_1 = 105$ nm, as mentioned above, in which the refraction of electric field energy density of the y -even true-slot mode is around 28% and the y -even W1-like mode confinement is around 31%.
- We increase W_{slot} to 200 nm in order to exploit the true-slot mode only while maintaining a high field/cladding material overlap fraction of around 29%.

These values will guide the investigations carried out in the next two chapters in the purpose of slot photonic crystal waveguides and resonators in view of photonic hybrid on-silicon integration.

1.3.4.3 Planar photonic crystal cavities

When a spatially localized defect is introduced in a 2D PhC planar structure, a localized mode exists and a PhC cavity is built. The performance of a cavity can be evaluated by the quality factor Q , which has been mentioned in section 1.3.3 for microring resonators, a concept determining how long the lifetime of photon confined in the cavity is, and the cavity mode volume V defining the cavity ability of spatial mode confinement.

Various kinds of 2D PhC slab cavities have been studied with the ambition to reach high Q s and small V s as most of light-matter interactions strengths scale increasingly for larger Q and smaller V values. For example, the operation energy for optical bistable devices scales as (V/Q^2) [116]. In a cavity quantum electrodynamics (QED) system, *i.e.* interaction between a quantum emitter and a single radiation-field mode [117], depending on the kind of coupling regime, the same dependence is to be considered. In the strong coupling regime, *e.g.* interaction between the photonic crystal cavity and a single quantum dot, vacuum-field Rabi splitting exceeds the decoherence linewidths of both the nanocavity and the quantum dot [118]; the condition for strong coupling, *i.e.* the ratio (g/κ) (where g is the coupling strength and κ is the decay rate of the cavity) is determined by (Q/\sqrt{V}) . On the other hand, in the weak coupling regime of the interaction between a photonic crystal cavity and a single quantum dot in photoluminescence [119], the quantum dot radiative lifetime is modified and a modification of the spontaneous

emission rate compared with that in free space occurs that scales as (Q/V) [120]. **To sum up, in all situations, light-matter interactions increase for larger Q s and smaller V s. In the frame of this work, (Q/V) has been retained as the reference metrics for the comparison between PhC cavities.**

To return to the realization itself of the cavities, there are different ways to form PhC cavities. They can be created by shifting several holes in the Γ -K direction to make “point-shift” or “zero-cell” cavity (H0), removing one hole from a triangular lattice of air holes (H1), removing three or more holes in the line defect (L_n), or chirping the 2D PhC lattice constant to form a heterostructure cavity, as depicted in Fig. 1.3.11. Many attempts have been made in order to increase Q factor and make V decrease by minimizing the k -components situated above the light line, *i.e.* by suppressing out-of-slab photon leakage to satisfy the conditions for total internal reflection at the slab-air interface [121].

Fig. 1.3.11(a) depicts an H0 PhC cavity consisting 2D hexagonal air holes, which is based on a silicon slab and two air claddings in the vertical direction. This kind of cavities can support an estimated Q value of 1.12×10^5 and a mode volume of $0.28(\lambda_0/n)^3$ at resonance wavelength of 1564 nm (where λ_0 and n are the wavelength in vacuum and the refractive index of the material, respectively) [122]. These values can increase up to Q of 2.8×10^5 with a mode volume of $0.23(\lambda_0/n)^3$ after optimization of the displacements of the hexagonal-lattice air holes in the Γ -M direction to smoothly modify electric field distribution [123]. This kind of cavity was further designed to reach $Q = 1.7 \times 10^6$ and the measurement of a H0 cavity based on SOI wafer showed Q of 4×10^5 with a mode volume of $0.34(\lambda_0/n)^3$ at resonant mode of $1.59 \mu\text{m}$ [124].

A free-standing H1 hexagonal PhC InGaAsP slab configuration provided an estimated Q up to 2×10^6 and a mode volume of $(\lambda_0/n)^3$ with a hexapole mode resonance frequency of around $0.3(a/\lambda)$ in the case where six nearest-neighbour holes were both pushed away and tuned in size [125]. A dipole mode could be realized by modifying the sizes and positions of the air-holes near to the defect cavity (as illustrated in Fig. 1.3.11(b)). Experiments revealed $Q = 2.5 \times 10^4$ and a mode volume of $0.47(\lambda_0/n)^3$ at resonance wavelength of 950 nm in a fabricated air-bridge cavity using a GaAs wafer [126].

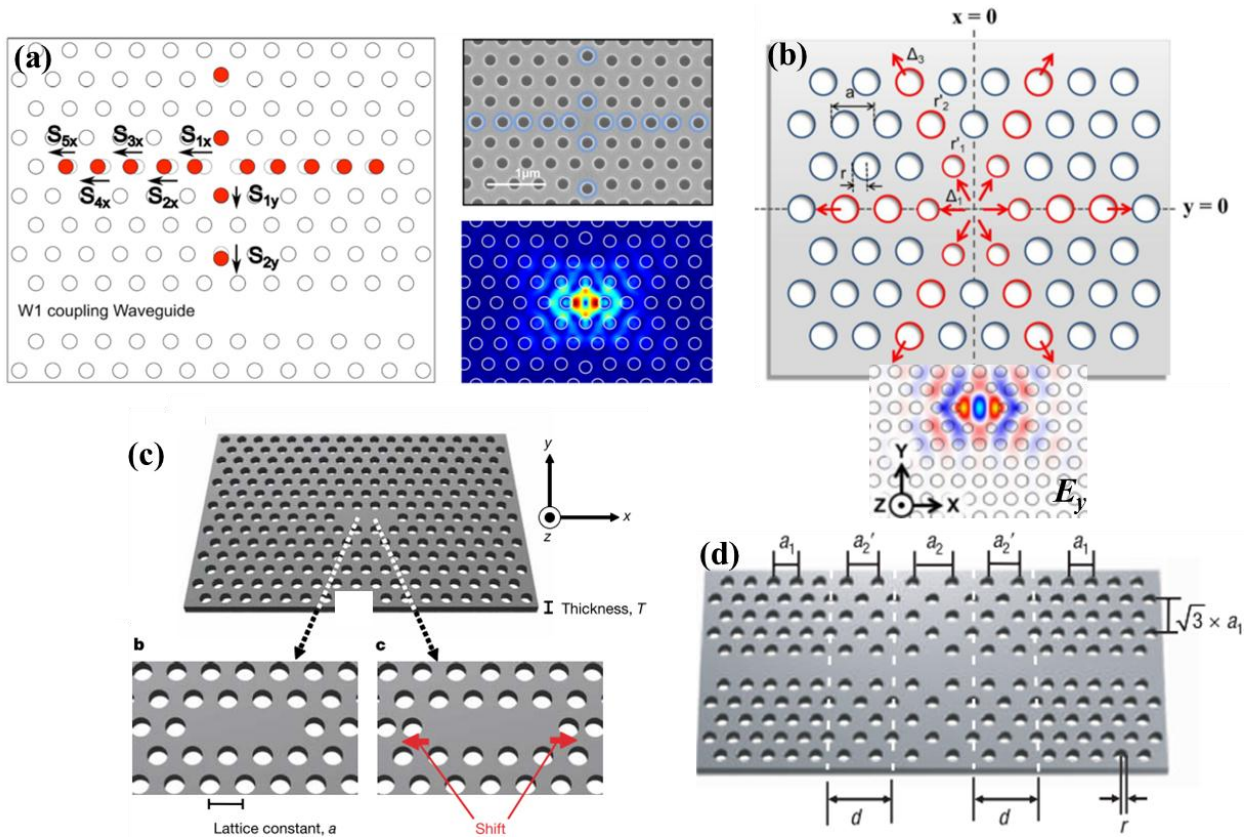


Fig. 1.3.11 Different kinds of PhC cavities (a) H0 PhC cavity [124] (b) H1 PhC cavity and the E_y profile of the dipole mode [126] (c) L3 PhC cavity [127] and (d) PhC heterostructure cavity [121].

To further describe typical works published in the literature, 2D PhC slab L3 cavities, formed by removing three holes (see Fig. 1.3.11(c)), have been optimized by shifting the two edge air holes in order to obtain a gentle electric field profile: experimental Q factor of 4.5×10^4 and mode volume $V = 0.69(\lambda_0/n)^3$ at a resonance wavelengths ranging from $\lambda = 1500$ nm to $\lambda = 1600$ nm were obtained [127]. Further optimization was obtained by playing on the six edge holes, to attain $Q = 10^5$ and $V = 0.71(\lambda_0/n)^3$ in air-bridge Silicon based 2D PhC L3 cavity [128]. In 2014, Minkov *et al.* [129] also investigated air-bridge planar PhC H0, H1 and L3 cavities and successfully reached Q s around 10^6 . Among those, the planar PhC heterostructure cavity configuration, as presented in Fig. 1.3.11(d), created by chirping the lattice constant in the light propagation direction to attain a theoretical Q of 2×10^7 [121], while the experimentally obtained value on the SOI platform was $\sim 10^6$ [130], with V of $\sim 1.23(\lambda_0/n)^3$ at a resonance wavelength of ~ 1580 nm. Q could even reach 9×10^6 at a resonance wavelength of ~ 1570 nm by optimizing the ambient

humidity exposed to the cavity in the measurement, *i.e.* the cavities were placed in a chamber filled with dry N₂ to prevent H₂O molecules from adhering to the Si surface[131].

Most of these impressive results have been obtained for non-slotted structures, the optical cavity modes being mainly confined in the high-index core material. While being inspired by all these interesting works, our approach has been to focus on slotted cavity geometries, in which the overlap between the cavity mode field and the hybrid-soft materials integrated on-chip is maximized.

1.3.4.4 Slot photonic crystal cavities

Originated from the idea of Almeida [92] about slot-waveguide structures, Robinson *et al.*[132] theoretically showed that if an air-slot waveguide (*i.e.* with 20 nm slot width) would be surrounded by a 1D PhC on its two sides, a fully 3D localized mode could be trapped in a volume less than a tenth of a cubic half (free space) wavelength, *i.e.* $10^{-2}(\lambda/2n)^3$. Based on the advantage of the slot electric-field discontinuity effect at the dielectric boundaries, a cavity mode can indeed be locally enhanced inside the slot. This field concentration drastically reduces the effective mode volume by a factor of $(\varepsilon_H / \varepsilon_L)^{5/2}$ (where ε_L , ε_H are the dielectric permittivity of the slot and of the PhC slab materials, respectively). Then Yamamoto *et al.* [133] used a 2D PhC to create a similarly small mode volume cavity in a wider slot. This air-slot PhC cavity was defined by locally modifying just a few of the holes nearest to the slot (as shown in Fig. 1.3.12(a)) and calculated Q of 2×10^5 with V of $0.1(\lambda_0/n)^3$ at around 1.45 μm resonance wavelength. Di Falco *et al.* [134] demonstrated slot PhC heterostructure cavities, as illustrated in Fig. 1.3.12(b) by making the lattice constant of the surrounding PhC vary along the slot waveguide. This slot SOI PhC cavity provided experimental Q of 50 000 at resonance wavelength of 1559.2 nm in the case of top-cladding air-confinement, and dropped to 4 000 at resonance wavelength of 1590 nm when infiltrated with water (refractive index of 1.315 at $\lambda = 1550$ nm), then further showed its sensing application potential [78]. Freestanding silicon membrane L3 to L11 air-slot PhC cavities were also investigated for gas sensing [135] (see Fig. 1.3.12(c)). L9 air-slot PhC cavities produced experimental Q exceeding 30 000 with mode volume $0.086 \mu\text{m}^3$ at resonance wavelength around 1515 nm. Fig. 1.3.12(d) shows a freestanding silicon membrane air-slot PhC

cavity in which the width of slot was modulated and gave Q of 26 000 with a mode volume of $0.05(\mu\text{m})^3$ at 1570 nm resonance wavelength [136].

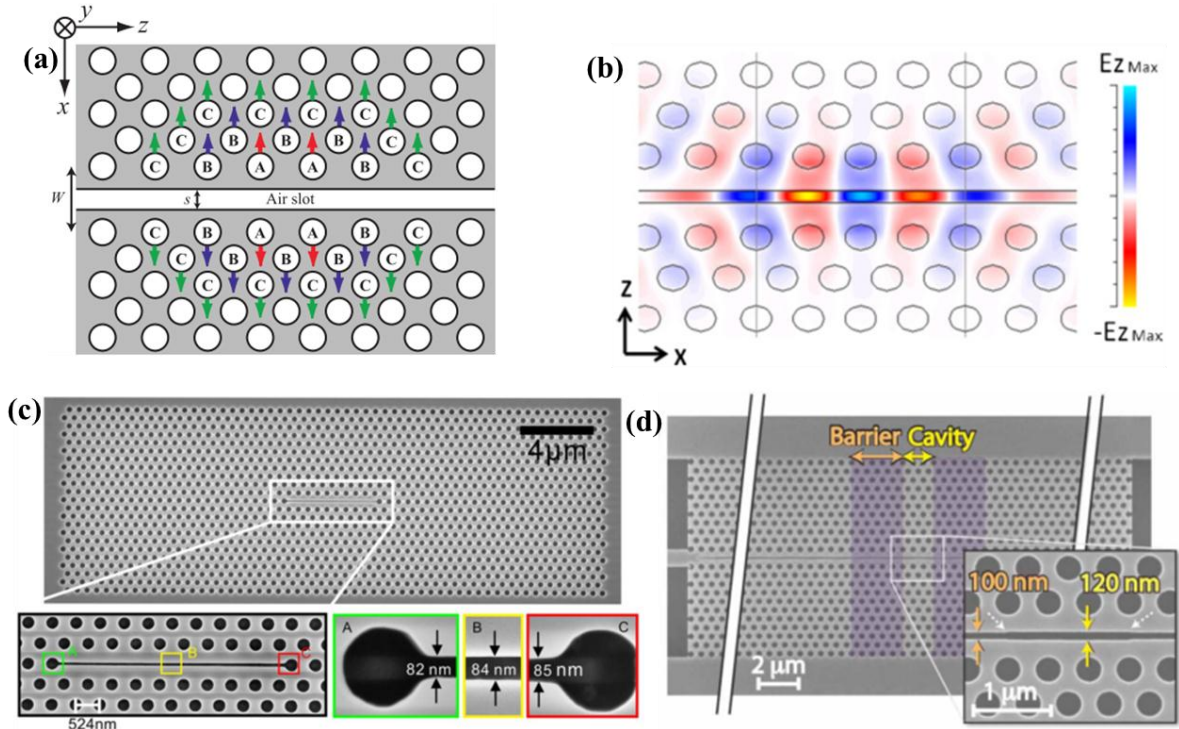


Fig. 1.3.12 (a) Design of an air-slot PhC slab nanocavity realized by local line-defect-width modulation. Air holes labeled A, B, and C are shifted outward by d_A , d_B , and d_C , respectively [133] (b) 2D-FDTD simulation of slotted PhC air heterostructure cavity by chirping lattice constant showing E_z component of mode profile at cavity resonance wavelength [78] (c) SEM image of an L9 air-slot cavity [135] (d) SEM image of the air-slot modified slot width cavity, inset depicts different values of slot width [136].

Regarding the sensing applications, from Table 1.1 in section 1.2.2, one can see the perspectives of slot PhC cavities in sensing as compared with other sensing systems for their high Q_s , S_s and FOM_s while possessing small sizes. To quote a few typical examples, we can list out here the applications for gas sensing by using the SOI L_n slot PhC cavity [137], air-slot PhC cavity by modifying the width of the slot [136], liquid sensing with the heterostructure slot PhC cavity [138], and modified slot PhC cavity by shifting the holes around the slot [139].

However, these planar slot PhC cavities, as well as subsequent high Q PhC-based slot cavities, were based on “free-standing” structures where the underlying cladding layer was removed after the PhC structures were etched into the silicon. **In this thesis, we will study silicon slot PhC cavities designed to support high Q modes without having to remove the silicon dioxide**

layer beneath the cavities while suited for the integration of various active top cladding materials, including liquid and soft-matter materials.

1.4 Conclusion: motivations and manuscript outline

This chapter has brought an overview of hybrid integration in silicon photonics consisting in the integration of active materials in/on silicon photonic waveguide structures, including waveguide and optical resonators, for the realization of active integrated functions.

In this context, this manuscript is devoted to address the following points:

- Firstly, designing, fabricating, and characterizing slot SOI PhC cavities with high Q s and small V s with resonance wavelengths in the 1.3 μm –1.6 μm telecommunication range.
- Secondly, investigating the ability of filling the slot photonic crystal cavity modes from external waveguides, as well as studying the interaction between two slot mode cavities.
- Lastly, exploiting these silicon hollow core compact resonators integrated with active materials which have been rarely reported so far for photonic applications (carbon nanotubes). In this purpose, we will choose to study slot SOI PhC heterostructure cavities as they are able to support among the highest Q s with small V s.

For that purpose, the next parts of the **manuscript are organized as follows**.

Chapter 2 is dedicated to the design of slot PhC cavities with resonances in the telecom ranges. It also addresses the question of the possible PhC slot cavity excitation from a side-coupled waveguide. Coupled slot PhC cavities are also investigated in view to exploit their supermodes.

In **chapter 3**, the fabrication of the designed slot PhC cavities are presented. Then, the investigation of the refractive index sensing properties of slot PhC cavities around $\lambda = 1.58 \mu\text{m}$, as well as the integration of s-SWNTs in slot PhC cavities for light emission near $\lambda = 1.28 \mu\text{m}$, are carried out.

Finally, a summary and a conclusion to this Ph.D. work are achieved, before describing perspectives.

Chapter 2. Design of slot photonic crystal cavities for silicon hybrid integration

The rich and numerous applications of photonic crystals (PhCs), ranging from integrated lasers [140]–[144] to information processing [145], [146], [117], and sensing in Lab-on-a-Chip systems [78], [147], mainly stem from two main properties of planar PhCs: the photonic bandgap waveguiding mechanism which can achieve light propagation with a tight control of light dispersive properties, and photon confinement that enables light trapping under an amount of time in extremely small volumes.

This chapter focuses on the **design of slot photonic crystal waveguide cavities**. Our central motivation is to **define hollow core structures enabling the integration of active materials** (see chapter 3) by investigating the proper geometries leading to high overlaps between mode fields and cladding materials, the suited conditions to control resonance wavelengths of cavities, and explore more prospective issues like coupled cavities (*e.g.* photonic molecules) for the hybrid on-chip integration of diverse materials.

It contains four sections, as follows. We present in section 2.1 the design of slot silicon on insulator (SOI) PhC cavities. In section 2.2, the coupling between a slot PhC cavity and a slot PhC waveguide is investigated to show the ability to excite a true-slot mode PhC cavity by a slot PhC waveguide. Then, coupled slot PhC cavities are studied with their bonding and antibonding properties in section 2.3. Finally, we end the chapter with some conclusions in section 2.4 before moving to chapter 3 that gathers experimental results.

2.1 Design of slot photonic crystal cavities

2.1.1 Figures of merit of a photonic crystal cavity

As mentioned in chapter 1, a slot PhC cavity is a dielectric resonator which can enhance light-matter interaction and that can be used for hybrid integration due to its hollow core geometry that can be filled by various materials. Beyond this qualitative statement, it is necessary to

quantitatively evaluate the resonator metrics in order to estimate the suited condition to enhance physical effects.

In this section, we introduce the definition of the primary figures of merit of a PhC cavity, as shown in Fig. 2.1.1 (or of dielectric resonators in general). These quantities will be used to qualify the investigated cavity designs that will serve as the basis of the fabricated and characterized resonator structures presented in chapter 3. As mentioned in section 1.3.4.3 and section 1.3.4.4 (chapter 1), the figures of merit of a single-mode cavity mainly rely on two main parameters. (1) The Q -factor that indicates how long photons are confined in the cavity, and (2) the cavity mode-volume V that demonstrates its spatial capacity of light confinement. In order to design slot PhC cavities for hybrid on-chip integration, *i.e.* combining silicon hollow core structures with other active materials, it is typically important to achieve slot PhC cavities possessing high Q s and small V s.

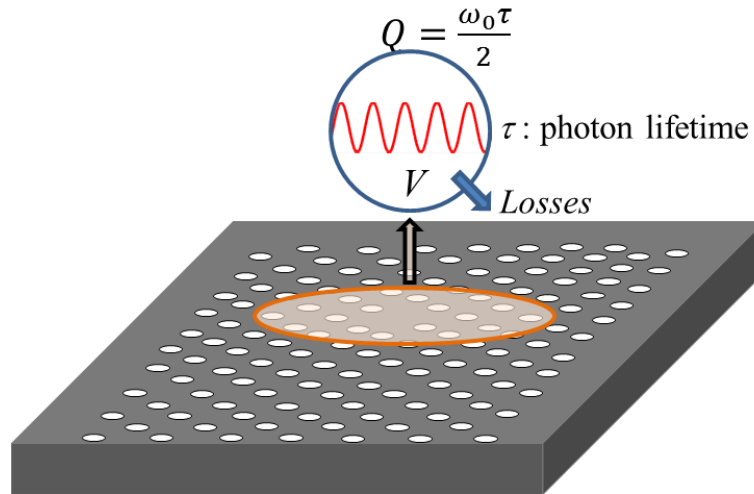


Fig. 2.1.1 Scheme of a PhC cavity created by introducing a defect in a planar PhC lattice.

2.1.1.1 Quality factor (Q)

As mentioned in section 1.3.4, for PhC structures, localized modes can be created by introducing a point defect in a 2D planar PhC lattice, as illustrated in Fig. 2.1.1. In that case, the electric field can be confined in and close to the defect area.

While PhC waveguides support continuous $\omega(\mathbf{k})$ photonic bands, PhC cavities have resonance frequencies with an indefinite wavevector. In order to excite a particular cavity oscillation, the

exciting frequency must match the chosen resonance frequency. In fact, excitation can occur in a narrow frequency range around the chosen eigenfrequency.

The quality factor Q of a cavity, which is a dimensionless number used to denote the losses present in a cavity, can also be defined as the frequency-to-bandwidth ratio of a cavity. As shown in textbooks and briefly recalled hereafter, the two definitions in fact coincide. Q can be defined as 2π times the ratio of the time-averaged electromagnetic energy stored in the cavity to the outgoing energy loss per cycle:

$$Q = \omega_0 \frac{U}{\text{Power loss}} \quad (2.1.1)$$

, where ω_0 is the angular resonance frequency of the cavity. By conservation of energy, the dissipated power is the negative of the time rate of change of the stored-energy U . So, from equation (2.1.1) the behavior of U can be written as a function of time as:

$$\frac{dU}{dt} = -\frac{\omega_0}{Q} U \quad (2.1.2)$$

with the following simple solution:

$$U = U_0 e^{-\omega_0 t / Q} \quad (2.1.3)$$

The energy within the cavity thus decays as $e^{-\omega_0 t / Q}$, meaning that the oscillation of the cavity field evolves in time as $e^{-\omega_0 t / 2Q}$:

$$E_c(t) = E_0 e^{-\omega_0 t / 2Q} e^{-i(\omega_0 + \Delta\omega)t} \quad (2.1.4)$$

, where $\Delta\omega$ is the shift of the resonance frequency due to the oscillation damping. A damped oscillation has no pure frequency, but a superposition of frequencies around $\omega = \omega_0 + \Delta\omega$.

Thus,

$$E_c(t) = \frac{1}{\sqrt{2\pi}} \int_{-\infty}^{\infty} E_c(\omega) e^{-i\omega t} d\omega \quad (2.1.5)$$

in which

$$E_c(\omega) = \frac{1}{\sqrt{2\pi}} \int_0^{\infty} E_0(\omega) e^{-\omega_0 t / 2Q} e^{i(\omega - \omega_0 - \Delta\omega)t} dt \quad (2.1.6)$$

In this Ph.D. work, we have used **Finite-difference time-domain (FDTD)** calculations performed with the Lumerical commercial software to estimate Q -factors of the investigated resonators.

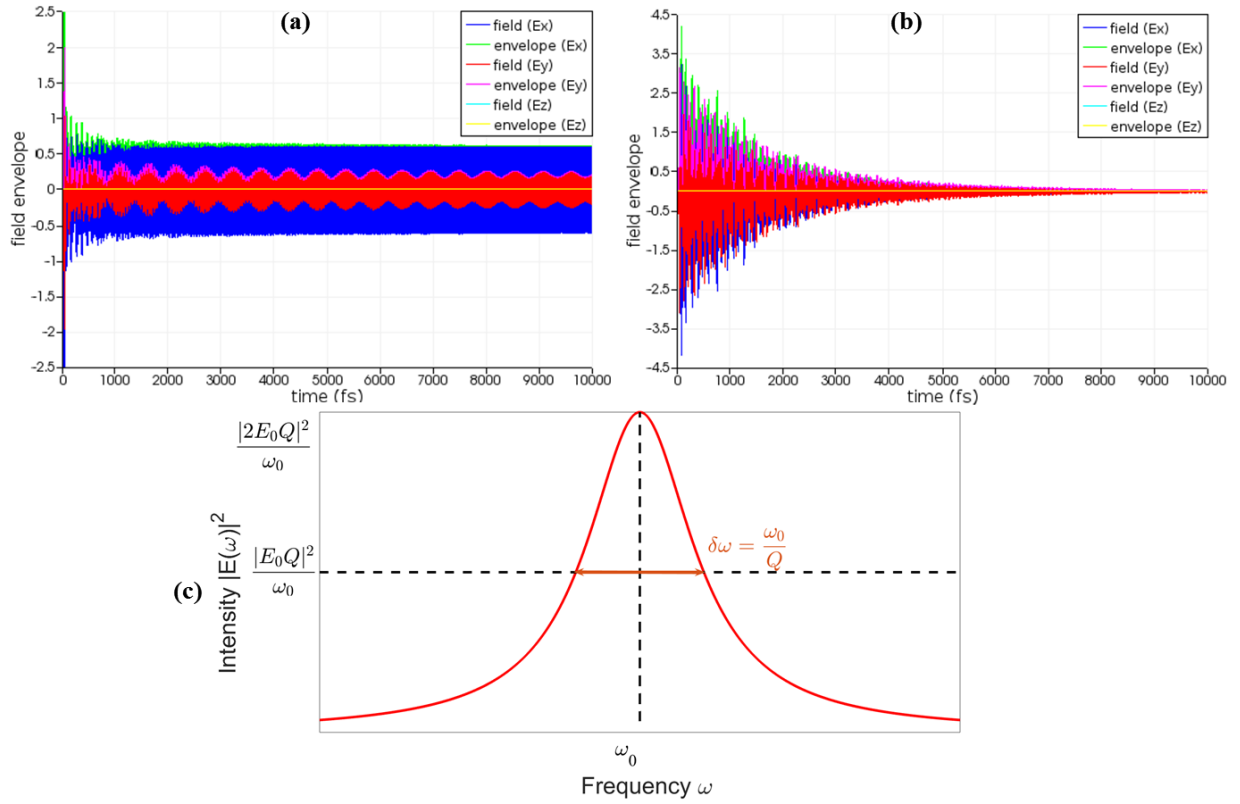


Fig. 2.1.2 Evolution of electric field components and their envelope decays in the time domain (obtained by using FDTD simulation) in order to compute cavity quality factors in the case of (a) A high Q -factor resonator (e.g. $Q \approx 100\,000$) in which the electromagnetic fields cannot completely decay from the simulation time window (b) A low Q -factor resonator (e.g. Q of hundreds) in which the electromagnetic fields can almost completely decay from the simulation time window, and (c) Cavity electric field frequency spectrum possesses a Lorentzian behavior.

In this method, the Q -factor of a cavity is computed from the extrapolation of the exponential decay of the field probed at a specific chosen location, as shown in Fig. 2.1.2(a) and (b) for the two cases of a high Q (e.g. in the order of 10^5) and a low Q (in the order of 100) resonators, respectively. In practice, the quality factor is determined by the slope of the envelope of the decaying signal using the formula: $Q = \frac{-\omega_0 \log_{10}(e)}{2m}$, where m is the slope of the decay in SI units.

The integral in (2.1.6) is elementary and leads to a frequency distribution for the energy in the cavity having a Lorentzian resonant line-shape:

$$|E_c(\omega)|^2 \propto \frac{1}{(\omega - \omega_0 - \Delta\omega)^2 + (\omega_0 / 2Q)^2} \quad (2.1.7)$$

Thus the cavity mode has a frequency spectrum formed by a Lorentzian distribution with centered frequency ω_0 and spectral full width at half-maximum (FWHM) $\delta\omega$, as presented in Fig. 2.1.2(c). This way, we recover in fact the frequency definition of Q mentioned above:

$$Q = \frac{\omega_0}{\delta\omega} \quad (2.1.8)$$

To determine the quality factor of a cavity, we can either rely on the time-domain definition of Q or on the frequency-domain one (when available, *e.g.* from experimental collected spectra).

2.1.1.2 Mode volume

About the behavior of a cavity, not only how long light can be trapped in the cavity is of interest but also the size of the region in which the mode is confined should be known as several (many) physical effects scale as the dielectric energy spatial density. That figure of merit is the cavity *effective mode volume*.

There are several ways to define the effective mode volume of a cavity mode depending on physical considerations. Regarding nonlinear effects, *e.g.* free-carrier absorption [148], the mode volume can be defined as:

$$V_{FCA}^2 = \frac{\left(\int \varepsilon(\mathbf{r}) |\mathbf{E}(\mathbf{r})|^2 d^3\mathbf{r} \right)^3}{\int \left(\varepsilon(\mathbf{r}) |\mathbf{E}(\mathbf{r})|^2 \right)^2 d^3\mathbf{r}} \quad (2.1.9)$$

In this manuscript, for the purpose of hybrid integration in the silicon platform, the definition of mode volume being derived with respect to the Purcell enhancement of the emission of a point emitter placed in the maximum of the electric field of a cavity mode has been considered [149], [150]. The reason for this choice comes from the fact that the spontaneous emission probability of nanoemitters placed in the dielectric resonator is proportional to the Q/V ratio. The related mode volume is defined as the total mode dielectric energy over the maximum of the dielectric energy density [132]:

$$V = \frac{\int \varepsilon(\mathbf{r}) |\mathbf{E}(\mathbf{r})|^2 d^3\mathbf{r}}{\max \left(\varepsilon(\mathbf{r}) |\mathbf{E}(\mathbf{r})|^2 \right)} \quad (2.1.10)$$

, where the integral is taken over all space.

From V , one can define the unit-less effective mode volume V_{eff} as follows:

$$V_{eff} = V \left(\frac{n(r_{max})}{\lambda} \right)^3 \quad (2.1.11)$$

, where n is the index of refraction at the peak field (r_{max}) and r_{max} is the location of the maximum squared field.

2.1.2 Numerical simulations allowed to design slot photonic crystal cavities

Consistently with the thesis objectives described at the end of chapter 1, numerical simulations have been achieved to extract Q and V quantities described above in different configurations of interest.

In order to design slot photonic crystal cavities, the following simulation steps have been followed, as illustrated in Fig. 2.1.3:

- First, the photonic bandgap of 2D bulk planar PhCs was determined by using the Plane Wave Expansion (PWE) method [151] implemented through the MIT Photonic-Bands (MPB) package in 2D or 3D.
- Second, slot PhC waveguides based on the previous 2D bulk planar PhCs were studied by (2D/3D)-PWE method in order to identify the frequency dispersion bands of the studied line-defect modes and compute their field spatial distributions. From that step, we identified the kind of modes to be exploited (*i.e.* W1-like or true-slot mode: see section 1.3.4.2 of chapter 1).
- Finally, in order to investigate the properties of slot PhC cavities, we used (2D/3D)-FDTD simulation to extract Q -factors and mode volumes of the resonance modes as well as their field distributions. A probe was located around the cavity area (but not at a spatial symmetry location), and a dipole source was positioned closely to the center of cavity to excite the mode for evaluating Q s and resonance wavelengths.

PWE and FDTD methods were used to simulate different slotted PhC resonating structures with operating wavelengths located in the telecommunication range and with cladding materials presenting optical index values close to 1.5.

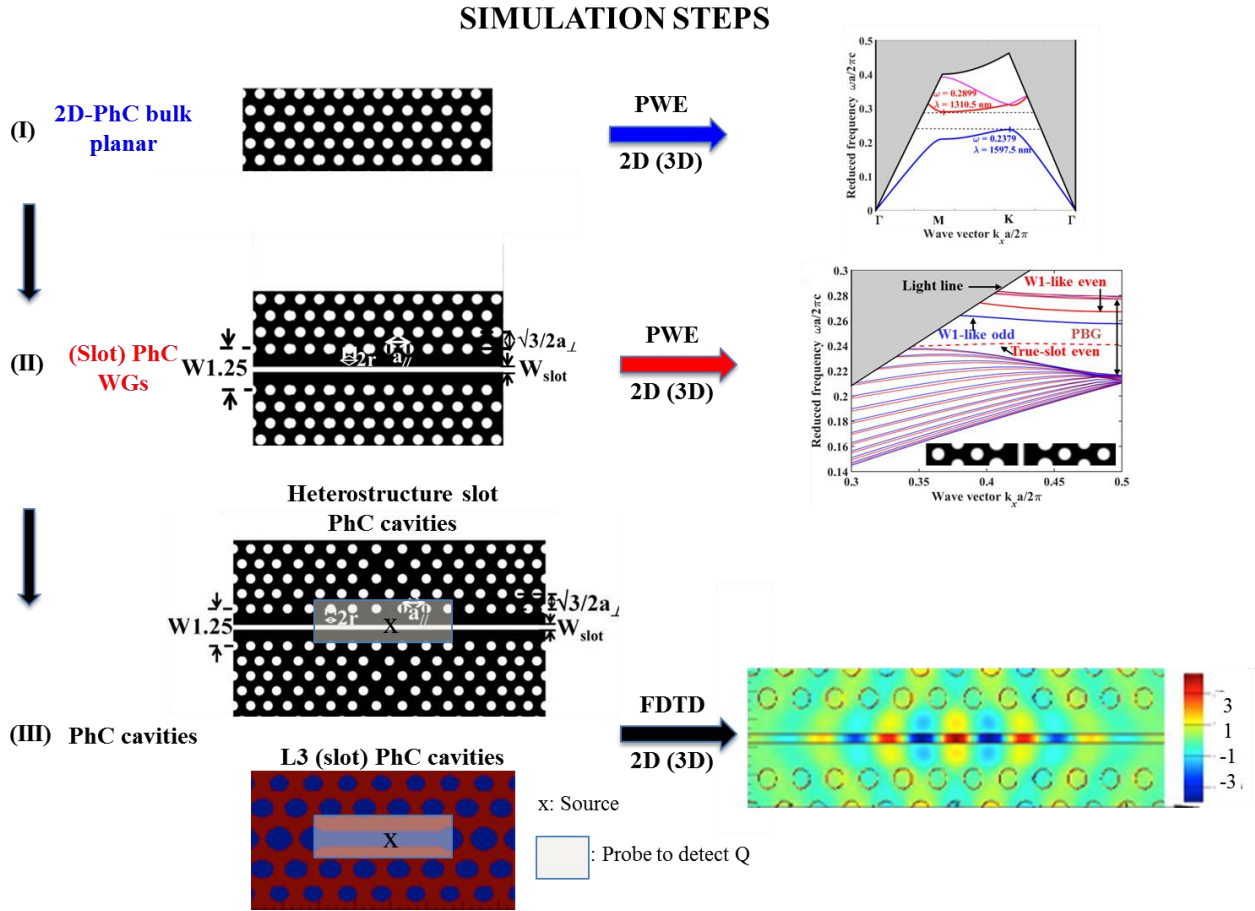


Fig. 2.1.3 Simulation steps(I) Photonic bandgap of 2D planar PhC structure obtained by (2D/3D)-PWE method (II) Dispersion diagram of (slot) PhC waveguide carried out by (2D/3D)-PWE method and (III) Quality factor, Mode volume and electric field distribution at resonance extracted from (2D/3D)-FDTD simulation.

Our reference set of parameters was based on a SOI wafer silicon thin film of thickness $h = 260$ nm, PhC lattice constants a ranging from 330 nm to 400 nm, hole radius $r = 105$ nm (*i.e.* of around $0.3a$) to ensure a wide TE bandgap, a slot width $W_{slot} \sim 100$ nm in order to exploit the W1-like mode and around 200 nm when exploiting the true-slot one [152]. Meanwhile, a refractive index of 3.48 at $\lambda = 1.55$ μm has been considered, with a default top cladding refractive index of 1.46 (that was further tuned up to a $n \pm 0.1$ shift around the default 1.46 value in some specific situations). **Unless otherwise stated, these values of the main opto-geometric parameters were used in the carried out simulations.**

2.1.2.1 Plane Wave Expansion (PWE)

We develop here a minimum information about the Plane Wave Expansion (PWE) method that has been used to calculate the dispersion diagrams of the studied dielectric periodical structures. More information can be found in [153].

Electromagnetic waves are studied by numerically solving the Maxwell's equations in the frequency domain. PWE calculation is based on the following principle: Bloch modes can be expressed as a superposition of a set of plane waves (Floquet's theorem) in Fourier series along the directions in which they are periodic. The PhC structure is characterized by its periodical dielectric constant $\varepsilon(\vec{r})$. The magnetic permeability $\mu(\vec{r})$ is considered constant and equal to one throughout the structure. By combining the Maxwell's equations, the fundamental equation for the electric field \vec{E} is obtained as:

$$\nabla \times \nabla \times \vec{E} = \frac{\omega^2}{c^2} \varepsilon(\vec{r}) \vec{E} \quad (2.1.11)$$

in which ω is the angular frequency and c is the speed of light. In PWE calculation, the dielectric constant and the electric field are also expanded in a sum of plane waves in terms of Fourier series and substituted into the fundamental equation. The following generalized eigenvalue problem is then obtained:

$$(\vec{k} + \vec{G}) \left[(\vec{k} + \vec{G}) \times \vec{E}(\vec{G}) \right] + \frac{\omega^2}{c^2} \sum_{\vec{G}'} \varepsilon(\vec{G} - \vec{G}') \vec{E}(\vec{G}') = 0 \quad (2.1.12)$$

where \vec{k} is the wave vector and \vec{G} are the reciprocal lattice vectors. The eigenvalue matrix equation is solved to obtain the eigenstate frequencies for the corresponding values of the wave vector \vec{k} . For particular structures, gaps can be found where the electromagnetic propagation is forbidden.

After finding the bandgap of a planar PhC and the dispersion diagram of a PhC waveguide (further studied by the supercell approach: see [151] and [103] for further details), the next step is to create a PhC cavity by introducing localized defects into the PhC structure and estimate its Q -factor and mode volume V by using the FDTD method, as presented in Fig. 2.1.3.

2.1.2.2 Finite-difference time-domain (FDTD)

The Finite-difference time-domain (FDTD) [154] method was used to find the solution of the Maxwell's equations directly in the time domain using a discrete mesh in both space and time, and starting with some current source $J(t)$. To simulate accurately, the mesh must be chosen to be sufficiently fine. To respect the algorithm stability criterion, the time step Δt must decrease proportionally to the spatial step Δx , then the computational time for a 2D structure scales with the third power of the linear resolution, and similarly for a 3D structure it scales with the fourth power of the linear resolution. The method allows to analyze the propagation of the electromagnetic fields in real space, and the spectral response is then obtained by Fourier transforming signals. The FDTD method has the disadvantages of being memory-intensive, to present long calculation time because the fields are calculated at each point of the cell. Moreover, the accuracy of the mesh may influence the results. Intrinsically, the method also provides limited information to the physical interpretation of results due to its non-modal character but it is simultaneously powerful due to its calculation mechanism. In addition to the discretization of space and time, the boundary conditions, *i.e.* absorbing and periodic boundary conditions, must be applied properly. In our study, we used Perfectly Match Layers (PML) as the boundary condition. The quality factor of the localized modes can be computed from the extrapolation of the exponential decay of the fields as discussed in the section 2.1.1.1. In this thesis frame, we have used the FDTD solver delivered by Lumerical to calculate Q -factors and mode volumes V of slot PhC cavities.

2.1.3 Design slot photonic crystal heterostructure cavities

We describe here the design principle of a slot PhC heterostructure cavity as a typical example of photonic crystal cavity design. The role of this cavity in our studies has indeed been mentioned in chapter 1 and also corresponds to the cavity family chosen for our experimental realizations, as shown in chapter 3.

As shown in [155], a PhC heterostructure cavity can be formed for example by the longitudinal elongation of the lattice constant of a PhC waveguide in order to create a photonic quantum well.

Starting from initial SPCWs, slot PhC heterostructure cavities can be studied accordingly to the simulation steps shown in Fig. 2.1.3.

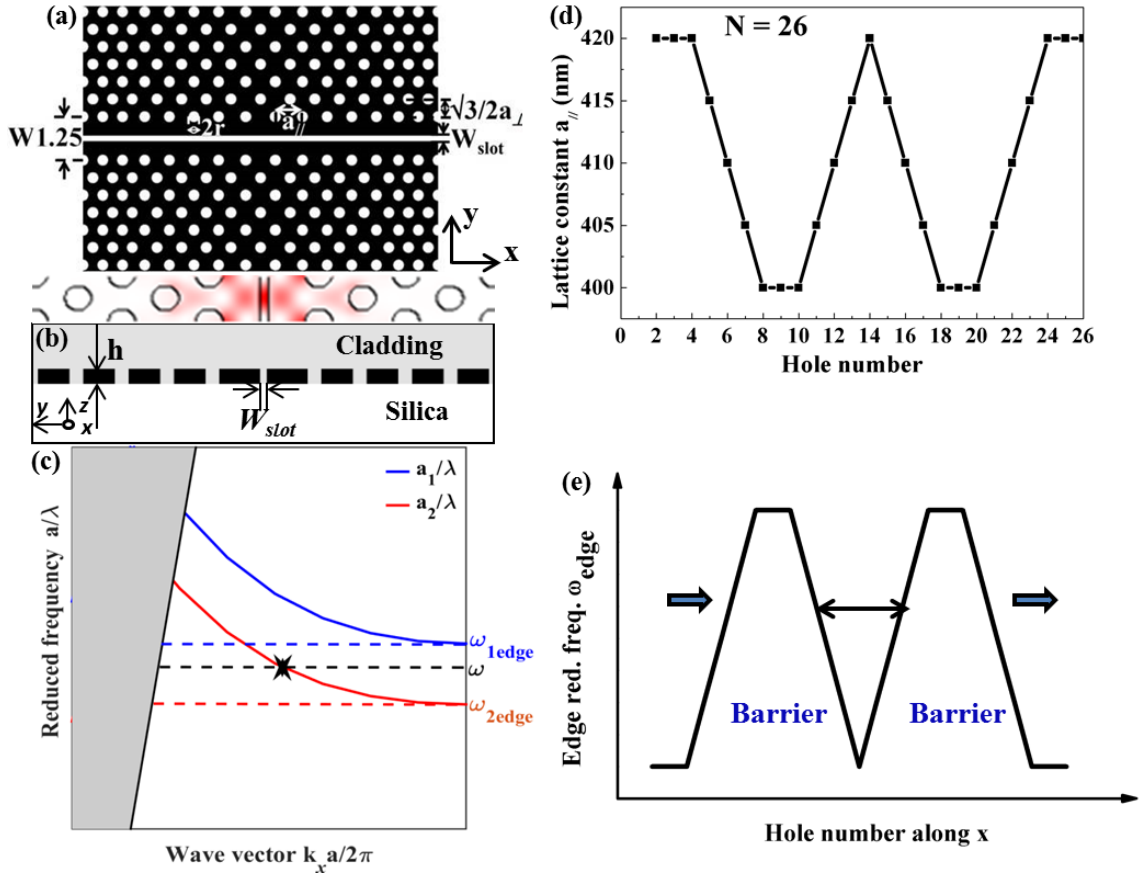


Fig. 2.1.4(a) Scheme of PhC structure in horizontal view with the chirp of the parallel lattice constant $a_{//}$ for a fixed perpendicular lattice constant a_{\perp} **(b)** Vertical view of the slot photonic crystal waveguide geometry on which the cavity geometry is based with the following parameters: hole radius $r = 105$ nm, lateral lattice constants $a_{//}$ are 400 nm, 410 nm and 420 nm, while $a_{\perp} = 400$ nm, a slot width $W_{slot} = 100$ nm, waveguide width of $W1.25 = 1.25\sqrt{3}a$, as well as the electric-field energy density distribution $|E|^2$ in horizontal view. The considered cladding index is $n_{clad} = 1.46$ **(c)** Dispersion diagram of two arbitrary SPCWs with parallel lattice constants a_2 and a_1 in which $a_2 > a_1$, with $a_{\perp} = a_1$, which opens the possibility of occurring resonant modes in the $\omega_{2edge} - \omega_{1edge}$ range **(d)** Profile of the parallel lattice constant for 26 center holes in the first row closest to the slot corresponding to the case $a_{\perp} = 400$ nm and **(e)** Schematic view of the edge frequencies of different SPCWs corresponding to $a_{//}$ in Fig. 2.1.4(d): guided modes occur in the photonic quantum well formed by the largest $a_{//}$ area.

The scheme of the investigated slot PhC heterostructure cavity is illustrated in Fig. 2.1.4 (a) for the horizontal view and in Fig. 2.1.4(b) for the vertical view, respectively. The cavity structure is based on the chirp of the longitudinal lattice parameter $a_{//}$ along the direction of light propagation of a linear defect between a_1 and a_2 while maintaining the perpendicular lattice a_{\perp} constant. Fig. 2.1.4(c) depicts the W1-like modes of two SPCWs corresponding to the two different parallel lattice constants, *i.e.* $a_2 > a_1$ with $a_{\perp} = a_1$.

The trend observed in Fig. 2.1.4(c) can be qualitatively understood and even serves as the guideline for the cavity design: when increasing the lattice constant, the PhC filling factor (r/a) decreases so the planar waveguide effective index increases and the PhC frequency eigenvalues decrease. Let notice that a similar effect would be obtained by tuning the hole radius values. As a result of the obtained dispersion modes realized for a_1 and a_2 , there is possibility of creating resonance modes in the $\omega_{2edge}-\omega_{1edge}$ range. However, in order to prevent radiative mode leakage above the light cone, the modulation step of the chirped lattice constant should be small ($< \sim 1\%$), contributing to create a spatial Gaussian envelope function of the electric field that minimizes the out-of-light-cone wavevector components and that thus helps to obtain high Q -factor values [156].

As one typical example, the chosen design is based on the chirp of the longitudinal lattice parameter with a 20 nm step (Fig. 2.1.4(d)) with $a_{\perp} = 400$ nm and with 26 holes in the center of the structure. The a_{\parallel} and a_{\perp} lattice constants and the SPCW width (W1.25) were chosen from PWE calculations in order to adjust the cavity mode resonance wavelength in the ~ 1570 nm- ~ 1615 nm range. The PhC heterostructure cavity was then constructed symmetrically. The concept of heterostructure cavity relies on the presence of two regions with lowest lattice constants that induce a double barrier of the photonic bandgap frequency edge (Fig. 2.1.4(e)). Each half part begins with the $a_{\perp} + 20$ nm region to guide the light, then is smoothly reduced to one period of $a_{\perp} + 10$ nm to three periods of a_{\perp} , which are the barriers of the cavity.

The resonant modes were calculated by 3D-FDTD simulation. The FDTD calculation region was set to cover the cavity part with a refined mesh in the center ($dx = 8$ nm and $dy = 6$ nm). The mesh was chosen as a compromise of accuracy and time consumption and also related to the e-beam lithography fabrication accuracy with a beam step size of 5 nm. The boundary conditions were chosen as PMLs with a thickness of 24 cells in order to absorb unwanted light reflections properly. The cavity was excited by a TM dipole source with a 1.4 μm -1.64 μm wavelength range and located in the cavity area.

We could obtain the field profile (Fig. 2.1.5(a)) at the resonance wavelength $\lambda_{res} = 1.57 \mu\text{m}$ and estimated Q to $\sim 120\,000$ with a mode volume $V \approx 0.03(\lambda/n_{clad})^3$, with $n_{clad} = 1.46$ the refractive index of the top cladding filling material.

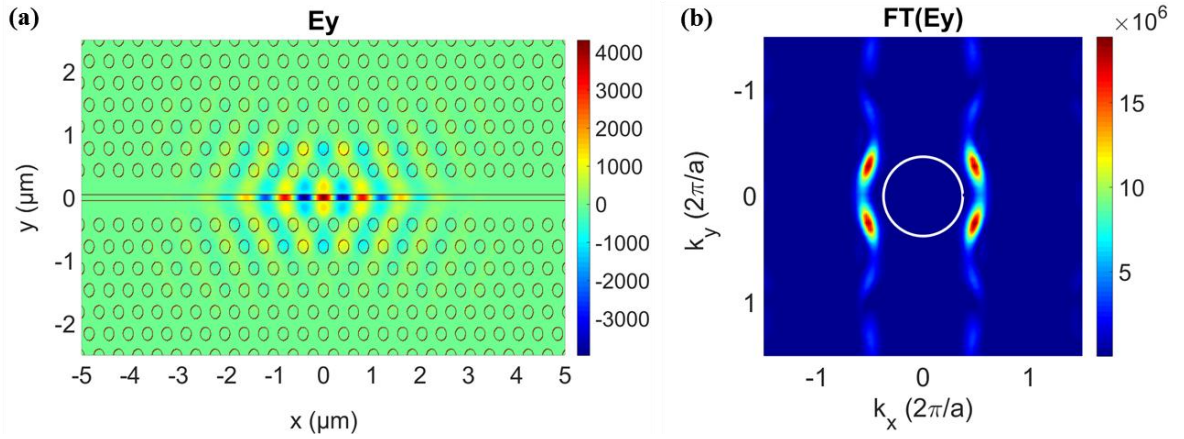


Fig. 2.1.5(a) E_y component of the resonant mode ($\lambda_{res} = 1570 \text{ nm}$) for the slot PhC heterostructure cavity corresponding to $a_{//} = 400 \text{ nm}$, 410 nm and 420 nm , respectively, while $a_{\perp} = 400 \text{ nm}$ by 3D-FDTD simulation **(b)** The corresponding E_y Fourier transform in wavevector space with the light-cone (white circle).

We notice that the resonance wavelength obtained by 3D-FDTD is consistent with the PWE bandgap engineering results. Regarding the cavity quality factor cavity figure of merit, the performed FDTD simulation is higher than previous values experimentally attained in previous works for similar structures, especially the $Q = 4\,000$ reported for SOI slot heterostructure cavities infiltrated by water in Ref. [134]. Fig. 2.1.5(b) presents the Fourier transform of the E_y field component and provides a confirmation that the smoothness of the adopted design efficiency allows to minimize out-of plane leakage due to the coupling of wavevector components to the continuum of radiation modes.

By a similar approach based on a double heterostructure lattice chirp, other configurations have also been studied. The main applied considered change consisted in a modification of the perpendicular lattice constant a_{\perp} . By reducing a_{\perp} down to 330 nm , it was possible to reduce the slot PhC resonance wavelength down to $\lambda_{res} = 1.28 \mu\text{m}$. Even for $a_{\perp} = 330 \text{ nm}$, 3D-FDTD simulation provided $Q \approx 21\,000$ and $V \approx 0.024(\lambda/n_{clad})^3$ for slotted PhC structures filled with a cladding material of 1.46 index. Hence, in all configurations, the Q/V ratio proved to be large enough for in/on-silicon hybrid integration of active materials. We fabricated a series of slot PhC heterostructure cavities with perpendicular lattice constant ranging from 330 nm to 400 nm

which provided resonances in the telecom range (*i.e.* 1.28 μm –1.6 μm) with Q -factors of several tens of thousands in order to serve hybrid integration purpose. The related experimental works are presented in chapter 3.

2.1.4. Conclusion of section 2.1

In this section, after introducing the figures of merit of PhC cavities, namely the Q -factor and mode volume, and the principles of the numerical tools (PWE and FDTD) used in this work, designs of **SOI slot PhC heterostructure cavities dedicated to hybrid integration** have been proposed. These cavities are based on slot PhC waveguides with perpendicular lattice constant a_{\perp} ranging from 330 nm to 400 nm, hole radius $r = 105$ nm, slot width $W_{slot} = 100$ nm and a waveguide width $W_{1.25} = 1.25a\sqrt{3}$ fabricated by starting from on a 260 nm Si thin film wafer. These cavities can support Q -factors of several tens of thousands while their mode volumes are of around $0.03(\lambda/n)^3$, which yields high Q/V ($>600\ 000$), **strengthening strong light-matter interaction.**

2.2 Coupling slot photonic crystal cavities and waveguides

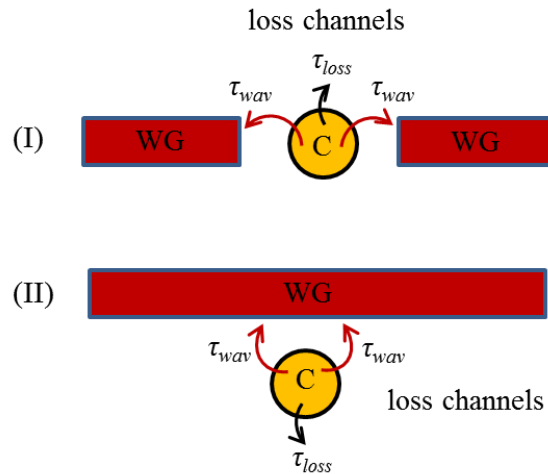


Fig. 2.2.1 Scheme of Cavity (“C”)–Waveguide (“WG”) coupling, (I) Butt coupling and (II) Lateral coupling with loss channels including intrinsic loss of uncoupled cavity τ_{loss} and waveguide coupling channels ($2\tau_{wav}$).

Slot waveguide resonators provide strongly confined modes with a partial dielectric energy confinement in the slot of around $\sim 20 - 30\%$, which is intrinsically a desired property for the enhancement of light-matter interactions. Simultaneously, this feature also raises a possible

challenge with respect to the excitation of the localized modes from outside. Their unusual mode field profiles may indeed make them difficult to excite from waveguides, whereas this point is critical with respect to hybrid integration.

From a general point of view, the coupling between localized high Q modes and propagating waveguide modes opens room to many interesting phenomena, *e.g.* channel add-drop filters [157], [158], switches [159]–[161], or sensing [162]. From a practical point of view, there are mainly two different schemes of cavity - waveguide coupling, as illustrated in Fig. 2.2.1: the butt-coupling and the lateral - coupling approaches.

The interaction of the cavity with the waveguide is determined by the cavity spectral function and the waveguide density of states, so the strength of the PhC cavity mode coupling with the PhC waveguide increases at the PhC waveguide band-edge where light group velocity vanishes. For the evanescent coupling, the cavity and the waveguide are brought into proximity, and the coupling coefficients depend on the spatial overlap integrals of the waveguide Bloch states and the cavity mode according to the following equations [163]:

$$\kappa_{ba}(k) \propto \left(\int dr \frac{\Delta \varepsilon_w(r)}{c^2} e^{-ikx} \mathbf{B}_k \cdot \mathbf{A}^* \right) \quad (2.2.1)$$

$$\kappa_{ab}(k) \propto \left(\int dr \frac{\Delta \varepsilon_c(r)}{c^2} e^{-ikx} \mathbf{A} \cdot \mathbf{B}_k^* \right) \quad (2.2.2)$$

, where $\Delta \varepsilon_{c,w} = \varepsilon_t - \varepsilon_{c,w}$, ε_t is the relative dielectric constant for the coupled system, ε_c and ε_w are the relative dielectric constant for the cavity and for the waveguide, respectively. \mathbf{B}_k and \mathbf{A} , which represent the waveguide Bloch state and cavity mode, respectively can be expressed as:

$$\mathbf{E}_w = \mathbf{B}_k(r) e^{i(\omega(k)t - kz)} \quad (2.2.3)$$

$$\mathbf{E}_c = \mathbf{A}(r) e^{i\omega_c t} \quad (2.2.4)$$

And are solutions of the wave equation:

$$\nabla \times \nabla \times \mathbf{E} + \frac{\varepsilon(r)}{c^2} \frac{\partial^2 \mathbf{E}}{\partial t^2} = 0 \quad (2.2.5)$$

PhC waveguide and cavity coupling efficiency has been studied for efficient implementation of photonic circuits [164], [165] and can be described by the FDTD methods [158], [166], [167], the coupled mode theory (CMT) [163], [168], [169] or the scattering analysis [170].

In this manuscript, the two main coupling geometries have been addressed:

- The butt - coupling approach has been chosen for the experimental investigation of single slot PhC heterostructure cavities (see chapter 3).
- The lateral - coupling approach has been chosen for design studies conducted in this chapter due to its versatility for the future side-by-side integration of several slot PhC cavities along a given waveguide.

Similarly, we have selected one of the two modes of slot PhC waveguides and have chosen the true-slot mode of SPCW due to its deep location below the light line and its strong spatial confinement (see section 1.3.4.2 of chapter 1).

To sum up, **the chosen reference configuration** that was selected to assess the possible excitation of slot PhC cavities from external waveguides for hybrid on silicon integration of active materials **is based on the lateral coupling between a slot PhC waveguide mode and a true-slot mode PhC cavity**. A configuration derived from an L3 cavity geometry was chosen as a typical example of PhC cavity giving rise to large Q s and small mode volumes [127], [128], [171].

FDTD and time-domain coupled mode (CMT) calculations have been used to study slot PhC cavity - SPCWs coupling. Details about the CMT-based derivation that was done can be found in Appendix A, yielding especially the build-up factor F giving rise to a quantitative estimation of light-matter interaction strength in the hollow core PhC cavity filled with an active material.

Calculations have been based on 2D-PWE and 2D-FDTD simulations in order to minimize the needed computational effort. The performed proof of concept studies can be considered as a good guide for further experimental investigations. Due to the 2D simulation approach, the estimation of Q values of the studied loaded cavities was not listed among the waited outputs.

In the following sections:

- First, we design a true-slot mode SPCW, *i.e.* supporting only the true-slot mode of slot PhC waveguides.

- In a second step, a true-slot cavity mode generated from the true-slot mode waveguide is prepared with a proper resonance wavelength.
- Finally, the coupling between this true-slot mode cavity and a true-slot mode SPCW is studied.

2.2.1 Design of a true-slot mode cavity

In order to design a true-slot mode L3 PhC cavity, the first task is to design a single-mode true-slot mode SPCW. As discussed in section 1.3.6, in order to exploit only the waveguide true-slot mode, it is necessary to use a wide slot width and/or to increase the hole radius in the first row in order to pull the true-slot mode in the center of PBG of the 2D planar PhC dispersion diagram. We started here with the following typical parameters: a SPCW based on a 105 nm radius hole, a lattice constant $a = 380$ nm, and a slot width of $W_{slot} = 200$ nm introduced in a waveguide of $W = 1.25\sqrt{3}a$ hole to hole width (*i.e.* $1.25W_1$ waveguide). An effective index $n = 2.95$ of the 2D PhC was considered, corresponding to the effective index of a slab SOI with thickness $h = 260$ nm (at $\lambda = 1.50$ μm) with a top cladding index of $n_{clad} = 1.44$.

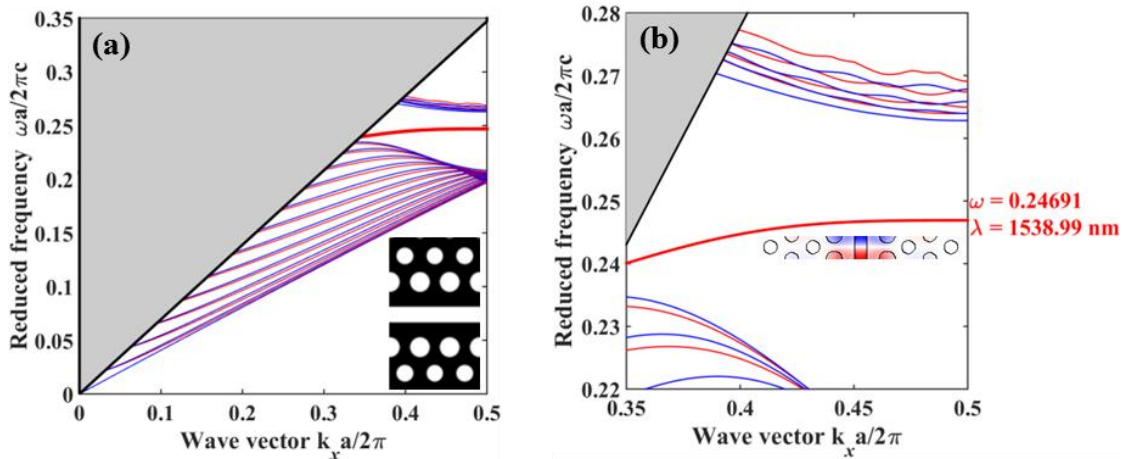


Fig. 2.2.2(a) Dispersion diagram and the structure of the SPCW with 105 nm radius hole, a lattice constant $a = 380$ nm, and a slot width of $W_{slot} = 200$ nm introduced in a waveguide of $WG_{1.25} = 1.25\sqrt{3}a$, an effective index $n = 2.95$ of the 2D PhC corresponding to the effective index of a slab SOI with thickness $h = 260$ nm (at $\lambda = 1.50$ μm) with a top cladding index of $n_{clad} = 1.44$ in the case radius hole of first row $r_1 = 125$ nm **(b)** Zoom of dispersion diagram of the true-slot mode (red curve) and the related profile of the E_y component of the y -even mode.

We first used 2D-PWE simulation to calculate the photonic bandgap of the bulk 2D planar PhC structure based on these parameters for the TE light polarization. A TE bandgap exists from $a/\lambda = 0.2379$ to $a/\lambda = 0.2899$, corresponding to the 1310.5 nm–1597.5 nm wavelength range. The

dispersion diagram of the SPCW, with radii of the first two rows of holes increased to 125 nm is depicted in Fig. 2.2.2(a), while Fig. 2.2.2(b) presents a zoom centered on the true-slot mode frequency range. As seen in Fig. 2.2.2(b) focusing on the dispersion diagram of the true-slot mode, this SPCW provides a single true-slot mode with a TE-like y -even distribution of the E_y component with an edge frequency around 0.24691 ($\lambda \approx 1539$ nm).

Based on this SPCW, a PhC slot L3 cavity was created by removing three rows of holes and inserting a slot in the light propagation direction to generate a true-slot cavity mode with a possible resonance wavelength around $\lambda = 1539$ nm. Fig. 2.2.3(a) presents the geometry of the PhC slot L3 cavity formed by removing three holes and introducing a 200 nm width slot in the defect line. The radii of the holes in the center around the slot were also increased to $r_{ct} = 150$ nm to reinforce lateral barriers needed to light reflection.

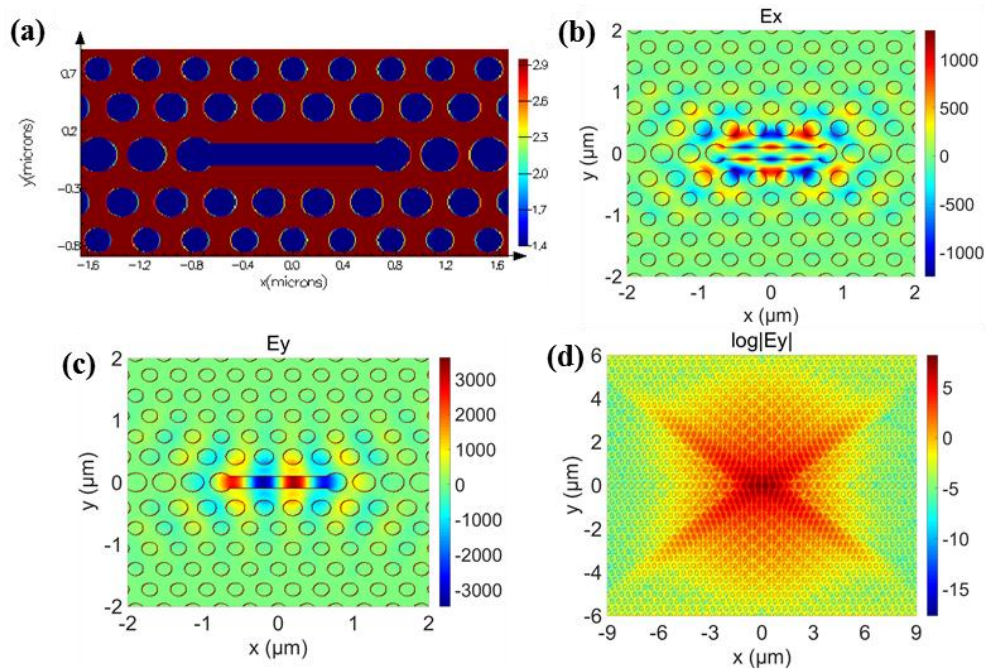


Fig. 2.2.3(a) Refractive index profile of the 200 nm slot L3 PhC cavity and its **(b)** E_x component **(c)** E_y component and **(d)** Log of magnitude of the E_y component of the cavity mode at $\omega = 0.248$ ($\lambda = 1532.51$ nm) resonance frequency.

We then obtained a cavity mode with $Q = 3.323 \cdot 10^7 \pm 8170$ at the resonance wavelength of 1532.41 nm by using 2D-FDTD simulation. This Q value is meaningless because vertical losses are not included in the 2D-FDTD simulation scheme, but this large Q value is yet the clear signature of the confined mode and provides a confirmation of the resonance. Its E_x , E_y components in linear scale and in log scale are depicted in Fig. 2.2.3(b)-(c)-(d), respectively.

The profile of the E_y component of the cavity mode obtained by 2D-FDTD simulation is in good agreement with the guided mode of the waveguide from which the cavity is generated. The resonance wavelength of the cavity is around $\lambda_{res} = 1532.51$ nm ($\lambda_{res}/a \sim 0.248$), *i.e.* slightly higher than the edgefrequency of the true-slot mode waveguide obtained by 2D-PWE, which may come from the difference between the two employed meshes and the numerical method principles. From the distribution of E_y magnitude in log scale, we also notice that the coupling between the cavity mode and a waveguide is likely to be strong only if the distance between them is no more than a few PhC unit cells.

2.2.2 Coupling between a true-slot mode photonic crystal L3 cavity and a true-slot mode photonic crystal waveguide

We investigate in this section the possibility to fill the true-slot mode cavity studied above from a waveguide, as illustrated in Fig. 2.2.4.

The cavity being characterized by the resonance mode appearing in black dotted lines in Fig. 2.2.4(b), a SPCW is designed with dispersion property (*e.g.* see the red line) adjusted to cross the true-slot mode cavity at different frequency crossing points corresponding to different SPCW group velocities.

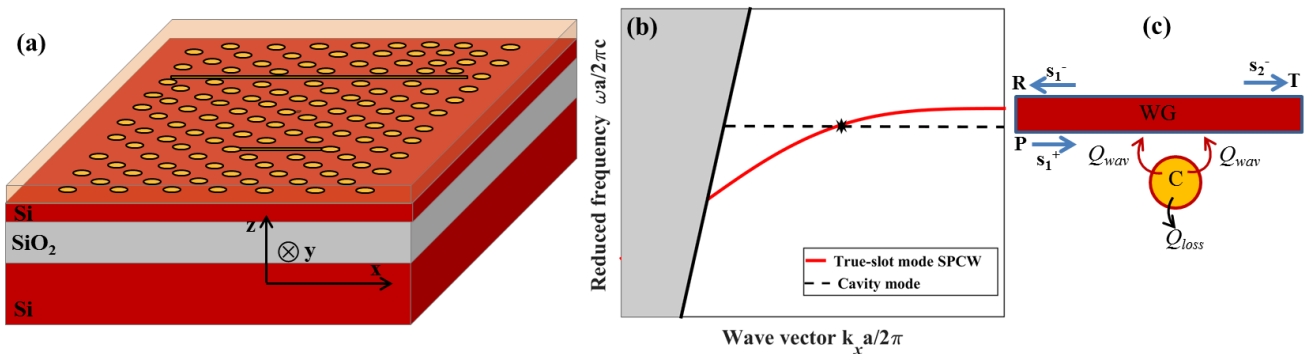


Fig. 2.2.4(a) Schematic view of the lateral-coupling between a slot photonic crystal waveguide (SPCW) and a slot photonic crystal cavity; the precise design of the cavity is based on a 105 nm radius hole, a lattice constant of $a = 380$ nm, and a slot width of $W_{slot} = 200$ nm **(b)** Dispersion diagram of the true-slot mode SPCW and the resonance cavity mode in black dotted line and **(c)** Their coupling scheme.

As discussed in Appendix A related to the coupling mechanism of a cavity and a waveguide using the coupled mode theory (CMT), the build-up factor, which is defined by the ratio of the energy of the cavity mode and the incoming power of the waveguide mode evolves as a function

of the coupling cavity/waveguide strength, *i.e.* on Q_{wav} or Q_{wav}/Q_{loss} , as shown in Fig. 2.2.5, where Q_{loss} and Q_{wav} are the quality factor of the unloaded cavity and in the case of coupling with a waveguide, respectively. The build-up factor at resonance $F(\omega_0)$ only depends on the intrinsic properties of the cavity and reaches the maximum of $(Q_{loss}/2\omega_0)$ when Q_{wav} and Q_{loss} satisfy the relationship $Q_{wav} = 2Q_{loss}$ (see Appendix A).

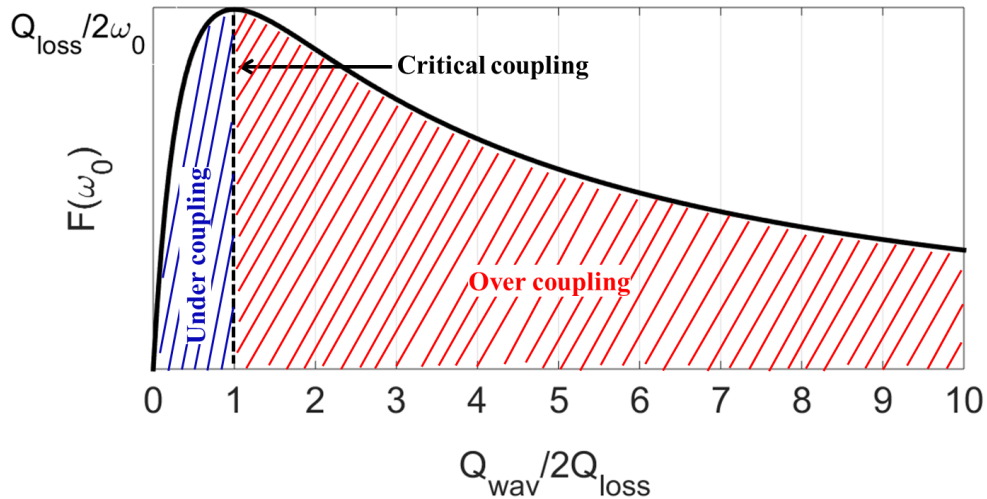


Fig. 2.2.5 Build-up factor at resonance as a function of $(Q_{wav}/2Q_{loss})$.

Our target was to study the case in which the crossing point is close to the band-edge of the guided mode. We thus played with the parameters of the SPCW to achieve this condition. At the same time, propagation losses of PhC waveguides are known to increase due to extrinsic optical losses which scale inversely with the light group velocity square due to backscattering of light [172]. Hence, for a compromise between coupling efficiency and reasonable slot waveguide propagation losses in the coupled PhC cavity/waveguide system, the crossing point between the resonant cavity and the guided modes should typically be limited to situations in which the SPCW mode group index n_g in ranges between 20 and 60 [173].

Using these design guidelines, the radius of the first two rows of holes closest to the slot, *i.e.* r_1 , was swept in the 105 nm–150 nm range. Fig. 2.2.6(a) shows the dispersion diagram of the SPCW corresponding to $r_1 = 130$ nm with a value of targeting edge-band frequency around 0.24952 (*e.g.* $\lambda \sim 1523$ nm).

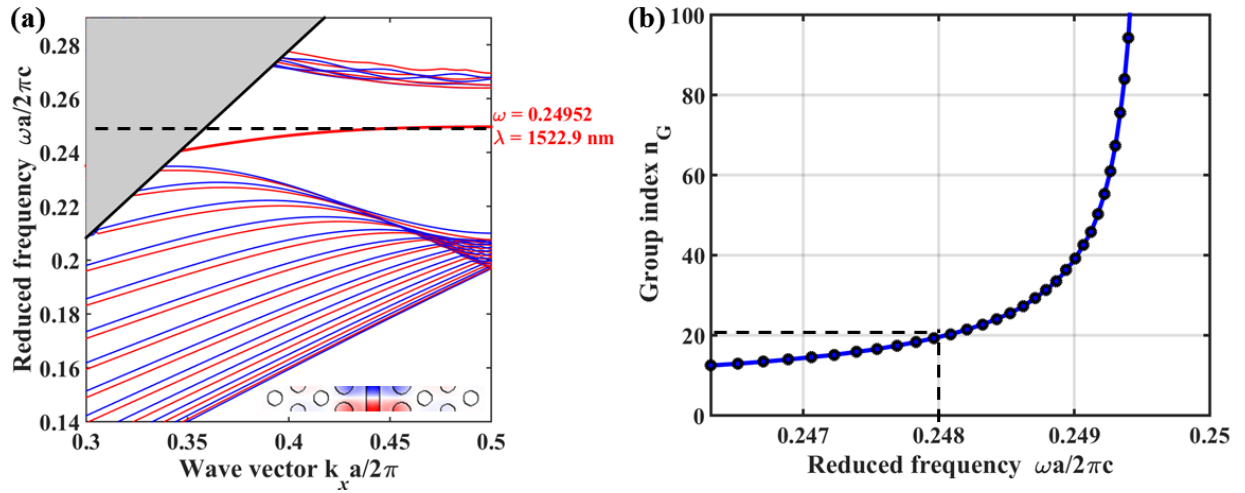


Fig. 2.2.6(a) Dispersion diagram and the structure of the SPCW in the case $r_l = 130$ nm (inset the E_y component of the y-even true-slot mode profile) **(b)** The related mode group index versus the reduced frequency.

In this configuration, the SPCW supports a single mode: the true-slot mode, which features a nearly flat band near the bandedge and also satisfies the matching of the parity and pattern with the true-slot cavity mode. In addition, at the cavity resonance $\omega = 0.248$, the group index n_G of the guided mode is moderately high, *i.e.* $n_G = 20$ as shown in Fig. 2.2.6(b). In order to achieve strong coupling, from the log scale of the magnitude of the electric field, we decided to study the side-coupling between the PhC slot L3 cavity and the SPCW at a distance of five rows of holes, as depicted in Fig. 2.2.7:

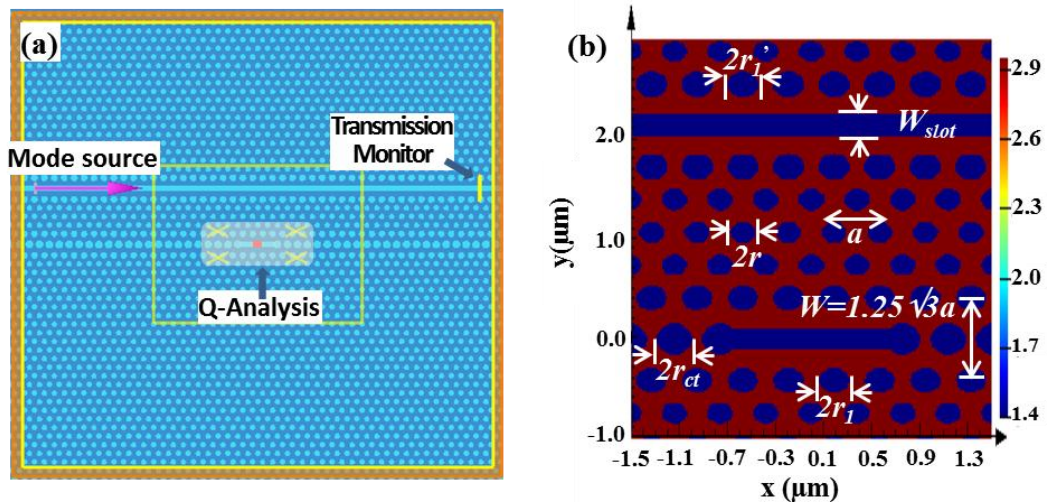


Fig. 2.2.7(a) Scheme of the coupling between the SPCW and the L3 true slot mode PhC cavity using 2D-FDTD simulation **(b)** Description of the parameters of the coupling system: lattice constant: $a = 380$ nm, hole radius: $r = 105$ nm; hole radius in the row closest to the slot of cavity: $r_l = 125$ nm, hole radius along the slot of cavity: $r_{ct} = 150$ nm, hole radius in the row closest to slot of waveguide: $r_l' = 130$ nm, slot width: $W_{slot} = 200$ nm and the waveguide width $W_{1.25} = 1.25\sqrt{3}a$.

- First, we excited the cavity mode by putting a dipole source in the cavity area to collect the resonance mode of the cavity and its Q -factor by using 2D-FDTD simulation. The simulation area was set to a size of $18 \mu\text{m} \times 17 \mu\text{m}$ covered by the yellow boundary as shown in Fig. 2.2.7. The PML boundary was chosen at 24 layers to absorb out-going radiation, and the grid size was around 12 nm. The resonance of cavity in this coupling configuration was detected at $\lambda = 1532.84 \text{ nm}$, with thus a little shift compared with the single cavity case ($\lambda_{res} = 1532.51 \text{ nm}$) due to the influence of the waveguide.
- Second, we put a mode source in the input of the waveguide (Fig. 2.2.7(a)) with the wavelength range around the resonance of the cavity to collect the transmission spectrum in the output of the waveguide and also capture the excited mode profile in the cavity.

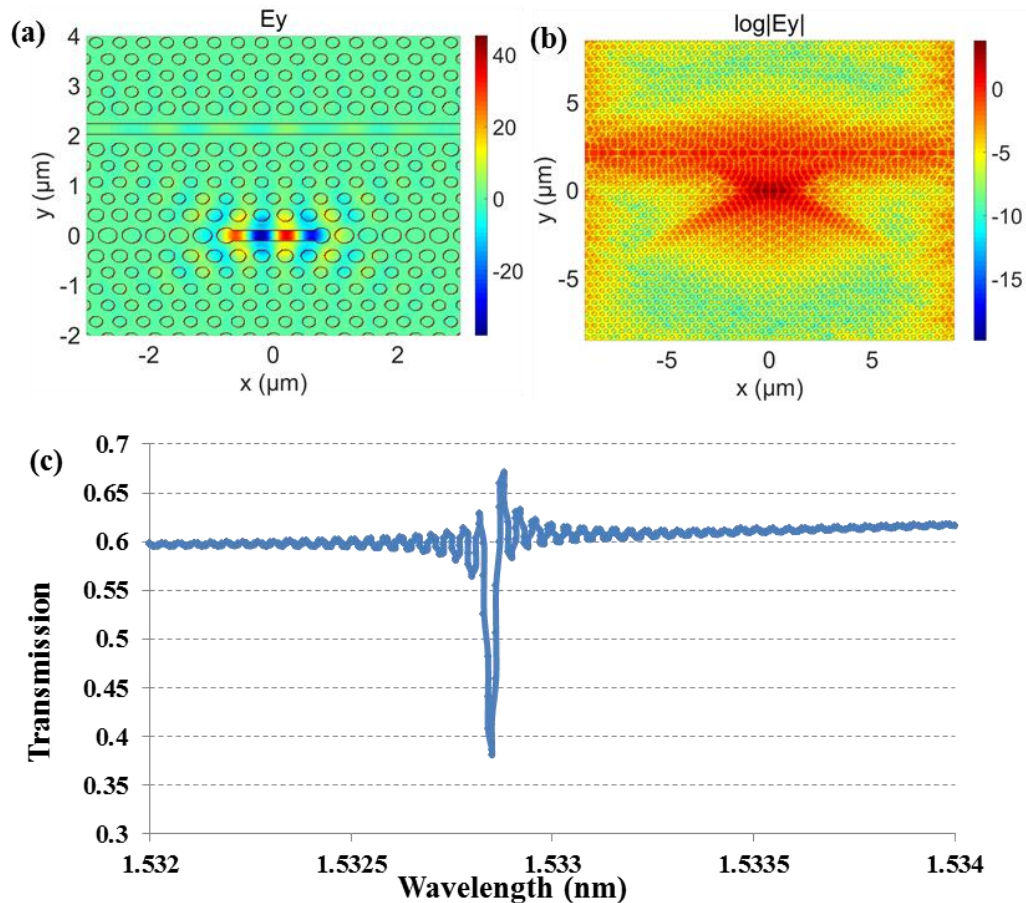


Fig. 2.2.8 Excitation of light from the slot Photonic crystal waveguide: (a) E_y distribution of the slot L3 PhC cavity and (b) Log-scale of E_y at resonance wavelength $\lambda = 1532.84 \text{ nm}$ (c) Normalized transmittance collected at the output of the SPCW.

The profile of the E_y component of the coupling system in linear and in log scales at resonance wavelength $\lambda = 1532.84 \text{ nm}$ are depicted in Fig. 2.2.8(a) and Fig. 2.2.8 (b), respectively.

The distribution of E_y shows that the slot L3 PhC cavity can effectively be excited through the slot Photonic crystal waveguide. Moreover, **the transmission at the output of the in Fig. 2.2.8(c) provides a confirmation that the cavity can be excited.** The transmission indeed drops to around 0.38 (~63% of the transmission maximum) at resonance while $T(\omega) = 0.25$ in case of critical coupling (as presented in Appendix A), which shows that for a distance of 5 rows of holes is not far from the critical coupling condition, slightly undercoupled.

2.2.3 Conclusion of section 2.2

To conclude this part, we have explored the ability to excite an L3 true-slot mode PhC cavity through a true-slot SPCW as a proof of concept study of the possible excitation of slot cavity modes from external waveguides.

In a complementary fashion, we explore in the next part of the coupling between two slot PhC cavities as a first milestone towards the realization of arrays of coupled PhC cavities and waveguides that may be used for switching [174], [175] in the frame of on-silicon hybrid integration.

2.3 Coupled slot photonic crystal cavities

In addition to single cavities, coupled PhC cavities are very interesting because they open the possibility to get several localized modes with different symmetries. Moreover, with the versatility of PhCs, the relative energy and spatial distribution of these modes can be adjusted. Combining these specific features with active materials could open potential applications such as sensing [176], quantum optical information processing (*e.g.* the optical switch of the far field pattern of quantum emitters) [177], all optical switching [178], or slow light engineering [179].

2.3.1 Photonic molecules in planar guided wave optics

As seen in section 2.2, optical micro- and nano- cavities are structures in which light is confined in small volumes. They can be called “photonic atoms” for their properties of photon state confinement. Coupling photonic atoms in “photonic molecules” (PMs) is a pretty straightforward

further direction that has been explored in a large set of previous work [180] - [56]. Various kinds of PMs have been proposed corresponding to different morphologies of coupled resonators (Fig. 2.3.1), such as identical microdisks [181] or different radius ones [182], microspheres [183]–[185], coupled microrings in the vertical direction [186] or in the horizontal one [187], [188], supporting whispering gallery mode (WGMs) resonances, Fabry-Perot ones [189], [190] and strongly confined PhC nanocavities [174], [179], [191]–[197].

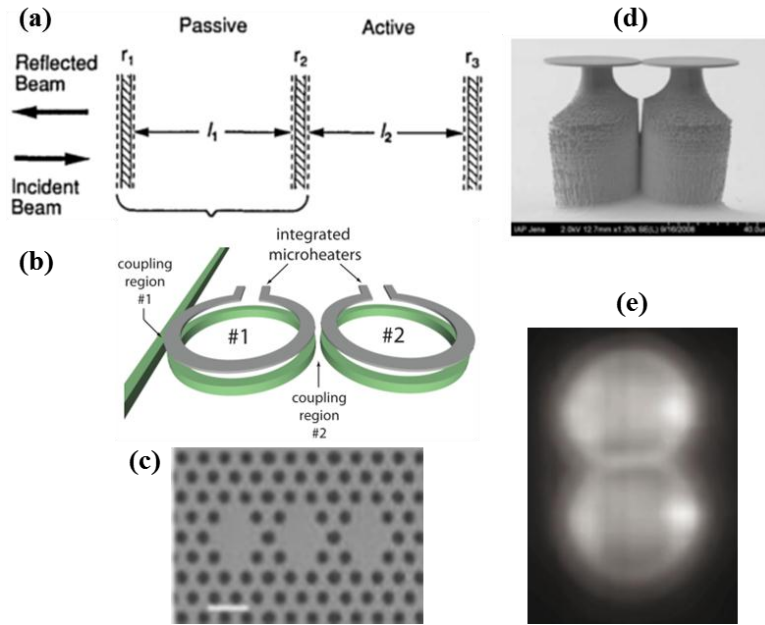


Fig. 2.3.1 Different configurations of photonic molecules based on different resonator kinds: (a) Compound Fabry-Perot resonators consisting of three mirrors, a passive and nonabsorptive FB cavity coupled to an active FB cavity [189] (b) Dual-cavity coupled microring resonators [188] (c) Coupled located defects in PhC cavities [196] (d) Coupled Silica disk microresonators [181] and (e) Bisphere photonic molecule [183].

As in atomic systems, the interaction between coupled resonators brings bonding and antibonding states. In coupled microspheres, these states can be expressed as a linear combination of the Mie resonance states of each sphere while in coupled PhC cavities, these states are formed by the superposition of the single-cavity photonic states [191]. When two identical photonic resonators with resonance frequency ω_0 are put in close proximity, their optical modes interact and yield two supermodes with resonance frequencies ω_B and ω_{AB} . The “B” and “AB” labels refer here to the supermodes field parities in term of bonding (“B”) and antibonding (“AB”) distributions, in analogy with the bonding and antibonding orbitals in diatomic molecules, as illustrated in Fig. 2.3.2 [198]. However, contrary to electronic states of diatomic molecules where the bonding and antibonding frequencies verify $\omega_B < \omega_{AB}$ (*i.e.* the

bonding mode is the ground state and the antibonding mode is the upper energy), in PhC molecules the bonding mode can have a higher or a lower energy than the **antibonding** one [177], [193], [194].

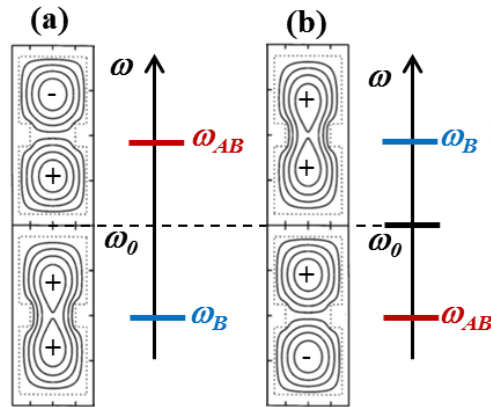


Fig. 2.3.2 Splitting of bonding (“B”) and antibonding (“AB”) states in a coupled system, (a) Bonding mode is the ground state and (b) Antibonding mode is the ground state.

Coming back to photonic crystal “photonic molecules”, several studies have been based on different kinds of coupled PhC cavities (Fig. 2.3.3).

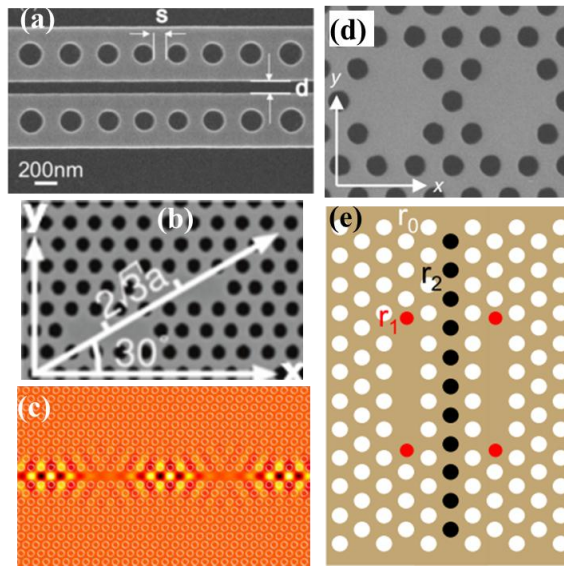


Fig. 2.3.3 Various types of PhC photonic molecules: (a) Coupled PhC nanobeam cavities [192] (b) Coupled PhC L3 cavities [193] in different coupling direction or (e) Coupled PhC L3 cavities with tuning the barrier to tailor the supermodes [194] (c) Coupled multiple heterostructure cavities [175] (d) Coupled D2 PhC cavities [199].

Some studies were devoted to simple coupled nanobeam cavities consisting of two parallel suspended wires perforated by one-dimensional lines of air holes and separated by a small gap (Fig. 2.3.3(a)). In this scheme, the optical resonances were experimentally investigated by

considering different coupling strengths by changing the inter-cavity gap distance. In this situation, the coupling strength and the Q -factor of the even modes strongly depend on the nanobeam distance, which can be useful for bio-sensing and opto-mechanical applications. Coupled PhC L3 cavities have also been investigated theoretically and experimentally. The mode splitting, quality factor and light polarization influences were studied in different coupling configurations (Fig. 2.3.3(b)) by tuning the coupling strength without changing the inter-cavity distance (Fig. 2.3.3(e)). Coupled D2 cavities (removing 4 holes in a diamond-like geometry (Fig. 2.3.3(d)) were also studied to engineer the mode parity of the ground state and tailor the photon hopping due to the coupling direction [177], [196], [200]. Coupled heterostructure cavities (Fig. 2.3.3(c)) were also of interest to engineer the group velocity of light over a wide range.

Nevertheless, to the best of our knowledge, there has been no research on coupled slot PhC cavities in which the cavities modes were tightly confined in the slot. This encouraged us to:

- (1) Address the coupling between two slot PhC cavities and verify that they can be weakly or strongly coupled.
- (2) Investigate the beating sign between the bonding and the antibonding states in this kind of hollow core resonators.

In order to perform these studies, we have tried to rely on a semi-analytical method able to describe the cavity-cavity interaction derived from solid-state physics: the “**Tight-binding**” approach.

2.3.2 Tight-binding approximation applied to slot photonic crystal cavities

2.3.2.1 Principle of the tight-binding approximation

The tight-binding (TB) formulation is useful in studying the electronic properties of solids [201]. In analogy between confined photon states in PhCs and electron states in solids, the TB approach can also be applied to photonics [202]. It is a perturbative method, and its principle is that in coupled cavities the “wave functions” (*e.g.* the fields) are tightly confined in each cavity. The eigenmodes of the individual cavities are then coupled to yield cavity supermodes. Coupling between neighboring cavities is due to the overlap of the “eigenfunctions” of the isolated cavity modes.

The TB approach has been used to study various photonic structures. It is a common approach to model the dispersion in infinite chains of coupled cavities [203]–[206]. The impurity modes of the electromagnetic field in a chain of impurities cells in a photonic insulator were described by the TB model [207], in which the authors introduced a simple model of impurity photonic bands, or in [31] where the TB approximation was used to find the high- and low-reflectance frequency regions of deep Bragg 1D superstructure gratings [208]. It was also applied in the description of resonator/optical waveguide coupled systems through weak coupling approximation [202]. A good agreement was found between PWE method and a phenomenological TB model to reproduce the band structure of different high dielectric contrast 2D lattices composed of cylinders with and without defects [209]. Moreover, the TB photon scheme was exploited to explain the splitting of the coherent coupling of whispering-gallery modes in quartz polystyrene bispheres [210]. The optical modes of the PM formed by coupling pairs of micrometer-sized semiconductor cavities via narrow channel numerically obtained by this approach were also successfully compared with experimental results [180]. In the TB photonic approach, the optical waves can be guided by connecting the units in the arbitrarily shaped microstructures starting from microspheres [183], [211]. TB calculation was also used to describe the behavior of dispersion relationships of guided modes in coupled PhC waveguides [212]. In general, each resonator is the optical counterpart of the isolated atoms.

In a similar sense, the PMs made of PhC cavities have been investigated widely by the TB approach to predict the bonding and antibonding modes which can be based on the concept of generalized Wannier function [213], and then to study the eigenmode splitting due to the coupling of the evanescent defect modes and dispersion relation in three-dimensional PhCs [214] or 2D triangular PhCs [215]. In these structures, the electromagnetic waves are tightly confined at the defect position or the localized mode and photons can propagate by hopping through the interactions between neighboring evanescent cavity modes.

In this Ph.D. work, investigation of the properties of photonic molecules made of coupled slot PhC cavities for hybrid integration of active materials in silicon photonics has been achieved. We indeed anticipate that coupled slot cavities could provide supermode fields bringing degrees of freedom for hybrid integration and the development of applications including optical sensing,

optical switching, and the design optical functions based on nonlinear effects exploiting doubly or triply resonance cavities.

Only few works have been clearly devoted to the coupling between only two PhC cavities in the frame of the TB approach. For instance, the coupling strength between two cavities was interpreted within a Fabry-Perot model based on the bouncing of a single Bloch mode between two PhC mirrors in Ref. [194]. This matter of fact encouraged us to push this investigation towards the study of two slot PhC cavities. Meanwhile, the study of two classical L3 PhC cavities was first derived as an intermediate state.

2.3.2.2 Bonding and antibonding photonic molecule supermodes seen by the tight-binding approach

In photonics, confined photon states are described by the Maxwell equations. In the case of two coupled identical PhC cavities, the coupling between identical localized photonic modes creates a frequency splitting of the two modes. The bonding mode or the even molecular state corresponds to the 0 -phase difference between two original localized modes. Meanwhile, the other one is the antibonding mode or the odd molecular state is related to a π -phase difference between the two original localized modes.

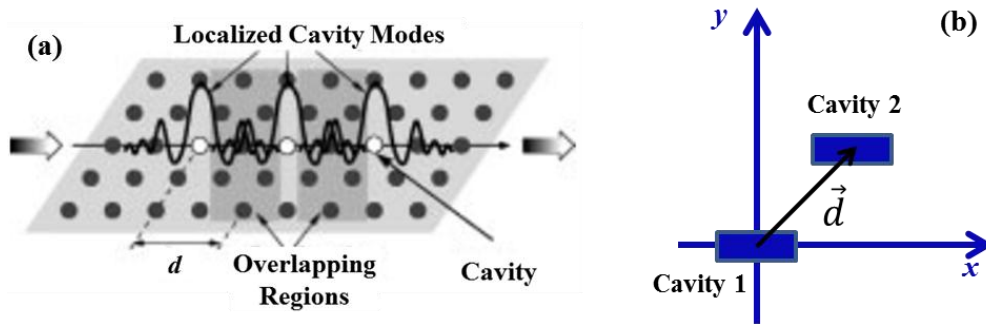


Fig. 2.3.4(a) Scheme of coupled Photonic crystal molecules in which a tightly confined cavity mode interacts weakly with the neighboring cavity modes [215] **(b)** Sketched view of two coupled cavities at distance d along a nearby arbitrary direction.

Starting with the master equation to describe the spatial part of the individual localized mode $E_{\Omega}^{\mathbf{r}}(\mathbf{r})$ of a single defect cavity mode:

$$\nabla \times \nabla \times \mathbf{E}_{\Omega}^{\mathbf{r}}(\mathbf{r}) = \varepsilon_0(\mathbf{r}) \left(\frac{\Omega}{c} \right)^2 \mathbf{E}_{\Omega}^{\mathbf{r}}(\mathbf{r}) \quad (2.3.2.1)$$

, where without any restriction to the generality of the results, $\vec{E}_\Omega(\vec{r})$ can be considered as a real vector, $\varepsilon_0(\vec{r})$ is the dielectric constant of the single defect, and Ω is the corresponding eigenfrequency, the following results can be obtained (see Appendix B):

$$\omega_B = \Omega(1 - \kappa) \quad (2.3.3.2a)$$

$$\omega_{AB} = \Omega(1 + \kappa) \quad (2.3.3.2b)$$

, where
$$\kappa = \frac{\left(\int d^3\vec{r} \frac{\Delta\varepsilon(\vec{r})}{2} \vec{E}_\Omega(\vec{r}) \cdot \vec{E}_\Omega(\vec{r} - \vec{d}) \right)}{\left(\int d^3\vec{r} \frac{\varepsilon_0(\vec{r})}{2} \|\vec{E}_\Omega(\vec{r})\|^2 \right)} \quad (2.3.3.2c)$$

is the coupling coefficient, and the deviation of the dielectric constant:

$$\Delta\varepsilon(\vec{r}) = (\varepsilon(\vec{r}) - \varepsilon_0(\vec{r})) \quad (2.3.3.2d)$$

$\vec{E}_\Omega(\vec{r})$, $\vec{E}_\Omega(\vec{r} - \vec{d})$ represent here the electric field of the original cavity and the “shifted” one, respectively.

$\varepsilon_0(\vec{r})$, $\varepsilon(\vec{r})$ are the dielectric constant of the original cavity and the coupled cavities system, respectively, as illustrated in Fig. 2.3.5(a) and Fig. 2.3.5(b).

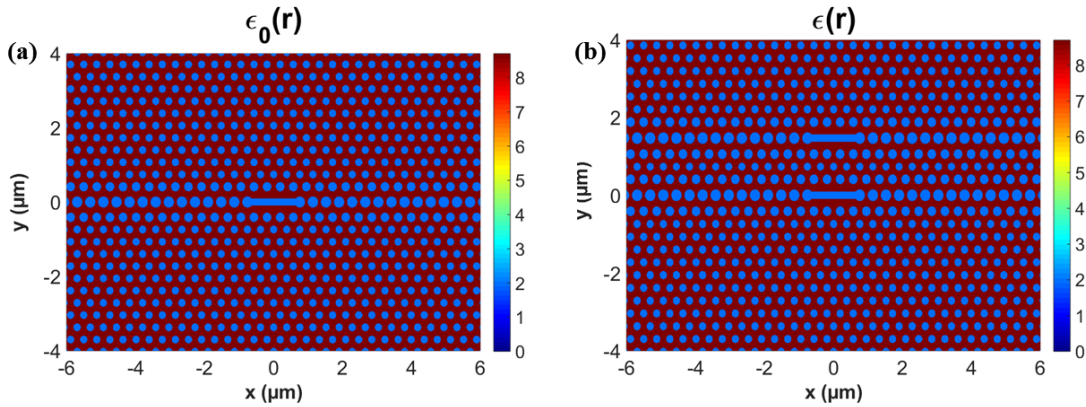


Fig. 2.3.5 Illustration of PhC cavity's dielectric constant distributions: (a) The original cavity, and (b) The coupled cavities system.

The spatial parts of bonding and antibonding fields can also be expressed as:

$$\vec{E}_{\omega_B}(\vec{r}) \cong \frac{1}{\sqrt{2}} \left(\vec{E}_\Omega(\vec{r}) + \vec{E}_\Omega(\vec{r} - \vec{d}) \right) \quad (2.3.2.4a)$$

$$\vec{E}_{\omega_{AB}}(\vec{r}) \cong \frac{1}{\sqrt{2}} \left(\vec{E}_\Omega(\vec{r}) - \vec{E}_\Omega(\vec{r} - \vec{d}) \right) \quad (2.3.2.4b)$$

In addition, from equations (2.3.3.2a) and (2.3.3.2b) the difference between these two frequencies can be expressed as:

$$\boxed{(\omega_B - \omega_{AB}) = -2\kappa\Omega} \text{ or } \boxed{\left(\frac{\omega_B - \omega_{AB}}{\Omega}\right) = -2\kappa} \quad (2.3.3.4)$$

The value of κ thus decides the sign of the coupling, *i.e.* the relative positions of bonding or antibonding modes as the excited or ground states, as well as the cavity/cavity coupling strength.

In equation (2.3.3.4) if $\kappa < 0$, $\omega_B > \omega_{AB}$ then ω_B corresponds to the excited state and ω_{AB} corresponds to the ground state. Inversely, in the case $\kappa > 0$. This shows that the TB approach is able to describe the fact that bonding or antibonding can either become the ground state or excited state in coupled cavities. **As the supermode splitting sign depends only on the sign of the coupling coefficient κ , it appears to be related to the interference pattern sign between the cavity mode $\overset{\perp}{E}_\Omega(\vec{r})$ and the displaced cavity mode $\overset{\perp}{E}_\Omega(\vec{r} - \vec{d})$, as seen from equation (2.3.3.2c).** In addition, equation (2.4.3.2.c) raises the possibility of adjusting the splitting between supermodes by properly choosing the geometry of the coupled slot PhC cavities.

We can add here some few comments from the derived TB analysis:

- The field distributions of bonding and antibonding modes are yielded from the superposition of the two localized fields as presented in equations (2.3.2.4a) and (2.3.2.4b). The bonding mode hence has the quasi-symmetric profile because it is the sum of two electric fields while the antibonding mode possesses the quasi-antisymmetric one.
- It is possible to obtain degenerate supermodes when the integral of the scalar product between $\overset{\perp}{E}_\Omega(\vec{r})$ and $\overset{\perp}{E}_\Omega(\vec{r} - \vec{d})$ is equal to 0, thus corresponding to a specific interference pattern.
- This approach is versatile and powerful from a practical point of view as only the single cavity mode is to be calculated, while after, further calculations are semi-analytical giving room to shift the second cavity in several directions and distances (controlling \vec{d}).

2.3.2.3 Coupled photonic crystal L3 cavities

In a first approach, we study here, in a benchmarking purpose coupled PhC L3 cavities using the TB approach and 2D-FDTD calculation.

We start for that with the following set of parameters: lattice constant $a = 380$ nm, hole radius $r = 105$ nm, 2.95 - the effective index of the planar waveguide at $\lambda = 1.5$ μm , with SiO_2 holes (refractive index: 1.44). Meanwhile, the width of the PhC waveguide is set to $\text{WG1} = \sqrt{3}a$ (“W1 waveguide”). We study hereafter the Photonic bandgap of the bulk 2D PhC cavity, and then the dispersion diagram of the W1 PhC waveguide to evaluate the localized mode energy in the bandgap in order to design a single cavity. Finally, several coupled L3 PhC cavity configurations (as depicted in Fig. 2.3.6) are studied both by 2D-FDTD simulation and TB calculation.

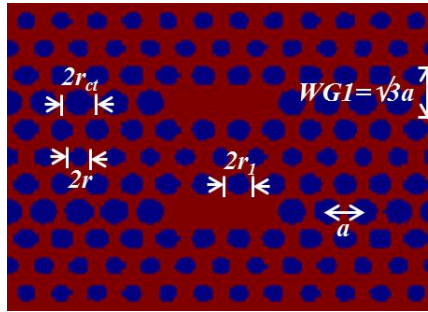


Fig. 2.3.6 Scheme of coupled L3 PhC cavities with lattice constant $a = 380$ nm, hole radius $r = 105$ nm and width of waveguide $\text{WG1} = \sqrt{3}a$, effective index of the planar waveguide at $\lambda = 1.5$ μm is 2.95.

2.3.2.3.1 Design of a photonic crystal L3 cavity

The simulation steps described in section 2.2 were first applied to the design of a single L3 PhC cavity. We quickly summarize the main related outputs: a TE bandgap exists from $a/\lambda = 0.2379$ to $a/\lambda = 0.2899$ in normalized frequency, corresponding to the 1310.5 nm-1597.5 nm wavelength range (Fig. 2.3.7(a)).

The L3 PhC cavity design started by preparing a single-mode TE-light W1 waveguide mode that will correspond to the cavity core geometry. In order to exploit only y -even mode in the PBG, we increased the radius of the first two rows of holes r_1 closest to the waveguide from 105 nm to 125 nm. In that case we obtained the dispersion diagram shown in Fig. 2.3.7(b), showing that only the W1 y -even mode frequency exists in the photonic bandgap at edge frequency around 0.2457 ($\lambda \approx 1546.67$ nm).

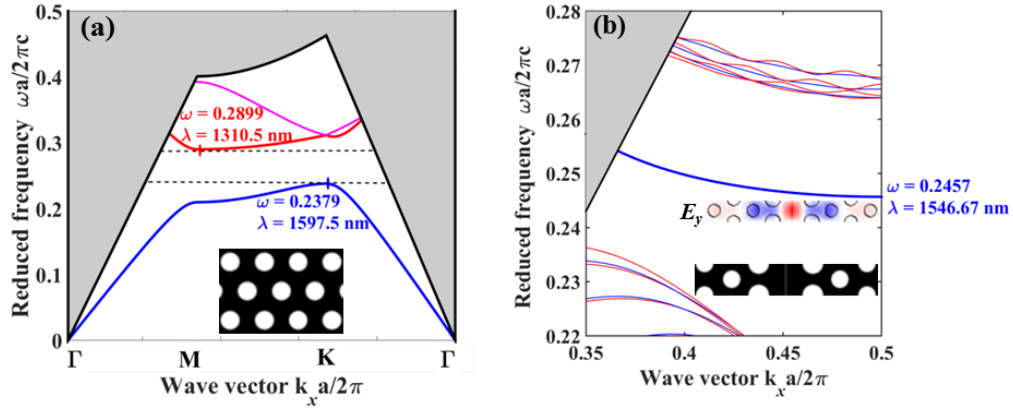


Fig. 2.3.7(a) PBG of 2D planar PhC structure in which hole radius $r = 105$ nm, lattice constant $a = 380$ nm, effective index 2.95 for TE light polarization (b) Dispersion diagram of PhC waveguide based on 2D planar PhC structure in (a) in the case radii of first two rows of hole closest to WG $r_l = 125$ nm and the E_y field profile of the gap-guided mode.

Fig. 2.3.8 presents the geometry of the L3 PhC cavity.

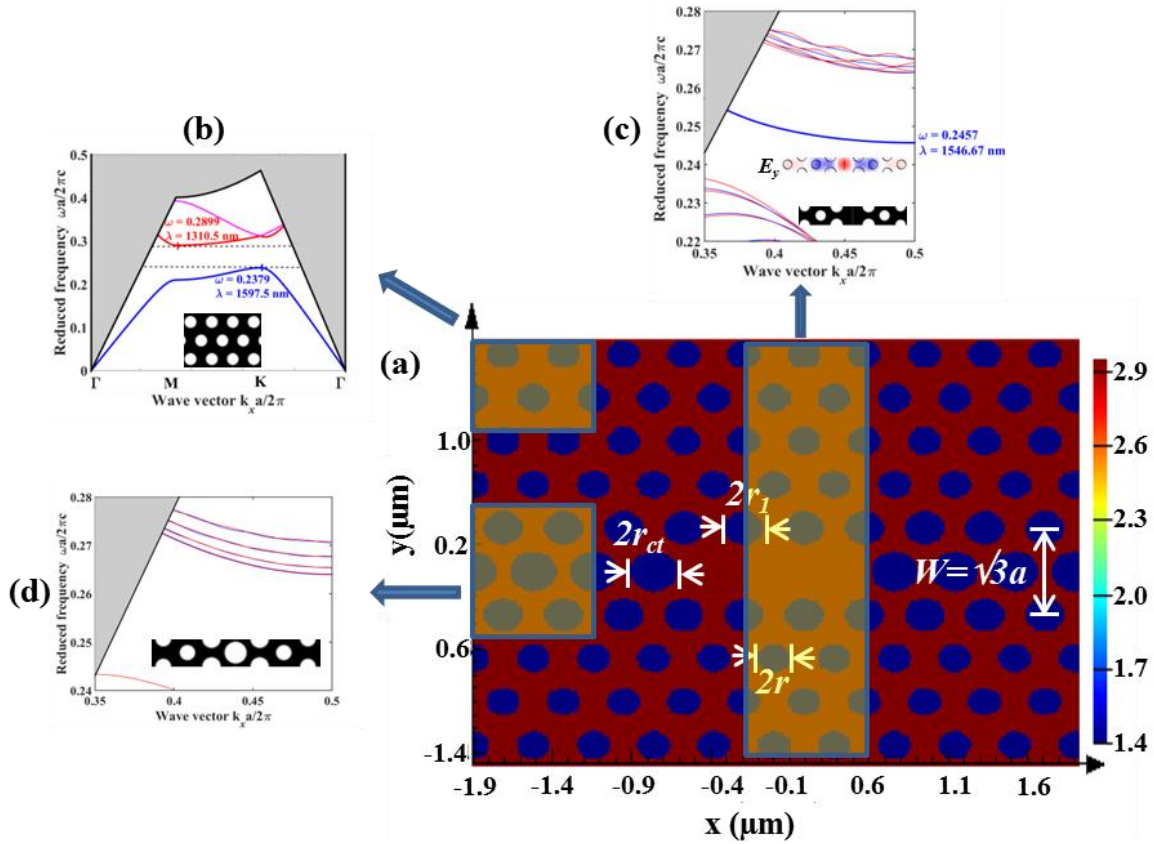


Fig. 2.3.8(a) Refractive index profile of the L3 PhC cavity with hole radius: $r = 105$ nm, lattice constant: $a = 380$ nm and dispersion diagrams of its different parts (b) PBG of planar PhC structure with effective index at $1.5 \mu\text{m}$ of 2.95 (c) Dispersion diagram of W1 PhC waveguide with radius of first two rows of holes closest to waveguide $r_l = 125$ nm, providing one W1 y -even mode at around 0.2457 ($\lambda \approx 1546.67$ nm) and (d) Dispersion diagram of W1 PhC waveguide consisted of hole radius $r = 105$ nm, $r_l = 125$ nm and radius of holes in the center row $r_{ct} = 150$ nm which creates a lateral barrier, obtained by 2D-PWE calculation.

We then performed FDTD simulation to estimate the cavity-mode resonance frequency and the corresponding electromagnetic field. From the knowledge of the photonic bandgap cut-off

frequencies, we choose a source with a spectrum extending from $\lambda = 1.3$ to $\lambda = 1.7$ μm and spatially located close to the center of the cavity to excite the modes. The FDTD simulation area was set to $12 \mu\text{m} \times 8 \mu\text{m}$, the simulation time was 8000 fs to excite the cavity, and the mesh accuracy was chosen as $16 \text{ nm} \times 13 \text{ nm}$. We considered the mode profiles of the resonances in order to understand the origin of the cavity modes, which confirmed our first conclusion from Q -analysis results.

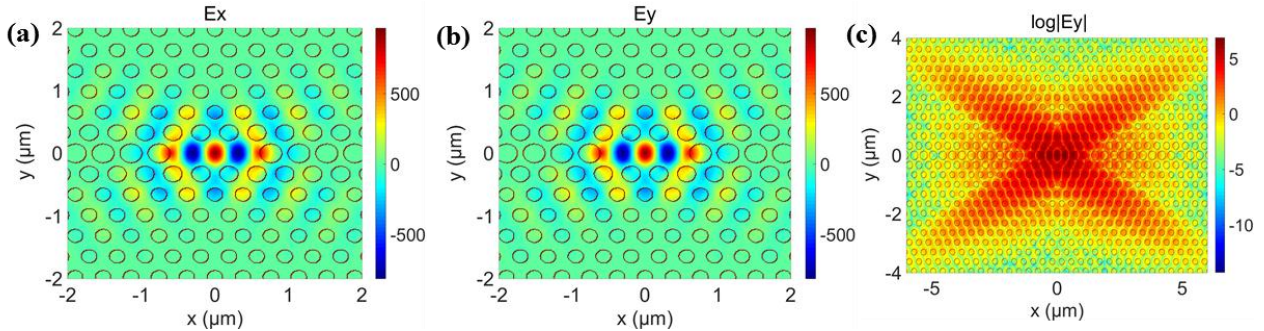


Fig. 2.3.9 Considered L3 photonic crystal cavity (see Fig. 2.3.8 for a complete description of the opto-geometrical parameters): (a) E_x component (b) E_y component and (c) Log of magnitude of E_y component of the TE-like resonance mode at $\lambda = 1498.42$ nm.

The resonance wavelength of the cavity was 1498.42 nm ($Q = 5.31164 \cdot 10^7 \pm 56\,439$). In this 2D-FDTD simulation, the value of Q is meaningless as it does not take into account light vertical loss, but this large Q value shows that the confined mode corresponds to the waited resonance. The E_x and E_y components and the log of magnitude of the electric field components of the cavity mode are shown in Fig. 2.3.9, respectively. It can be seen that the E_y component of the cavity mode obtained using FDTD simulation matches well with the E_y component of the y -even mode predicted by the PWE calculation and depicted in Fig. 2.3.7(b).

2.3.2.3.2 Coupled photonic crystal L3 cavities

The set of steps to investigate photonic molecules based on the L3 cavity designed in the previous section was the following:

- Begin from the single cavity resonance frequency and field profile.
- Perform a full 2D-FDTD simulation of two coupled cavities to predict the bonding and antibonding modes, and also estimate these modes by the TB approach.
- Finally, compare the obtained results between FDTD simulation and TB approximation.

The refractive index distribution of this coupled PhC L3 cavities benchmarking configuration is shown in Fig. 2.3.10. As visible, three rows of holes were chosen as a separation between both cavities while considering a variable horizontal dx shift ($dx = 4a$ in Fig. 2.3.10).

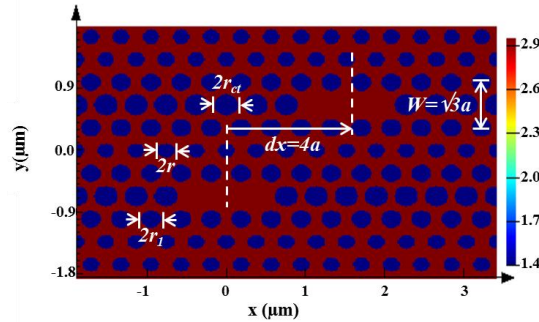


Fig. 2.3.10 Refractive index profile of the coupled PhC L3 cavities in the case $dx = 4a$.

The two coupled PhC L3 cavities have been placed in parallel, *i.e.* $dx = 0$, then the upper cavity has been shifted by step of lattice constant a to study the frequency evolution of the bonding and antibonding modes as a function of dx .

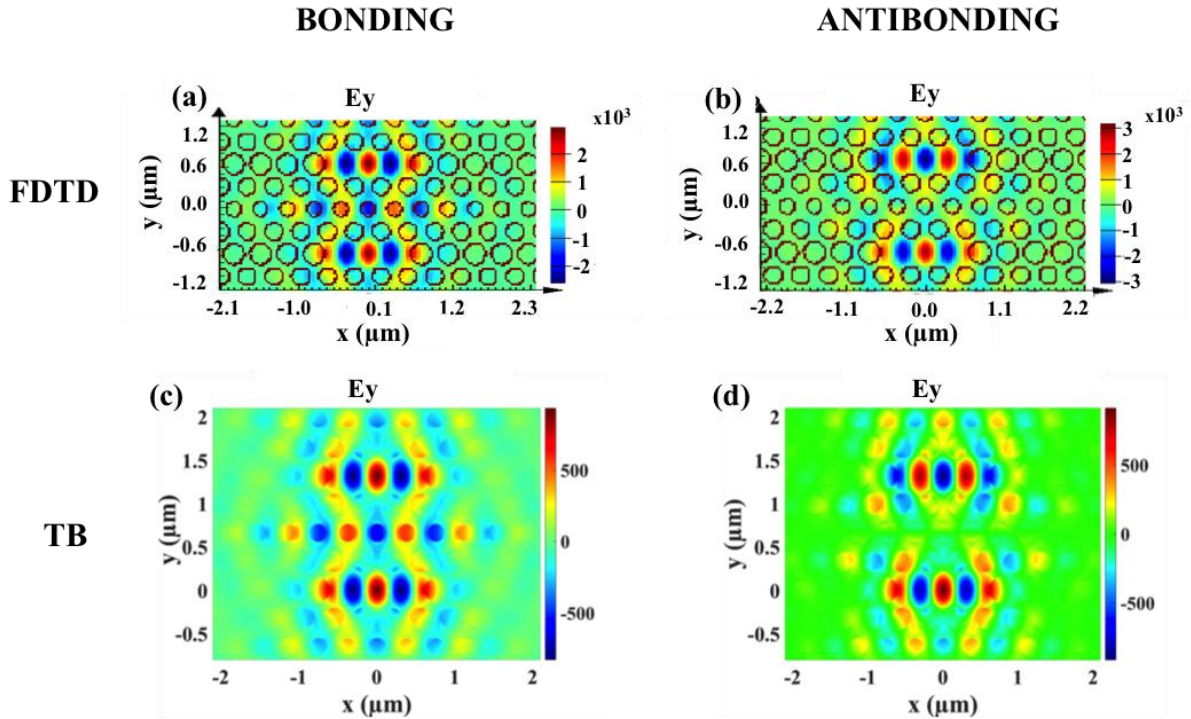


Fig. 2.3.11 E_y component of the coupled PhC L3 cavities for $dx = 0$ of (a) Bonding mode at $\lambda_B = 1500.91$ nm, and (b) Antibonding mode at $\lambda_{AB} = 1498.02$ nm obtained directly by 2D-FDTD simulation (c) Bonding mode at $\lambda_B = 1500.86$ nm and (d) Antibonding mode at $\lambda_{AB} = 1495.99$ nm obtained by TB method from the 2D-FDTD field of the isolated PhC cavity.

The E_y component of the bonding and antibonding supermodes obtained through 2D-FDTD simulation are depicted in Fig. 2.3.11(a) and in Fig. 2.3.11(b) in the case $dx = 0$, with resonance wavelengths of $\lambda_B = 1500.91$ nm and $\lambda_{AB} = 1498.02$ nm, respectively.

Next, we applied the TB approach to this coupled PhC L3 cavities scheme to predict the bonding and antibonding modes from the FDTD simulation results of the isolated PhC cavity. We duplicated for that the single cavity to the new desired position and calculated the supermodes formed by the two specified localized modes by using equations (2.3.3.2a-c) and (2.3.2.4a-b). Fig. 2.3.11(c) and Fig. 2.3.11(d) present the E_y component of the bonding and antibonding modes at the resonance wavelengths predicted by TB. The good agreement between the two methods can be observed through the profiles of E_y component of supermodes. After this first qualitative inspection for a given cavity/cavity distance, Fig. 2.3.12(a) shows a global picture of the comparison between the two methods for dx ranging between $dx = 0a$ and $dx = 15a$.

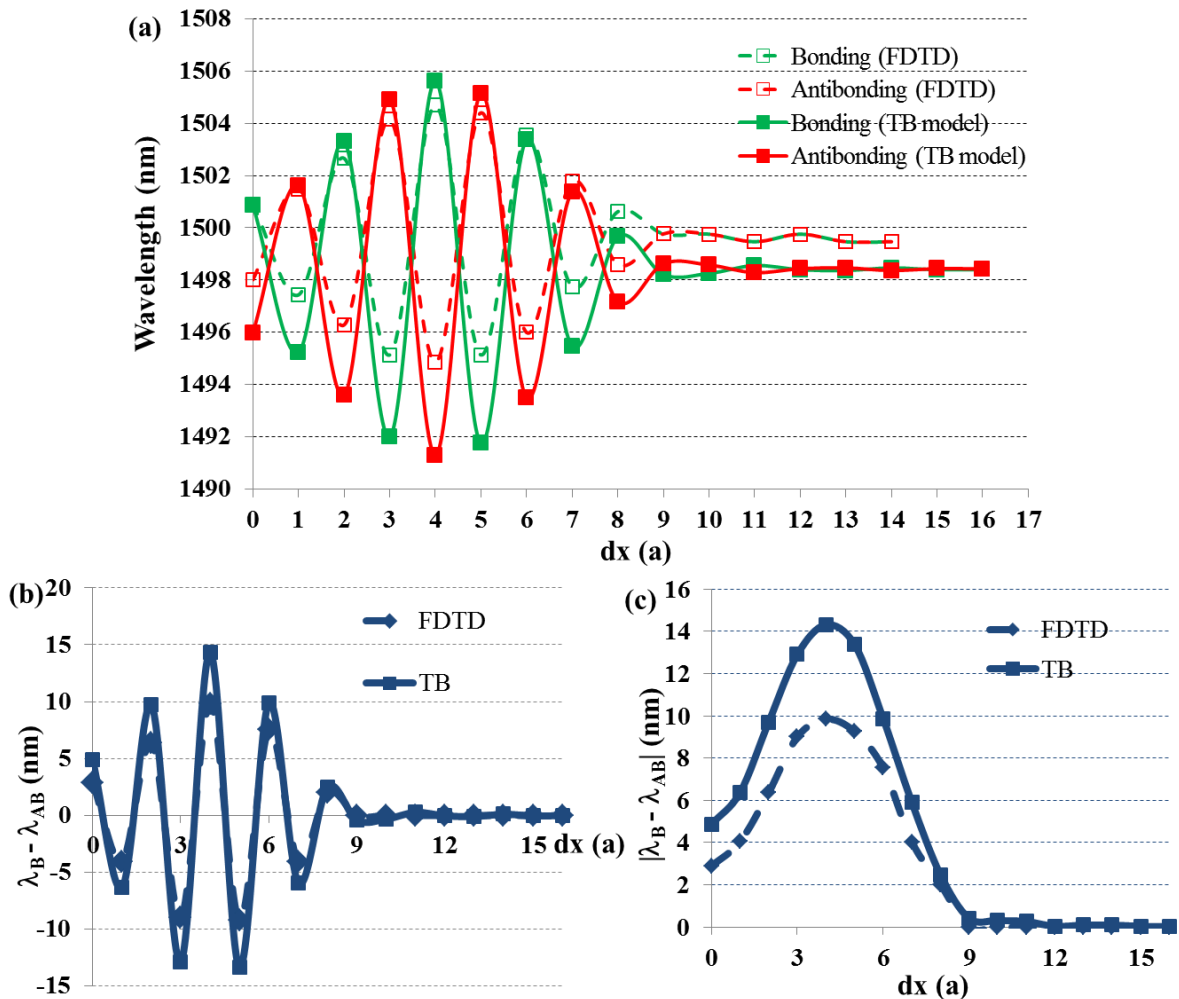


Fig. 2.3.12 (a) Bonding (green-line) and antibonding (red-line) modes of coupled PhC L3 cavities obtained by FDTD simulation (dash line) and TB approximation (solid line), (b) The wavelength difference between the bonding and antibonding modes and (c) the absolute value of wavelength difference between the bonding and antibonding modes obtained by 2D-FDTD simulation (dash line) and TB approximation (solid line) as functions of dx .

As it can be seen in Fig. 2.3.12(a)-(b) and (c):

- The two supermodes oscillate around the mode of the single cavity and the two cavities become isolated again at the distance $dx \sim 9a$.
- A good global agreement is obtained between these two approaches.
- **The beating between the resonance wavelengths of the two supermodes and the sign exchange of $(\lambda_B - \lambda_{AB})$ as a function of increasing cavity/cavity distance can be well explained by the TB approach, *i.e.* by the relative interference pattern between the original cavity mode and itself but displaced by a few PhC lattice periods.**
- Last, the maximum of the supermode splitting is obtained for $dx \sim 4a$: and the splitting wavelength $\Delta\lambda$ is then around 10-15 nm (see Fig. 2.3.12(b)).

As can be seen in Fig. 2.3.9(c) of the E_y electric field component in log scale, this situation corresponds to those when the direction of the coupling between two cavities is similar to the direction in which the single cavity electric field is strongly distributed. Consistently to that observation, the coupling strength is then anticipated to be the largest (*i.e.* around 30° with respect to the initial cavity main direction).

To sum up, **the TB method can reproduce the FDTD simulation results and can predict properly the main trends.** The small discrepancy between the FDTD and TB approaches mainly come from the numerical condition employed in FDTD which can affect the results (*i.e.* mesh quality, size of simulation area...), while the TB method also intrinsically relies on a perturbative approximation condition, yet providing a semi-analytic description that brings insight into the physics of the studied coupled cavities.

On the purpose of investigating coupled slot PhC cavities for hybrid integration, we now introduce in the next section a slot in each the two coupled cavities. As seen in section 1.3.6, slot PhC waveguides can sustain both W1-like mode and true-slot modes. So, we will investigate the two cases of coupled slot PhC L3 cavities relying on a narrow slot ($W_{slot} = 100$ nm) to manipulate the W1-like mode, and on a large slot ($W_{slot} = 200$ nm) to exploit the true slot mode, respectively. In this view, the main addressed questions are:

- i. As slot PhC modes are more confined than standard W1 ones, is the TB approach also be able to describe similarly coupled slot PhC cavities?

- ii. Can we observe the same bonding/antibonding modes beating effect between the two supermodes when coupling slot PhC cavities?

2.3.2.4 Investigation of coupled slot photonic crystal L3 cavities by FDTD simulation and tight-binding approach

2.3.2.4.1 Coupled true-slot mode photonic crystal L3 cavities ($W_{slot} = 200 \text{ nm}$)

Based on previous study on coupled PhC L3 cavities, we first investigate coupled 200 nm slot PhC L3 cavities consisting of two 200 nm slot PhC L3 cavities based on $r = 105 \text{ nm}$ radius hole triangular lattice PhC with $a = 380 \text{ nm}$, *i.e.* of the same value as for the cavity studied in section 2.2.1. The two cavities are again separated by three rows of holes in the ΓM direction (Fig. 2.3.13). Then, the upper cavity is shifted by steps of lattice constant a while the lower one is fixed, *i.e.* $dx = 0, a, 2a, \dots$, and the supermodes frequencies and spatial distributions are studied by both 2D-FDTD simulation and TB approximation.

The same methodology as for the previous study is used.

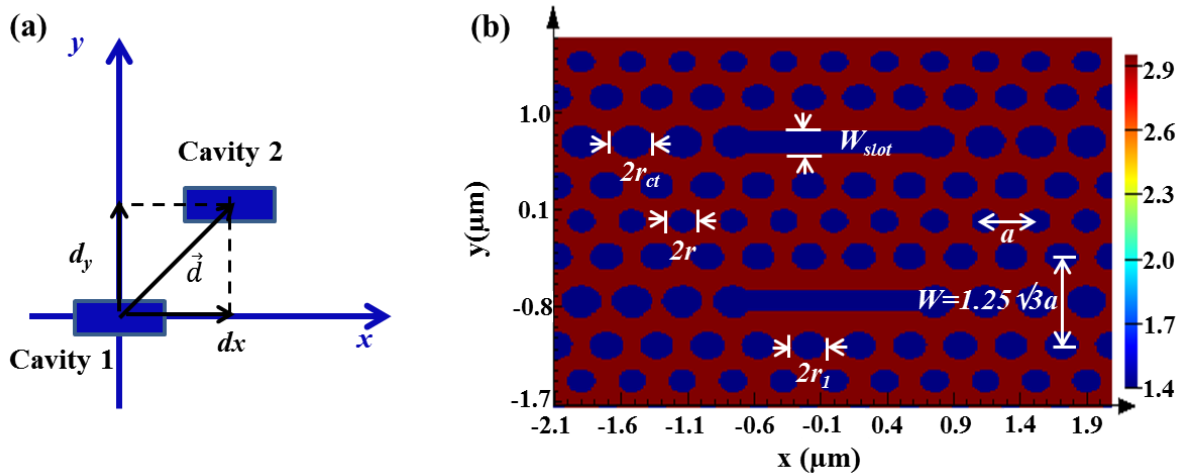


Fig. 2.3.13 (a) Scheme of the coupled cavities at distance d , (b) Refractive index profile of the coupled 200 nm slot PhC L3 cavities in the case $dx = 0$.

The electric field components and log of magnitude of the E_y electric field component at resonance of the 200 nm slot L3 PhC cavity ($W_{slot} = 200 \text{ nm}$) obtained by 2D-FDTD simulation are represented in Fig. 2.3.14.

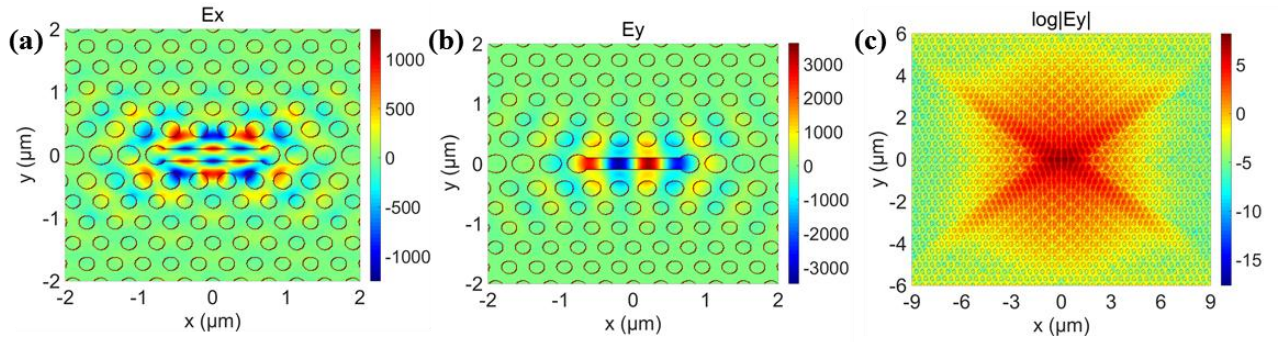


Fig. 2.3.14(a) E_x component (b) E_y component and (c) Log of magnitude of the electric field of the cavity mode at 1532.51 nm resonance of 200 nm slot L3 PhC cavity.

Fig. 2.3.15 then depicts the profile of E_y components of bonding and antibonding modes obtained by 2D-FDTD and TB approximation for $dx = 0$.

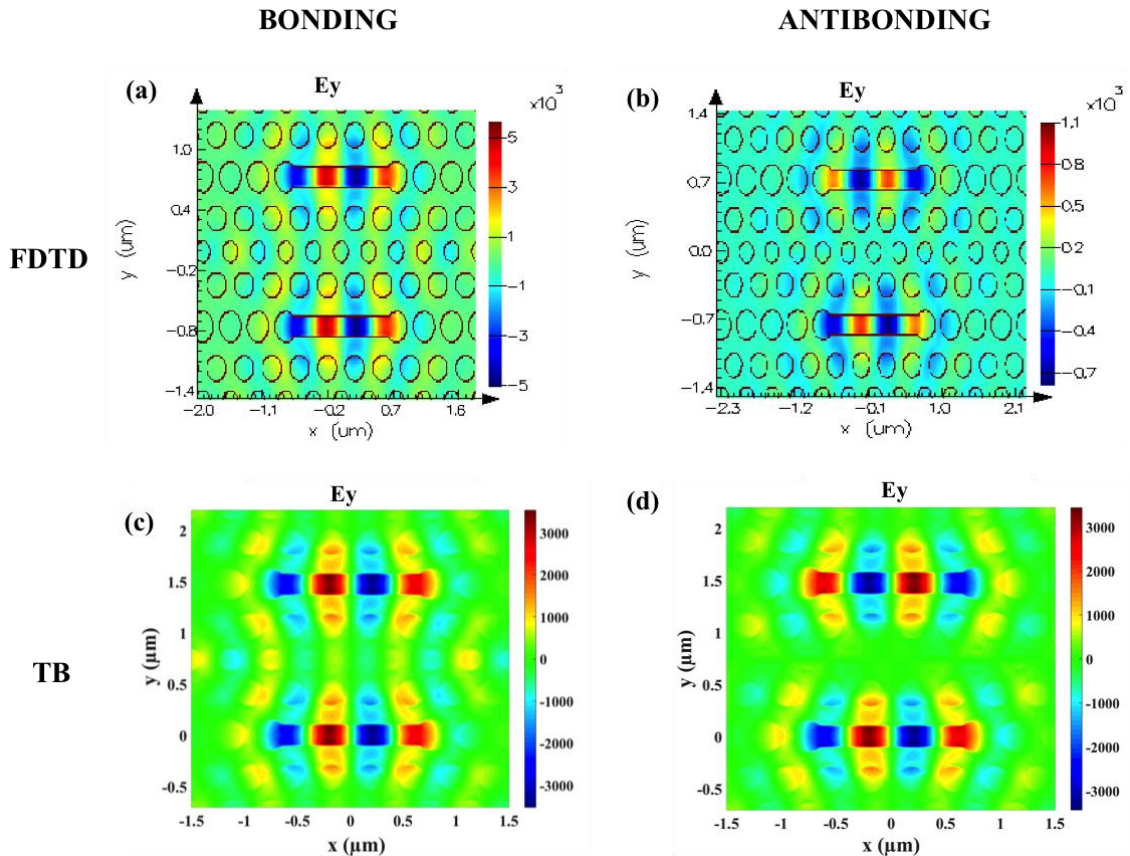


Fig. 2.3.15 E_y component of the coupled 200 nm slot PhC L3 cavities for $dx = 0$ of (a) Bonding mode at $\lambda_B = 1528.57$ nm and (b) Antibonding mode at $\lambda_{AB} = 1534.3$ nm obtained directly by 2D-FDTD simulation (c) Bonding mode at $\lambda_B = 1530.47$ nm and (d) Antibonding mode at $\lambda_{AB} = 1534.4$ nm obtained by TB method.

In the $dx = 0$ case, the antibonding mode is the ground state and the bonding mode is the excited state. Their corresponding wavelengths are $\lambda_B = 1528.47$ nm (Fig. 2.3.15(a)) and

$\lambda_{AB} = 1534.3$ nm (Fig. 2.3.15(b)), respectively, obtained by 2D-FDTD and $\lambda_B = 1530.47$ nm (Fig. 2.3.15(c)) and $\lambda_{AB} = 1534.4$ nm (Fig. 2.3.15(d)), respectively, obtained by the TB approach.

The global evolution of the bonding and antibonding modes wavelength predicted by 2D-FDTD simulation and the TB method are shown in Fig. 2.3.16(a) and Fig. 2.3.16(b), respectively.

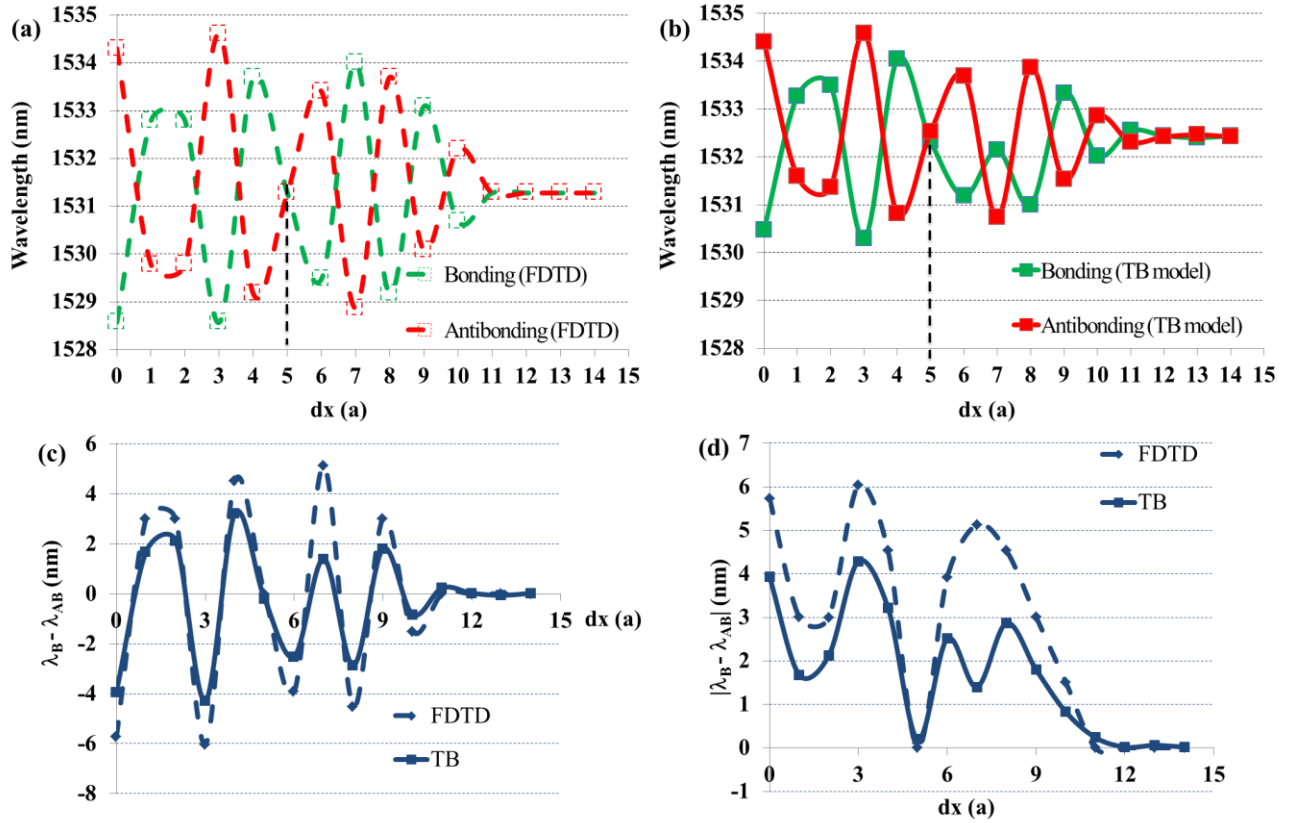


Fig. 2.3.16 Bonding (blue-line) and antibonding (red-line) modes of coupled 200 nm slot PhC L3 cavities obtained by (a) 2D-FDTD simulation (dash line) (b) TB approximation (solid line). (c) The wavelength difference between bonding and antibonding modes and (d) The absolute value of wavelength difference between bonding and antibonding modes obtained by 2D-FDTD simulation (dash line) and TB approximation (solid line) as functions of dx .

- A good agreement between both methods is also observed, especially considering the wavelength difference evolution (*i.e.* $(\lambda_B - \lambda_{AB})$).
- It is worth noticing that a supermode degeneracy occurs at $dx = 5a$ (the two supermodes have then the same resonance frequency), and that the coupling is the strongest at $dx = 3a$.
- The cavities begin to be isolated each one with respect to the other at $dx \sim 11a$.
- We also notice that the maximum splitting wavelength $\Delta\lambda$ is around 6 nm as shown in Fig. 2.3.16(c), *i.e.* smaller than in the case of coupled L3 non-slotted PhC cavities in which $(\Delta\lambda)_{\max}$ was approximately 15 nm (Fig. 2.3.12(c)-(d)). This difference probably originates

from the fact that the mode confinements in the two configurations are different. When introducing the slot, the true-slot mode is much more tightly confined and locates deeply below the light line. The interaction between two confined modes of two slotted PhC cavities is thus more difficult.

- Last, it is observed that the global envelope of the bonding-antibonding modes wavelength difference, *i.e.* the evolution of $|\lambda_B - \lambda_{AB}|$ as a function of dx is not the same for the L3 true-slot PhC coupled cavities configuration as for the non-slotted case. In the explored true-slot mode configuration, $|\lambda_B - \lambda_{AB}|$ presents two successive local maxima, while only one was present in the W1 L3 non-slotted case (see Fig. 2.3.12). In the first of the two configurations, the cavity/cavity coupling strength is for example stronger for $dx = 7a$ than for $dx = 5a$.

To sum up, the TB approach is also able to reproduce the full FDTD simulation in the case of coupled true-slot mode PhC cavities. In addition, **we can control $\Delta\lambda = (\lambda_B - \lambda_{AB})$ in sign and amplitude, and this kind of coupled true-slot mode cavities could be used for hybrid integration as it supports two different controllable resonance modes.**

We will now study the other kind of slot mode, *i.e.* the W1-like mode one.

2.3.2.4.2 Coupled W1-like mode photonic crystal L3 cavities ($W_{slot} = 100$ nm)

In this last case, we study coupled PhC L3 slotted cavities for the W1-like mode with the same approach as the one followed in previous sections. However, this last study relies on 3D simulation in order to verify at least one time if the TB approximation can be also a predictive tool for “real” applications. The cavities considered here have not been optimized in term of Q -factors.

The slot W1-like mode PhC L3 cavity is designed based on the SPCW with similar parameters as the ones given in section 2.3.2.4.1: radius holes $r = 105$ nm, lattice constant $a = 380$ nm, and waveguide width $W1.25$ infiltrated by a cladding with refractive index of 1.46. The cavity is constructed by starting from a SOI wafer ($n_{Si} = 3.48$) of thickness $h = 260$ nm, with a silicon oxide below as the optical substrate ($n_{sub} = 1.44$). Meanwhile, a slot width $W_{slot} = 100$ nm is considered to exploit the W1-like mode. The schematic view of the cavity geometry of the cavity is depicted in Fig. 2.3.17(a).

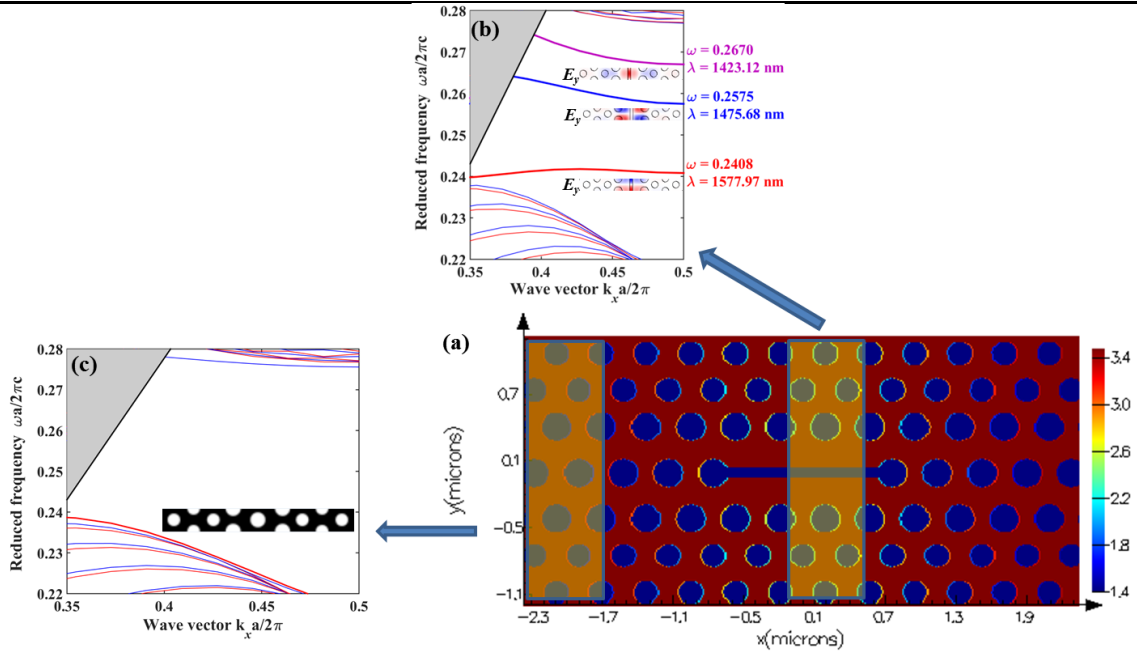


Fig. 2.3.17 (a) Refractive index profile of the 100 nm slot L3 PhC cavity with hole radius $r = 105$ nm (b) Dispersion diagram and the structure of the 100 nm SPCW in the case radius of the first row of holes: $r_l = 125$ nm, the true-slot mode (red curve) and W1-like modes (blue and violet curves) in the bandgap (c) Dispersion diagram and the structure of the PCW in the case radius of the center row of holes $r_{cl} = 125$ nm which creates a lateral barrier, obtained by 3D-PWE calculation.

FDTD simulation with 12 nm grid size in each direction was used to predict the cavity modes. Consistently with the dispersion diagram of Fig. 2.3.17(b), two modes were detected by 3D-FDTD simulation, the first one corresponding to the true-slot mode of the SPCW ($\lambda_1 = 1567.82$ nm, $Q_1 = 841.68 \pm 0.0057$), and the second one to the W1-like one ($\lambda_2 = 1383.13$ nm, $Q_2 = 864.95 \pm 0.00023$). We observe here a drop of Q values compared with those obtained by 2D-FDTD simulation in previous sections because the vertical loss channel is now included.

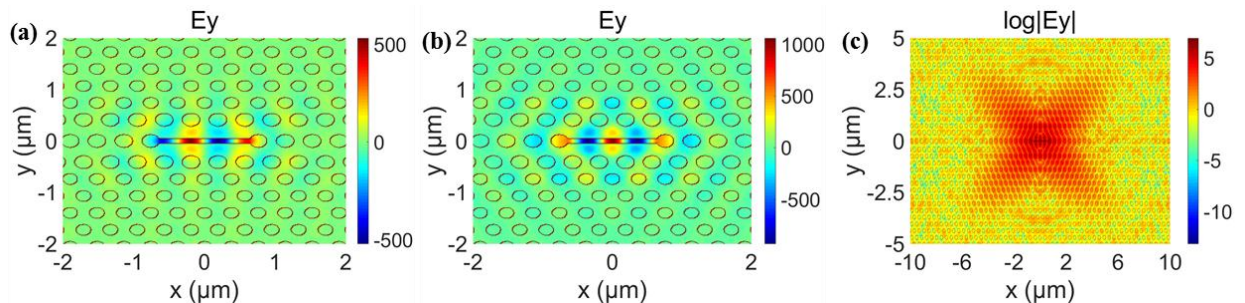


Fig. 2.3.18 E_y component of the (a) True-slot mode at resonance wavelength $\lambda_1 = 1567.82$ nm and (b) W1-like mode at resonance wavelength $\lambda_2 = 1383.13$ nm (c) The magnitude of electric field of the W1-like mode in log scale at resonance wavelength $\lambda_2 = 1383.13$ nm.

E_y components of two modes and the magnitude of electric field in log scale of the W1-like mode are presented in Fig. 2.3.18.

Coupled cavities have then studied from this starting point.

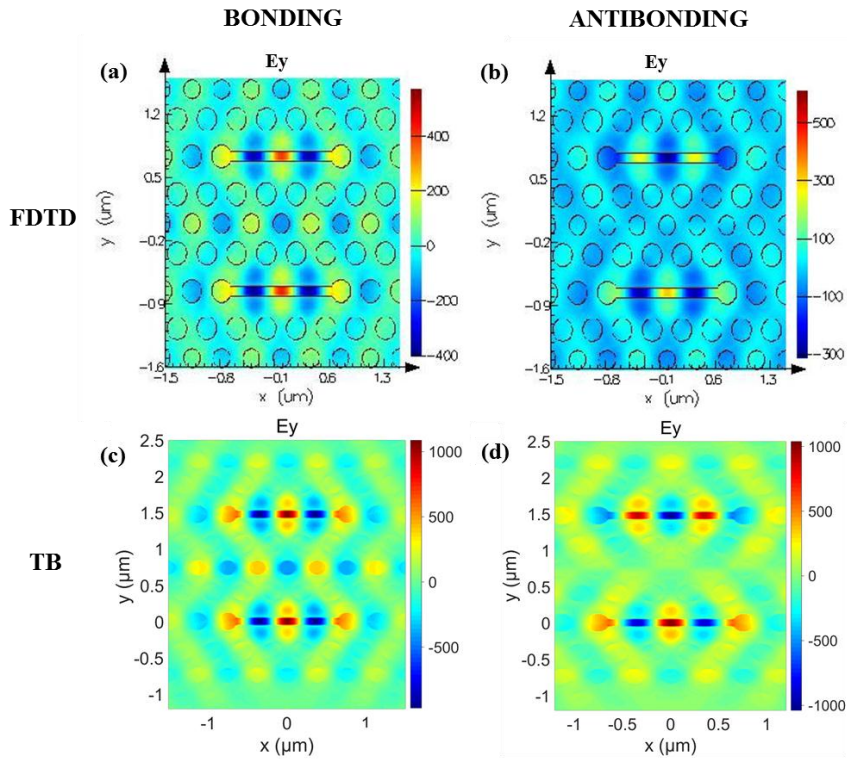


Fig. 2.3.19 E_y component of (a) Bonding mode at $\lambda_B = 1387.96$ nm and (b) Antibonding mode at $\lambda_{AB} = 1382.95$ nm of the coupled 100 nm slot PhC L3 cavities and waveguide width WG1.25 for the case $dx = 0$ directly obtained by 3D-FDTD and (c) Bonding mode at $\lambda_B = 1388.87$ nm and (d) Antibonding mode at $\lambda_{AB} = 1377.44$ nm obtained by the TB method.

Fig. 2.3.19 shows the obtained fields for $dx = 0$, for which the bonding mode is the ground state and the antibonding mode is the excited one. The fields directly obtained by 3D-FDTD simulation (Fig. 2.3.19(a)-(b)) as well as by the TB approach (Fig. 2.3.19(c)-(d)) can be compared.

The global results obtained as a function of the dx spatial shift are shown in Fig. 2.3.20. Once again, a correct agreement in the trends provided by the two methods is observed if one disregards a fixed offset mainly related to mesh errors.

As in previous cases, wavelengths of the two supermodes oscillate and the global curve envelop presents a single maximum value for $dx = a$. The largest wavelength splitting $\Delta\lambda$ is around 10 nm, which is larger than for the case of coupled true-slot mode cavities.

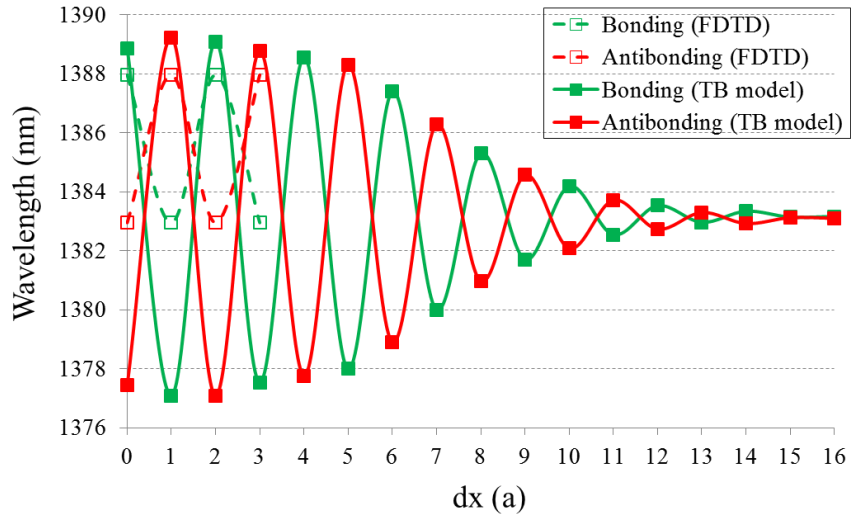


Fig. 2.3.20 Bonding (green-line) and antibonding (red-line) modes of coupled 100 nm slot PhC L3 cavities obtained by FDTD simulation (dash line) and TB approximation (solid line) for the W1-like cavity mode.

Full 3D-FDTD simulation was limited to the $0-3adx$ range due to excessive 3D-FDTD computational time but yet provided enough information to show that the TB approximation of coupled PhC cavities can also reproduce the main properties of coupled slot PhC cavities in 3D geometries. Hence, this semi-analytical approach could be used to predict light-matter interactions for the purpose of integrating active materials in hollow core coupled optical resonators for light-matter enhancement and applications.

These new investigations belong to the immediate perspectives of the present Ph.D. work.

2.3.3 Conclusion of section 2.3

In this section, we have applied the tight-binding (TB) approach to predict the bonding and antibonding modes resonance frequencies and spatial distributions of coupled non-slot and slot PhC cavities based on a first single cavity mode. The single cavity mode was first studied by FDTD calculation. Then this localized mode was used to predict the supermodes properties in various geometrical configurations.

Coupled slot cavities relying both on the true-slot mode and on the W1-like mode of slot photonic crystal waveguides have been explored. A good agreement was found between the results obtained using the two methods, *i.e.* the perturbative TB approach relying on a semi-analytic description and the full numerical FDTD calculation. **The frequency beating sign between the**

bonding and antibonding supermodes was successfully reproduced by the TB approach, giving a direct confirmation that this effect can be also interpreted in PhC slotted waveguide cases from the interference pattern between the cavity and its shifted counterpart.

For the studied true-slot mode case, which was studied by 2D simulation, the largest splitting wavelength was 4 nm and a degeneracy point at the distance between two cavities of $dx = 5a$ was found. Meanwhile for the W1-like mode, which was investigated by 3D simulation, the two supermodes also oscillate and a largest splitting wavelength between both supermodes was found (around 10 nm).

2.4. Conclusion of chapter 2

For hybrid integration purpose, by using both PWE and FDTD calculations, we have first designed a series of SOI slot PhC heterostructure cavities in the telecommunication range, *i.e.* 1.3 μm –1.6 μm with simulated Q -factors of around several tens of thousands and mode volumes around $0.03(\lambda/n)^3$ after being infiltrated by cladding materials with typical index values around 1.5. The fabrication and characterization of these cavities as well as their possible use for integration of active materials are presented in chapter 3.

As a milestone towards the use of slotted resonators for silicon hybrid integration, we have also studied the coupling between a slot PhC cavity and a slot PhC waveguide using the CMT to estimate the cavity build-up factor (detail in Appendix A) and showed the ability to excite the cavity from a waveguide by using FDTD simulation. At resonance, a drop of the transmission of the output of waveguide to around 38% (see Fig. 2.2.8) in the case of coupled true-slot mode slot PhC L3 cavity and true-slot mode slot PhC waveguide was predicted by FDTD simulation. Results showed that the slot PhC cavity efficient excitation is possible from an external waveguide laterally coupled to such a slotted PhC cavity.

Finally, as a preliminary step towards the use of several coupled slotted cavities for future hybrid integration schemes, we have investigated in a last part the situation of two coupled slot PhC cavities providing two different supermodes (bonding and antibonding) with controllable wavelength splitting. The tight-binding (TB) approach, which relies on the overlap of the two

tightly confined cavity electric fields, has been successfully applied to predict the supermodes frequencies and spatial distributions in several coupled slot PhC cavity configurations.

In the next chapter, we will present the fabrication and characterization results obtained in this Ph.D. work.

Chapter 3. Hybrid silicon photonic crystal cavities: experimental results

The primary purpose of this Ph.D. work is to design and fabricate slot PhC cavities in order to proceed to the hybrid integration of active materials in silicon and bring by this way additional functionalities to silicon material for the realization of integrated active functions. As discussed in chapter 2, slot PhC cavities with resonance wavelengths in the 1.3 μm to 1.6 μm telecommunication range were designed for this purpose.

This chapter aims at describing the fabrication and characterization of part of these slot PhC cavities, as well as the implementation of hybrid integration schemes performed in two situations: related to index sensing and enhancement of carbon-based active material photoluminescence, respectively. All the fabrication and optical characterization processes presented in this chapter have been developed in the Centrale de Technologie Universitaire (CTU), the clean room of the Center for Nanosciences and Nanotechnologies (C2N), under the supervision of Xavier Le Roux, clean room senior engineer of the C2N.

We first address the full fabrication process of 2D planar slot PhC cavities on SOI in section 3.1, from the preparation of e-beam masks to the lithography step itself. We also describe the optical characterization of samples performed to evaluate their behaviors. Then, section 3.2 is devoted to the demonstration of their ability of index-sensing when being infiltrated with liquids of different refractive index values of around 1.44-1.50.

Last, in a more prospective part, we explore in section 3.3 the possible integration of semiconducting single-walled carbon nanotubes (s-SWNTs) in these hollow core hybrid on silicon resonators for the enhancement of nanotube photoluminescence, before concluding in section 3.4.

3.1 Fabrication of SOI slot photonic crystal waveguide cavities operating in the 1.3-1.6 μm range

This section presents the fabrication processes of all passive silicon photonic devices realized in this work. They include strip and slot waveguides, and more importantly slot PhC waveguide cavities. The covered aspects stem from the design and the preparation of *.gds-II* masks, including the description of the coupling and reference testing structures, to the description of the performed technological steps.

The devices were defined depending on the configurations proposed and described in chapter 2. Photonic lattice constants, including the perpendicular one (a_{\perp}) that was introduced in chapter 2 for the design of heterostructure PhC slot cavities, were typically chosen in the 330 nm-400 nm range. By default, slot PhC waveguides and slot PhC waveguide cavities were considered as made of 105 nm hole radius, with a slot width $W_{slot} = 100$ nm and a waveguide width of $1.25\sqrt{3}a_{\perp}/2$ (i.e. W1.25).

Structures were fabricated by starting from SOITEC SOI wafers having a 260.0 ± 20.5 nm silicon thick on top of a 2 μm BOX layer, with a $\langle 100 \rangle$ crystal orientation. The fabrication procedure was made of two next main steps. The first step consisting in generating *.gds-II* files defining the desired devices with parameters as mentioned in chapter 2. In the second step, waveguide patterns (including tapers, photonic crystals, etc.) were defined by electron beam lithography. Etching was then achieved by low-pressure plasma etching with an Inductively Coupled Plasma (ICP) to transfer the patterned structures into the silicon thin film layer. After that, samples were mechanically cleaved to lead to ~ 5 mm long chips including the tapers and the access waveguides for further optical characterization.

3.1.1 Mask preparation for electron-beam lithography

Based on the simulation results reported in chapter 2, we prepared *.gds-II* masks for the electron-beam (E-Beam) lithography step. This work was performed by the use of the Clewin and KLayout softwares.

First, we took into account practical information coming from the available experimental setup that fixed the length of final samples to around 5 mm while relying on the butt-coupling technique

for input light injection into the fabricated samples from a lensed-fiber with a similar scheme for the sample output. Input and output waveguides were thus considered in mask designs for the injection and collection of light, respectively. An overview of a whole typical sample comprising a series of PhC slot devices is shown in Fig. 3.1.1(a).

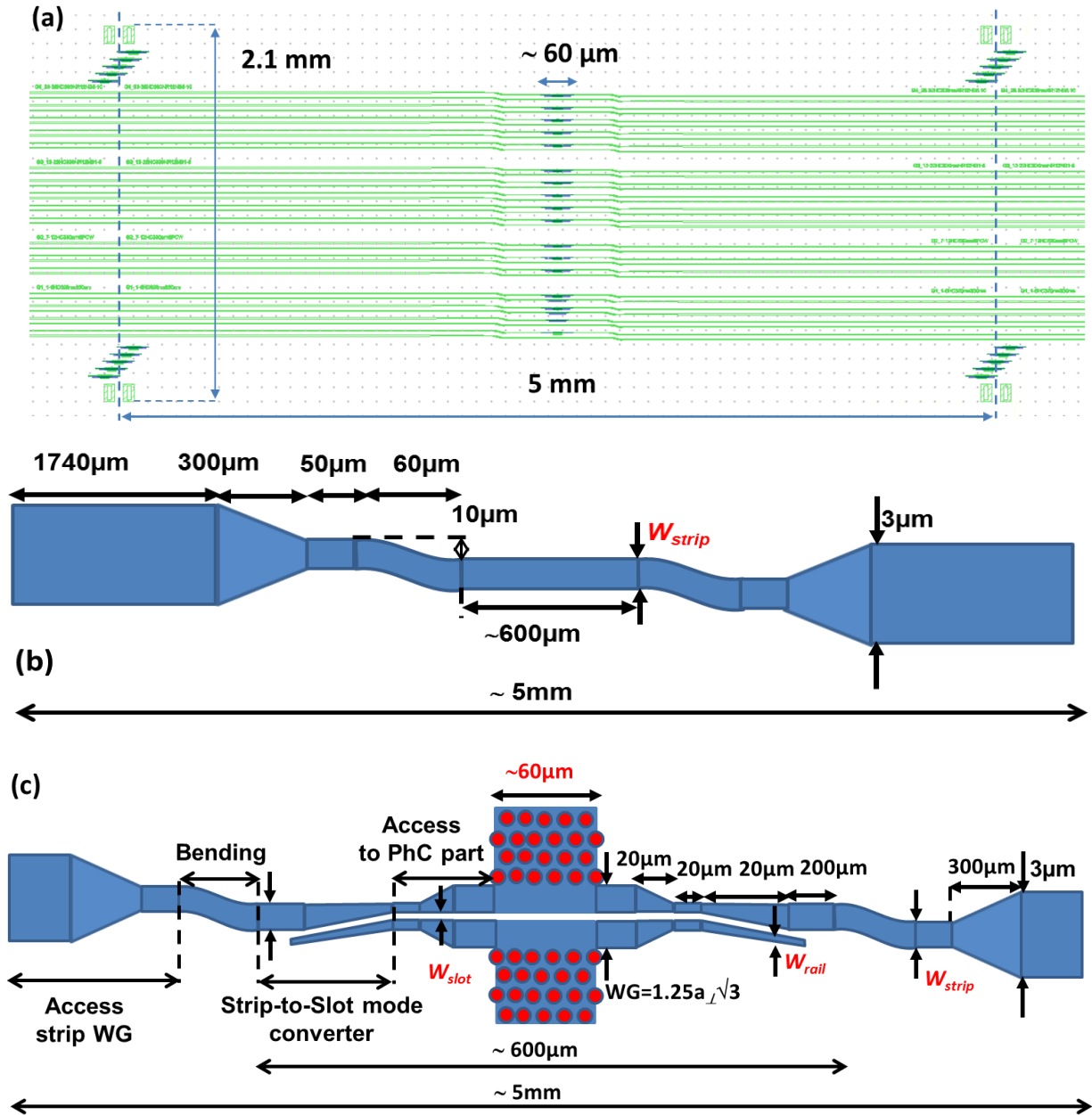


Fig. 3.1.1(a) Overview of one typical sample (*.gds-II*) mask. The two dash lines represent the positions for the sample cleaving and thus for the sample for characterization (b) Schematic of a typical reference strip waveguide system with a single-mode strip waveguide of W_{strip} width to fiber high-order optical modes and couple light properly into a single-mode slot waveguide (c) Schematic of a typical chip of slot PhC waveguide cavities (the illustrated lengths of different components are not proportional to their values).

As said above, its length is set to 5 mm after cleaving of the two lateral additional parts. More precisely, the sample consists of slot PhC waveguides (SPCWs), slot PhC waveguide cavities

(SPCW cavities), and strip waveguides. The following approach was followed to prepare the characterization of slotted PhC waveguide devices. As explained just hereafter, specific light injectors are needed to excite SPCWs and SPCW cavity modes. In order to subtract the transmission of these injectors from the total collected transmission of the slot waveguide devices of interest, reference strip-to-strip waveguide tapers were considered as illustrated in Fig. 3.1.1(b). Slot photonic devices under interest were placed near the sample center and connected to the sample left and right edges by similar access strip waveguide couplers made of 3 μm -wide strip waveguides followed by a linear transition to W_{strip} -width strip waveguides (see Figs. 3.1.1(b) and (c)). This way, transmission of the configuration described in Fig. 3.1.1(c) was normalized with respect to the transmission collected in the Fig. 3.1.1(b) case.

The remaining of the mask design approach was to scale the set of input and output access waveguides depending on the studied photonic crystal configuration. The motivation for that approach was the need to maintain single-mode waveguiding operation whatever the PhC lattice was. Short resonance wavelength cavities (*e.g.* with a resonance wavelength close to $\lambda = 1.3 \mu\text{m}$) indeed need a narrow width of input and output strip waveguides to cancel any risk of multimode operation, *e.g.* downsizing W_{strip} (see Fig. 3.1.1(b)) should be applied. Meanwhile, W_{strip} can be increased for larger resonance wavelength cavities (*e.g.* with a resonance wavelength close to $\lambda = 1.6 \mu\text{m}$). In that sense, W_{strip} was chosen from 260 nm to 410 nm while the related lengths of different parts of the strip were fixed. Details of the chosen values of the strip width are summarized in Table 3.1. Waveguide bending parts were introduced to filter optical noise coming from the collection of residual straightforward optical signal propagation. The performance of strip waveguides will be shown later in the characterization section.

Tapers for efficient light injection into slot PhC waveguides:

We now come back to the important question of light injection into slot PhC waveguides, that was briefly mentioned above. Considering solely a standard silicon slot waveguide (*e.g.* without any photonic crystal patterning) creates a large mode mismatch of the afore mentioned fundamental slot mode with the one of a strip waveguide. As a consequence, the direct coupling between strip and slot mode waveguides results in strong mode impedance-mismatch losses ($\gg 1\text{dB}$).

Several solutions have been proposed in the literature to solve this problem, such as using V-shape mode converters [216] or adiabatic mode converters [217], [218]. In this work, we adopted a nearly adiabatic strip-to-slot mode converter [218]. Fig. 3.1.1(c) presents a schematic view of a typical SPCW cavity designed for the case perpendicular lattice constant $a_{\perp} = 340$ nm, *i.e.* for a targeted resonance wavelength around $\lambda = 1.3$ μm . The core of the light injector comprises a gradual narrowing of the single-mode strip waveguide and a progressive coupling to the slot mode.

In Ref. [217], an adiabatic logarithmical taper of the strip-to-slot mode slope was proposed, as shown in Fig. 3.1.2. In our case, we considered a linear tapering along 20 μm long taper because of the fabrication uncertainties in the design of a logarithmic profile and due to the already low loss theoretical value obtained in the linear simpler case (<0.1 dB).

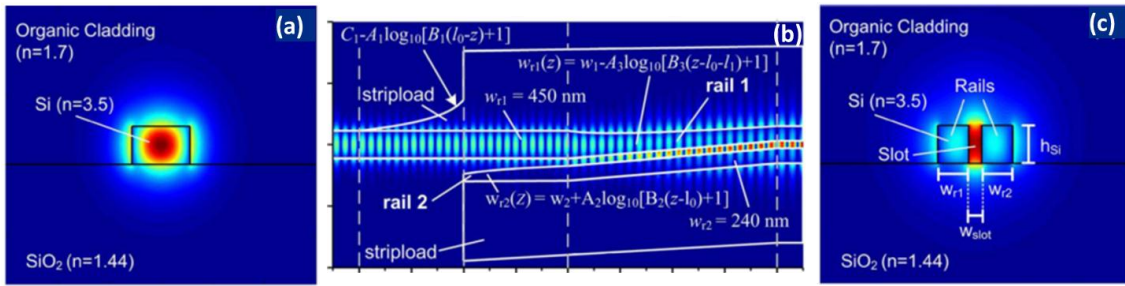


Fig. 3.1.2 Principle of the considered strip-to-slot converter: (a) Strip mode (b) Transition mode converter based on a logarithmic taper (c) Slot mode [217].

Table 3.1 reports the condition of SOI strip widths and mode converter rail widths corresponding to different cavity resonance wavelengths.

Table 3.1 Main parameters considered of the testing structure scheme shown in Fig. 3.1.1. Different sets are considered to address targeted cavity resonance wavelengths

Strip width W_{strip} (nm)	Rail width W_{rail} (nm)	Wavelength λ (nm)	Corresponding perpendicular lattice constant a_{\perp} (nm)
260	150	1200–1600	330–400
280	160	1300–1600	350–400
340	190	1400–1600	370–400
410	210	1500–1600	390–400

The results were obtained by considering a slab thickness of 260 nm, refractive index values for silicon, silica, and a top cladding of 1.46 at $\lambda = 1.5$ μm . In each case, the length of the PhC region

is around $60 \mu\text{m}$, exactly depending on the value of the perpendicular lattice constant a_{\perp} considered in the different SPCW cavity configurations. The targeted dimensions of the rails and strip waveguides were chosen 10 nm smaller than the largest value supporting a mono TE-fundamental mode given in Table 3.1 in order to guide light properly while avoiding the risk of larger dimensions coming from the fabrication process, *i.e.* in order to prevent multimode operation. Additionally, all geometry dimensions were collected in the design of *gds-II* mask in order to properly pre-chirp dimension drifts due to the e-beam and etching processes (see section 3.1.2). The typical applied corrections are shown in Table 3.2.

Table 3.2 Shift of dimensions in *.gds-II* and desired values of the fabricated chip (parameters denoted with red color in Fig. 3.1.1(c))

Name	Desired values (nm)	Size on mask (nm)
Slot width	W_{slot}	$W_{slotgds} = W_{slot} - 40$
Hole diameter	$2r$	$2r_{gds} = 2r - 30$
Rail width	W_{rail}	$W_{rail} + 60$
Strip width	W_{strip}	$W_{strip} + 60$

Fig. 3.1.3(a) shows the *gds-II* description of the center part of a typical slot PhC cavity with a set of holes and the slot. Holes are defined by a 180 nm diameter 32-point polygon.

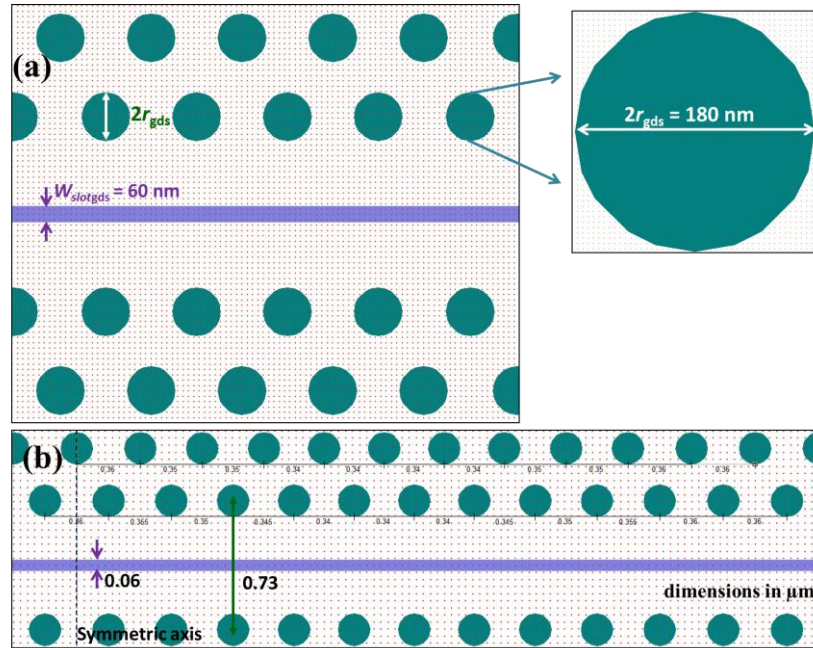


Fig. 3.1.3 *Gds-II* mask edition: example of one part of one sample (a) Drawing details of slot and holes in the center part of a SPCW cavity (b) An example of the lattice distribution in case of a SPCW cavity with perpendicular lattice constant $a_{\perp} = 340 \text{ nm}$; the dash line shown on the left is the symmetric axis of the device (dimensions are in μm).

In that precise case, the value of the slot width considered on the *.gds-II* mask is 60 nm to target a 100 nm slot width after fabrication. In a complementary fashion, Fig. 3.1.3(b) presents the distribution of lattice constants on one side of the slot.

3.1.2 Fabrication process

The devices were fabricated following the fabrication steps described in Fig. 3.1.4. We started with 260 nm Si thick SOI wafers (Fig. 3.1.4(a)). After that, the wafers were masked by a ZEP-520A resist as shown in Fig. 3.1.4(b). Our scope was to optimize the writing resolution relying on the choice of resist, size of exposed beam and size of sub-main fields. So we selected the ZEP-520A instead of the standard positive resist PPMA (poly-methyl methacrylate) for its higher selectivity [219].

The ZEP-520A positive resist consists of a polymer chain sensitive to electronic exposition. The quality of the lithography relies on the proper electron penetration, which is decided by the deposited thickness and its homogeneity. In order to optimize this step, the resist was diluted in Anisole and deposited by spin-coating at 6000 rpm for a thickness of 90 nm. Then the sample was covered with resist deposited in a heated surface at 170°C for 3 minutes before being written by e-beam lithography.

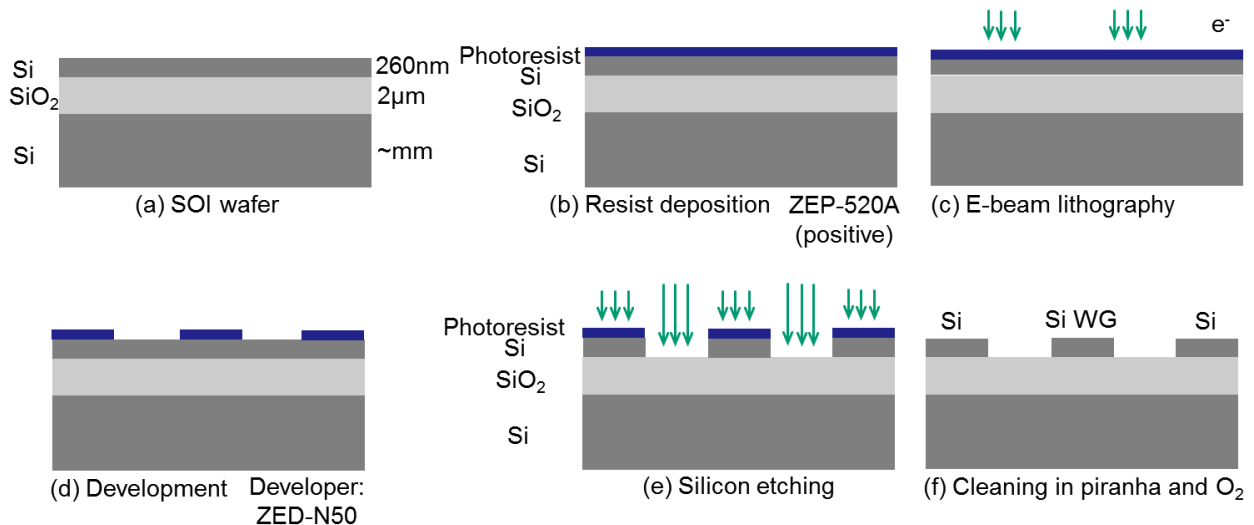


Fig. 3.1.4 Schematic of fabrication steps of Strip, Slot WGs and slot PhC cavity structure: (a) Preparation of SOI wafer (b) Resist deposition (c) E-beam lithography (d) Development (e) Etching the Si mask and (f) Cleaning step.

Fig. 3.1.4(c) illustrates the e-beam lithography step. The *.gds-II* files were fragmented into the nanobeam pattern format (*.npf*) file by the nbPat fracture software. These files included main and sub fields (see Fig. 3.1.5), as required for beam scanning, *i.e.* the regions in which the electron beam writes successively until finishing all patterns. Hence, stitching effects (positioning errors of the beam creating offsets between the photonic structures: < 20 nm for the used beam writer) can occur when the beam moves from one mainfield to another one. Inside each mainfield, the sample stage is fixed at the center and the beam is deflected by a coil to isolate the rest, so that the errors are minimized. In order to avoid electron beam aberrations, the size of the mainfields should ideally be minimized but this is obviously done at the expense of a larger amount of stitching errors. In addition, it is necessary to control the exposure dose parameters so that the machine practical limit drift speed (55 MHz) is not exceeded. To serve that purpose, the following optimal set of parameters was chosen: beam current of 2 nA, write step size of 5 nm and the required dose of 2.8-2.9 C/m². To correctly write the patterns by e-beam lithography, each SPCW device was positioned in the center of $70 \times 70 \mu\text{m}^2$ mainfield because the best resolution of the writing system is in the center of the mainfield, as depicted in Fig. 3.1.5(a).

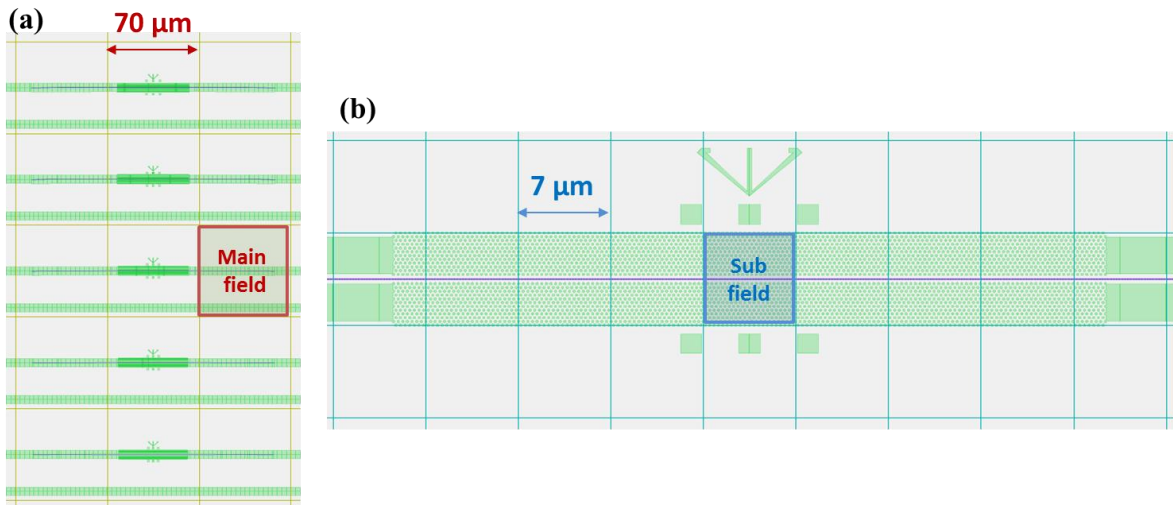


Fig. 3.1.5 Distribution of part of a chip with the descriptions of what are: (a) A mainfield (b) A subfield.

Furthermore, it is necessary to put the PhC device part inside a given subfield, the chosen size of subfield was $7 \times 7 \mu\text{m}^2$, as shown also in Fig. 3.1.5(b). The exact optimal dimensions of the subfields and mainfields were determined based on the width of the PhC structures. These values satisfied the possible value range of mainfields and subfields, *i.e.* the maximum/minimum sizes

for the mainfield being $1000 \times 1000 \mu\text{m}^2$ and $50 \times 50 \mu\text{m}^2$, respectively, while these values for the subfield were $20 \times 20 \mu\text{m}^2$ and $5 \times 5 \mu\text{m}^2$.

E-beam lithography was carried out by using a NanoBeam nB4 Ltd. writer. In this system, the electrons are accelerated from an electron gun with an energy of ~ 80 keV. This high potential helps reduce proximity effects. The electron beam moves onto the surface point by point following the *.npf* file instruction, as shown in Fig. 3.1.5. The subfield center being more accurate than around the edges regions (where the electronic beam should deflect), the sensitive parts were preferentially located in the central area. As shown in Fig. 3.1.5(b), the most sensitive part of the cavity where the lateral lattice constants were chirped was set to entirely reside inside a given subfield. The pattern was distributed into different writing areas, as depicted in Fig. 3.1.5(a).

After that, the samples were developed with ZED-N50 for 40-second and one more 30-second rinsed treatment with isopropanol was applied before drying the samples under nitrogen flow. The related development step is illustrated in Fig. 3.1.4(d).

The next step in the fabrication process was etching, which is intrinsically nearly as important as the lithographic writing one (see Fig. 3.1.4(e)). The features were transferred by an ICP reactive ion etching process using SF_6 and C_4F_8 gases. The ICP etching process was optimized, taking into account the different coils, the injected gas flux and etching time. The samples were then immersed in a Piranha (H_2SO_4 : H_2O_2 with the ratio 3:1 in volume) solution (Fig. 3.1.4(f)) to remove the remaining resist layer and one last step of plasma O_2 to dissipate the thin C_4F_8 film. Finally, the two facets of each sample were cleaved to prepare the optical characterization.

Despite major efforts to control the main errors of the technological process, errors were encountered on some samples. Our approach was to inventory them by controlling the quality of each sample by SEM imaging and by looking for defects preferentially to the places with medium/high probability of concentrating the defects. In this view, Fig. 3.1.6(a)-(b) show some cases of errors in the slot PhC area we faced during the fabrication. Some of them originate from the imperfect distribution of the resist, of local charge effects, or of the diffraction effects due to dust in the resist (see Fig. 3.1.6(a)-(b)). In some other cases, stitching errors are the likely source of observed fabrication errors (Fig. 3.1.6(c)-(d)-(e)).

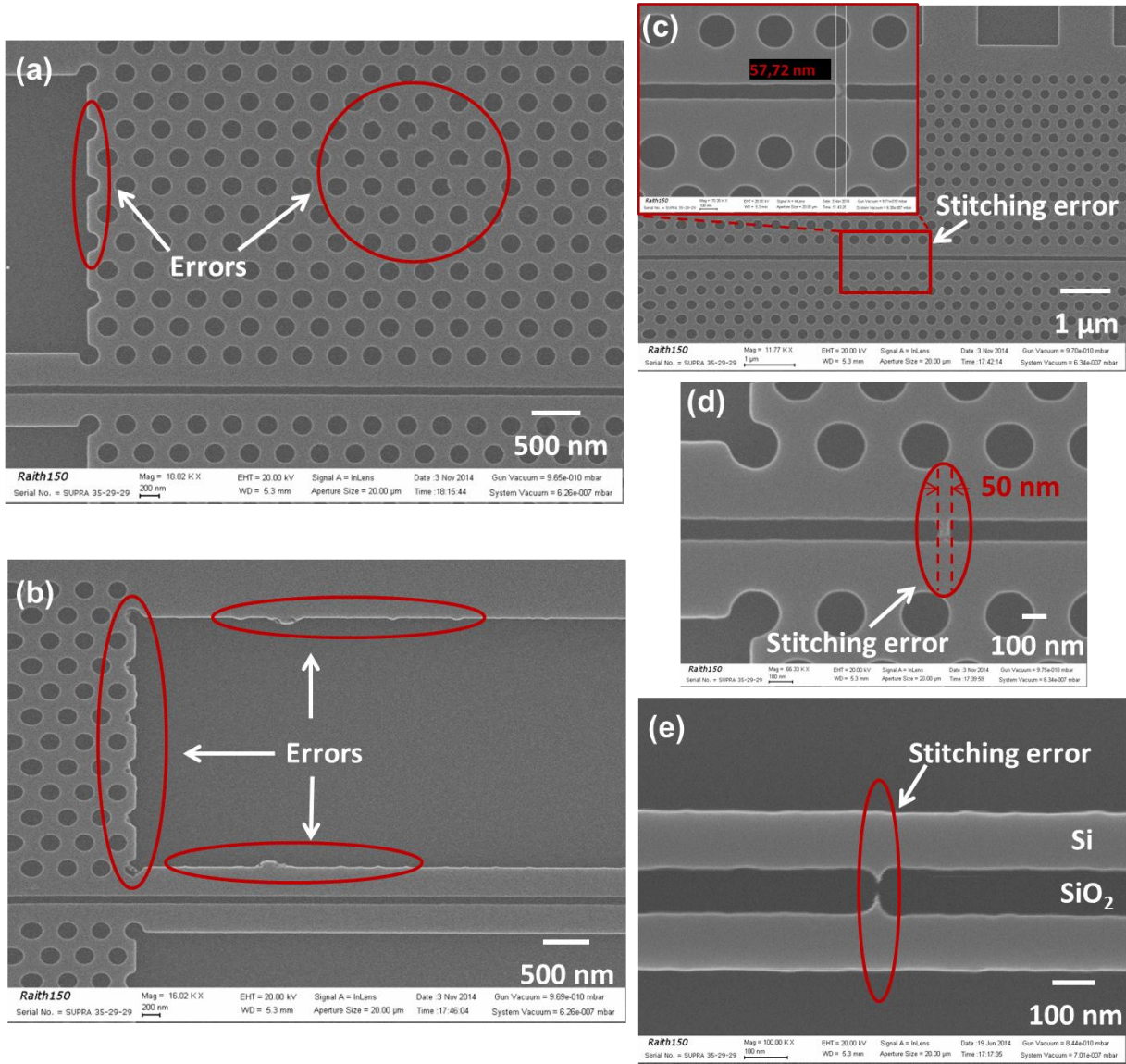


Fig. 3.1.6 Inventory of some typical errors: (a)-(b) Due to the inhomogeneity of the resist, (c)-(d)-(e) Due to stitching errors at the boundary of the mainfields.

Overall, the carried methodology of process error identification helped to proceed to several feedbacks between the optimization of *gds-II* masks and fabrication steps to reach a satisfying quality level of the fabricated photonic structures.

After cleaving of the samples, each one was mounted on a sample holder, its surface was covered with a Cargille commercial liquid of n_{clad} refractive index for characterization (by default, n_{clad} was chosen equal to 1.46).

Following this methodology, we fabricated a series of slot PhC heterostructure cavities obtained for different a_{\perp} values ranging from 330 nm to 400 nm with the purpose of producing cavities operating in the 1.3 μm -1.6 μm telecom range.

3.1.3 SEM images and analysis of the fabricated devices

Beyond the use of SEM images in the purpose of fabrication error detection, we envisaged their exploitation for the geometrical characterization of the PhC slotted photonic structures. From this point of view, caution was required insofar as the quality of the extracted information depends directly on the resolution of the images and the carried out statistical data processing. As will be seen hereafter, we have shown that relevant relative information can be extracted from the SEM images, sufficient for an extraction of the spatial profile of the photonic crystal heterostructures, thus indirectly validating the quality of the technological realization. The technique used, based in practice on image analyses carried out using a Matlab program, made it possible to go beyond a direct measurement of the PhC lattice mesh parameter of the heterostructure by a direct image viewing.

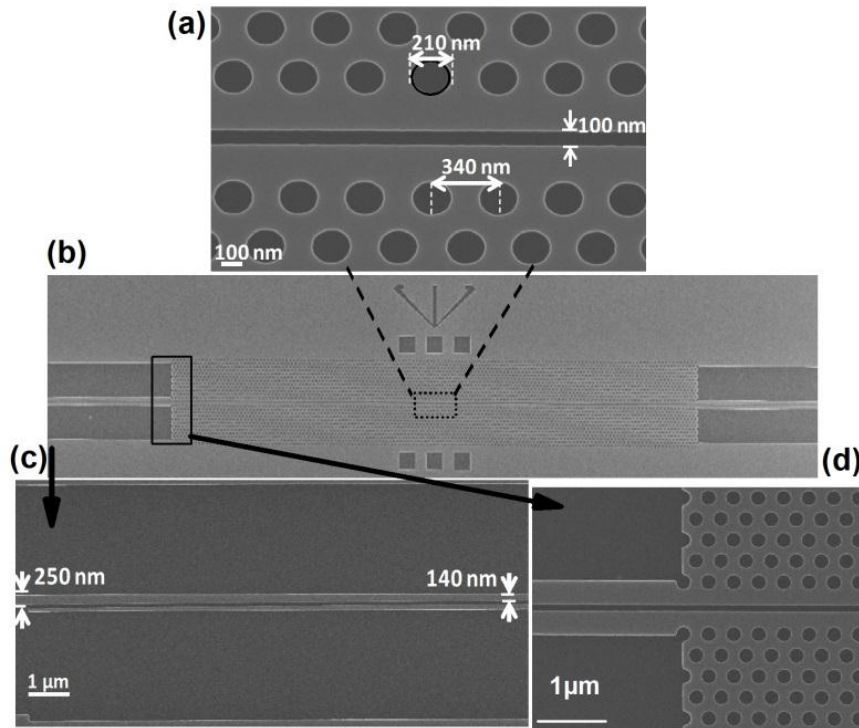


Fig. 3.1.7 SEM views of a fabricated slot PhC cavity structure: (a) Center part of the PhC cavity in which $a_{\perp} = 340$ nm (b) Taper and PhC parts (c) Strip-to-slot mode converter, and (d) Input access to the SPCW.

SEM views of one typical slotted PhC cavity device (for which $a_{\perp} = 340$ nm) with input and output access waveguides are shown in Fig. 3.1.7 (a)-(d): (a) zoom in the center part of the PhC cavity, (b) the taper and the PhC parts, (c) the strip-to-slot mode converter and (d) the input access to the SPCW. The accurate control of the targeted geometrical dimensions, which is apparent from these images, resulted from the optimization of the 80 keV EBL writing process as mentioned in the previous section. In particular, designing the *.gds-II* mask by explicitly forcing every point on the employed 5 nm grid size and slightly tuning the electron dose were found as critical parameters to minimize the loss level of the fabricated non-free standing membrane slot heterostructure cavities. We used a Matlab program written by Dr. Pierre Colman to evaluate the dimension of the parameters of the fabricated sample, *i.e.* the lattice constant from the position and the size of the holes.

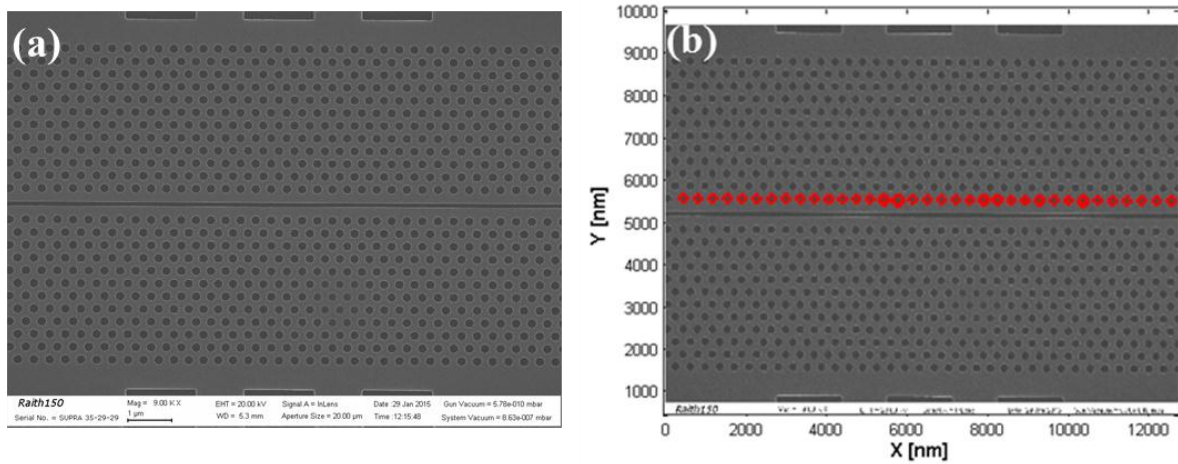


Fig. 3.1.8(a) SEM view with the 9 KX magnification factor of the PhC part of the slot PhC heterostructure cavity with the designed perpendicular lattice constant $a_{\perp} = 340$ nm, **(b)** SEM image with the location of the holes in the first row (the red curves).

We took the SEM image of the slot PhC heterostructure cavity with $a_{\perp} = 340$ nm as an example to use this tool and study the chirped lattice constant profile of the holes in the first row closest to the slot (Fig. 3.1.8(a), magnification factor $\times 9K$). The principle of the program is as following. From the original SEM image, the holes are determined by detecting different points based on the value of pixel averaging. Then, the position of the barycenter and the radius of each hole are identified from the coordinates of collected points. The quality of this investigation depends on the magnification of the SEM image. As shown in Fig. 3.1.8(b), the red circles depict the holes.

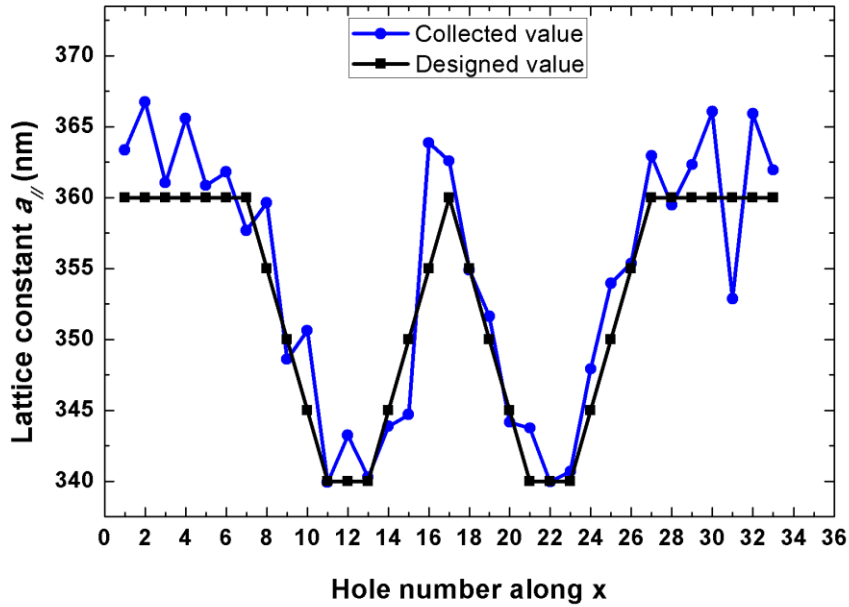


Fig. 3.1.9 Lateral lattice constant versus the hole number of the first row of holes of the slot PhC heterocavity (with the designed perpendicular lattice constant $a_{\perp} = 340$ nm).

The analysis data of 35 holes in the first row are presented in Fig. 3.1.9. The black line shows the designed values of the lattice constant of the holes and the collected values by the home made code is depicted by the blue line, which is very close to the values under consideration. The small error is the evidence that the quality of the fabrication is proper. It is also noticeable that a simple SEM image analysis allows to identify a photonic crystal lattice parameter chirp of around 20 nm.

3.1.4 Characterization

The samples were characterized by optical measurements which allowed the estimation of the optical transfer functions of structures (see Fig. 3.1.10). The cavity modes were probed by a continuous wave (CW) tunable external laser sources ranging from 1260 nm to 1640 nm, first guided to a polarization controller to provide either TE or TM polarized light and TE filter, Polarization Maintaining Filter (PMF) to maintain only TE polarization and then coupled into the fabricated devices through an input strip waveguide of 3 μm width by a taper lensed fiber. The samples were placed and well aligned on a holder, and the surface of each tested sample and the tip of the taper-lensed fiber was scanned on a screen by a microscope camera and an infrared camera placed vertically above the set-up. Light at the output facet of the cavity sample was then collected by a microscope objective, then a focal system and finally a photodetector (PD).

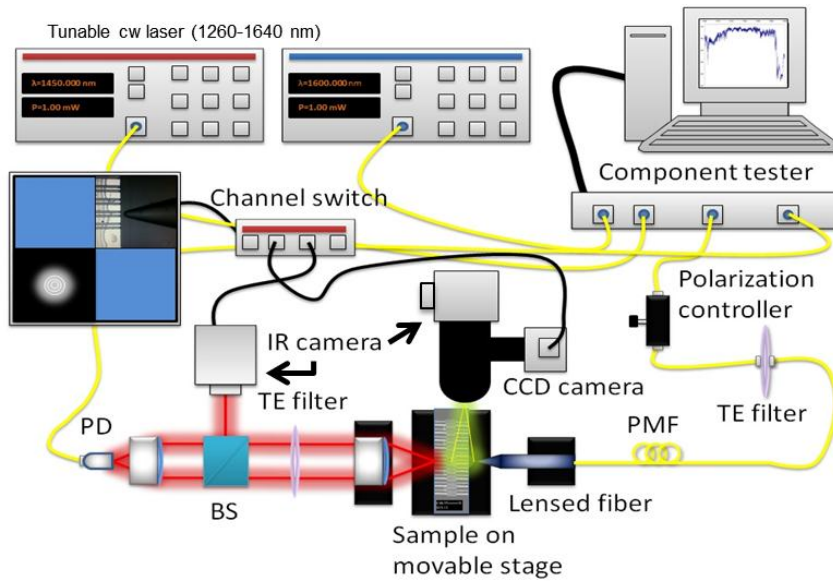


Fig. 3.1.10 Linear measurement set-up to characterize the samples.

The signal received from the detector was subsequently sent to a MT9820 or CT400 All-Band Optical Component Tester through a single mode FC/APC optical fiber connectors in order to analyze the optical transfer function. Each device optical transfer function was determined by comparing the intensity of the input signal received from a tunable laser diode (the source) to the intensity of the signal received at the detector. The employed setup comprised an automatic sweep and switch feature offering a nearly continuous (resolution of 1 pm) laser wavelength tuning in the 1260-1650 nm wavelength range directly controlled through a computer interface. All the FC/APC fiber connectors feature low loss and after optimizing the set-up, the level of obtained transmission from lensed fiber to objective without sample was of around -14 dBm with an injection power of 1 mW.

Strip and PhC slot waveguides:

Before characterizing slotted PhC cavities, optical transmission of strip and slot waveguides was achieved. Typical results are shown in Fig. 3.1.11 to prepare the design of slot PhC cavities in the 1250 nm-1650 nm range, consistently with dimensions reported in Table 3.1, *e.g.* for $W_{strip} = 250$ nm and $W_{rail} = 140$ nm, respectively (Design-A). As visible in Fig. 3.1.11(a) and (b), optical transmission from both kinds of waveguide systems (see the two insets of Fig. 3.1.11(a)) have comparable levels. This matter of fact shows the remarkable efficiency of the strip to slot

waveguide on-chip butt-coupling mode converters that were designed and fabricated. A close inspection to the data based on the filtering of the high-frequency Fabry-Perot fringes visible in Fig. 3.1.12(a) led to the following estimation: the additional insertion losses of the slot PhC waveguide scheme were less than 0.6 dB higher than the strip waveguide one in the 1270-1350 nm wavelength range, and approximately 1 dB in the 1490-1640 nm spectral window. We notice that for larger waveguide dimensions (Design-B intended to target later slot PhC cavities with resonance wavelengths in the wavelength range of 1500-1600 nm), the tested strip and slot access waveguides suffer from a transmission drop for shorter wavelengths (see Fig. 3.1.11(b)). This matter of fact can be interpreted by the multimode operation of the aforementioned waveguides for short wavelengths.

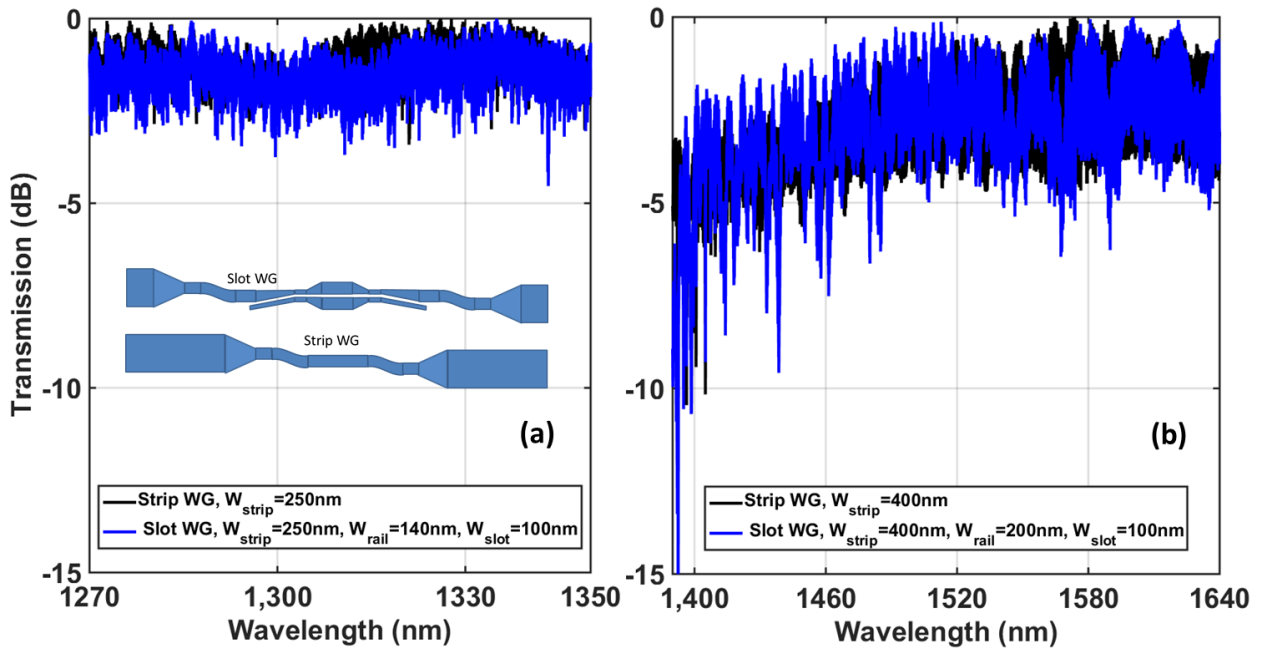


Fig. 3.1.11 Linear transmission of typical strip and slot PhC waveguides (TE-like polarization): (a) Design-A is made for slot PhC cavities with a resonance wavelength in the 1270-1350 nm range, with following dimensions: strip width $W_{strip} = 250$ nm, $W_{rail} = 140$ nm and $W_{slot} = 100$ nm. Insets: Schematic of strip WG and slot WG. (b) Design-B is made for slot PhC cavities with a resonance wavelength in the 1500-1600 nm range, with following dimensions: strip width $W_{strip} = 400$ nm, $W_{rail} = 200$ nm and $W_{slot} = 100$ nm.

Starting from a firm characterization of the access waveguide systems, we further achieved experiments to characterize the optimal transmission of PhC slot waveguide cavities. As discussed in section 2.2.3, slot PhC heterostructure cavities were designed based on the bandgap engineering method completed by 2D/3D FDTD simulation. We remind here that for a given

perpendicular lattice constant, namely $a_{\perp} = 400$ nm, the parallel lattice step was chirped between a_{\perp} ($= 400$ nm, here) and $a_{\perp} + 20$ nm ($= 420$ nm, here).

Control of the slot PhC waveguide band-edges by the 2D bulk lattice chirp:

As a preliminary assessment of the slot PhC waveguide (SPCW) band-edge sensitivity, we first characterized SPCWs made of a constant perpendicular lattice constant and elongated parallel ones, as illustrated in Fig. 3.1.12(a). Dispersion diagram of one typical SPCW with lattice constant $a_{\perp} = a_{\parallel} = 400$ nm, hole radius $r = 105$ nm, width of slot $W_{slot} = 100$ nm, waveguide width $1.25WG$ and filled with cladding material of 1.46 refractive index is presented in Fig. 3.1.12(b). The W1-like y -even mode (red line) is employed to create cavity mode when introducing the PhC structure as shown in Fig. 3.1.12(a). The value of corresponding edge-frequency is of around $0.256(a/\lambda)$.

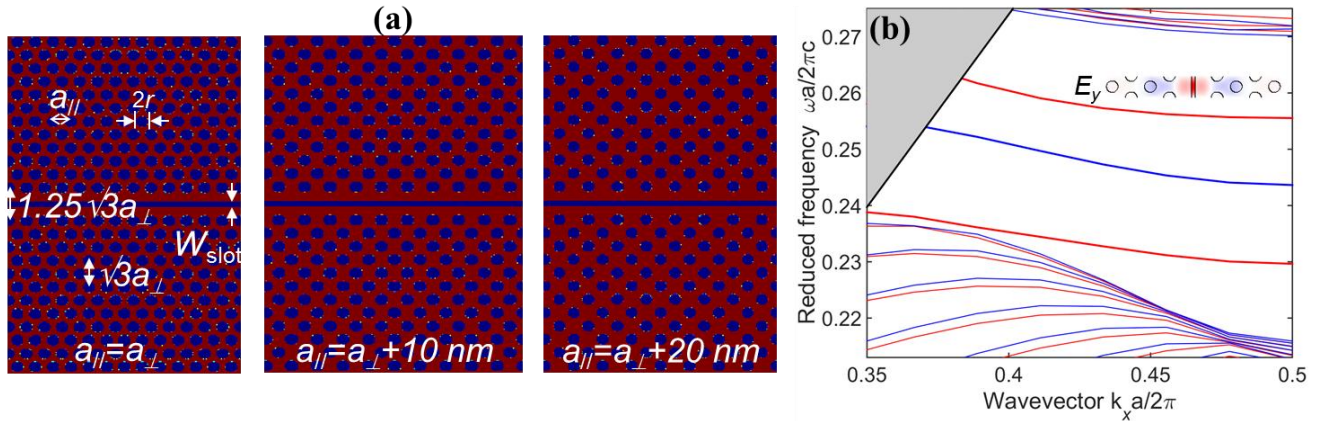


Fig. 3.1.12(a) Horizontal view of three considered slot PhC waveguides in which a_{\perp} is remained unchanged while a_{\parallel} is chirped between a_{\perp} and $a_{\perp} + 20$ nm **(b)** Dispersion diagram of a slot PhC waveguide constructed with lattice constant $a_{\perp} = a_{\parallel} = 400$ nm, hole radius $r = 105$ nm, width of slot $W_{slot} = 100$ nm, waveguide width $1.25WG$ and the top cladding refractive index $n_{clad} = 1.46$, inset, field distribution of E_y component.

Considering all the opto-geometrical dimensions described in section 2.1.3, SPCWs corresponding to a_{\parallel} is 400 nm, 410 nm and 420 nm, respectively, and $a_{\perp} = 400$ nm were simulated using 3D-PWE calculation and experimentally characterized (see Fig. 3.1.13).

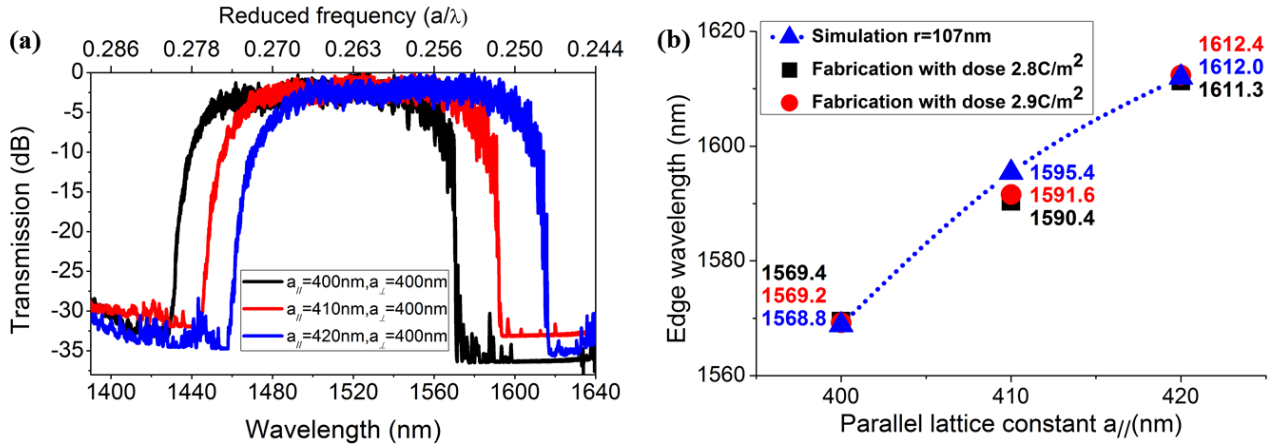


Fig. 3.1.13(a) Transmission spectra of three fabricated slot PhC waveguides filled with top cladding material of 1.46 refractive index in which $a_{||}$ is 400 nm, 410 nm and 420 nm, respectively, and $a_{\perp} = 400$ nm; **(b)** Simulation and experimental results for the edge wavelength of these three SPCWs using two doses 2.8 C/m² and 2.9 C/m².

As visible in Fig. 3.1.13(a), the transmission spectra of the three SPCWs were found to be nearly flat in the W1-like SPCW mode pass-band. Moreover, the observed sharpness of the photonic band-edges proves the quality of the full fabrication process cycle. As visible also in Fig. 3.1.13(b), a correct agreement is obtained between the simulation (3D-PWE calculation) and the obtained experimental results for the photonic band-edge of the considered SPCWs with a fitted hole radius value of 107 nm (while the target value was 105 nm). In addition, a possible degree of freedom to control the size of structures by changing the electron beam dose only from 2.8 C/m² to 2.9 C/m² was also observed.

Optical characterization of slot PhC waveguide heterostructure cavities:

After these preliminary steps, we finally characterized the targeted SPCW heterostructure cavities. Fig. 3.1.14 shows a typical result obtained for a resonance wavelength around 1300 nm. As stated before, the strip input/output waveguide system (see section 3.1.1, Fig. 3.1.1) was considered as reference structure in order to normalize the PhC slot cavity power transmission.

The power transmission in the bandpass of PhC slot waveguide structure, including the series of coupling stages for light injection and light extraction, was maximized to around 4-6 dB below the level of the strip reference one, as it is noticeable from Fig. 3.1.14.

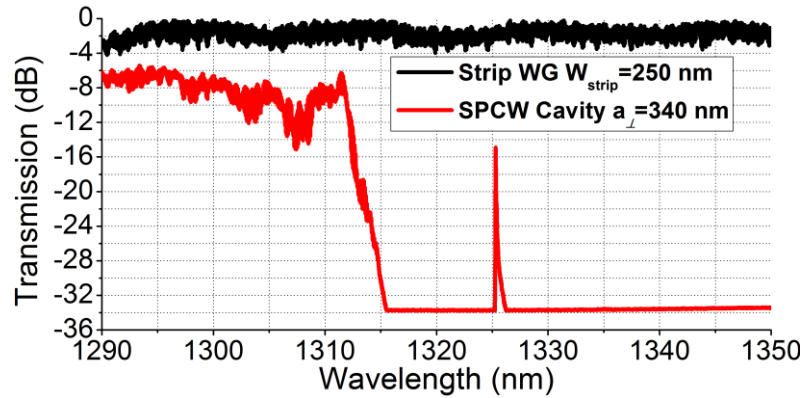


Fig. 3.1.14 Transmission spectra of the reference strip structure shown in Fig. 3.1.1(b) and of the slot PhC cavity one shown in Fig. 3.1.1(c) (for $a_{\perp} = 340$ nm), respectively. The devices were filled with material of 1.46 refractive index (Cargille liquid).

Fig. 3.1.15 shows the spectra obtained by gathering results related to individual cavity devices corresponding to different a_{\perp} values in the 330-400 nm range.

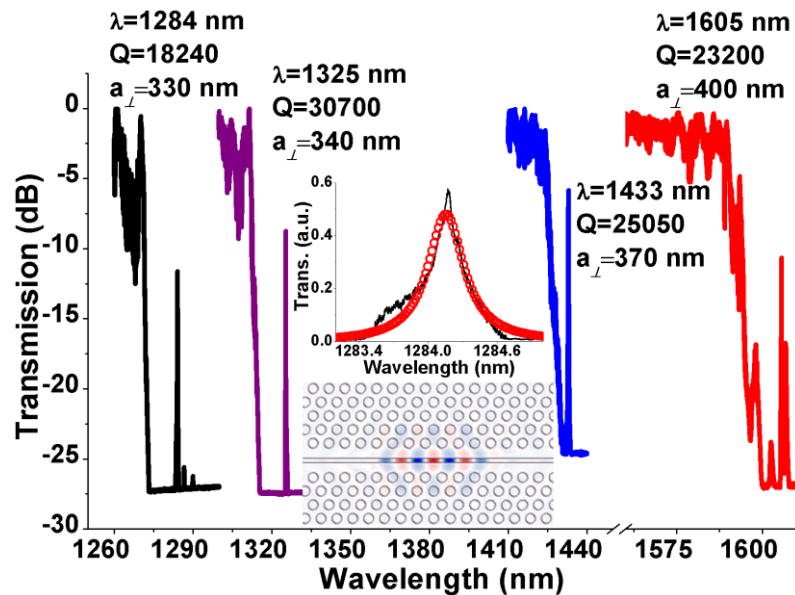


Fig. 3.1.15 Transmission spectra of slot PhC heterostructure cavities characterized by a_{\perp} ranging from 330 nm to 400 nm and their relative resonant wavelengths, as well as the obtained quality factors. Insert: Lorentzian fit of the resonance located at $\lambda = 1284.2$ nm and field distribution in the case of $a_{\perp} = 400$ nm, $FWHM = 0.07$ nm.

As expected, enlarging the basis perpendicular lattice value is responsible for an increase of the heterostructure cavity resonance wavelength. Interestingly, this approach enables to fill the gap between the two main telecommunication wavebands, *e.g.* the 1.3 μm and 1.55 μm wavelength ranges. Simultaneously, the loaded Q -factors remains above 18 000 in all cases and approaches 31 000 for $a_{\perp} = 340$ nm, which exceeds our previous reported values [152], [220]. The Q -factors

of these cavities were extracted by using Lorentzian fit. For example, in the case of $a_{\perp} = 400$ nm a fitting Lorentzian gave a FWHM of 0.07 nm and a Q -factor of 23,200 was estimated. From the inset of Fig. 3.1.15, the transmission level in the cavity can be estimated to be around 60% in comparison with the one in the SPCW. This high level assesses the good coupling between the cavity and the in/out waveguides, as well as the ability of using these designs in other integrated devices for further applications. As our previous calculations showed that this kind of slot photonic crystal cavities have mode volumes of around $0.03 (\lambda/n)^3$ [152], Q/V ratio thus typically remains above 600 000 and reaches 1 000 000 in the best case ($\lambda \approx 1.3 \mu\text{m}$), which represents higher values than those previously reported for filled slot PhC cavities [134], [152].

3.1.5 Conclusion of section 3.1

In conclusion, we succeeded in designing, fabricating, and characterizing slot PhC heterostructure cavities with low insertion losses and Q/V factors ranging between 600 000 and 1 000 000. Our approach relies on non-free standing membrane slotted PhC structures filled with a top cladding material of ~ 1.46 index in order to assess their possible exploitation for applications needing a mechanically-robust and reliable platform. With a demonstrated range of usable resonance wavelengths filling the gap between the $1.3 \mu\text{m}$ and $1.55 \mu\text{m}$ wavebands, these hollow core integrated cavities could serve a variety of on-chip applications relying on light-matter localized interactions, such as nonlinear effect, bio-sensing, or light-emission, if infiltrating with proper active materials is carried out.

As we will show later in following sections, we have applied these cavities in liquid index-sensing and used them for the on-chip integration of a semiconducting single-walled carbon nanotubes to investigate their prospective applications for on-chip light emission through short wavelength optical pumping.

3.2 Slot photonic crystal cavities for index-sensing

3.2.1 Slot photonic crystal waveguide cavities for index sensing

3.2.1.1 Index variation process

In order to study the behavior of the cavity under different top cladding materials, the simple process described in Fig. 3.2.1 was carried out. Different refractive commercial index liquids (Cargille company) were drop-casted onto the surface of the silicon sample before optical characterization (see Fig. 3.1.10). A simple cleaning step of the sample allowed to renew the process by drop casting another liquid (see Fig. 3.2.1). The samples were cleaned in the clean room by using ethanol and then isopropanol solutions. This experiment was repeated with liquids of refractive index values ranging from $n_{clad} = 1.35$ to $n_{clad} = 1.55$, namely $n_{clad} = 1.345$, $n_{clad} = 1.41$, $n_{clad} = 1.448$, $n_{clad} = 1.45$, $n_{clad} = 1.516$, and $n_{clad} = 1.55$ (at $\lambda = 1.55 \mu\text{m}$). This process proved to be simple and provide easy way for SOI sample reuse.



Fig. 3.2.1 Schematic of the experimental method used to proceed to SOI sample top cladding cleaning and drop casting of optical index.

3.2.1.2 Shift of cavity resonance wavelengths by cladding index variation

We characterized the linear transmission spectra of the cavity filled by four liquids ranging from 1.41 to 1.545 following the set-up presented in section 3.1.4.

The normalized spectra are depicted in Fig. 3.2.2. Normalization was done by averaging the transmission in the waveguide injected with an input laser power of 5 mW, and no filtering was applied to the data. The different spectra indicate a progressive increase of the transmission at resonance when increasing the refractive index, as well as a shift of the resonance wavelength.

For the smallest refractive index, the resonance mode is hardly distinguishable from the noise. The deterioration of the properties of the cavity is then due to the strong vertical asymmetry of the structure and pronounced frequency decrease of the PhC planar light line. Therefore, devices are more efficient when the refractive index infiltrating the slot and the holes is close to the one of the SOI buried silica optical substrate.

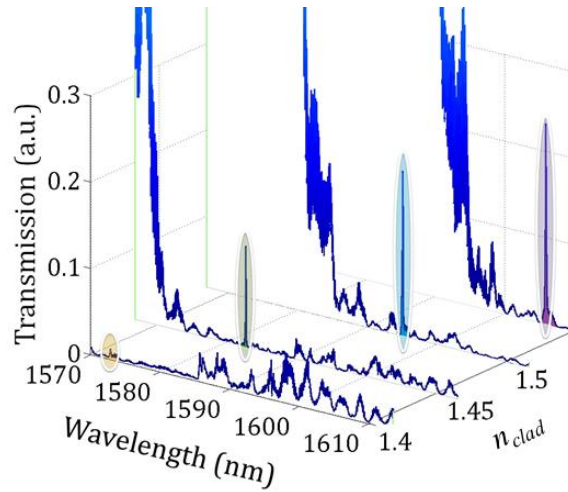


Fig. 3.2.2 Normalized transmission spectra obtained for a single slot PhC waveguide cavity for different values of the top cladding refractive index n_{clad} .

The corresponding resonance wavelengths and Q -factors are plotted as a function of the top cladding refractive index in Fig. 3.2.3(a).

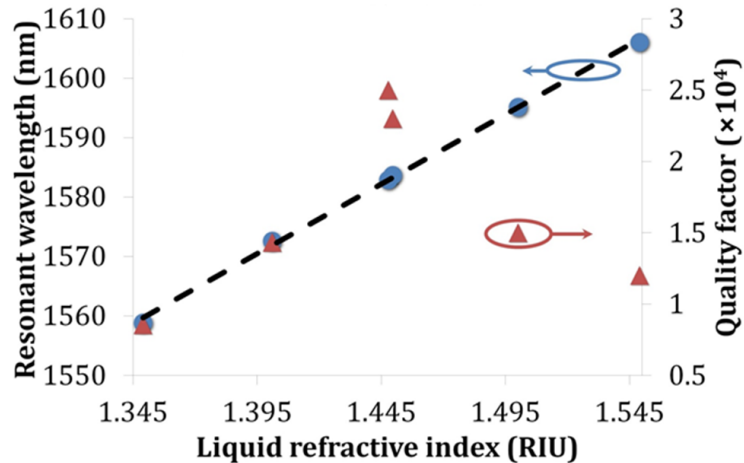


Fig. 3.2.3 Resonance wavelength as a function of the refractive index, showing a linear dependence yielding a sensitivity of 235 nm/RIU, and quality factor as a function of the refractive index, showing a maximum value of 25 000 around $n_{clad} = 1.44$.

As visible, the change of refractive index (over 0.2 RIU) leads to the linear shift of the resonance wavelength over around 55 nm. The slot PhC waveguide cavity yields a sensitivity of

235 nm/RIU by using a linear fit. This value is smaller than values mentioned in other works, *e.g.* over 1500 nm/RIU for chemical sensing [138], or around 500 nm/RIU for gas sensing [136]. However, this moderate wavelength sensitivities are counterbalanced by the obtained high Q values, typically ranging from 15 000 to 25 000. These values, obtained for non-free standing membrane PhC structures covered by liquids can be favorably compared with other slotted waveguide resonators. Previous works reported, for example, slotted nanoresonators with Q -factors of a few thousands only at $\lambda \approx 1.5 \mu\text{m}$ [134] although free-membrane slot photonic crystal devices immersed in liquids were considered.

In order to reintroduce the beneficial effect of the resonator quality factor on the selectivity of the detector scheme, the figure of merit of real-time and label-free sensors can be recalled [83],

$$\text{i.e. } : FOM = \frac{S}{FWHM} = \frac{SQ}{\lambda_0}, \text{ where } FWHM \text{ represents the smallest wavelength shift being}$$

detectable by the instrumentation system. In the hypothesis that, $FWHM$ is dominated by the resonator itself (and not by the full instrumentation chain), then the obtained FOM typically ranges from 1200 to 3700. These values are higher than those summarized in [221] for different kinds of sensing systems including Mach-Zehnder interferometers, whispering-gallery mode index sensors, and PhC based ones. Recently, higher theoretical FOM has been demonstrated at 4700 considering surround environment of around 1.33 refractive index (*i.e.* water) for multiple parallel PhC nanobeam cavities with tapered nano-gap separations [222]. However, this value was predicted only theoretically, and without considering the impact of water absorption leading to the decrease of Q . Comparing with other liquid index-sensing platforms, *e.g.* based on double metal plasmonic disk cavities [88], the sensitivity of slot PhC cavities is smaller. These plasmonic cavities can indeed detect liquid refractive index with sensitivity of around 1160 nm/RIU. In the same time, these double metal plasmonic disk cavities made up of two silver disks of radii R , separated by a gap of thickness t , supported a plasmonic resonance around 1550 nm with a quality factor Q of only 105. Thus, the FOM of these plasmonic cavities is much less than the one of slot PhC cavities.

In order to illustrate the benefits coming from the high Q factor obtained for compact slotted optical resonators, the wavelength shift obtained for small variations of refractive index was studied. As presented in Fig. 3.2.4, a wavelength shift of 0.75 nm was obtained for a liquid

refractive index change of only 0.02 RIU. This wavelength shift represents approximately 10 times the *FWHM*. This figure shows that the device allows a fine estimation of the concentration of an analyte in the liquid. Additionally, such device is compatible with an integration of multiple cavities coupled to the same waveguide [223], which could enable the multiplexing of many detection channels in a compact system [224].

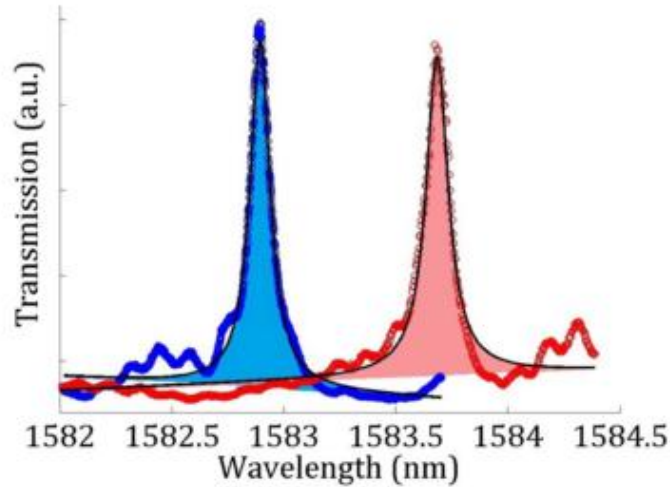


Fig. 3.2.4 Resonant spectra of the cavity for $n_{clad} = 1.448$ (blue) and $n_{clad} = 1.45$ (red) with Lorentzian fits (solid lines), showing a wavelength shift of 0.75 nm.

3.2.2 Conclusion of section 3.2

To conclude regarding the possible use of slot PhC waveguide cavities for index sensing, slotted PhC resonators with a sensitivity of ~ 235 nm/RIU and a *FOM* of 3700 have been reported. The experimentally quality factors stand from 8000 to 25 000 for top cladding liquids with refractive index values comprised between $n_{clad} = 1.345$ and $n_{clad} = 1.545$. A maximum *Q*-factor of 25 000 was achieved at $n_{clad} = 1.44$. The small footprint of the explored photonic devices could enable the integration of many cavities connected through the same bus waveguide [223], thus leaving opportunities for the multiplexing of many detection channels in a compact system [224] for the realization of Lab-on-a-chip bio-sensing chips [225].

3.3 Integration of single-walled carbon nanotubes in slot photonic crystal cavities

Based on previous encouraging results related to 2D PhC slot waveguide cavities, we have tackled in a last part a more prospective theme, that of the coupling of the emission of nanoemitters to the confined modes of the slot photonic crystal cavities studied previously. Consistently with the research themes of the group, our attention has been focused on the use of optical pumped thin layers doped with semiconducting carbon nanotubes.

As presented in section 1.2.2 chapter 1, semiconducting single-walled carbon nanotubes (s-SWNTs) indeed exhibit unique emission properties with an adjustable direct bandgap in the telecommunication wavelength ranges by tuning the chiral index, being exploitable for the implementation of integrated nano-sources.

In the continuity of previous results [67], [70], our interest has been specifically focused on the use of 2D PhC micro-resonators/nano-resonators [54], [56]–[58], [66], [73], [226] to enhance the photoluminescence (PL) of s-SWNTs optically pumped at short wavelength (~ 740 nm).

With respect to the state-of-the-art, our approach has been focused on the possible collection of nanotube PL emission in silicon waveguides as a first step towards the integration of s-SWNTs active media in silicon photonics.

Matching the PL nanotube peaks with resonance of slot photonic crystal waveguide cavities was done without strong difficulty as s-SWNTs present various absorption bands in the telecom ranges, *e.g.* photoluminescence peaks around $1.3 \mu\text{m}$, as shown in Fig. 1.2.6. In the same spirit, results of section 3.1.4 have shown that the fabricated slot PhC cavities exhibit resonances in those ranges, specifically at $\lambda = 1.284 \mu\text{m}$, $1.325 \mu\text{m}$, $1.433 \mu\text{m}$, $1.584 \mu\text{m}$ and $1.605 \mu\text{m}$ when infiltrating the top cladding with liquid of refractive index 1.46. For the coupling of SWNTs to slot PhC cavities, we thus first choose the slot PhC cavities with appropriate resonances existing around the emission wavelength of the exploited SWNTs.

We present just hereafter our contribution on the integration of SWNTs and $1.28 \mu\text{m}$ resonance slot PhC cavities. This work was implemented under a collaboration with Ms. Elena Duran, Ph.D. student within our group. We first describe the passive slot photonic crystal waveguide cavity

used for integration with SWNTs in section 3.3.1. Secondly, we present the preparation of SWNTs solution in section 3.3.2, before considering the two parts together in section 3.3.3.

3.3.1 Slot photonic crystal cavity at 1.28 μm resonance

We refer the reader to the description made in section 2.1.3 regarding PhC waveguide heterostructure cavities and recall here only the minimal elements relative to the resonator. The considered cavity possesses an experimental Q -factor of 18 240 at the resonance wavelength of 1284 nm, its mode volume is around $0.024(\lambda/n)^3$. So, its Q/V ratio is approximately 800 000, leading to strong light-matter interaction. Fig. 3.3.1 presents its linear transmission spectrum characterized by using the setup describing in section 3.1.4 (see Fig. 3.1.10).

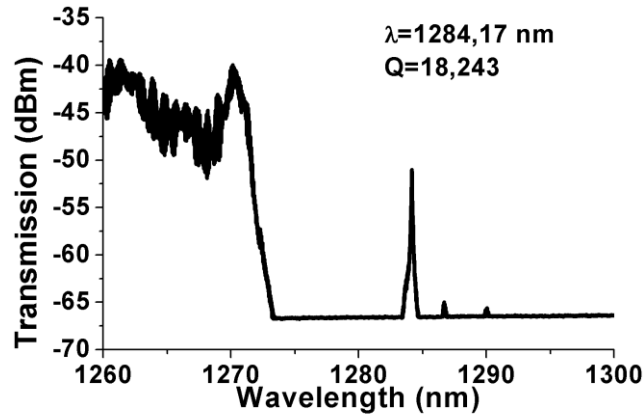


Fig. 3.3.1 Linear transmission spectrum of the slot PhC cavity chosen for the integration of s-SWNTs, having a resonance wavelength of 1.28 μm when filled with a 1.46 refractive index liquid as optical top cladding.

As presented in chapter 2, the slot PhC cavity was designed by the bandgap engineering technique with the PWE and 3D FDTD methods. Numerical simulation showed in fact that the employed cavity presents two confined modes.

Fig. 3.3.2(a)-(b) show the y -component of the electric fields of the two detected resonances, while the Fourier transforms of these E_y components are depicted in Fig. 3.3.3(c)-(d). The leaky regions correspond to the region inside the white circles (with diameter of k_0). It is seen that these FT spectra of two E_y components mainly distribute outside the leaky region. The first mode refers to the cavity mode localized in the photonic bandgap yielded by the bandgap engineering methodology, having a resonance wavelength of 1284.34 nm with a Q -factor of 21 000 and a mode volume of $0.024(\lambda/n)^3$. The second cavity mode predicted by 3D-FDTD simulation has a

resonance at 1271.2 nm, a Q -factor of 6000, and a mode volume of $0.11(\lambda/n)^3$. This mode is located at the limit of the edge of the photonic band and its signature is not clearly visible on the spectrum in transmission recorded experimentally.

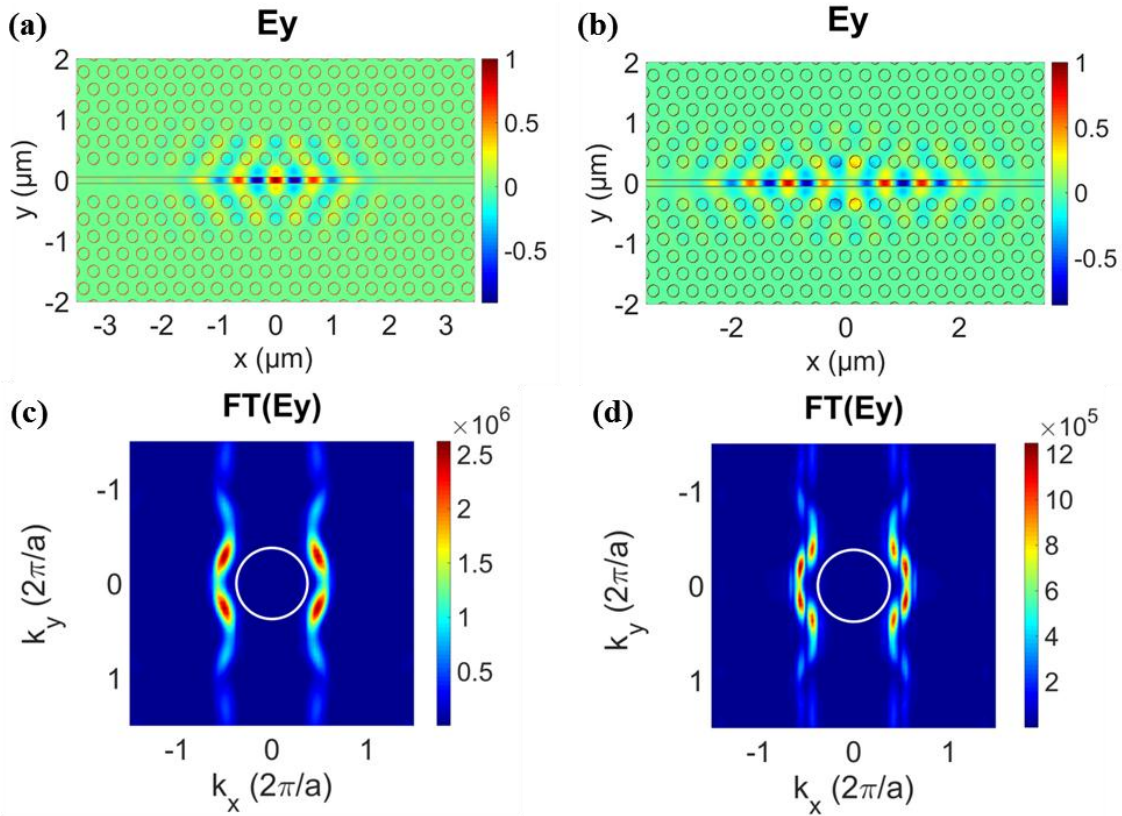


Fig. 3.3.2 E_y component of TE-like polarization cavity resonance modes: (a) First mode: $\lambda_1 = 1284.34$ nm, (b) Second $\lambda_2 = 1271.2$ nm, both obtained by 3D-FDTD simulation, and the corresponding E_y Fourier transforms in wavevector space for the two modes, respectively (c) and (d) with the light-cone as a white circle in each of the two figures.

As seen in Fig. 3.3.2, the first mode is localized in the quantum well between two barriers conducted by the smallest lattice constant while the second one is formed in the transition of the barriers to the two left and right to waveguide regions. In both cases, the field is highly concentrated within the slot region, promoting interaction with the surrounding medium where the SWNTs are placed.

3.3.2 Preparation of single-walled carbon nanotube solutions

Semiconducting single-walled carbon nanotubes (s-SWNTs) were considered for integration purpose on the silicon photonic platform.

The SWNTs solution was prepared to obtain purified s-SWNTs rich media by polymer-assisted selective extraction, as previously described in Ref [66]. The process started from a commercial dry CNTs powder (as-prepared HiPCO, Carbon Nanotechnologies Inc.) consisting of s-SWNTs and several m-SWNTs. This SWNTs powder was mixed with polymer Poly-9,9-di-n-octyl-fluorenyl-2,7-diyl (PFO, Sigma-Aldrich) in toluene in a ratio of SWNT (5 mg): PFO (20 mg): toluene (30 ml) and homogenized by sonication (for 1 h using a water-bath sonicator and 15 min using a tip sonicator). The polymer played the role on the selective dispersion of SWNTs [227] and the high speed sonication step was the main basis of the purification protocol. The raw mixing solutions are shown in Fig. 3.3.3(a). Then this mixture was ultra-centrifugated up to 150 000 g for 1 h.

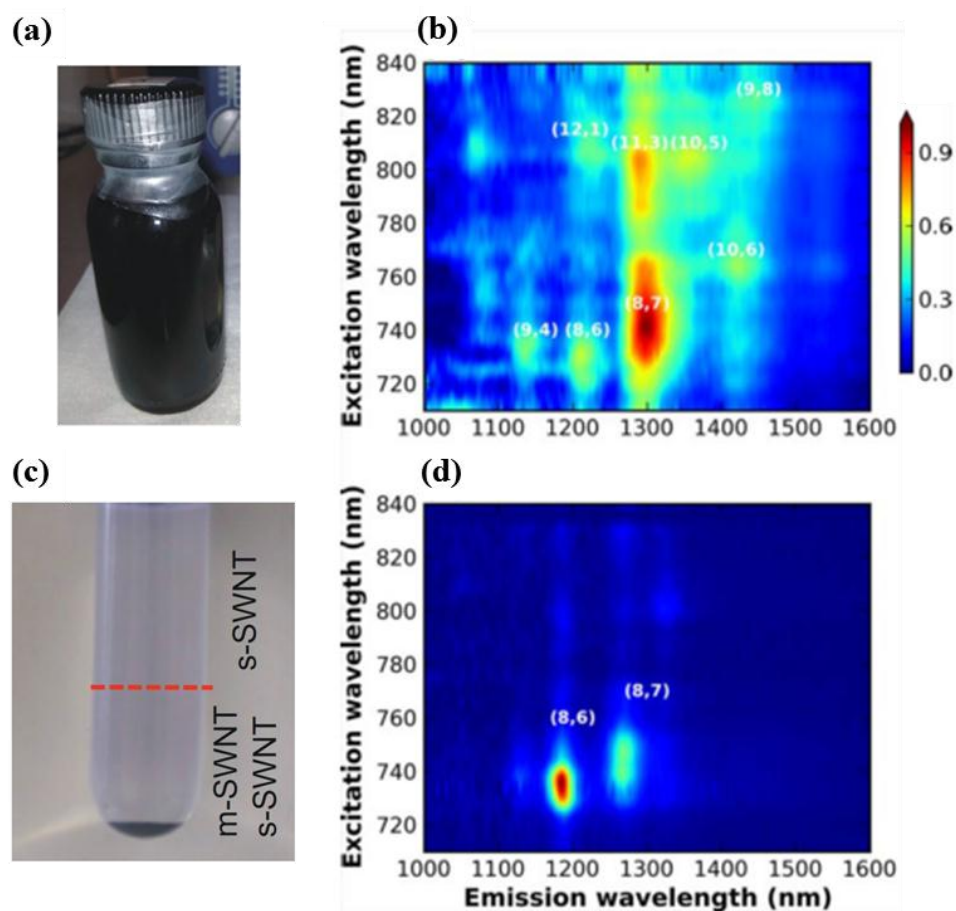


Fig. 3.3.3 Prepared s-SWNT solutions: (a) Before centrifugation and (b) Its PL map (c) After centrifugation and (d) The after centrifugation PL map [66].

This technique yielded a solution composed of polymer-wrapped s-SWNTs and excess polymer, and provided a mean to obtain well isolated PFO wrapped s-SWNTs displaying exploitable

electrical [74], optical [70] and electro-optical [228] properties. We then collected the s-SWNTs solution by taking approximately 80% of supernatant solution as seen in Fig. 3.3.3(c). From a refractive index point of view, this SWNT-enriched polymer layer can be modelled as a homogeneous medium of ~ 1.5 index.

Fig. 3.3.3(b)-(d) show the PL spectra of the raw solution and the purified one that were spin-coated onto glass substrates, respectively, each map being normalized by the maximum intensity. The two solutions were spin-coated several times onto glass substrates at 500 RPM for 60 s to achieve a layer of around 200 nm thickness, then annealed at 150°C for 15 min. The intensity of PL corresponding to (8,6) s-SWNTs of the solution after removal of m-SWNTs displayed a six-fold increase compared with the one before the process [66]. Details about the PL set-up are presented in the up-coming section.

Fig. 3.3.4 shows the absorption spectrum of these purified Polyfluorene-wrapped s-SWNTs in toluene collected by using a 400 nm-2 μm UV/Vis/NIR Spectrometer.

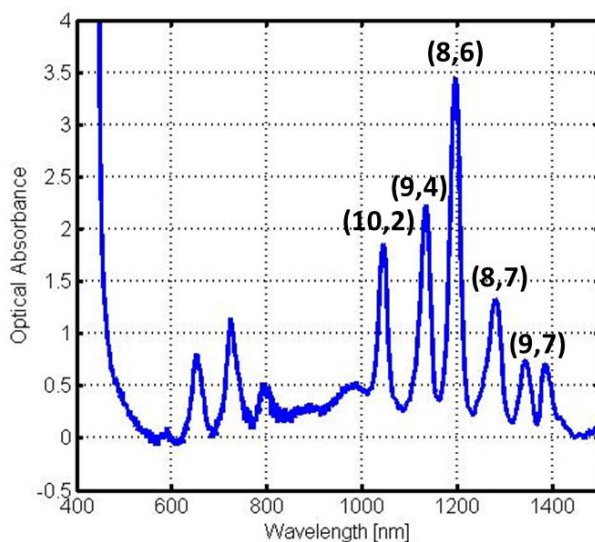


Fig. 3.3.4 Absorption spectrum of the prepared s-SWNTs solution.

The sharp peaks in the wavelength range of 1050-1400 nm (1.18-0.89 eV) and the peaks from 600-900 nm (2.07-1.38 eV) are the optical absorption bands corresponding to the first and second inter-band transitions between Van Hove singularities in the s-SWNT density of states, respectively. Normally, there exists peaks in the range 500-600 nm (2.48–2.07 eV) corresponding to the absorption bands of m-SWNTs [229], as seen in Fig. 3.3.4. The absence of

these peaks in the absorption spectrum is an indirect proof of the preparation method ability of efficiently removing the metallic tubes, as desired. The absorption peaks of different limited set of chiralities, *e.g.* (10,2), (9,4), (8,6), (8,7), (9,7), also proves the quality of our purification process to extract s-SWNTs thin films by the PFO centrifugation technique in which the use of the PFO as a matrix leads to the formation of well-isolated nanotube thin film.

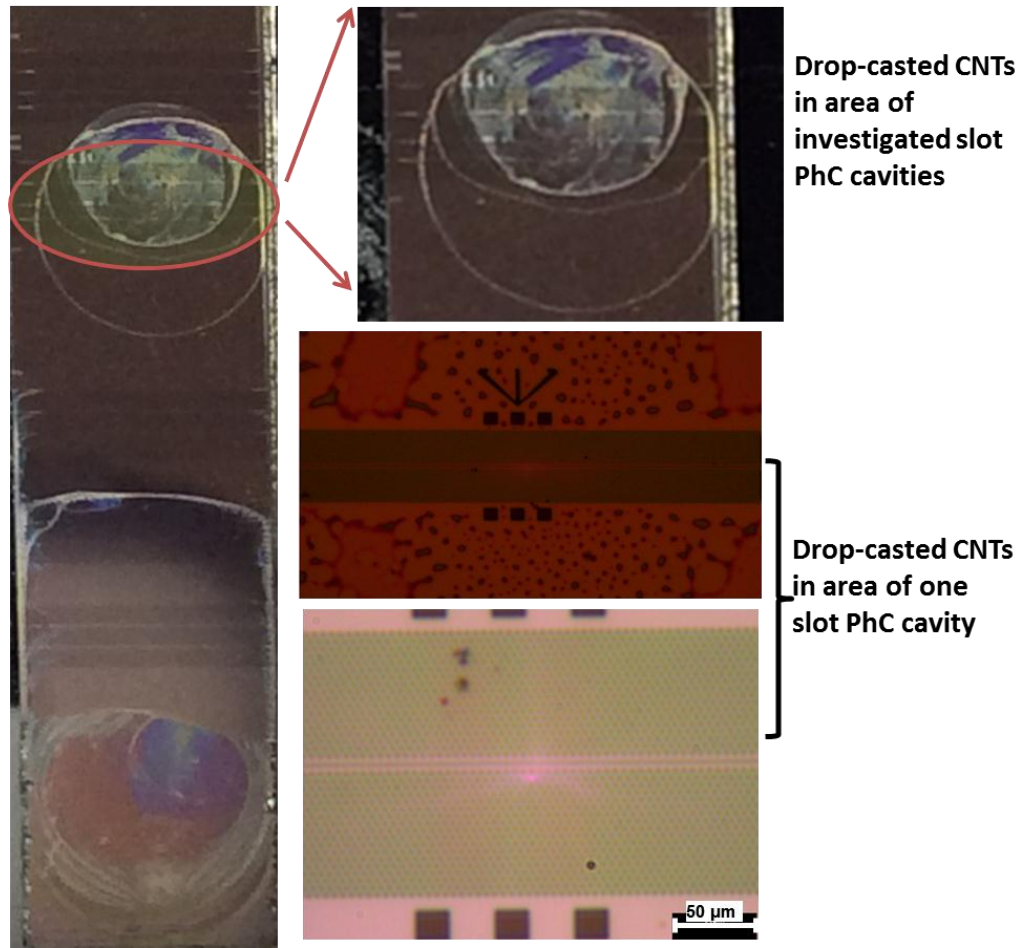


Fig. 3.3.5 Drop-casted prepared SWNTs solution on to the surface of slot PhC cavities. This figure shows the sample after being annealed at 180°C for 15 min.

These prepared s-SWNTs were then drop-casted onto the surface of slot PhC cavities followed by a thermal annealing at 180°C for 15 min to improve the optical quality of SWNTs/PFO layer. Fig. 3.3.5 presents the sample with annealed drop-casted s-SWNTs solution onto the surface of the investigated slot PhC cavities.

The prepared samples were then considered for further study.

3.3.3 Integration of single-walled carbon nanotubes in slot photonic crystal cavities

3.3.3.1 Linear transmission of slot photonic crystal cavity filled with s-SWNTS

In order to evaluate the behavior of the slot PhC cavities after drop-casting of s-SWNTs, we first characterized their linear transmission in two configurations: i) With a top cladding liquid of 1.46 index only, ii) After s-SWNT solution infiltration followed by drop casting the same liquid of 1.46 index to get a nearly symmetrical vertical optical confinement profile. The sample drop-casted with CNTs was characterized using different setup with the setup shown in Fig. 3.1.10. The new setup was adapted to photoluminescence study, as presented later in section 3.3.3.3 (Fig. 3.3.9). The main difference between these two linear characterization setups is that in the former, signal is injected from an optical fiber and collected by an objective while in the current setup the signal is injected from an optical fiber and collected by an optical fiber. The related results are shown in Fig. 3.3.6.

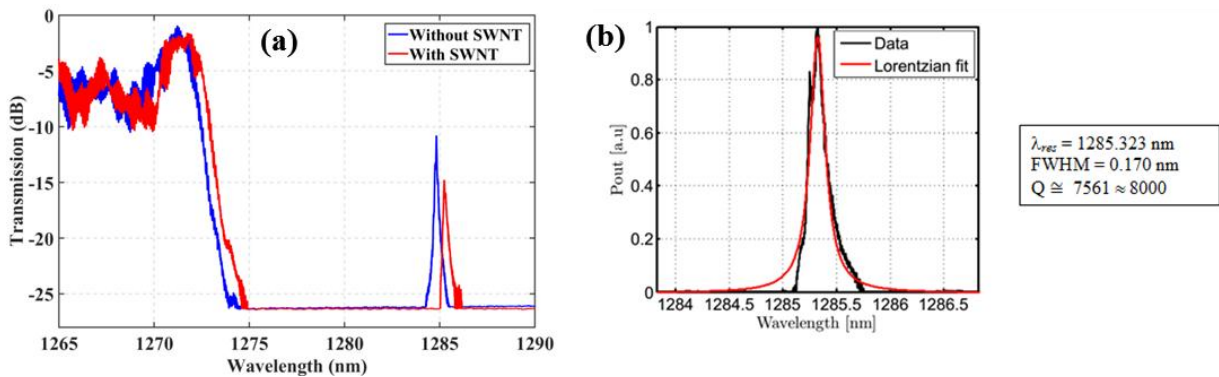


Fig. 3.3.6(a) Transmission spectra of slot PhC heterostructure cavity without SWNT drop-cast (blue curve) and with SWNT drop cast (red curve) **(b)** Lorentzian fitting of the transmission curve in case of drop-casting s-SWNTs and top cladding liquid configuration.

Due to absorption of deposited s-SWNTs, the resonance transmission level is reduced in excess of 5 dB and the quality factor of the fundamental cavity mode (estimated from the Lorentzian fit of the resonance at 1285 nm wavelength) falls from $Q \approx 18\,000$ to $Q = 8\,000$ as shown in Fig. 3.3.6(b). Moreover, a red-shift of the cavity resonance is visible on the transmission curve due to the difference between the refractive index of the employed top cladding Cargille liquid (~ 1.46) and the combined medium made of the thin SWNTs rich layer ($n \sim 1.50$) and refractive index liquid.

3.3.3.2 Time of Flight measurement

In order to study the photon delay time in the cavity we used an external interferometer inspired by the Optical Coherence Tomography (OCT) technique, which allowed to measure the time-frequency transmittance using a partially coherent source that enabled to extract quantities such as the complex frequency-dependence reflectance or the group velocity from fringes analysis [230]–[233]. This measurement was done by Samuel Serna, Ph.D. student within our research group. The set-up was mounted by Dr. Pierre Colman and calibrated for PhC structures by Samuel Serna. The simplified scheme of this setup is depicted in Fig. 3.3.7 [234].

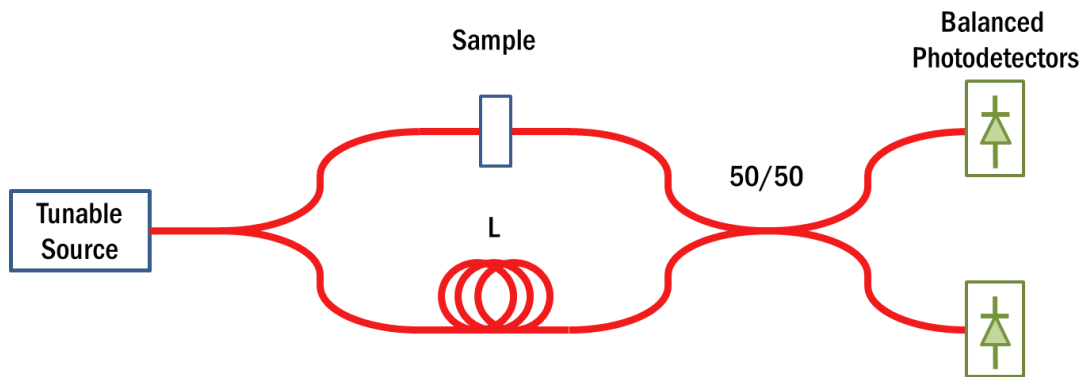


Fig. 3.3.7 Interferometric set-up to measure the transmittance maps [234].

It consists in placing the slot PhC cavity WG in one arm of a Mach-Zehnder interferometer (MZI). The set-up uses a tunable laser to sweep the input wavelength and two counter-balanced photodiodes to record the resulting interferometric pattern. Additionally to the group index, the measurement gives access to the distribution of energy at different arrival time, which is for example useful to study propagation losses introduced by disorder [230]. After the analysis of the interference fringes, the relative photon delay time can be inspected. As in other interferometric techniques, the larger phase difference between the two arms eases the interpretation of the output pattern. In our case, longer structures increase the delay time, typically in the order of ps . Also, there should be a large transmission intensity level in order to collect enough photons at distinguishable time-wavelength. In our case, the studied core PhC length was around $50\ \mu m$ while the total chip length was $5\ mm$.

The carried-out time of flight measurement result is shown in Fig. 3.3.8. As visible, two regions of photon signatures close to $\lambda \approx 1272\ nm$ and $\lambda \approx 1285\ nm$, respectively, can be identified. They

correspond to the two cavity modes predicted by 3D-FDTD simulation (see section 3.3.1). We observe that the time of flight of photon is around 80 ps, which corresponds to a light group index of around 480. Although this group index mode estimation is not relevant for purely confined cavity modes, this result is a confirmation by the time-of-flight method that the investigated structure presents optical modes with long photon lifetimes and large densities of states. Furthermore, the intensity of energy distribution of photon in the region in which wavelength is smaller than 1273 nm is larger than in the localized cavity mode region, which is in agreement with the -15 dB difference in these two regions, as observed from the linear transmission curve shown in Fig. 3.3.6(a).

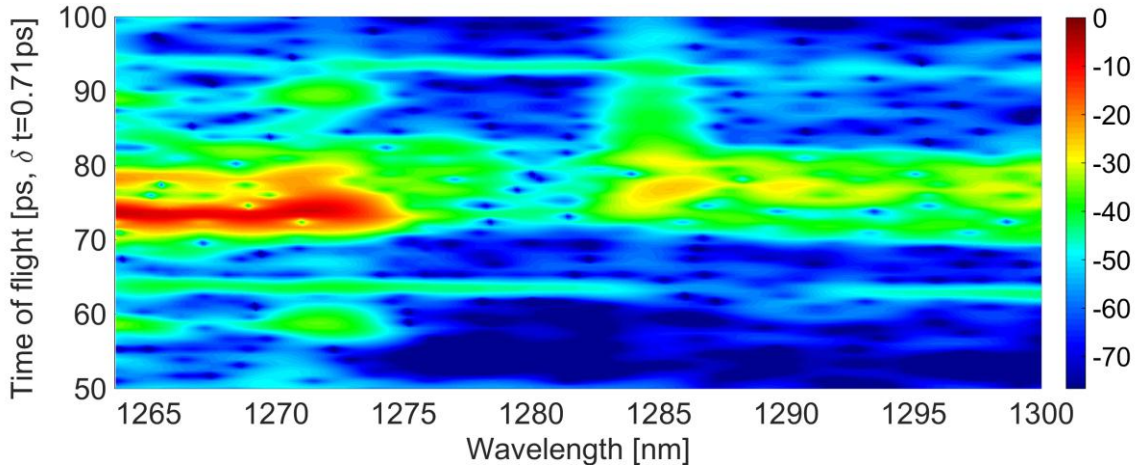


Fig. 3.3.8 Group delay map measurement spectrogram of the investigated slot PhC waveguide cavity.

As the SWNTs showed photoluminescence emission at around $\lambda \approx 1.28 \mu\text{m}$, corresponding to the s-SWNT of chirality (8,7), we then carried out complementary experiments to verify the ability of integration SWNT photoluminescence emission in slot PhC cavities at resonance wavelength of $1.28 \mu\text{m}$.

3.3.3.3 Photoluminescence set-up

We collected the photoluminescence spectra using the set-up depicted in Fig. 3.3.9. Because Si absorption wavelength edge is around $\lambda = 1.1 \mu\text{m}$, the direct excitation of the prepared s-SWNTs using input silicon bus waveguides was not possible. Hence, characterization was carried out in two steps.

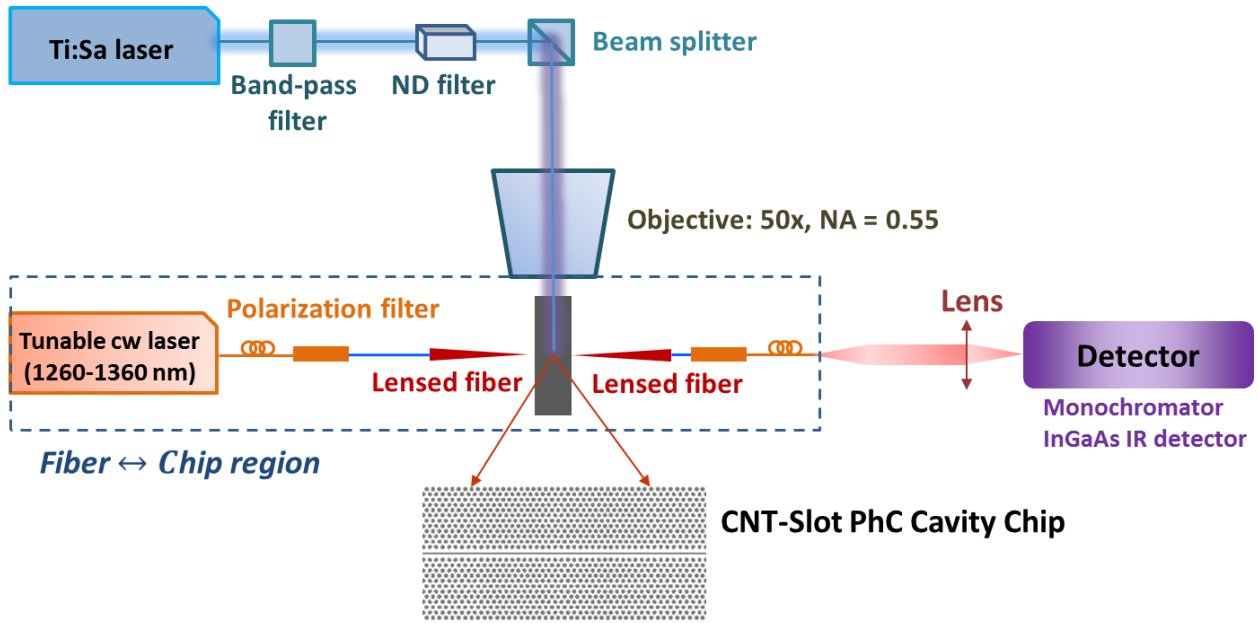


Fig. 3.3.9 PL measurement set-up to characterize PL enhancement of s-SWNT integrated in slot PhC waveguide cavities.

The continuous laser source visible in Fig. 3.3.9 used to collect the device direct transmission was switched off, and another Ti:Sapphire external CW laser source was used to pump the structures vertically. The incident signal was focused onto the sample through a 50x zoom microscope objective lens having a numerical aperture of 0.55, while the diameter of beam size was around $6 \mu\text{m}$ [235]. A low-pass wavelength filter was positioned after the Ti:Sapphire laser source in order to remove higher order harmonics of the laser before reaching the microscope objective and a neutral-density (ND) filter was used to adjust the power before reaching the sample. The collected signal from the output waveguide edge facet was then sent to polarization filters, rotators, high-pass wavelength filters in order to remove the excitation beam and finally penetrated into a nitrogen-cooled InGaAs photodetector array to extract the PL spectra. PL spectra were recorded with a 320 mm spectrometer with a 950 lines/mm grating, using a nitrogen-cooled 512-pixel linear InGaAs array. All measurements were carried out in air at room temperature.

3.3.3.4 Photoluminescence spectra

As mentioned above, after preparing the SWNTs solution, we drop-casted it onto the slot PhC cavity and annealed the device at 180°C in 15 min. Then the sample was ready for

characterization. We then illuminated the chip surface with the excitation beam, shown in Fig. 3.3.10.

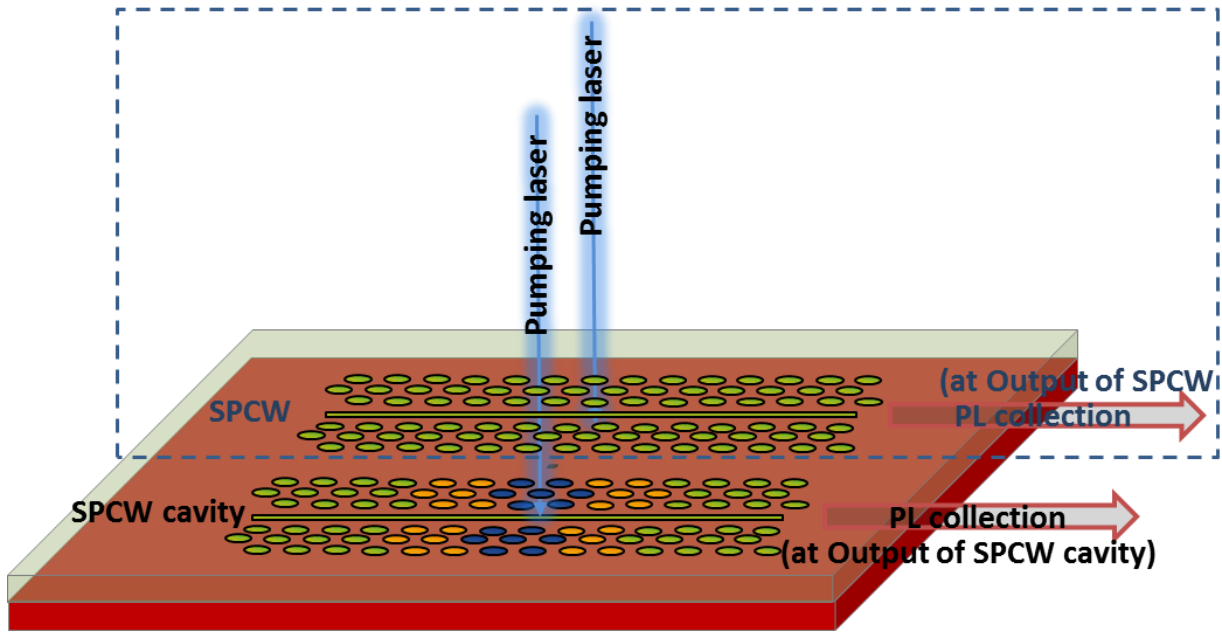


Fig. 3.3.10 Illustration of different pumping positions onto the surface of the sample, *i.e.* at location of a slot PhC waveguide or of a slot PhC waveguide cavity (in order to simplify the drawing, the light injection/collection systems made up of several waveguide tapers are not shown).

As seen in Fig. 3.3.3(d), the PL peak of s-SWNT around $1.28 \mu\text{m}$ came from an excitation wavelength around $\lambda = 735 \text{ nm}$. Hence, we decided to first pump the device with a laser wavelength of 735 nm . After trials with different powers ranging from 0.2 mW to 3 mW , the laser power level was finally set at 2.6 mW to efficiently excite the cavity.

Fig. 3.3.11 shows the obtained experimental result. We observe two sharp PL peaks corresponding to the generated SWNT PL coupled to the first and second order cavity modes, respectively. Moreover, the two peaks are well positioned with respect to the previously reported simulation results and the delay map measurements, respectively. As visible, the cavity mode PL peak at $\lambda = 1284.8 \text{ nm}$ exhibits a much narrower *FWHM* ($\Delta\lambda_1 = 0.3 \text{ nm}$) than the second order mode *FWHM* ($\Delta\lambda_2 = 2.3 \text{ nm}$). The related effective *Q* factors extracted from PL measurements are $Q_{1PL} \approx 4280$ and $Q_{2PL} \approx 550$, respectively. Although these values are smaller than the ones predicted by simulation probably due to the convolution of the employed setup with the sample intrinsic response, we notice that the two quality factors deduced from PL measurements are correctly ordered each one with respect to the other one, *i.e.* that $Q_1 > Q_2$. These results bring

confirmation of the tight relation between the mode quality factors and the bandwidth of the PL enhancement.

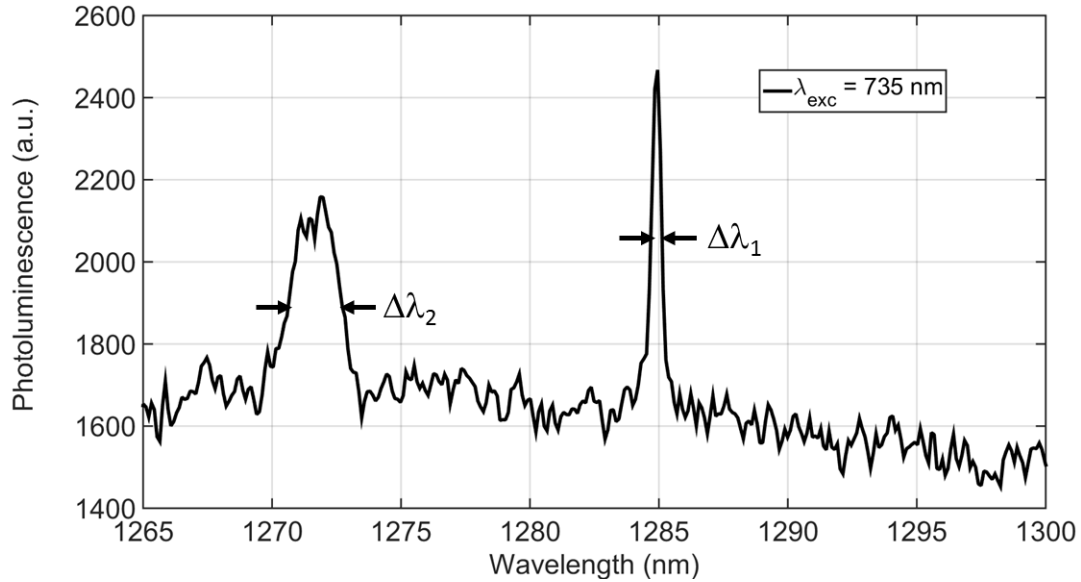


Fig. 3.3.11 PL spectrum of the slot PhC waveguide cavity filled with s-SWNTs and a 1.46 refractive index liquid (laser pumping wavelength $\lambda_{exc} = 735$ nm).

Interestingly, despite the fact that the micro-cavity spectrum had a lower linear transmission level (close to 12 dB attenuation difference) at $\lambda = 1285$ nm compared with that the recorded level at $\lambda = 1272$ nm (see Fig. 3.3.6), the intensity of PL peak response at $\lambda = 1285$ nm is higher by a factor of 1.15 than the PL peak recorded at $\lambda = 1272$ nm. This behavior suggests a substantially larger PL enhancement for the fundamental cavity mode if compared with the second order one of around 12-13 dB.

We also pumped the device by laser source at 770 nm, resulting in a non-resonant excitation of SWNTs, as shown in Fig. 3.3.12. It is seen that the back-ground noise of the PL measurements can be identified by this approach. In addition, we observe no significant difference when comparing the response with that recorded for a 735 nm pumping wavelength focused onto the SPCW only, *i.e.* far from the cavity itself (*e.g.* depicted in Fig. 3.3.10). This indicates that almost no generated PL was then coupled into the output waveguide. Therefore, we can conclude that resonant interactions in the slot PhC cavity play a key role in the process of coupling s-SWNT PL into the photonic waveguides.

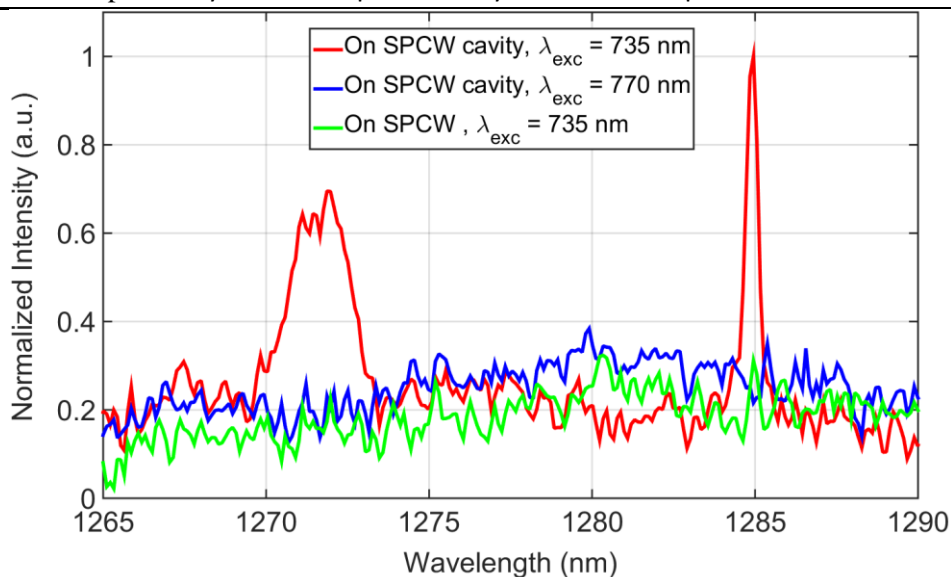


Fig. 3.3.12 PL responses when pumping on top of the slot PhC waveguide cavity at 735 nm (resonant SWNT excitation)—the red curve, 770 nm (non-resonant SWNT excitation)—the blue curve, and on top of the slot PhC waveguide at 735 nm—the green curve, different pumping locations are illustrated in Fig. 3.3.10.

We finally performed a PL excitation spectroscopy characterization, presented in Fig. 3.3.13, in which the pumping laser was swept from 710 nm to 770 nm. The PL map confirms that the two PL resonance-enhancement regions originate from the emission of s-SWNTs with (8,7) chirality, that were selected with the polymer-sorting technique, as discussed in section 3.3.2.

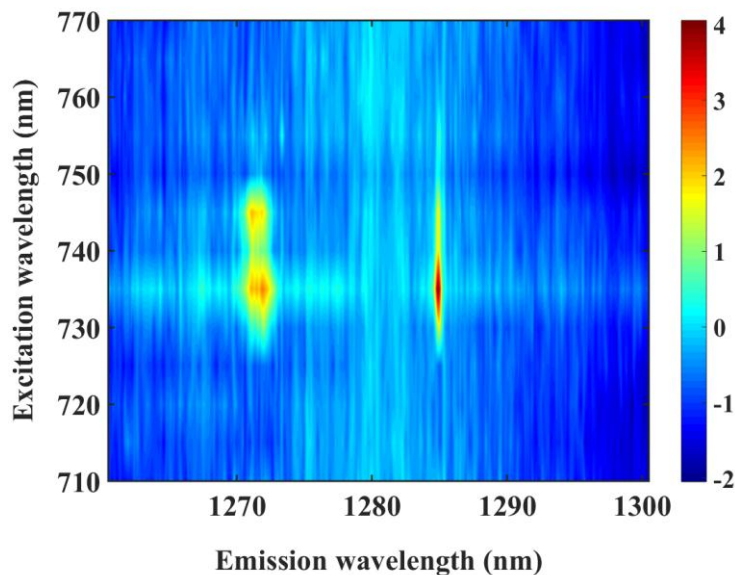


Fig. 3.3.13 PL spectra map collected by sweeping the wavelength of the pumping laser from 710 nm to 770 nm, the most efficient pumping wavelength is 735 nm for chirality (8,7) s-SWNTs.

3.3.4 Conclusion of section 3.3

To sum up, we succeeded in integrating carbon nanotubes in a slot PhC heterostructure cavity presenting a resonance at around $\lambda = 1.28 \mu\text{m}$. The interaction between sorted s-SWNTs and cavity modes resulted in enhanced PL collection. It was observed that the fundamental cavity mode photon recycling effect was strong enough to compensate a ~ 12 dB attenuation with respect to the second order cavity mode, finally bringing similar PL peaks in both cases (ratio of ~ 1.25).

Besides the quality of the purified s-SWNTs by polymer-assisted selective extraction process, these enhancements may result from the fact that carbon nanotubes interact primarily with light polarized along their axis [236] and that part of the nanotube distribution may spread onto or close to the slot PhC cavities, dominated by strongly confined TE-polarized modes.

With respect to previous works, preceding studies reported the PL coupling from individual CNT emitters grown directly on the PhC nanobeam cavities [57], [56], but optical pumping and collection of PL were both achieved in the vertical direction while in our study, PL collection was made from output silicon waveguide as a first assessment of the possible use of CNTs in planar integrated photonics. Additionally, this integration scheme takes advantage of a technique for separating nanotubes which makes it possible to select the semiconducting tubes making the entire integration process more efficient for the realization of on-chip active integrated functions [57].

3.4 Conclusion of chapter 3

In this chapter, we first presented the fabrication and characterization processes of a series of SOI slot PhC heterostructure cavities with resonances in the telecom wavelength range from $1.28 \mu\text{m}$ to $1.6 \mu\text{m}$, showing quality factors of several tens of thousands, *i.e.* from 18 000 to 31 000 and mode volume V of $\sim 0.03(\lambda/n)^3$ after being infiltrated with a liquid of 1.46 refractive index. This mechanically-robust approach relies on slot PhC cavities possessing Q/V ratio larger than 600 000, and reaching 1 000 000 in the best case (at $\lambda \approx 1.3 \mu\text{m}$), being thus candidates for sensing and basic integrated building blocks for the hybrid integration of active materials on silicon.

Slot PhC cavities have been further investigated in the perspective of index sensing by using different liquids with refractive index values ranging from 1.345 to 1.545. The investigated PhC resonators have shown quality factors of several tens of thousands with sensitivities of ~ 235 nm/RIU and index sensing *FOM* around 3700. These results have shown the potential of high-*Q*-factor SOI slot PhC cavities for index sensing.

Finally, photoluminescence (PL) emitting properties of s-SWNTs integrated in thin films deposited on top of silicon slot PhC waveguide resonators have been studied. Resonators matching the absorption peak resonances of nanotubes have been chosen, *e.g.* at $\lambda = 1.28$ μm in the studied case. The reported results provide an experimental demonstration of PL collection from a slotted resonators into millimeter long integrated silicon waveguides, for further collection of the nanotubes emission, providing a first proof-of-concept step towards nanotube/Si-PhC integration as an active photonic platform. The reported works bring a contribution to the feasibility of integrating telecommunication wavelength nanotube emitters in silicon photonics.

These results also emphasize the role of slot PhC cavities for on-chip hybrid integration.

Conclusion and perspectives

This manuscript presents our contribution to the modeling, experimental study of slot photonic crystal cavities for hybrid on-silicon integration. We have used plane wave expansion and finite-difference time-domain calculations to design a series of mechanically robust (non-free membrane) SOI slot photonic crystal heterostructure cavities with resonance wavelength in the telecommunication range, *i.e.* from 1.3 μm –1.6 μm , with Q -factors of around several tens of thousands and mode volumes around $0.03(\lambda/n)^3$ after being infiltrated by cladding materials with typical index values around 1.5.

We have analytically and numerically studied the coupling between a slot photonic crystal cavity and a slot photonic crystal waveguide by using the coupled mode theory and FDTD simulation. The cavity build-up factor was estimated and confirmed the ability to excite the cavity slot modes from an external waveguide was considered by using FDTD simulation.

As a preliminary step towards the use of several coupled slotted cavities for future hybrid integration schemes, we have numerically and semi-analytically investigated two coupled slot photonic crystal cavities providing two different supermodes (bonding and antibonding ones) with controllable wavelength splitting. We successfully employed the tight-binding (TB) approach, which relies on the overlap of the two tightly confined cavity electric fields, to predict the supermodes frequencies and spatial distributions in several coupled slot photonic crystal cavity configurations.

This exploratory work was supplemented by an **experimental part, which focused on a family of slot photonic crystal heterostructure cavities.** The fabricated silicon on insulator hollow core cavities showed quality factors of several tens of thousands, *i.e.* from 18 000 to 31 000 and mode volume V of $\sim 0.03(\lambda/n)^3$ after being infiltrated with liquids of ~ 1.46 refractive index, yielding Q/V ratio larger than 600 000, and reaching 1 000 000 in the best case (at $\lambda \approx 1.3 \mu\text{m}$).

This preliminary experimental stage gave rise to two types of additional developments. Firstly, the properties of the studied slot photonic crystal cavities have been investigated for **index**

sensing applications by using different liquids with refractive index values ranging from 1.345 to 1.545. The considered photonic crystal resonators have demonstrated quality factors of several tens of thousands with sensitivities of ~ 235 nm/RIU and index sensing *FOMs* around 3700, *i.e.* at the state of the art considering hollow core silicon integrated resonators.

Secondly, in the view of the integration of active materials on silicon, the **potential of these hollow core nanoresonators to enhance the photo-luminescence (PL) of semiconductor single-walled carbon nanotubes (SWNTs)** integrated in thin films deposited on top of silicon has been explored. We have brought the first experimental demonstration of SWNTs PL collection (at $\lambda \sim 1.28$ μm) under vertical pumping at short wavelength (~ 740 nm) from a slotted resonator into millimeter long integrated silicon waveguides, providing a first proof-of-concept step towards nanotube/Si-PhC integration as an active photonic platform. The reported works demonstrate the feasibility of integrating telecommunication wavelength nanotube emitters in silicon photonics and emphasize the role of slot photonic crystal cavities for on-chip hybrid integration.

This work opens prospective researches. In the short term regarding to light emission using s-SWNTs, complementary experimental works could be achieved to characterize the use of other kinds of s-SWNTs with different chiralities. A deal of work also would remain to be done to further quantify the s-SWNTs photoluminescence collection efficiency as a function of the position of the nanotubes and their orientation at the surface of the vicinity of the slot photonic crystal cavities. Finally, a specific task would have to be carried out to evaluate the possibility of electrical pumping of carbon nanotubes.

In another direction, the developed slotted cavities could also be used for the integration of other types of active materials, among which are, for example, colloidal quantum dots, whose recent developments in integrated photonics have been rapid, or nonlinear third-order optical materials (*e.g.* polymers).

About the coupled slot photonic crystal cavities, we could expand the studies from two cavities as carried out in this work to three or multiple coupled slot photonic crystal cavities in view of exploiting multicavity modes.

APPENDIX A

Coupled slot photonic crystal cavity and slot photonic crystal waveguide by the time-domain coupled mode theory (CMT)

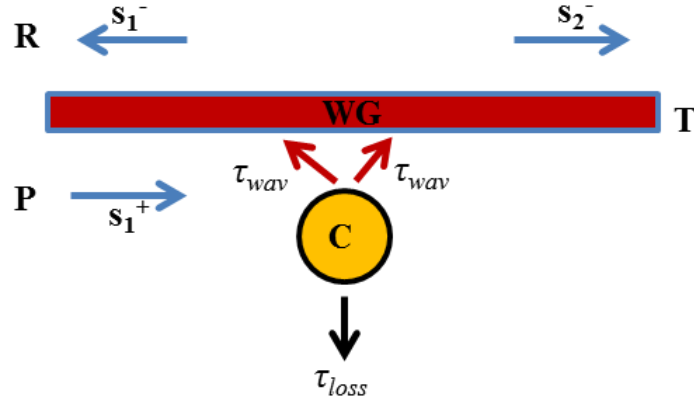


Fig. 2A.1 Scheme of a coupled photonic crystal waveguide (“WG”) and photonic crystal cavity (“C”).

Fig. 2A.1 illustrates the scheme of a resonant cavity coupled to a waveguide. The cavity has a resonance frequency ω_0 and decays with lifetimes τ_{wav} into the two sides of waveguide and τ_{loss} to the loss channel side.

The coupled mode theory is based on the following assumptions: weak coupling, linearity, time-invariance (*i.e.* the materials/ geometry do not change over time), conservation of energy [103]. The complex amplitude of the cavity mode is A and we use the normalized unit that $|A|^2$ is the electromagnetic energy stored in the cavity. The fields in the waveguide are expressed as the sum of the incoming and outgoing waveguide modes using the following amplitudes: s_1^+ denotes the amplitude of incident wave towards the cavity, s_1^- denotes the reflected wave away from the cavity and s_2^- denotes transmitted wave to the output of the waveguide. Accordingly, $|s_1^+|^2$, $|s_1^-|^2$ and $|s_2^-|^2$ represent the incoming to cavity, reflecting and outgoing powers to/from the waveguide. Overall, the cavity has three loss mechanisms, with decay constants τ_{wav} (left), τ_{wav} (right) and

τ_{loss} and the net lifetime is given by $\frac{1}{\tau} = \frac{2}{\tau_{wav}} + \frac{1}{\tau_{loss}}$. The amplitude A satisfies the differential equation:

$$\frac{dA}{dt} = -i\omega_0 A - \frac{A}{\tau} \quad (2.2.1)$$

So the solution is:

$$A = A_0 e^{-i\omega_0 t - \frac{t}{\tau}} \quad (2.2.2)$$

As the cavity is coupled to the waveguide, input energy from s_1^+ can couple into the cavity so the equation (2.2.1) becomes:

$$-i\omega A = -i\omega_0 A - 2\frac{A}{\tau_{wav}} - \frac{A}{\tau_{loss}} + \sqrt{\frac{2}{\tau_{wav}}} s_1^+ \quad (2.2.3)$$

$$\Rightarrow \sqrt{\frac{2}{\tau_{wav}}} s_1^+ = -i(\omega - \omega_0) A + 2\frac{A}{\tau_{wav}} + \frac{A}{\tau_{loss}}$$

$$s_1^+ = \sqrt{\frac{\tau_{wav}}{2}} \left[-i(\omega - \omega_0) A + 2\frac{A}{\tau_{wav}} + \frac{A}{\tau_{loss}} \right] \quad (2.2.3)$$

However, the energy from the cavity must also flow into s_1^- , and s_2^- :

$$s_1^- = \sqrt{\frac{\tau_{wav}}{2}} A \quad (2.2.4)$$

$$s_2^- = \sqrt{\frac{\tau_{wav}}{2}} A - s_1^+ \quad (2.2.6)$$

Replacing (2.2.3) to (2.2.6) gives:

$$\begin{aligned} s_2^- &= \sqrt{\frac{2}{\tau_{wav}}} A - \sqrt{\frac{2}{\tau_{wav}}} \left[-i(\omega - \omega_0) A + \frac{A}{\tau_{wav}} + \frac{A}{\tau_{loss}} \right] \\ &= \sqrt{\frac{2}{\tau_{wav}}} A \left[1 + i(\omega - \omega_0) - \left(\frac{2}{\tau_{wav}} + \frac{1}{\tau_{loss}} \right) \right] \end{aligned} \quad (2.2.7)$$

Then the transmittance can be expressed as:

$$t = \frac{s_2^-}{s_1^+} = \sqrt{\frac{2}{\tau_{wav}}} \frac{A}{s_1^+} - 1 \quad (2.2.8)$$

Combining equations (2.2.7) and (2.2.8) we obtain:

$$\frac{A}{s_1^+} = \sqrt{\frac{2}{\tau_{wav}}} \frac{1}{-i(\omega - \omega_0) + \left(\frac{2}{\tau_{wav}} + \frac{1}{\tau_{loss}} \right)} \quad (2.2.9)$$

So the transmittance can be written as:

$$\begin{aligned} t(\omega) &= \frac{s_2^-}{s_1^+} = \sqrt{\frac{2}{\tau_{wav}}} \frac{A}{s_1^+} - 1 = \sqrt{\frac{2}{\tau_{wav}}} \sqrt{\frac{2}{\tau_{wav}}} \frac{1}{-i(\omega - \omega_0) + \left[\frac{2}{\tau_{wav}} + \frac{1}{\tau_{loss}} \right]} - 1 = \\ &= \sqrt{\frac{2}{\tau_{wav}}} \frac{1}{-i(\omega - \omega_0) + \left[\frac{2}{\tau_{wav}} + \frac{1}{\tau_{loss}} \right]} - 1 = \frac{\frac{2}{\tau_{wav}} + i(\omega - \omega_0) - \left[\frac{2}{\tau_{wav}} + \frac{1}{\tau_{loss}} \right]}{-i(\omega - \omega_0) + \left[\frac{2}{\tau_{wav}} + \frac{1}{\tau_{loss}} \right]} = \\ &= \frac{i(\omega - \omega_0) - \frac{1}{\tau_{loss}}}{-i(\omega - \omega_0) + \left[\frac{2}{\tau_{wav}} + \frac{1}{\tau_{loss}} \right]} = \frac{\frac{-2}{\omega_0 \tau_{loss}} + \frac{2i(\omega - \omega_0)}{\omega_0}}{\left[\frac{4}{\omega_0 \tau_{wav}} + \frac{2}{\omega_0 \tau_{loss}} \right] - \frac{2i(\omega - \omega_0)}{\omega_0}} \end{aligned}$$

Finally, the transmittance can be rearranged as:

$$t(\omega) = \frac{\frac{-1}{Q_{loss}} + 2i \frac{(\omega - \omega_0)}{\omega_0}}{\left(\frac{2}{Q_{wav}} + \frac{1}{Q_{loss}} \right) - 2i \frac{(\omega - \omega_0)}{\omega_0}} \quad (2.2.10)$$

In which Q_{loss} and Q_{wav} are the Q -factor of the cavity alone and of the cavity in case of coupled with waveguide.

The power transmission spectrum is thus:

$$T(\omega) = |t(\omega)|^2 = \left(\frac{\frac{-1}{Q_{loss}} + \frac{2i(\omega - \omega_0)}{\omega_0}}{\left(\frac{2}{Q_{wav}} + \frac{1}{Q_{loss}}\right) - \frac{2i(\omega - \omega_0)}{\omega_0}} \right) \left(\frac{\frac{-1}{Q_{loss}} - \frac{2i(\omega - \omega_0)}{\omega_0}}{\left(\frac{2}{Q_{wav}} + \frac{1}{Q_{loss}}\right) + \frac{2i(\omega - \omega_0)}{\omega_0}} \right) = \quad (2.2.11)$$

$$= \frac{1}{Q_{loss}^2} + \frac{4(\omega - \omega_0)^2}{\omega_0^2} \bigg/ \left(\frac{2}{Q_{wav}} + \frac{1}{Q_{loss}} \right)^2 + \frac{4(\omega - \omega_0)^2}{\omega_0^2}$$

In different coupling configurations between the cavity and waveguide, the behaviors of transmission as a function of wavelength are presented in Fig. 2A.2.

- For the type of **under coupling**, *i.e.* $Q_{wav} \gg 2Q_{loss}$, then $T \approx 1$ as shown in Fig. 2A.2(a). In this case, the cavity mode is not strongly excited.
- While in case of **over coupling**, *i.e.* $Q_{wav} \ll 2Q_{loss}$; T at resonance can reach to 0, meaning that no power is present at the output of the waveguide, as seen in Fig. 2A.2(c).
- In the coupling configuration satisfying $Q_{wav} = 2Q_{loss}$, the transmission at the output of waveguide at resonance is 0.25 and the cavity mode is excited properly, this configuration is called **critical coupling** (Fig. 2A.2(b)).

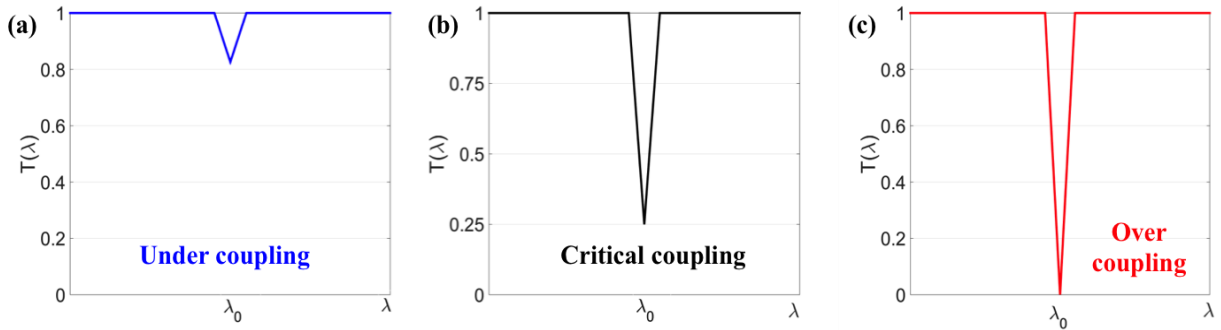


Fig. 2A.2 Transmission of the waveguide in coupled waveguide-cavity as a function of wavelength in different coupling configurations (a) Under coupling (b) Critical coupling and (c) Over coupling.

From equation 2.2.11, the transmission spectrum at resonance is:

$$T(\omega_0) = \frac{1}{\left(1 + \frac{2Q_{loss}}{Q_{wav}}\right)^2} \quad (2.2.12)$$

Hence the transmission at resonance as a function of $(Q_{wav}/2Q_{loss})$ is depicted in Fig. 2A.3, which shows that the case of critical coupling in which $Q_{wav}/2Q_{loss} = 1$ corresponds to $T(\omega_0) = 0.25$.

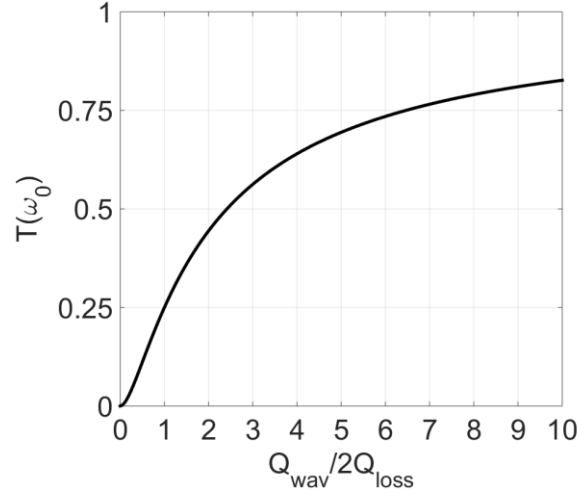


Fig. 2A.3 Transmission at resonance as a function of $(Q_{wav}/2Q_{loss})$.

On its side, the reflectance is:

$$\begin{aligned}
 r(\omega) &= \frac{s_1^-}{s_1^+} = \sqrt{\frac{2}{\tau_{wav}}} \frac{A}{s_1^+} = \sqrt{\frac{2}{\tau_{wav}}} \sqrt{\frac{2}{\tau_{wav}}} \frac{1}{-i(\omega - \omega_0) + \left[\frac{2}{\tau_{wav}} + \frac{1}{\tau_{loss}} \right]} = \\
 &= \frac{2}{\tau_{wav}} \frac{1}{-i(\omega - \omega_0) + \left[\frac{2}{\tau_{wav}} + \frac{1}{\tau_{loss}} \right]}
 \end{aligned} \tag{2.2.13}$$

Similarly to the transmittance, the reflectance can be expressed as:

$$\begin{aligned}
 r(\omega) &= \frac{2 \cdot \frac{2}{\tau_{wav} \cdot \omega_0}}{-i \frac{2(\omega - \omega_0)}{\omega_0} + \left[\frac{2}{\tau_{wav}} \cdot \frac{2}{\omega_0} + \frac{2}{\tau_{loss} \cdot \omega_0} \right]} \\
 r(\omega) &= \frac{2}{-2i \frac{\omega - \omega_0}{\omega_0} + \left(\frac{2}{Q_{wav}} + \frac{1}{Q_{loss}} \right)}
 \end{aligned} \tag{2.2.14}$$

And at resonance:

$$r(\omega_0) = \frac{\frac{2}{Q_{wav}}}{\frac{2}{Q_{wav}} + \frac{1}{Q_{loss}}} = \frac{2Q_{loss}}{2Q_{loss} + Q_{wav}} = \frac{1}{1 + \frac{Q_{wav}}{2Q_{loss}}}$$

$$r(\omega_0) = \frac{1}{1 + \frac{Q_{wav}}{2Q_{loss}}} \quad (2.2.15)$$

The power reflection spectrum at resonance is thus:

$$R(\omega_0) = |r(\omega_0)|^2 = \frac{1}{\left(1 + \frac{Q_{wav}}{2Q_{loss}}\right)^2} \quad (2.2.16)$$

The total of transmission and reflection spectrum at resonance is:

$$T(\omega_0) + R(\omega_0) = \frac{1}{\left(1 + \frac{2Q_{loss}}{Q_{wav}}\right)^2} + \frac{1}{\left(1 + \frac{Q_{wav}}{2Q_{loss}}\right)^2} =$$

$$= \frac{Q_{wav}^2 + 4Q_{loss}^2}{(Q_{wav} + 2Q_{loss})^2} < 1 \quad (2.2.17)$$

Hence we can estimate the loss in this coupling system at resonance as:

$$L(\omega_0) = 1 - [T(\omega_0) + R(\omega_0)] =$$

$$= \frac{4Q_{wav}Q_{loss}}{(Q_{wav} + 2Q_{loss})^2} \quad (2.2.18)$$

The build-up factor which is defined as the ratio of the energy of the cavity mode and the incoming power of the waveguide, presents how long the interaction between the cavity and the waveguide is:

$$F = \frac{|A|^2}{|s_1^+|^2} \quad (2.2.19)$$

Combining the equations (2.2.9) to (2.2.19) it reads:

$$\begin{aligned}
 F(\omega) &= \frac{2}{\tau_{wav}} \frac{1}{\left[-i(\omega - \omega_0) + \left(\frac{2}{\tau_{wav}} + \frac{1}{\tau_{loss}} \right) \right]^2} = \\
 &= \frac{2.4}{\tau_{wav} \omega_0^2} \frac{1}{\left[\frac{-2i(\omega - \omega_0)}{\omega_0} + \left(\frac{2.2}{\tau_{wav} \cdot \omega_0} + \frac{2}{\tau_{loss} \cdot \omega_0} \right) \right]^2} = \frac{8}{\tau_{wav} \omega_0^2} \frac{1}{\left[\frac{-2i(\omega - \omega_0)}{\omega_0} + \left(\frac{2}{Q_{wav}} + \frac{1}{Q_{loss}} \right) \right]^2} = \\
 &= \frac{4Q_{wav}}{\omega_0} \frac{1}{\left[\frac{-2i(\omega - \omega_0)}{\omega_0} + \left(\frac{2}{Q_{wav}} + \frac{1}{Q_{loss}} \right) \right]^2}
 \end{aligned}$$

So at the resonance, the build-up factor becomes:

$$\begin{aligned}
 F(\omega_0) &= \frac{2}{\tau_{wav}} \frac{1}{\left(\frac{2}{\tau_{wav}} + \frac{1}{\tau_{loss}} \right)^2} = \frac{2.4}{\tau_{wav} \omega_0^2} \frac{1}{\left(\frac{2.2}{\tau_{wav} \cdot \omega_0} + \frac{2}{\tau_{loss} \cdot \omega_0} \right)^2} = \\
 &= \frac{4}{\omega_0 \cdot Q_{wav}} \frac{1}{\left(\frac{2}{Q_{wav}} + \frac{1}{Q_{loss}} \right)^2} = \frac{4}{\omega_0} \frac{Q_{wav}}{\left(2 + \frac{Q_{wav}}{Q_{loss}} \right)^2}
 \end{aligned}$$

$$\boxed{F(\omega_0) = \frac{4}{\omega_0} \frac{Q_{wav}}{\left(2 + \frac{Q_{wav}}{Q_{loss}} \right)^2}} \quad (2.2.20)$$

As $\omega_0 = \frac{2\pi c}{\lambda_0}$ then we obtain build-up factor as function of resonance wavelength:

$$F(\lambda_0) = \frac{2\lambda_0}{\pi c} \frac{Q_{wav}}{\left(2 + \frac{Q_{wav}}{Q_{loss}} \right)^2} \quad (2.2.21)$$

We will find the condition of the relationship between Q_{loss} and Q_{wav} to achieve maximum build-up factor:

$$\frac{dF(\omega_0)}{dQ_{wav}} = 0 \Leftrightarrow Q_{wav} = 2Q_{loss} \quad (2.2.22)$$

$$\Rightarrow \max F(\omega_0) \Big|_{Q_{\text{wav}}=Q_{\text{loss}}} = \frac{4}{\omega_0} \frac{2Q_{\text{loss}}}{4^2} = \frac{8Q_{\text{loss}}}{16\omega_0} = \frac{Q_{\text{loss}}}{2\omega_0} \quad (2.2.23)$$

as shown in Fig. 2A.4. **The maximum value of build-up factor thus depends only on Q_{loss} , i.e. on the quality of the technology.**

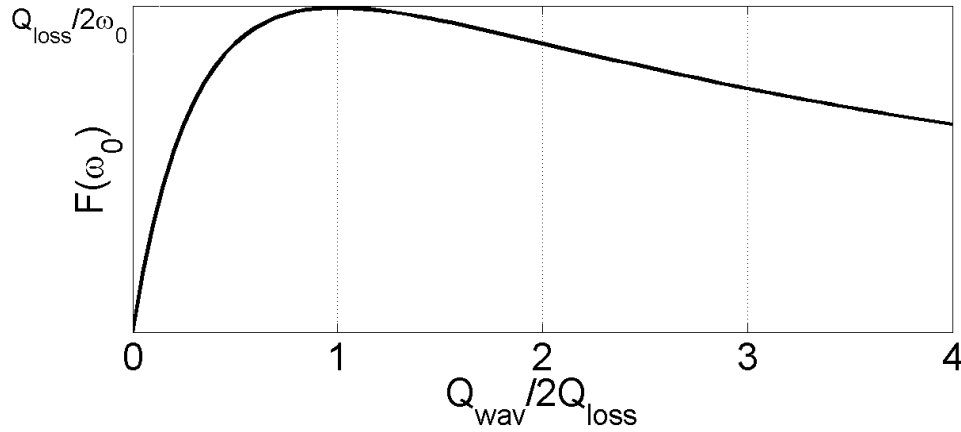


Fig. 2A.4 Build-up factor at resonance as a function of $(Q_{\text{wav}}/2Q_{\text{loss}})$.

For example, considering the case in which Q -factor $Q_{\text{loss}} = 5 \cdot 10^5$ at resonance $\lambda_0 = 1.5 \cdot 10^{-6} \text{ m}$.

Then

$$\begin{aligned} F(\omega_0)_{\text{max}} &= \frac{2 \cdot 1.5 \cdot 10^{-6}}{9 \cdot \pi \cdot 3 \cdot 10^8} \cdot 5 \cdot 10^5 \\ &= 3.5 \cdot 10^{-16} \cdot 5 \cdot 10^5 \\ &= 1.7 \cdot 10^{-10} (\text{s}) \end{aligned}$$

So in this case, the maximum build-up factor is 0.17 ns.

APPENDIX B

Supermodes of coupled slot photonic crystal cavities calculated by tight-binding approximation

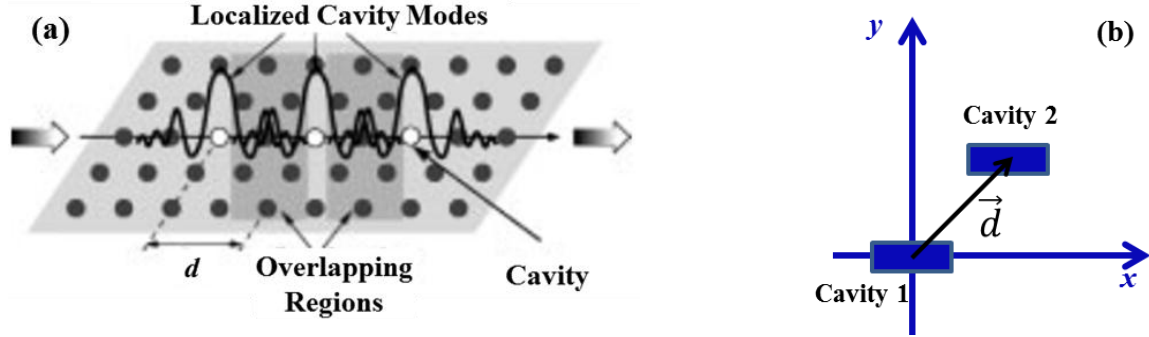


Fig. 2B.1(a) Scheme of coupled PhC molecules in which tightly confined cavity mode interacts weakly with the neighboring cavity modes, and therefore the electromagnetic waves can propagate through coupled cavities [215] **(b)** Sketched view of two coupled cavities at distance d .

Starting with the master equation, the spatial parts of individual localized mode $\overset{\perp}{E}_{\Omega}(\vec{r})$ of a defect cavity obeys this formula

$$\nabla \times \nabla \times \overset{\perp}{E}_{\Omega}(\vec{r}) = \varepsilon_0(\vec{r}) \left(\frac{\Omega}{c} \right)^2 \overset{\perp}{E}_{\Omega}(\vec{r}) \quad (2.3.1)$$

, where without any restriction to the generality of the results, $\overset{\perp}{E}_{\Omega}(\vec{r})$ can be considered as a real vector, $\varepsilon_0(\vec{r})$ is the dielectric constant of the single defect, and Ω is the corresponding eigenfrequency.

In the tight-binding (TB) approximation, when two cavities are placed in close proximity, the eigenmode of the set of coupled resonators (the “supermodes”) can be written as a superposition of the individual defect modes: $E_{\omega}(\vec{r}) = AE_{\Omega}(\vec{r}) + BE_{\Omega}(\vec{r} - \overset{\perp}{d})$, where ω is the eigenfrequency of the coupled defect mode and $\overset{\perp}{d}$ is the displacement of the second cavity center with respect to the first one (Fig. 2B.1). The eigenmode $E_{\omega}(\vec{r})$ also satisfies equation (2.3.1) where $\varepsilon_0(\vec{r})$ is replaced by $\varepsilon(\vec{r})$, the dielectric constant of the coupled cavity system and Ω is replaced by ω the eigenfrequency of the coupled defect mode.

By symmetry condition between the two cavities, $|A| = |B|$.

Then putting the new field $E_\omega(\mathbf{r})$ into the master equation (2.3.1) gives:

$$\nabla \times \nabla \times E_\omega(\mathbf{r}) = \varepsilon(\mathbf{r}) \left(\frac{\omega}{c} \right)^2 E_\omega(\mathbf{r}), \quad (2.3.2)$$

$$\text{leading to: } \nabla \times \nabla \times [AE_\Omega(\mathbf{r}) + BE_\Omega(\mathbf{r} - \mathbf{d})] = \varepsilon(\mathbf{r}) \left(\frac{\omega}{c} \right)^2 [AE_\Omega(\mathbf{r}) + BE_\Omega(\mathbf{r} - \mathbf{d})]$$

$$A\nabla \times \nabla \times E_\Omega(\mathbf{r}) + B\nabla \times \nabla \times E_\Omega(\mathbf{r} - \mathbf{d}) = A\varepsilon(\mathbf{r}) \left(\frac{\omega}{c} \right)^2 E_\Omega(\mathbf{r}) + B\varepsilon(\mathbf{r}) \left(\frac{\omega}{c} \right)^2 E_\Omega(\mathbf{r} - \mathbf{d})$$

From equation (2.3.1) then we have:

$$A \left(\frac{\Omega}{c} \right)^2 \varepsilon_0(\mathbf{r}) E_\Omega(\mathbf{r}) + B \left(\frac{\Omega}{c} \right)^2 \varepsilon_0(\mathbf{r} - \mathbf{d}) E_\Omega(\mathbf{r} - \mathbf{d}) = A\varepsilon(\mathbf{r}) \left(\frac{\omega}{c} \right)^2 E_\Omega(\mathbf{r}) + B\varepsilon(\mathbf{r}) \left(\frac{\omega}{c} \right)^2 E_\Omega(\mathbf{r} - \mathbf{d})$$

Multiplying both sides from the left by $E_\Omega(\mathbf{r})$, we get:

$$\begin{aligned} & A \left(\frac{\Omega}{c} \right)^2 \varepsilon_0(\mathbf{r}) E_\Omega(\mathbf{r})^2 + B \left(\frac{\Omega}{c} \right)^2 \varepsilon_0(\mathbf{r} - \mathbf{d}) E_\Omega(\mathbf{r}) E_\Omega(\mathbf{r} - \mathbf{d}) = \\ & = A \left(\frac{\omega}{c} \right)^2 \varepsilon(\mathbf{r}) E_\Omega(\mathbf{r})^2 + B \left(\frac{\omega}{c} \right)^2 \varepsilon(\mathbf{r}) E_\Omega(\mathbf{r}) E_\Omega(\mathbf{r} - \mathbf{d}) \end{aligned}$$

Spatially integrating the two sides of this equation is then made as follows:

$$\begin{aligned} & \int d\mathbf{r} A \left(\frac{\Omega}{c} \right)^2 \varepsilon_0(\mathbf{r}) E_\Omega(\mathbf{r})^2 + \int d\mathbf{r} B \left(\frac{\Omega}{c} \right)^2 \varepsilon_0(\mathbf{r} - \mathbf{d}) E_\Omega(\mathbf{r}) E_\Omega(\mathbf{r} - \mathbf{d}) = \\ & = \int d\mathbf{r} A \left(\frac{\omega}{c} \right)^2 \varepsilon(\mathbf{r}) E_\Omega(\mathbf{r})^2 + \int d\mathbf{r} B \left(\frac{\omega}{c} \right)^2 \varepsilon(\mathbf{r}) E_\Omega(\mathbf{r}) E_\Omega(\mathbf{r} - \mathbf{d}) \end{aligned}$$

Taking into account the field normalization condition for the individual localized modes, we obtain:

$$\begin{aligned} & A \left(\frac{\Omega}{c} \right)^2 + B \left(\frac{\Omega}{c} \right)^2 \left(\int d\mathbf{r} \varepsilon_0(\mathbf{r} - \mathbf{d}) E_\Omega(\mathbf{r}) E_\Omega(\mathbf{r} - \mathbf{d}) \right) = \\ & = A \left(\frac{\omega}{c} \right)^2 \left(\int d\mathbf{r} \varepsilon(\mathbf{r}) E_\Omega(\mathbf{r})^2 \right) + B \left(\frac{\omega}{c} \right)^2 \left(\int d\mathbf{r} \varepsilon(\mathbf{r}) E_\Omega(\mathbf{r}) E_\Omega(\mathbf{r} - \mathbf{d}) \right) \end{aligned} \quad (2.3.3)$$

Considering that the global field is normalized, too, *i.e.* that: $\int d\mathbf{r} \varepsilon(\mathbf{r}) E_\omega(\mathbf{r})^2 = 1$

$$\text{i.e. } \int d\mathbf{r} \varepsilon(\mathbf{r}) [AE_\Omega(\mathbf{r}) + BE_\Omega(\mathbf{r} - \mathbf{d})]^2 = 1$$

$$A^2 \left(\int d\vec{r} \varepsilon(\vec{r}) E_{\Omega}(\vec{r})^2 \right) + B^2 \left(\int d\vec{r} \varepsilon(\vec{r}) E_{\Omega}(\vec{r}-\vec{d})^2 \right) + 2AB \left(\int d\vec{r} \varepsilon(\vec{r}) E_{\Omega}(\vec{r}) E_{\Omega}(\vec{r}-\vec{d}) \right) = 1$$

we find that: $A^2 + B^2 + 2\alpha_1 AB = 1$

Reminding that $|A| = |B|$, and introducing $\alpha_1 = \int d\vec{r} \varepsilon(\vec{r}) E_{\Omega}(\vec{r}) E_{\Omega}(\vec{r}-\vec{d})$, coupled cavity modes can be finally obtained by considering the $A = B$ and $A = -B$ cases, respectively:

i, Case 1: $A = B$

$$A^2 + A^2 + 2\alpha_1 A^2 = 1 ; 2(1 + \alpha_1) A^2 = 1 ; A = \frac{1}{\sqrt{2(1 + \alpha_1)}} ; B = \frac{1}{\sqrt{2(1 + \alpha_1)}}$$

ii, Case 2: $B = -A$

$$A^2 + A^2 - 2\alpha_1 A^2 = 1 ; 2(1 - \alpha_1) A^2 = 1 ; A = \frac{1}{\sqrt{2(1 - \alpha_1)}} ; B = -\frac{1}{\sqrt{2(1 - \alpha_1)}}$$

Introducing new parameters:

$$\beta_1 = \int d\vec{r} \varepsilon_0(\vec{r}-\vec{d}) E_{\Omega}(\vec{r}) E_{\Omega}(\vec{r}-\vec{d}) \text{ and}$$

$$\Delta\alpha = \int d\vec{r} (\varepsilon(\vec{r}) - \varepsilon_0(\vec{r})) E_{\Omega}(\vec{r})^2 ,$$

the master equation becomes:

$$A \left(\frac{\Omega}{c} \right)^2 + B \left(\frac{\Omega}{c} \right)^2 \beta_1 = A \left(\frac{\omega}{c} \right)^2 (1 + \Delta\alpha) + B \left(\frac{\omega}{c} \right)^2 \alpha_1 \quad (2.3.4)$$

We then consider the two previous cases to obtain the bonding and antibonding frequencies and mode expansions:

i, Case 1: $A = B$

$$A \left(\frac{\Omega}{c} \right)^2 + A \left(\frac{\Omega}{c} \right)^2 \beta_1 = A \left(\frac{\omega}{c} \right)^2 (1 + \Delta\alpha) + A \left(\frac{\omega}{c} \right)^2 \alpha_1$$

$$1 + \beta_1 = \left(\frac{\omega}{\Omega} \right)^2 (1 + \Delta\alpha) + \left(\frac{\omega}{\Omega} \right)^2 \alpha_1$$

$$\omega_+ = \Omega \sqrt{\frac{1 + \beta_1}{1 + \alpha_1 + \Delta\alpha}} \quad (2.3.5)$$

ii, Case 2: $B = -A$

$$A\left(\frac{\Omega}{c}\right)^2 - A\left(\frac{\Omega}{c}\right)^2 \beta_1 = A\left(\frac{\omega}{c}\right)^2 (1 + \Delta\alpha) - A\left(\frac{\omega}{c}\right)^2 \alpha_1$$

$$1 - \beta_1 = \left(\frac{\omega}{\Omega}\right)^2 (1 + \Delta\alpha) - \left(\frac{\omega}{\Omega}\right)^2 \alpha_1$$

$$\omega_- = \Omega \sqrt{\frac{1 - \beta_1}{1 - \alpha_1 + \Delta\alpha}} \quad (2.3.6)$$

Then the corresponding bonding and antibonding fields are:

$$E_{\omega_+}(\mathbf{r}) = \frac{1}{\sqrt{2(1 + \alpha_1)}} \left(E_{\Omega}(\mathbf{r}) + E_{\Omega}(\mathbf{r} - \mathbf{d}) \right)$$

$$E_{\omega_-}(\mathbf{r}) = \frac{1}{\sqrt{2(1 - \alpha_1)}} \left(E_{\Omega}(\mathbf{r}) - E_{\Omega}(\mathbf{r} - \mathbf{d}) \right)$$

Let notice that:

$$\omega_+ = \Omega \sqrt{\frac{1 + \beta_1}{1 + \alpha_1 + \Delta\alpha}} \cong \Omega \sqrt{(1 + \beta_1)(1 - \alpha_1 - \Delta\alpha)} = \Omega (1 + \beta_1 - \alpha_1 - \Delta\alpha - \alpha_1 \beta_1 - \beta_1 \Delta\alpha)^{1/2} \cong \Omega \left[1 + \frac{\beta_1 - \alpha_1}{2} \right]$$

$$\omega_- = \Omega \sqrt{\frac{1 - \beta_1}{1 - \alpha_1 + \Delta\alpha}} \cong \Omega \sqrt{(1 + \beta_1)(1 + \alpha_1 - \Delta\alpha)} = \Omega (1 + \beta_1 + \alpha_1 - \Delta\alpha - \alpha_1 \beta_1 + \beta_1 \Delta\alpha)^{1/2} \cong \Omega \left[1 - \frac{\beta_1 - \alpha_1}{2} \right]$$

The difference in frequency between two supermodes is thus $\Delta\omega = \omega_+ - \omega_- = \Omega(\beta_1 - \alpha_1)$.

The sign of $(\omega_+ - \omega_-)$ is the one of $(\beta_1 - \alpha_1)$

$$(\beta_1 - \alpha_1) = \int d\mathbf{r} \left(\varepsilon_0(\mathbf{r} - \mathbf{d}) - \varepsilon(\mathbf{r}) \right) E_{\Omega}(\mathbf{r}) E_{\Omega}(\mathbf{r} - \mathbf{d})$$

Hence:

$$\omega_+ = \Omega \left[1 - \left(\int d\mathbf{r} \frac{(\varepsilon(\mathbf{r}) - \varepsilon_0(\mathbf{r} - \mathbf{d}))}{2} E_{\Omega}(\mathbf{r}) E_{\Omega}(\mathbf{r} - \mathbf{d}) \right) \right]$$

$$\omega_- = \Omega \left[1 + \left(\int d\mathbf{r} \frac{(\varepsilon(\mathbf{r}) - \varepsilon_0(\mathbf{r} - \mathbf{d}))}{2} E_{\Omega}(\mathbf{r}) E_{\Omega}(\mathbf{r} - \mathbf{d}) \right) \right]$$

Or, if we look at a more exact calculation:

$$\delta = \frac{\omega_+^2 - \omega_-^2}{\Omega^2} = \frac{1 + \beta_1}{1 + \alpha_1 + \Delta\alpha} - \frac{1 - \beta_1}{1 - \alpha_1 + \Delta\alpha} = \frac{2(\beta_1 - \alpha_1 + \beta_1\Delta\alpha)}{(1 + \Delta\alpha)^2 - \alpha_1^2}$$

If we consider that:

$$\Delta\alpha \ll 1$$

$$\beta_1\Delta\alpha \ll \beta_1$$

then

$$\delta \approx \frac{2(\beta_1 - \alpha_1)}{1 - \alpha_1^2}$$

$$\alpha_1^2 \ll 1$$

so the sign of δ is the sign of $(\beta_1 - \alpha_1)$.

Now, we consider the deviation of dielectric constant $(\varepsilon(\mathbf{r}) - \varepsilon_0(\mathbf{r} - \mathbf{d}))$ in which

$(\varepsilon(\mathbf{r}) - \varepsilon_0(\mathbf{r} - \mathbf{d}))$ describes the whole region around $\mathbf{r} = \mathbf{0}$

$(\varepsilon(\mathbf{r}) - \varepsilon_0(\mathbf{r}))$ describes the whole region around $\mathbf{r} = \mathbf{d}$

Due to the symmetry condition, after multiplying both sides from the left with $E_\Omega(\mathbf{r})E_\Omega(\mathbf{r} - \mathbf{d})$

and then spatially integrating, one gets:

$$\omega_+ = \Omega \left[1 - \left(\int d\mathbf{r} \frac{\Delta\varepsilon(\mathbf{r})}{2} E_\Omega(\mathbf{r}) E_\Omega(\mathbf{r} - \mathbf{d}) \right) \right] \quad \text{and} \quad \omega_- = \Omega \left[1 + \left(\int d\mathbf{r} \frac{\Delta\varepsilon(\mathbf{r})}{2} E_\Omega(\mathbf{r}) E_\Omega(\mathbf{r} - \mathbf{d}) \right) \right], \quad \text{with}$$

$$\Delta\varepsilon(\mathbf{r}) = (\varepsilon(\mathbf{r}) - \varepsilon_0(\mathbf{r}))$$

Reintroducing unnormalized fields, we get:

$$\omega_+ = \Omega \left[1 - \frac{\left(\int d\mathbf{r} \frac{\Delta\varepsilon(\mathbf{r})}{2} E_\Omega(\mathbf{r}) E_\Omega(\mathbf{r} - \mathbf{d}) \right)}{\left(\int d\mathbf{r} \frac{\varepsilon_0(\mathbf{r})}{2} E_\Omega(\mathbf{r})^2 \right)} \right] : \text{frequency of the bonding state} \quad (2.3.7)$$

$$\omega_- = \Omega \left[1 + \frac{\left(\int d\mathbf{r} \frac{\Delta\varepsilon(\mathbf{r})}{2} E_\Omega(\mathbf{r}) E_\Omega(\mathbf{r} - \mathbf{d}) \right)}{\left(\int d\mathbf{r} \frac{\varepsilon_0(\mathbf{r})}{2} E_\Omega(\mathbf{r})^2 \right)} \right] : \text{frequency of the antibonding state} \quad (2.3.8)$$

Where, the numerator $\left(\int d^3\mathbf{r} \frac{\Delta\varepsilon(\mathbf{r})}{2} E_{\Omega}(\mathbf{r}) E_{\Omega}(\mathbf{r}-\mathbf{d}) \right)$ is the **dielectric perturbative energy** and the denominator $\left(\int d^3\mathbf{r} \frac{\Delta\varepsilon(\mathbf{r})}{2} E_{\Omega}(\mathbf{r})^2 \right)$ is the **total dielectric energy of the mode**.

Reintroducing also vector fields, we finally get the bonding and anti-bonding frequencies written as:

$$\omega_+ = \Omega \left[1 - \frac{\left(\int d^3\mathbf{r} \frac{\Delta\varepsilon(\mathbf{r})}{2} E_{\Omega}(\mathbf{r}) \cdot E_{\Omega}(\mathbf{r}-\mathbf{d}) \right)}{\left(\int d^3\mathbf{r} \frac{\varepsilon_0(\mathbf{r})}{2} \|E_{\Omega}(\mathbf{r})\|^2 \right)} \right] = \Omega(1-\kappa) \quad (2.3.9a)$$

$$\omega_- = \Omega \left[1 + \frac{\left(\int d^3\mathbf{r} \frac{\Delta\varepsilon(\mathbf{r})}{2} E_{\Omega}(\mathbf{r}) \cdot E_{\Omega}(\mathbf{r}-\mathbf{d}) \right)}{\left(\int d^3\mathbf{r} \frac{\varepsilon_0(\mathbf{r})}{2} \|E_{\Omega}(\mathbf{r})\|^2 \right)} \right] = \Omega(1+\kappa) \quad (2.3.9b)$$

, where $\kappa = \frac{\left(\int d^3\mathbf{r} \frac{\Delta\varepsilon(\mathbf{r})}{2} E_{\Omega}(\mathbf{r}) \cdot E_{\Omega}(\mathbf{r}-\mathbf{d}) \right)}{\left(\int d^3\mathbf{r} \frac{\varepsilon_0(\mathbf{r})}{2} \|E_{\Omega}(\mathbf{r})\|^2 \right)}$ is the **coupling coefficient**.

With the deviation of the dielectric constant: $\Delta\varepsilon(\mathbf{r}) = (\varepsilon(\mathbf{r}) - \varepsilon_0(\mathbf{r}))$ (2.3.9c)

The bonding and anti-bonding fields are then also read:

$$\begin{aligned} E_{\omega_+}(\mathbf{r}) &= \frac{1}{\sqrt{2(1+\alpha_1)}} \left(E_{\Omega}(\mathbf{r}) + E_{\Omega}(\mathbf{r}-\mathbf{d}) \right) \\ &\cong \frac{1}{\sqrt{2}} \left(E_{\Omega}(\mathbf{r}) + E_{\Omega}(\mathbf{r}-\mathbf{d}) \right) \end{aligned} \quad (2.3.9d)$$

$$\begin{aligned} E_{\omega_-}(\mathbf{r}) &= \frac{1}{\sqrt{2(1-\alpha_1)}} \left(E_{\Omega}(\mathbf{r}) - E_{\Omega}(\mathbf{r}-\mathbf{d}) \right) \\ &\cong \frac{1}{\sqrt{2}} \left(E_{\Omega}(\mathbf{r}) - E_{\Omega}(\mathbf{r}-\mathbf{d}) \right) \end{aligned} \quad , \text{ in which } \alpha_1 = \int d^3\mathbf{r} \varepsilon(\mathbf{r}) E_{\Omega}(\mathbf{r}) E_{\Omega}(\mathbf{r}-\mathbf{d}) \quad (2.3.9e)$$

Publications

1. **Thi-Hong-Cam Hoang**, Weiwei Zhang, Samuel F. Serna-Otalvaro, Charles Caer, Xavier Le Roux, Laurent Vivien, and Eric Cassan, “SOI Slotted Photonic crystal cavities spanning from 1.3 to 1.6 μm with Q/V factors above 800 000”, *IEEE Photonics Technology Letters* 27 20 (2015).
2. Elena Duran Valdeiglesias, Weiwei Zhang, Adrien Noury, Carlos Alonso Ramos, **Thi-Hong Cam Hoang**, Samuel Serna, Xavier Le Roux, Eric Cassan, Nicolas Izard, Francesco Sarti, Ughetta Torrini, Francesco Biccari, Anna Vinattieri, Matteo Balestrieri, Al-Saleh Keita, Hongliu Yang, Viktor Bezugly, Gianarelio Cuniberti, Arianna Filoramo, Massimo Gurioli and Laurent Vivien, "Integration of CarbonNanotubes in Silicon Strip and Slot Waveguide Microring Resonators", *IEEE Transactions on Nanotechnology*, 15(4)(2016). DOI:10.1109/TNANO.2016.2556225.
3. F. Biccari, F. Sarti, N. Caselli, A. Vinattieri, E. Durán-Valdeiglesias, W. Zhang, C. Alonso-Ramos, **T. H. C. Hoang**, S. Serna, X. LeRoux, E. Cassan, L. Vivien, M. Gurioli, “Single walled carbon nanotubes emission coupled with a silicon slot-ring resonator”, *Journal of Luminescence* (2016),DOI: 10.1016/j.jlumin.2016.11.040.
4. Niccolo Caselli, **Thi-Hong Hoang**, Xavier Le roux, Francesco Sarti, Francesco Biccari, Federico La China, Francesca Intonti, Anna Vinattieri, Laurent Vivien, Eric Cassan, Massimo Gurioli, “ Vectorial near-field imaging of silicon heterostructure photonic-crystal cavities in air-slot waveguides”, *IEEE Photonics Technology Letters* (99) (2017), DOI: 10.1109/LPT.2017.2664900.

List of Figures

- Fig. 1.1.1 (a) 1D-silicon photonic crystal electro-optic modulator with Insertion Loss $IL = 1$ dB, Extinction ratio $ER = 8$ dB at a modulation speed of 3 Gbps [11], (b) Schematic view of a lateral pin Ge photodetector integrated at the end of a Si waveguide with responsivity of 0.8 A/W at 0.1 V bias, and a dark-current density of 80 A/cm² bandwidth up to 120 GHz at $\lambda = 1550$ nm, an open eye diagrams at 40 Gb/s were obtained under zero-bias [14]. 3
- Fig. 1.1.2 Schematic of electronic-photonic hybrid chip [20]..... 4
- Fig. 1.2.1 (a) Scheme of the hybrid III-V/Si laser in top and side views [36] (b) Integration of AlGaInAs-silicon evanescent amplifier, the optical mode can obtain electrically pumped gain from the III-V region why being guided by the underlying silicon waveguide region [37]. 7
- Fig. 1.2.2 (a) Cross-section of a slotted SOI silicon waveguide covered by a nonlinear optical organic material (NL), w , h are the width and height of the ribs, respectively and w_{slot} is the width of the slot. The E_x component of the fundamental quasi-TE mode is confined in the slot and strongly enhanced within the low-index material filling in the slot. (b) Molecular structure of the organic material DDMEBT (c) Transmission spectra of SOH waveguide (green) and after band-pass filtering (blue) [41]..... 8
- Fig. 1.2.3 (a) Cross-sectional diagram of HSQDL device (b) Scanning electron micrograph of a polished cross section. The tapers were polished off in order to show the gain region. The air trench between the rib waveguide and the silicon cladding is filled with polishing residue [44]...... 10
- Fig. 1.2.4 Schematic of a graphene-hexagonal Boron Nitride (hBN) heterostructure-based planar electro-optic modulator. The dual-layer graphene capacitor on quartz substrate is optically coupled to the photonic crystal cavity [49]. 11
- Fig. 1.2.5 (a) Chiral vector indicates the rolling up direction (b) Different morphologies of CNTs (c) Single-walled CNTs (SWNTs), and (d) Multi-walled CNTs (MWNTs). 13
- Fig. 1.2.6(a) The electronic dispersion relation of SWNTs (comprising the excitonic correction) [61] (b) Associated with each subband is a density of states that exhibit a singularity called a van Hove singularity of the semiconducting SWNTs. Solid line arrows depict the optical excitation and emission transitions of interest, while the dashed arrows denote non-radiative relaxation of the electron (in the conduction band) and hole (in the valence band) before emission [62]. 15
- Fig. 1.2.7 Photoluminescence excitation maps of SWNTs in toluene solution prepared using nanotubes grown by the HiPCO process as starting material, and selectively solubilized by polymer poly(9,9-dioctylfluorenyl2,7-divyl) PFO-P. The red crosses correspond to the family of tubes with $n-m = 3q-1$ and the black squares to those for $n-m = 3q+1$ [63]. 16
- Fig. 1.2.8 (a) Schematic representation of a variable strip length experiment to estimate optical gain of s-SWNTs (b) High resolution normalized spectra of the amplified spontaneous emission fluences with an excitation wavelength of 740 nm. A 29% linewidth narrowing (FWHM) from 63 to 45 nm was observed on the photoluminescence of (8,7) nanotube at 1300 nm and linewidth narrowing of 28% (FWHM) from 44 to 32 nm was also observed for the (8,6) nanotube at 1200 nm [70]. 17
- Fig. 1.2.9 (a) Evanescent wave detection principle [77] (b) Schematic of slotted photonic crystal sensors with integrated PDMS microfluidics [78]. 18

- Fig. 1.3.1 (a) Schematic of a strip waveguide (b) TE and TM modes in a silicon on insulator strip waveguide with an $h = 220$ nm wafer thickness and a waveguide width $W = 450$ nm. The upper cladding has the same refractive index as silica at the wavelength of 1550 nm [89]. 21
- Fig. 1.3.2 (a) Schematic of a slot waveguide (b) 3D surface plot of transverse E -field profile of the quasi-TE mode in a SOI-based slot waveguide at $\lambda_0 = 1.55$ μm , with $n_H = 3.48$, $n_S = n_C = 1.44$, $w_H = 180$ nm, $w_S = 50$ nm and $h = 300$ nm. The origin of the coordinate system is located at the center of the waveguide, with a horizontal x axis and a vertical y axis [92] (c) Simulated mode profile for the fundamental quasi-TE mode. $W_{\text{arm}} = 270$ nm, $W_{\text{slot}} = 150$ nm, $H = 220$ nm, and the top cladding material is silicon oxide [93].
..... 22
- Fig. 1.3.3 (A) All-pass and (B) add-drop ring resonator [96]. 23
- Fig. 1.3.4 (a) μ -ring resonators [97] and (b) Slot μ -ring racetrack add-drop resonator [94]. 24
- Fig. 1.3.5 (a) SOI PhC slab and (b) the concept of light cone in SOI slab where n_1, n_2 corresponds to n_{SiO_2} and n_{Si} , respectively. 25
- Fig. 1.3.6 Band diagram for SOI PhC of Fig. 1.3.5(a) in which hole radius $r = 0.276a$, slab thickness $h = 0.684a$. The grey shaded area is the light cone, corresponding to the extended modes. Below it are the TE-like guided bands localized to the slab: a TE-like gap is present from $\omega = 0.2399$ to 0.2839 (a/c).
..... 25
- Fig. 1.3.7 (a) Scheme of SOI W1 PhC waveguide and its horizontal view (b) Dispersion diagram of W1 PhC WG with the silicon core slab thickness $h = 0.684a$ and the hole radius $r = 0.276a$ with top cladding material of 1.46 refractive index (c) Zoom in of the dispersion diagram in (b) with two W1 TE-like even (blue curve) and odd (red curve) modes (insets correspond to the E_y field profiles). 27
- Fig. 1.3.8 (a) Scheme of SOI SPCW and (b) Horizontal view of SOI SPCW infiltrated with a cladding material. 28
- Fig. 1.3.9 (a) Dispersion diagram of SPCW with lattice constant $a = 380$ nm, slab thickness $h = 260$ nm, slot width $W_{\text{slot}} = 100$ nm and waveguide width $W_{1.25}$ (*i.e.* $1.25\sqrt{3}a$), hole radius $r = 105$ nm radius of the holes in the first two rows closet to the slot is $r_1 = 125$ nm and inset is its schematic view of the unit cell (b) Zoom of dispersion diagram focusing on three TE-like gap-guided modes: y -even true-slot mode (dash-red curve), y -odd W1-like mode (blue curve), y -even W1-like mode (red curve) and their field profiles of E_y components. 28
- Fig. 1.3.10 Fraction of electric field energy density of cladding region as a function of slot width and radius of the holes in the first two rows and width of the slot of (a) True-slot mode and (b) W1-like mode in different SPCWs with hole radius r of 105 nm, lattice constant a of 400 nm, slab thickness h of 260 nm and a cover cladding material of 1.52 refractive index as a function of r_1 and W_{slot} , insets are two kinds of modes. 30
- Fig. 1.3.11 Different kinds of PhC cavities (a) H0 PhC cavity [124] (b) H1 PhC cavity and the E_y profile of the dipole mode [126] (c) L3 PhC cavity [127] and (d) PhC heterostructure cavity [121]. 33
- Fig. 1.3.12 (a) Design of an air-slot PhC slab nanocavity realized by local line-defect-width modulation. Air holes labeled A, B, and C are shifted outward by d_A , d_B , and d_C , respectively [133] (b) 2D-FDTD simulation of slotted PhC air heterostructure cavity by chirping lattice constant showing E_z component of mode profile at cavity resonance wavelength [78] (c) SEM image of an L9 air-slot cavity [135] (d) SEM image of the air-slot modified slot width cavity, inset depicts different values of slot width [136].
..... 35
- Fig. 2.1.1 Scheme of a PhC cavity created by introducing a defect in a planar PhC lattice. 39

- Fig. 2.1.2 Evolution of electric field components and their envelopes decays in the time domain (obtained by using FDTD simulation) in order to compute cavity quality factors in the case of (a) A high Q -factor resonator (*e.g.* $Q \approx 100\,000$) in which the electromagnetic fields cannot completely decay from the simulation time window (b) A low Q -factor resonator (*e.g.* Q of hundreds) in which the electromagnetic fields can almost completely decay from the simulation time window, and (c) Cavity electric field frequency spectrum possesses a Lorentzian behavior. 41
- Fig. 2.1.3 Simulation steps (I) Photonic bandgap of 2D planar PhC structure obtained by (2D/3D)-PWE method (II) Dispersion diagram of (slot) PhC waveguide carried out by (2D/3D)-PWE method and (III) Quality factor, Mode volume and electric field distribution at resonance extracted from (2D/3D)-FDTD simulation. 44
- Fig. 2.1.4 (a) Scheme of PhC structure in horizontal view with the chirp of the parallel lattice constant $a_{//}$ for a fixed perpendicular lattice constant a_{\perp} (b) Vertical view of the slot photonic crystal waveguide geometry on which the cavity geometry is based with the following parameters: hole radius $r = 105$ nm, lateral lattice constants $a_{//}$ are 400 nm, 410 nm and 420 nm, while $a_{\perp} = 400$ nm, a slot width $W_{slot} = 100$ nm, waveguide width of $W_{1.25} = 1.25\sqrt{3}a$, as well as the electric-field energy density distribution $|E|^2$ in horizontal view. The considered cladding index is $n_{clad} = 1.46$ (c) Dispersion diagram of two arbitrary SPCWs with parallel lattice constants a_2 and a_1 in which $a_2 > a_1$, with $a_{\perp} = a_1$, which opens the possibility of occurring resonant modes in the $\omega_{edge} - \omega_{ledge}$ range (d) Profile of the parallel lattice constant for 26 center holes in the first row closest to the slot corresponding to the case $a_{\perp} = 400$ nm and (e) Schematic view of the edge frequencies of different SPCWs corresponding to $a_{//}$ in Fig. 2.1.4(d): guided modes occur in the photonic quantum well formed by the largest $a_{//}$ area. 47
- Fig. 2.1.5 (a) E_y component of the resonant mode ($\lambda_{res} = 1570$ nm) for the slot PhC heterostructure cavity corresponding to $a_{//} = 400$ nm, 410 nm and 420 nm, respectively, while $a_{\perp} = 400$ nm by 3D-FDTD simulation (b) The corresponding E_y Fourier transform in wavevector space with the light-cone (white circle). 49
- Fig. 2.2.1 Scheme of Cavity (“C”)–Waveguide (“WG”) coupling, (I) Butt coupling and (II) Lateral coupling with loss channels including intrinsic loss of uncoupled cavity τ_{loss} and waveguide coupling channels ($2\tau_{wav}$). 50
- Fig. 2.2.2 (a) Dispersion diagram and the structure of the SPCW with 105 nm radius hole, a lattice constant $a = 380$ nm, and a slot width of $W_{slot} = 200$ nm introduced in a waveguide of $W_{1.25} = 1.25\sqrt{3}a$, an effective index $n = 2.95$ of the 2D PhC corresponding to the effective index of a slab SOI with thickness $h = 260$ nm (at $\lambda = 1.50$ μm) with a top cladding index of $n_{clad} = 1.44$ in the case radius hole of first row $r_1 = 125$ nm (b) Zoom of dispersion diagram of the true-slot mode (red curve) and the related profile of the E_y component of the y -even mode. 53
- Fig. 2.2.3 (a) Refractive index profile of the 200 nm slot L3 PhC cavity and its (b) E_x component (b) E_y component and (c) Log of magnitude of the E_y component of the cavity mode at $\omega = 0.248$ ($\lambda = 1532.51$ nm) resonance frequency. 54
- Fig. 2.2.4 (a) Schematic view of the lateral-coupling between a slot photonic crystal waveguide (SPCW) and a slot photonic crystal cavity; the precise design of the cavity is based on a 105 nm radius hole, a lattice constant of $a = 380$ nm, and a slot width of $W_{slot} = 200$ nm (b) Dispersion diagram of the true-slot mode SPCW and the resonance cavity mode in black dotted line and (c) Their coupling scheme. 55
- Fig. 2.2.5 Build-up factor at resonance as a function of $(Q_{wav}/2Q_{loss})$ 56

- Fig. 2.2.6 (a) Dispersion diagram and the structure of the SPCW in the case $r_l = 130$ nm (inset the E_y component of the y-even true-slot mode profile) (b) The related mode group index versus the reduced frequency. 57
- Fig. 2.2.7 (a) Scheme of the coupling between the SPCW and the L3 true slot mode PhC cavity using 2D-FDTD simulation (b) Description of the parameters of the coupling system: lattice constant: $a = 380$ nm, hole radius: $r = 105$ nm; hole radius in the row closest to the slot of cavity: $r_l = 125$ nm, hole radius along the slot of cavity: $r_{ct} = 150$ nm, hole radius in the row closest to slot of waveguide: $r_l' = 130$ nm, slot width: $W_{slot} = 200$ nm and the waveguide width $W_{1.25} = 1.25\sqrt{3}a$ 57
- Fig. 2.2.8 Excitation of light from the slot Photonic crystal waveguide: (a) E_y distribution of the slot L3 PhC cavity and (b) Log-scale of E_y at resonance wavelength $\lambda = 1532.84$ nm (c) Normalized transmittance collected at the output of the SPCW. 58
- Fig. 2.3.1 Different configurations of photonic molecules based on different resonator kinds: (a) Compound Fabry-Perot resonators consisting of three mirrors, a passive and nonabsorptive FB cavity coupled to an active FB cavity [189] (b) Dual-cavity coupled microring resonators [188] (c) Coupled located defects in PhC cavities [196] (d) Coupled Silica disk microresonators [181] and (e) Bisphere photonic molecule [183]. 60
- Fig. 2.3.2 Splitting of bonding (“B”) and antibonding (“AB”) states in a coupled system, (a) Bonding mode is the ground state and (b) Antibonding mode is the ground state. 61
- Fig. 2.3.3 Various types of PhC photonic molecules: (a) Coupled PhC nanobeam cavities [192] (b) Coupled PhC L3 cavities [193] in different coupling direction or (e) Coupled PhC L3 cavities with tuning the barrier to tailor the supermodes [194] (c) Coupled multiple heterostructure cavities [175] (d) Coupled D2 PhC cavities [199]. 61
- Fig. 2.3.4 (a) Scheme of coupled Photonic crystal molecules in which a tightly confined cavity mode interacts weakly with the neighboring cavity modes [215] (b) Sketched view of two coupled cavities at distance d along a nearby arbitrary direction. 64
- Fig. 2.3.5 Illustration of PhC cavity’s dielectric constant distributions: (a) The original cavity, and (b) The coupled cavities system. 65
- Fig. 2.3.6 Scheme of coupled L3 PhC cavities with lattice constant $a = 380$ nm, hole radius $r = 105$ nm and width of waveguide $WG1 = \sqrt{3}a$, effective index of the planar waveguide at $\lambda = 1.5$ μm is 2.95. 67
- Fig. 2.3.7 (a) PBG of 2D planar PhC structure in which hole radius $r = 105$ nm, lattice constant $a = 380$ nm, effective index 2.95 for TE light polarization (b) Dispersion diagram of PhC waveguide based on 2D planar PhC structure in (a) in the case radii of first two rows of hole closest to WG $r_l = 125$ nm and the E_y field profile of the gap-guided mode. 68
- Fig. 2.3.8 (a) Refractive index profile of the L3 PhC cavity with hole radius: $r = 105$ nm, lattice constant: $a = 380$ nm and dispersion diagrams of its different parts (b) PBG of planar PhC structure with effective index at 1.5 μm of 2.95 (c) Dispersion diagram of W1 PhC waveguide with radius of first two rows of holes closest to waveguide $r_l = 125$ nm, providing one W1 y-even mode at around 0.2457 ($\lambda \approx 1546.67$ nm) and (d) Dispersion diagram of W1 PhC waveguide consisted of hole radius $r = 105$ nm, $r_l = 125$ nm and radius of holes in the center row $r_{ct} = 150$ nm which creates a lateral barrier, obtained by 2D-PWE calculation. 68

- Fig. 2.3.9 Considered L3 photonic crystal cavity (see Fig. 2.3.8 for a complete description of the opto-geometrical parameters): (a) E_x component (b) E_y component and (c) Log of magnitude of E_y component of the TE-like resonance mode at $\lambda = 1498.42\text{nm}$ 69
- Fig. 2.3.10 Refractive index profile of the coupled PhC L3 cavities in the case $dx = 4a$ 70
- Fig. 2.3.11 E_y component of the coupled PhC L3 cavities for $dx = 0$ of (a) Bonding mode at $\lambda_B = 1500.91\text{ nm}$, and (b) Antibonding mode at $\lambda_{AB} = 1498.02\text{ nm}$ obtained directly by 2D-FDTD simulation (c) Bonding mode at $\lambda_B = 1500.86\text{ nm}$ and (d) Antibonding mode at $\lambda_{AB} = 1495.99\text{ nm}$ obtained by TB method from the 2D-FDTD field of the isolated PhC cavity. 70
- Fig. 2.3.12 (a) Bonding (green-line) and antibonding (red-line) modes of coupled PhC L3 cavities obtained by FDTD simulation (dash line) and TB approximation (solid line), (b) The wavelength difference between the bonding and antibonding modes and (c) the absolute value of wavelength difference between the bonding and antibonding modes obtained by 2D-FDTD simulation (dash line) and TB approximation (solid line) as functions of dx 71
- Fig. 2.3.13 (a) Scheme of of the coupled cavities at distance d , (b) Refractive index profile of the coupled 200 nm slot PhC L3 cavities in the case $dx = 0$ 73
- Fig. 2.3.14 (a) E_x component (b) E_y component and (c) Log of magnitude of the electric field of the cavity mode at 1532.51 nm resonance of 200 nm slot L3 PhC cavity. 74
- Fig. 2.3.15 E_y component of the coupled 200 nm slot PhC L3 cavities for $dx = 0$ of (a) Bonding mode at $\lambda_B = 1528.57\text{ nm}$ and (b) Antibonding mode at $\lambda_{AB} = 1534.3\text{ nm}$ obtained directly by 2D-FDTD simulation (c) Bonding mode at $\lambda_B = 1530.47\text{ nm}$ and (d) Antibonding mode at $\lambda_{AB} = 1534.4\text{ nm}$ obtained by TB method. 74
- Fig. 2.3.16 Bonding (blue-line) and antibonding (red-line) modes of coupled 200 nm slot PhC L3 cavities obtained by (a) 2D-FDTD simulation (dash line) (b) TB approximation (solid line). (c) The wavelength difference between bonding and antibonding modes and (d) The absolute value of wavelength difference between bonding and antibonding modes obtained by 2D-FDTD simulation (dash line) and TB approximation (solid line) as functions of dx 75
- Fig. 2.3.17 (a) Refractive index profile of the 100 nm slot L3 PhC cavity with hole radius $r = 105\text{ nm}$ (b) Dispersion diagram and the structure of the 100 nm SPCW in the case radius of the first row of holes: $r_1 = 125\text{ nm}$, the true-slot mode (red curve) and W1-like modes (blue and violet curves) in the bandgap (c) Dispersion diagram and the structure of the PCW in the case radius of the center row of holes $r_{ct} = 125\text{ nm}$ which creates a lateral barrier, obtained by 3D-PWE calculation. 77
- Fig. 2.3.18 E_y component of the (a) True-slot mode at resonance wavelength $\lambda_1 = 1567.82\text{ nm}$ and (b) W1-like mode at resonance wavelength $\lambda_2 = 1383.13\text{ nm}$ (c) The magnitude of electric field of the W1-like mode in log scale at resonance wavelength $\lambda_2 = 1383.13\text{ nm}$ 77
- Fig. 2.3.19 E_y component of (a) Bonding mode at $\lambda_B = 1387.96\text{ nm}$ and (b) Antibonding mode at $\lambda_{AB} = 1382.95\text{ nm}$ of the coupled 100 nm slot PhC L3 cavities and waveguide width WG1.25 for the case $dx = 0$ directly obtained by 3D-FDTD and (c) Bonding mode at $\lambda_B = 1388.87\text{ nm}$ and (d) Antibonding mode at $\lambda_{AB} = 1377.44\text{ nm}$ obtained by the TB method. 78
- Fig. 2.3.20 Bonding (green-line) and antibonding (red-line) modes of coupled 100 nm slot PhC L3 cavities obtained by FDTD simulation (dash line) and TB approximation (solid line) for the W1-like cavity mode. 79
- Fig. 3.1.1 (a) Overview of one typical sample (.gds-II) mask. The two dash lines represent the positions for the sample cleaving and thus for the sample for characterization (b) Schematic of a typical reference

strip waveguide system with a single-mode strip waveguide of W_{strip} width to fiber high-order optical modes and couple light properly into a single-mode slot waveguide (c) Schematic of a typical chip of slot PhC waveguide cavities (the illustrated lengths of different components are not proportional to their values). 84

Fig. 3.1.2 Principle of the considered strip-to-slot converter: (a) Strip mode (b) Transition mode converter based on a logarithmic taper (c) Slot mode [217]. 86

Fig. 3.1.3 *Gds-II* mask edition: example of one part of one sample (a) Drawing details of slot and holes in the center part of a SPCW cavity (b) An example of the lattice distribution in case of a SPCW cavity with perpendicular lattice constant $a_{\perp} = 340$ nm; the dash line shown on the left is the symmetric axis of the device (dimensions are in μm). 87

Fig. 3.1.4 Schematic of fabrication steps of Strip, Slot WGs and slot PhC cavity structure: (a) Preparation of SOI wafer (b) Resist deposition (c) E-beam lithography (d) Development (e) Etching the Si mask and (f) Cleaning step. 88

Fig. 3.1.5 Distribution of part of a chip with the descriptions of what are: (a) A mainfield (b) A subfield. 89

Fig. 3.1.6 Inventory of some typical errors: (a)-(b) Due to the inhomogeneity of the resist, (c)-(d)-(e) Due to stitching errors at the boundary of the mainfields. 91

Fig. 3.1.7 SEM views of a fabricated slot PhC cavity structure: (a) Center part of the PhC cavity in which $a_{\perp} = 340$ nm (b) Taper and PhC parts (c) Strip-to-slot mode converter, and (d) Input access to the SPCW. 92

Fig. 3.1.8 (a) SEM view with the 9 KX magnification factor of the PhC part of the slot PhC heterostructure cavity with the designed perpendicular lattice constant $a_{\perp} = 340$ nm, (b) SEM image with the location of the holes in the first row (the red curves). 93

Fig. 3.1.9 Lateral lattice constant versus the hole number of the first row of holes of the slot PhC heterocavity (with the designed perpendicular lattice constant $a_{\perp} = 340$ nm). 94

Fig. 3.1.10 Linear measurement set-up to characterize the samples. 95

Fig. 3.1.11 Linear transmission of typical strip and slot PhC waveguides (TE-like polarization): (a) Design-A is made for slot PhC cavities with a resonance wavelength in the 1270-1350 nm range, with following dimensions: strip width $W_{strip} = 250$ nm, $W_{rail} = 140$ nm and $W_{slot} = 100$ nm. Insets: Schematic of strip WG and slot WG. (b) Design-B is made for slot PhC cavities with a resonance wavelength in the 1500-1600 nm range, with following dimensions: strip width $W_{strip} = 400$ nm, $W_{rail} = 200$ nm and $W_{slot} = 100$ nm. 96

Fig. 3.1.12 (a) Horizontal view of three considered slot PhC waveguides in which a_{\perp} is remained unchanged while a_{\parallel} is chirped between a_{\perp} and $a_{\perp} + 20$ nm (b) Dispersion diagram of a slot PhC waveguide constructed with lattice constant $a_{\perp} = a_{\parallel} = 400$ nm, hole radius $r = 105$ nm, width of slot $W_{slot} = 100$ nm, waveguide width $1.25WG$ and the top cladding refractive index $n_{clad} = 1.46$, inset, field distribution of E_y component. 97

Fig. 3.1.13 (a) Transmission spectra of three fabricated slot PhC waveguides filled with top cladding material of 1.46 refractive index in which a_{\parallel} is 400 nm, 410 nm and 420 nm, respectively, and $a_{\perp} = 400$ nm; (b) Simulation and experimental results for the edge wavelength of these three SPCWs using two doses 2.8 C/m^2 and 2.9 C/m^2 98

Fig. 3.1.14 Transmission spectra of the reference strip structure shown in Fig. 3.1.1 (b) and of the slot PhC cavity one shown in Fig. 3.1.1 (c) (for $a_{\perp} = 340$ nm), respectively. The devices were filled with material of 1.46 refractive index (Cargille liquid).	99
Fig. 3.1.15 Transmission spectra of slot PhC heterostructure cavities characterized by a_{\perp} ranging from 330 nm to 400 nm and their relative resonant wavelengths, as well as the obtained quality factors. Insert: Lorentzian fit of the resonance located at $\lambda = 1284.2$ nm and field distribution in the case of $a_{\perp} = 400$ nm, $FWHM = 0.07$ nm.....	99
Fig. 3.2.1 Schematic of the experimental method used to proceed to SOI sample top cladding cleaning and drop casting of optical index.	101
Fig. 3.2.2 Normalized transmission spectra obtained for a single slot PhC waveguide cavity for different values of the top cladding refractive index n_{clad}	102
Fig. 3.2.3 Resonance wavelength as a function of the refractive index, showing a linear dependence yielding a sensitivity of 235 nm/RIU, and quality factor as a function of the refractive index, showing a maximum value of 25 000 around $n_{clad} = 1.44$	102
Fig. 3.2.4 Resonant spectra of the cavity for $n_{clad} = 1.448$ (blue) and $n_{clad} = 1.45$ (red) with Lorentzian fits (solid lines), showing a wavelength shift of 0.75 nm.....	104
Fig. 3.3.1 Linear transmission spectrum of the slot PhC cavity chosen for the integration of s-SWNTs, having a resonance wavelength of 1.28 μm when filled with a 1.46 refractive index liquid as optical top cladding.	106
Fig. 3.3.2 E_y component of TE-like polarization cavity resonance modes: (a) First mode: $\lambda_1 = 1284.34$ nm, (b) Second $\lambda_2 = 1271.2$ nm, both obtained by 3D-FDTD simulation, and the corresponding E_y Fourier transforms in wavevector space for the two modes, respectively (c) and (d) with the light-cone as a white circle in each of the two figures.	107
Fig. 3.3.3 Prepared s-SWNT solutions: (a) Before centrifugation and (b) Its PL map, (c) After centrifugation and (d) The after centrifugation PL map [66].....	108
Fig. 3.3.4 Absorption spectrum of the prepared s-SWNTs solution.	109
Fig. 3.3.5 Drop-casted prepared SWNTs solution on to the surface of slot PhC cavities. This figure shows the sample after being annealed at 180°C for 15 min.	110
Fig. 3.3.6 (a) Transmission spectra of slot PhC heterostructure cavity without SWNT drop-cast (blue curve) and with SWNT drop cast (red curve), (b) Lorentzian fitting of the transmission curve in case of drop-casting s-SWNTs and top cladding liquid configuration.....	111
Fig. 3.3.7 Interferometric set-up to measure the transmittance maps [234].....	112
Fig. 3.3.8 Group delay map measurement spectrogram of the investigated slot PhC waveguide cavity.	113
Fig. 3.3.9 PL measurement set-up to characterize PL enhancement of s-SWNT integrated in slot PhC waveguide cavities.	114
Fig. 3.3.10 Illustration of different pumping positions onto the surface of the sample, <i>i.e.</i> at location of a slot PhC waveguide or of a slot PhC waveguide cavity (in order to simplify the drawing, the light injection/collection systems made up of several waveguide tapers are not shown).	115
Fig. 3.3.11 PL spectrum of the slot PhC waveguide cavity filled with s-SWNTs and a 1.46 refractive index liquid (laser pumping wavelength $\lambda_{exc} = 735$ nm).	116

Fig. 3.3.12 PL responses when pumping on top of the slot PhC waveguide cavity at 735 nm (resonant SWNT excitation)–the red curve, 770 nm (non-resonant SWNT excitation)–the blue curve, and on top of the slot PhC waveguide at 735 nm–the green curve, different pumping locations are illustrated in Fig. 3.3.10..... 117

Fig. 3.3.13 PL spectra map collected by sweeping the wavelength of the pumping laser from 710 nm to 770 nm, the most efficient pumping wavelength is 735 nm for chirality (8,7) s-SWNTs..... 117

List of Tables

Table 1.1 Sensitivity, Quality factor (Q), FOM of various optical sensing systems..... 20

Table 3.1 Main parameters considered of the testing structure scheme shown in Fig. 3.1.1. Different sets are considered to address targeted cavity resonance wavelengths 86

Table 3.2 Shift of dimensions in *.gds-II* and desired values of the fabricated chip (parameters denoted with red color in Fig. 3.1.1(c)) 87

Bibliography

- [1] L. Vivien and L. Pavesi, *Handbook of Silicon Photonics*. Taylor & Francis, 2013.
- [2] S. K. Selvaraja, G. Murdoch, A. Milenin, C. Delvaux, P. Ong, S. Pathak, D. Vermeulen, G. Sterckx, G. Winroth, P. Verheyen, G. Lepage, W. Bogaerts, R. Baets, J. Van Campenhout, and P. Absil, “Advanced 300-mm Waferscale Patterning for Silicon Photonics Devices with Record Low Loss and Phase Errors,” in *17th Opto-Electronics and Communications Conference Technical Digest*, 2012, pp. 15–16.
- [3] Y. A. Vlasov and S. J. Mcnab, “Losses in single-mode silicon-on-insulator strip waveguides and bends,” *Opt. Express*, vol. 12, no. 8, pp. 1622–1631, 2004.
- [4] D. Dai, J. Wang, and Y. Shi, “Silicon mode (de)multiplexer enabling high capacity photonic networks-on-chip with a single-wavelength-carrier light,” *Opt. Lett.*, vol. 38, no. 9, pp. 1422–1424, 2013.
- [5] Q. Xu, S. Manipatruni, B. Schmidt, J. Shakya, and M. Lipson, “12.5 Gbit/s silicon micro-ring silicon modulators,” *Opt. Express*, vol. 15, no. 2, pp. 430–436, 2007.
- [6] A. Liu, L. Liao, D. Rubin, H. Nguyen, B. Ciftcioglu, Y. Chetrit, N. Izhaky, and M. Paniccia, “High-speed optical modulation based on carrier depletion in a silicon waveguide,” *Opt. Express*, vol. 15, no. 2, pp. 660–668, 2007.
- [7] F. Y. Gardes, D. J. Thomson, N. G. Emerson, and G. T. Reed, “40 Gb/s silicon photonics modulator for TE and TM polarisations,” *Opt. Express*, vol. 19, no. 12, pp. 11804–11814, 2011.
- [8] A. Samani, M. Chagnon, D. Patel, V. Veerasubramanian, S. Ghosh, M. Osman, Q. Zhong, and D. V. Plant, “A low-voltage 35-GHz silicon photonic modulator-enabled 112-Gb/s transmission system,” *IEEE Photonics J.*, vol. 7, no. 3, p. 7901413, 2015.
- [9] V. Sih, S. Xu, Y.-H. Kuo, H. Rong, M. Paniccia, O. Cohen, and O. Raday, “Raman amplification of 40 Gb/s data in low-loss silicon waveguides,” *Opt. Express*, vol. 15, no. 2, pp. 357–362, 2007.
- [10] G. T. Reed, G. Mashanovich, F. Y. Gardes, and D. J. Thomson, “Silicon optical modulators,” *Nat. Photonics*, vol. 4, no. 8, pp. 518–526, Aug. 2010.
- [11] A. Shakoob, K. Nozaki, E. Kuramochi, K. Nishiguchi, A. Shinya, and M. Notomi, “Compact 1D-silicon photonic crystal electro-optic modulator operating with ultra-low switching voltage and energy,” *Opt. Express*, vol. 22, no. 23, p. 28623, Nov. 2014.
- [12] S. Akiyama, M. Imai, T. Baba, T. Akagawa, N. Hirayama, Y. Noguchi, M. Seki, K. Koshino, M. Toyama, T. Horikawa, and T. Usuki, “Compact PIN-Diode-Based Silicon Modulator Using Side-Wall-Grating Waveguide,” *IEEE J. Sel. Top. Quantum Electron.*, vol. 19, no. 6, pp. 74–84, Nov. 2013.
- [13] S. Manipatruni, Q. Xu, M. Lipson, C. Hong, M. Lipson, J. Liu, J. Michel, D. Pan, S. S. Patel, A. T. Pomerene, M. Rasras, and D. K. Sparacin, “PINIP based high-speed high-extinction ratio micron-size silicon electro-optic modulator,” vol. 15, no. 20, pp. 13035–13042, 2007.
- [14] L. Vivien, A. Polzer, D. Marris-Morini, J. Osmond, J.-M. Hartmann, P. Crozat, E. Cassan, C. Kopp, H. Zimmermann, and J. M. Fédéli, “Zero-bias 40Gbit/s germanium waveguide photodetector on silicon,” *Opt. Express*, vol. 20, no. 2, pp. 1096–1101, 2012.

- [15] J. K. Doylend, P. E. Jessop, and A. P. Knights, "Silicon photonic resonator-enhanced defect-mediated photodiode for sub-bandgap detection," *Opt. Express*, vol. 18, no. 14, pp. 14671–14678, 2010.
- [16] Y. Kang, H.-D. Liu, M. Morse, M. J. Paniccia, M. Zadka, S. Litski, G. Sarid, A. Pauchard, Y.-H. Kuo, H.-W. Chen, W. S. Zaoui, J. E. Bowers, A. Beling, D. C. McIntosh, X. Zheng, and J. C. Campbell, "Monolithic germanium/silicon avalanche photodiodes with 340 GHz gain–bandwidth product," *Nat. Photonics*, vol. 3, pp. 59–63, 2008.
- [17] D. Ahn, C. Hong, J. Liu, W. Giziewicz, M. Beals, L. C. Kimerling, and J. Michel, "High performance, waveguide integrated Ge photodetectors," *Opt. Express*, vol. 15, no. 7, pp. 3916–3921, 2007.
- [18] H. K. Tsang and Y. Liu, "Nonlinear optical properties of silicon waveguides," *Semicond. Sci. Technol.*, vol. 23, no. 6, p. 64007, Jun. 2008.
- [19] H. K. Tsang, C. S. Wong, T. K. Liang, I. E. Day, S. W. Roberts, A. Harpin, J. Drake, and M. Asghari, "Optical dispersion, two-photon absorption and self-phase modulation in silicon waveguides at 1.5 μm wavelength," *Appl. Phys. Lett.*, vol. 80, no. 3, pp. 416–418, Jan. 2002.
- [20] O. Jambois, Y. Berencen, K. Hijazi, M. Wojdak, A. J. Kenyon, F. Gourbilleau, R. Rizk, and B. Garrido, "Current transport and electroluminescence mechanisms in thin SiO₂ films containing Si nanocluster-sensitized erbium ions," *J. Appl. Phys.*, vol. 106, p. 63526, 2009.
- [21] O. Jambois, F. Gourbilleau, A. J. Kenyon, J. Montserrat, R. Rizk, and B. Garrido, "Towards population inversion of electrically pumped Er ions sensitized by Si nanoclusters," *Opt. Express*, vol. 18, no. 3, pp. 2230–2235, 2010.
- [22] H. Park, A. W. Fang, S. Kodama, and J. E. Bowers, "Hybrid silicon evanescent laser fabricated with a silicon waveguide and III-V offset quantum wells," *Opt. Express*, vol. 13, no. 23, pp. 9460–9464, 2005.
- [23] G. Roelkens, D. Van Thourhout, R. Baets, R. Nötzel, and M. Smit, "Laser emission and photodetection in an InP/InGaAsP layer integrated on and coupled to a Silicon-on-Insulator waveguide circuit," *Opt. Express*, vol. 14, no. 18, pp. 8154–8159, 2006.
- [24] A. W. Fang, H. Park, O. Cohen, R. Jones, M. J. Paniccia, and J. E. Bowers, "Electrically pumped hybrid AlGaInAs-silicon evanescent laser," *Opt. Express*, vol. 14, no. 20, pp. 9203–9210, 2006.
- [25] A. W. Fang, R. Jones, H. Park, O. Cohen, O. Raday, M. J. Paniccia, and J. E. Bowers, "Integrated AlGaInAs-silicon evanescent racetrack laser and photodetector," *Opt. Express*, vol. 15, no. 5, pp. 2315–2322, 2007.
- [26] J. Van Campenhout, P. Rojo-Romeo, P. Regreny, C. Seassal, D. Van Thourhout, S. Verstuyft, L. Di Cioccio, J. M. Fedeli, C. Lagahe, and R. Baets, "Electrically pumped InP-based microdisk lasers integrated with a nanophotonic silicon-on-insulator waveguide circuit," *Opt. Express*, vol. 15, no. 11, pp. 6744–6749, 2007.
- [27] M. N. Sysak, H. Park, A. W. Fang, J. E. Bowers, R. Jones, O. Cohen, O. Raday, and M. Paniccia, "Experimental and theoretical thermal analysis of a Hybrid Silicon Evanescent Laser," *Opt. Express*, vol. 15, no. 23, pp. 15041–15046, 2007.
- [28] A. W. Fang, E. Lively, Y.-H. Kuo, D. Liang, and J. E. Bowers, "A distributed feedback silicon evanescent laser," *Opt. Express*, vol. 16, no. 7, pp. 4413–4419, 2008.
- [29] J. Van Campenhout, L. Liu, P. Rojo Romeo, D. Van Thourhout, C. Seassal, P. Regreny, L. Di Cioccio, J. M. Fedeli, and R. Baets, "A compact SOI-integrated multiwavelength laser source

- based on cascaded InP microdisks,” *IEEE Photonics Technol. Lett.*, vol. 20, no. 16, pp. 1345–1347, 2008.
- [30] A. W. Fang, B. R. Koch, R. Jones, E. Lively, D. Liang, Y.-H. Kuo, and J. E. Bowers, “A distributed Bragg reflector silicon evanescent laser,” in *2008 5th International Conference on Group IV Photonics, GFP*, 2008, pp. 1667–1669.
- [31] T. Spuesens, L. Liu, T. De Vries, P. R. Romeo, P. Regreny, and D. Van Thourhout, “Improved design of an InP-based microdisk laser heterogeneously integrated with SOI,” in *IEEE International Conference on Group IV Photonics GFP*, 2009, pp. 202–204.
- [32] D. Liang, J. E. Bowers, D. C. Oakley, A. Napopleone, D. C. Chapman, C.-L. Chen, P. W. Juodawlkis, and O. Rada, “High-Quality 150 mm InP-to-Silicon Epitaxial Transfer for Silicon Photonic Integrated Circuits,” *Electrochem. Solid-State Lett.*, vol. 12, 2009.
- [33] V. Passaro, C. Tullio, B. Troia, M. Notte, G. Giannoccaro, and F. Leonardis, “Recent Advances in Integrated Photonic Sensors,” *Sensors*, vol. 12, no. 12, pp. 15558–15598, Nov. 2012.
- [34] G. Roelkens, A. Abassi, P. Cardile, U. Dave, A. de Groot, Y. de Koninck, S. Dhoore, X. Fu, A. Gassenq, N. Hattasan, Q. Huang, S. Kumari, S. Keyvaninia, B. Kuyken, L. Li, P. Mechet, M. Muneeb, D. Sanchez, H. Shao, T. Spuesens, A. Z. Subramanian, S. Uvin, M. Tassaert, K. van Gasse, J. Verbist, R. Wang, Z. Wang, J. Zhang, J. Van Campenhout, X. Yin, J. Bauwelinck, G. Morthier, R. Baets, and D. van Thourhout, “III-V-on-Silicon Photonic Devices for Optical Communication and Sensing,” *Photonics*, vol. 3, pp. 969–1004, 2015.
- [35] Y. Halioua, A. Bazin, P. Monnier, T. J. Karle, G. Roelkens, I. Sagnes, R. Raj, and F. Raineri, “Hybrid III-V semiconductor/silicon nanolaser,” *Opt. Express*, vol. 19, no. 10, p. 9221, May 2011.
- [36] Guang-Hua Duan, C. Jany, A. Le Liepvre, A. Accard, M. Lamponi, D. Make, P. Kaspar, G. Levaufre, N. Girard, F. Lelarge, J.-M. Fedeli, A. Descos, B. Ben Bakir, S. Messaoudene, D. Bordel, S. Menezo, G. de Valicourt, S. Keyvaninia, G. Roelkens, D. Van Thourhout, D. J. Thomson, F. Y. Gardes, and G. T. Reed, “Hybrid III-V on Silicon Lasers for Photonic Integrated Circuits on Silicon,” *IEEE J. Sel. Top. Quantum Electron.*, vol. 20, no. 4, pp. 158–170, Jul. 2014.
- [37] H. Park, A. W. Fang, O. Cohen, R. Jones, M. J. Paniccia, and J. E. Bowers, “A Hybrid AlGaInAs–Silicon Evanescent Amplifier,” *IEEE PHOTONICS Technol. Lett.*, vol. 19, no. 4, pp. 230–232, 2007.
- [38] L. Liu, J. Van Campenhout, G. Roelkens, R. A. Soref, D. Van Thourhout, P. Rojo-Romeo, P. Regreny, C. Seassal, J.-M. Fédéli, and R. Baets, “Carrier-injection-based electro-optic modulator on silicon-on-insulator with a heterogeneously integrated III-V microdisk cavity,” *Opt. Lett.*, vol. 33, no. 21, pp. 2518–2520, 2008.
- [39] Y. Shi, C. Zhang, H. Zhang, J. H. Bechtel, L. R. Dalton, B. H. Robinson, and W. H. Steier, “Low (Sub-1-Volt) Halfwave Voltage Polymeric Electro-optic Modulators Achieved by Controlling Chromophore Shape,” *Science (80-.)*, vol. 288, pp. 119–122, 2000.
- [40] J. Luo, S. Huang, Y. J. Cheng, T. D. Kim, Z. Shi, X. H. Zhou, and A. K. Y. Jen, “Phenyltetraene-based nonlinear optical chromophores with enhanced chemical stability and electrooptic activity,” *Org. Lett.*, vol. 9, no. 22, pp. 4471–4474, 2007.
- [41] C. Koos, P. Vorreau, T. Vallaitis, P. Dumon, W. Bogaerts, R. Baets, B. Esembeson, I. Biaggio, T. Michinobu, F. Diederich, W. Freude, and J. Leuthold, “All-optical high-speed signal processing with silicon–organic hybrid slot waveguides,” *Nat. Photonics*, vol. 3, no. 4, pp. 216–219, Apr. 2009.

- [42] W. Zhang, S. Serna, N. Dubreuil, and E. Cassan, “Nonlinear optimization of slot Si waveguides: TPA minimization with FOMTPA up to 4.25,” *Opt. Lett.*, vol. 40, no. 7, p. 1212, Apr. 2015.
- [43] A. Y. Liu, S. Srinivasan, J. Norman, A. C. Gossard, and J. E. Bowers, “Quantum dot lasers for silicon photonics [Invited],” *Photonics Res.*, vol. 3, no. 5, p. B1, Oct. 2015.
- [44] G. Kurczveil, D. Liang, M. Fiorentino, and R. G. Beausoleil, “Robust hybrid quantum dot laser for integrated silicon photonics,” *Opt. Express*, vol. 24, no. 14, pp. 16167–16174, 2016.
- [45] M. Sugawara and M. Usami, “Quantum dot devices handling the heat,” *Nat. Photonics*, vol. 3, pp. 30–31, 2009.
- [46] G. Park, O. B. Shchekin, D. L. Huffaker, and D. G. Deppe, “Low-threshold oxide-confined 1.3- μm quantum-dot laser,” *IEEE Photonics Technol. Lett.*, vol. 13, no. 3, pp. 230–232, 2000.
- [47] A. Pospischil, M. Humer, M. M. Furchi, D. Bachmann, R. Guider, T. Fromherz, and T. Mueller, “CMOS-compatible graphene photodetector covering all optical communication bands,” *Nat. Photonics*, vol. 7, no. 11, pp. 892–896, Sep. 2013.
- [48] M. Liu, X. Yin, E. Ulin-Avila, B. Geng, T. Zentgraf, L. Ju, F. Wang, and X. Zhang, “A graphene-based broadband optical modulator,” *Nature*, vol. 474, no. 7349, pp. 64–67, Jun. 2011.
- [49] Y. Gao, R.-J. Shiue, X. Gan, L. Li, C. Peng, I. Meric, L. Wang, A. Szep, D. Walker, J. Hone, and D. Englund, “High-Speed Electro-Optic Modulator Integrated with Graphene-Boron Nitride Heterostructure and Photonic Crystal Nanocavity,” *Nano Lett.*, vol. 15, no. 3, pp. 2001–2005, Mar. 2015.
- [50] D. Thomson, A. Zilkie, J. E. Bowers, T. Komljenovic, G. T. Reed, L. Vivien, D. Marris-Morini, E. Cassan, L. Virost, J.-M. Fédéli, J.-M. Hartmann, J. H. Schmid, D.-X. Xu, F. Boeuf, P. O’Brien, G. Z. Mashanovich, and M. Nedeljkovic, “Roadmap on silicon photonics,” *J. Opt.*, vol. 18, no. 7, p. 73003, Jul. 2016.
- [51] F. Bonaccorso, Z. Sun, T. Hasan, and A. C. Ferrari, “Graphene photonics and optoelectronics,” *Nat. Photonics*, vol. 4, no. 9, pp. 611–622, Sep. 2010.
- [52] S. J. Koester, H. Li, and M. Li, “Switching energy limits of waveguide-coupled graphene-on-graphene optical modulators,” *Opt. Express*, vol. 20, no. 18, p. 20330, Sep. 2012.
- [53] N. Youngblood and M. Li, “Integration of 2D materials on a silicon photonics platform for optoelectronics applications,” *Nanophotonics*, vol. 0, no. 0, Jan. 2016.
- [54] A. Noury, X. Le Roux, L. Vivien, and N. Izard, “Controlling carbon nanotube photoluminescence using silicon microring resonators,” *Nanotechnology*, vol. 25, no. 21, p. 215201, May 2014.
- [55] A. Noury, X. Le Roux, L. Vivien, and N. Izard, “Enhanced light emission from carbon nanotubes integrated in silicon micro-resonator,” *Nanotechnology*, vol. 26, no. 34, p. 345201, Aug. 2015.
- [56] R. Watahiki, T. Shimada, P. Zhao, S. Chiashi, S. Iwamoto, Y. Arakawa, S. Maruyama, and Y. K. Kato, “Enhancement of carbon nanotube photoluminescence by photonic crystal nanocavities,” *Appl. Phys. Lett.*, vol. 101, no. 14, p. 141124, Oct. 2012.
- [57] R. Miura, S. Imamura, R. Ohta, A. Ishii, X. Liu, T. Shimada, S. Iwamoto, Y. Arakawa, and Y. K. Kato, “Ultralow mode-volume photonic crystal nanobeam cavities for high-efficiency coupling to individual carbon nanotube emitters,” *Nat. Commun.*, vol. 5, p. 5580, Nov. 2014.
- [58] F. Pyatkov, V. Fütterling, S. Khasminskaya, B. S. Flavel, F. Hennrich, M. M. Kappes, R. Krupke, and W. H. P. Pernice, “Cavity-enhanced light emission from electrically driven carbon nanotubes,” *Nat. Photonics*, vol. 10, no. 6, pp. 420–427, Apr. 2016.

- [59] P. Avouris, M. Freitag, and V. Perebeinos, "Carbon-nanotube photonics and optoelectronics," *Nat. Photonics*, vol. 2, no. 6, pp. 341–350, Jun. 2008.
- [60] R. Jansen and P. Wallis, "Manufacturing, Characterization and Use of Single Walled Carbon Nanotubes," *Mater. Matters*, vol. 4, no. 1, pp. 23–27, Sep. 2009.
- [61] A. Jorio, G. Dresselhaus, and M. S. Dresselhaus, *Carbon nanotubes: Advanced Topics in Synthesis, Structure, Properties and Applications*. Berlin, Heidelberg: Springer Berlin Heidelberg, 2008.
- [62] S. M. Bachilo, M. S. Strano, C. Kittrell, R. H. Hauge, R. E. Smalley, and R. B. Weisman, "Structure-Assigned Optical Spectra of Single-Walled Carbon Nanotubes," *Science (80-.)*, vol. 298, no. 5602, pp. 2361–2366, Dec. 2002.
- [63] A. Nish, J.-Y. Hwang, J. Doig, and R. J. Nicholas, "Highly selective dispersion of single-walled carbon nanotubes using aromatic polymers," *Nat. Photonics*, vol. 2, pp. 640–646, 2007.
- [64] M. J. O'Connell, S. M. Bachilo, C. B. Huffman, V. C. Moore, M. S. Strano, E. H. Haroz, K. L. Rialon, P. J. Boul, W. H. Noon, C. Kittrell, J. Ma, R. H. Hauge, R. B. Weisman, and R. E. Smalley, "Band Gap Fluorescence from Individual Single-Walled Carbon," *Science (80-.)*, vol. 297, pp. 593–596, 2002.
- [65] J. A. Misewich, R. Martel, P. Avouris, J. C. Tsang, S. Heinze, and J. Tersoff, "Electrically Induced Optical Emission from a Carbon Nanotube FET," *Angew. Chem. Int. Ed. Engl. Angew. Chem. Int. Ed. J. Bai, A. V. Virovets, M. Scheer, Angew. Chem. Int. Ed*, vol. 300, pp. 783–786, 2003.
- [66] E. Gauffrès, N. Izard, L. Vivien, S. Kazaoui, D. Marris-Morini, and E. Cassan, "Enhancement of semiconducting single-wall carbon-nanotube photoluminescence," *Opt. Lett.*, vol. 34, no. 24, p. 3845, Dec. 2009.
- [67] E. Gauffrès, N. Izard, A. Noury, X. Le Roux, G. Rasigade, A. Beck, and L. Vivien, "Light Emission in Silicon from Carbon Nanotubes," *ACS Nano*, vol. 6, no. 5, pp. 3813–3819, May 2012.
- [68] M. Freitag, Y. Martin, J. A. Misewich, | R Martel, and P. Avouris, "Photoconductivity of Single Carbon Nanotubes," *Nano Lett.*, vol. 3, no. 8, pp. 1067–1071, 2003.
- [69] V. A. Margulis, E. A. Gaiduk, and E. N. Zhidkin, "Quadratic electro-optic effects in semiconductor carbon nanotubes," *Phys. Lett. A*, vol. 258, pp. 394–400, 1999.
- [70] E. Gauffrès, N. Izard, X. Le Roux, D. Marris-Morini, S. Kazaoui, E. Cassan, and L. Vivien, "Optical gain in carbon nanotubes," *Appl. Phys. Lett.*, vol. 96, no. 23, p. 231105, 2010.
- [71] D. Legrand, C. Roquelet, G. Lanty, P. Roussignol, X. Lafosse, S. Bouchoule, E. Deleporte, C. Voisin, and J. S. Lauret, "Monolithic microcavity with carbon nanotubes as active material," *Appl. Phys. Lett.*, vol. 102, p. 153102, 2013.
- [72] M. Fujiwara, D. Tsuya, and H. Maki, "Electrically driven, narrow-linewidth blackbody emission from carbon nanotube microcavity devices," *Cit. Appl. Phys. Lett. J. Appl. Phys. J. Appl. Phys. Phys. Lett. Appl. Phys. Lett*, vol. 103, no. 10, pp. 143122–44327, 2013.
- [73] S. Imamura, R. Watahiki, R. Miura, T. Shimada, and Y. K. Kato, "Optical control of individual carbon nanotube light emitters by spectral double resonance in silicon microdisk resonators," *Appl. Phys. Lett.*, vol. 102, no. 16, p. 161102, 2013.
- [74] N. Izard, S. Kazaoui, K. Hata, T. Okazaki, T. Saito, S. Iijima, and N. Minami, "Semiconductor-enriched single wall carbon nanotube networks applied to field effect transistors," *Appl. Phys. Lett.*, vol. 92, no. 24, p. 243112, 2008.

- [75] M. C. Estevez, M. Alvarez, and L. M. Lechuga, "Integrated optical devices for lab-on-a-chip biosensing applications," *Laser Photon. Rev.*, vol. 6, no. 4, pp. 463–487, Jul. 2012.
- [76] J. V. Jokerst, J. W. Jacobson, B. D. Bhagwandin, P. N. Floriano, N. Christodoulides, and J. T. McDevitt, "Programmable Nano-Bio-Chip Sensors: Analytical Meets Clinical," *Anal. Chem.*, vol. 82, no. 5, pp. 1571–1579, Mar. 2010.
- [77] A. Fernández Gavela, D. Grajales García, J. Ramirez, and L. Lechuga, "Last Advances in Silicon-Based Optical Biosensors," *Sensors*, vol. 16, no. 3, p. 285, Feb. 2016.
- [78] M. G. Scullion, A. Di Falco, and T. F. Krauss, "Slotted photonic crystal cavities with integrated microfluidics for biosensing applications," *Biosens. Bioelectron.*, vol. 27, no. 1, pp. 101–105, Sep. 2011.
- [79] D. Duval and L. M. Lechuga, *Optical Waveguide Biosensors. In Photonics: Scientific Foundations, Technology and Applications, IV*. NJ, USA: John Wiley & Sons: Hoboken, 2015.
- [80] J. T. Kirk, G. E. Fridley, J. W. Chamberlain, E. D. Christensen, M. Hochberg, and D. M. Ratner, "Multiplexed inkjet functionalization of silicon photonic biosensors," *Lab Chip*, vol. 11, no. 7, p. 1372, 2011.
- [81] K. De Vos, I. Bartolozzi, E. Schacht, P. Bienstman, and R. Baets, "Silicon-on-Insulator microring resonator for sensitive and label-free biosensing," *Opt. Express*, vol. 15, no. 12, p. 7610, 2007.
- [82] I. M. White and X. Fan, "On the performance quantification of resonant refractive index sensors," *Opt. Express*, vol. 16, no. 2, p. 1020, Jan. 2008.
- [83] L. J. Sherry, S.-H. Chang, G. C. Schatz, R. P. Van Duyne, B. J. Wiley, and Y. Xia, "Localized Surface Plasmon Resonance Spectroscopy of Single Silver Nanocubes," *Nano Lett.*, vol. 5, no. 10, pp. 2034–2038, Oct. 2005.
- [84] J. Yang, L. Jiang, S. Wang, B. Li, M. Wang, H. Xiao, Y. Lu, and H. Tsai, "High sensitivity of taper-based Mach–Zehnder interferometer embedded in a thinned optical fiber for refractive index sensing," *Appl. Opt.*, vol. 50, no. 28, pp. 5503–5507, 2011.
- [85] W. Zhang, S. Serna, X. Le Roux, L. Vivien, and E. Cassan, "Highly sensitive refractive index sensing by fast detuning the critical coupling condition of slot waveguide ring resonators," *Opt. Lett.*, vol. 41, no. 3, pp. 532–535, 2016.
- [86] S. Kim, H.-M. Kim, and Y.-H. Lee, "Single nanobeam optical sensor with a high Q-factor and high sensitivity," *Opt. Lett.*, vol. 40, no. 22, pp. 5351–5354, 2015.
- [87] M. El Beheiry, V. Liu, S. Fan, and O. Levi, "Sensitivity enhancement in photonic crystal slab biosensors," *Opt. Express*, vol. 18, no. 22, pp. 22702–22714, 2010.
- [88] Soon-Hong Kwon, "Deep Subwavelength-Scale Metal-Insulator-Metal Plasmonic Disk Cavities for Refractive Index Sensors," *IEEE Photonics J.*, vol. 5, no. 1, pp. 4800107–4800107, Feb. 2013.
- [89] D. X. Xu, J. H. Schmid, G. T. Reed, G. Z. Mashanovich, D. J. Thomson, M. Nedeljkovic, X. Chen, D. Van Thourhout, S. Keyvaninia, and S. K. Selvaraja, "Silicon photonic integration platform—Have we found the sweet spot?," *IEEE J. Sel. Top. Quantum Electron.*, vol. 20, no. 4, p. 8100217, 2014.
- [90] S. Xiao, M. H. Khan, H. Shen, and M. Qi, "Compact silicon microring resonators with ultra-low propagation loss in the C band.," *Opt. Express*, vol. 15, no. 22, pp. 14467–14475, 2007.
- [91] S. K. Selvaraja, P. De Heyn, G. Winroth, P. Ong, G. Lepage, C. Cailler, A. Rigny, K. K. Bourdelle, W. Bogaerts, D. Van Thourhout, J. Van Campenhout, and P. Absil, "Highly uniform and low-loss

- passive silicon photonics devices using a 300mm CMOS platform,” in *Conference on Optical Fiber Communication, Technical Digest Series*, 2014.
- [92] V. R. Almeida, Q. Xu, C. A. Barrios, and M. Lipson, “Guiding and confining light in void nanostructure,” *Opt. Lett.*, vol. 29, no. 11, p. 1209, Jun. 2004.
- [93] X. Wang, S. Grist, J. Flueckiger, N. A. F. Jaeger, and L. Chrostowski, “Silicon photonic slot waveguide Bragg gratings and resonators,” *Opt. Express*, vol. 21, no. 16, pp. 19029–19039, 2013.
- [94] W. Zhang, S. Serna, X. Le Roux, C. Alonso-Ramos, L. Vivien, and E. Cassan, “Analysis of silicon-on-insulator slot waveguide ring resonators targeting high Q-factors,” *Opt. Lett.*, vol. 40, no. 23, p. 5566, Dec. 2015.
- [95] P. A. Anderson, B. S. Schmidt, and M. Lipson, “High confinement in silicon slot waveguides with sharp bends,” *Opt. Express*, vol. 14, no. 20, pp. 9197–9202, 2006.
- [96] W. Bogaerts, P. de Heyn, T. van Vaerenbergh, K. de Vos, S. Kumar Selvaraja, T. Claes, P. Dumon, P. Bienstman, D. van Thourhout, and R. Baets, “Silicon microring resonators,” *Laser Photonics Rev.*, vol. 6, no. 1, pp. 47–73, 2012.
- [97] J. Niehusmann, A. Vörckel, P. H. Bolivar, T. Wahlbrink, W. Henschel, and H. Kurz, “Ultrahigh-quality-factor silicon-on-insulator microring resonator,” *Opt. Lett.*, vol. 29, no. 24, p. 2861, Dec. 2004.
- [98] L.-W. Luo, G. S. Wiederhecker, J. Cardenas, C. Poitras, and M. Lipson, “High quality factor etchless silicon photonic ring resonators,” *Opt. Express*, vol. 19, no. 7, pp. 6284–6289, 2011.
- [99] T. Baehr-Jones, M. Hochberg, C. Walker, and A. Scherer, “High-Q optical resonators in silicon-on-insulator-based slot waveguides,” *Appl. Phys. Lett.*, vol. 86, p. 81101, 2005.
- [100] T. Claes, W. Bogaerts, and P. Bienstman, “Experimental characterization of a silicon photonic biosensor consisting of two cascaded ring resonators based on the Vernier-effect and introduction of a curve fitting method for an improved detection limit,” *Opt. Express*, vol. 18, no. 22, pp. 22747–22761, 2010.
- [101] V. M. N. Passaro, B. Troia, and F. De Leonardis, “A generalized approach for design of photonic gas sensors based on Vernier-effect in mid-IR,” *Sensors Actuators, B Chem.*, vol. 168, pp. 402–420, 2012.
- [102] M. La Notte, B. Troia, T. Muciaccia, C. E. Campanella, F. De Leonardis, and V. M. N. Passaro, “Recent Advances in Gas and Chemical Detection by Vernier Effect-Based Photonic Sensors,” *Sensors*, vol. 14, pp. 4831–4855, 2014.
- [103] J. J. D. Joannopoulos, S. Johnson, J. N. J. Winn, and R. R. D. Meade, *Photonic crystals: molding the flow of light*. 2008.
- [104] A. Chutinan and S. Noda, “Waveguides and waveguide bends in two-dimensional photonic crystal slabs,” *Phys. Rev. B*, vol. 62, no. 7, pp. 4488–4492, 2000.
- [105] M. Notomi, A. Shinya, K. Yamada, J. Takahashi, C. Takahashi, and I. Yokohama, “Singlemode transmission within photonic bandgap of width-varied single-line-defect photonic crystal waveguides on SOI substrates,” *Electron. Lett.*, vol. 37, no. 5, pp. 293–295, 2001.
- [106] T. Baba, A. Motegi, T. Iwai, N. Fukaya, Y. Watanabe, and A. Sakai, “Light propagation characteristics of straight single-line-defect waveguides in photonic crystal slabs fabricated into a silicon-on-insulator substrate,” *IEEE J. Quantum Electron.*, vol. 38, no. 2, pp. 743–752, 2002.
- [107] E. Kuramochi, M. Notomi, S. Hughes, A. Shinya, T. Watanabe, and L. Ramunno, “Disorder-

- induced scattering loss of line-defect waveguides in photonic crystal slabs,” *Phys. Rev. B - Condens. Matter Mater. Phys.*, vol. 72, p. 161318, 2005.
- [108] M. Lončar, T. Doll, J. Vučkovi, and A. Scherer, “Design and Fabrication of Silicon Photonic Crystal Optical Waveguides,” *J. Light. Technol.*, vol. 18, no. 10, pp. 1402–1411, 2000.
- [109] C. Jamois, R. B. Wehrspohn, L. C. Andreani, C. Hermann, O. Hess, and U. Gösele, “Silicon-based two-dimensional photonic crystal waveguides,” *Photonics Nanostructures - Fundam. Appl.*, vol. 1, pp. 1–13, 2003.
- [110] Y. A. Vlasov, M. O’Boyle, H. F. Hamann, and S. J. Mcnab, “Active control of slow light on a chip with photonic crystal waveguides,” *Nature*, vol. 483, pp. 65–69, 2005.
- [111] S. Mazoyer, J. P. Hugonin, and P. Lalanne, “Disorder-induced multiple scattering in photonic-crystal waveguides,” *Phys. Rev. Lett.*, vol. 103, p. 63903, 2009.
- [112] S. A. Schulz, L. O’Faolain, D. M. Beggs, T. P. White, A. Melloni, and T. F. Krauss, “Dispersion engineered slow light in photonic crystals: a comparison,” *J. Opt.*, vol. 12, p. 104004, 2010.
- [113] A. Di Falco, L. O’Faolain, and T. F. Krauss, “Photonic crystal slotted slab waveguides,” *Photonics Nanostructures - Fundam. Appl.*, vol. 6, pp. 38–41, 2008.
- [114] A. Di Falco, L. O’Faolain, and T. F. Krauss, “Dispersion control and slow light in slotted photonic crystal waveguides,” *Appl. Phys. Lett.*, vol. 92, p. 83501, 2008.
- [115] J. Wu, C. Peng, Y.-P. Li, and Z.-Y. Wang, “Light Localization in Slot Photonic Crystal Waveguide,” *Chin. Phys. Lett.*, vol. 26, no. 1, p. 14209, 2009.
- [116] T. Tanabe, M. Notomi, S. Mitsugi, A. Shinya, and E. Kuramochi, “Fast bistable all-optical switch and memory on a silicon photonic crystal on-chip,” *Opt. Lett.*, vol. 30, no. 19, p. 2575, Oct. 2005.
- [117] K. Hennessy, A. Badolato, M. Winger, D. Gerace, M. Atatüre, S. Gulde, S. Fält, E. L. Hu, and A. Imamoglu, “Quantum nature of a strongly coupled single quantum dot–cavity system,” *Nature*, vol. 445, no. 7130, pp. 896–899, Feb. 2007.
- [118] T. Yoshie, A. Scherer, J. Hendrickson, G. Khitrova, H. M. Gibbs, G. Rupper, C. Ell, O. B. Shchekin, and D. G. Deppe, “Vacuum Rabi splitting with a single quantum dot in a photonic crystal nanocavity,” *Nature*, vol. 432, no. 7014, pp. 200–203, Nov. 2004.
- [119] D. Englund, D. Fattal, E. Waks, G. Solomon, B. Zhang, T. Nakaoka, Y. Arakawa, Y. Yamamoto, and J. Vučkovi, “Controlling the spontaneous emission rate of single quantum dots in a two-dimensional photonic crystal,” *Phys. Rev. Lett.*, vol. 95, no. 1, pp. 2–5, 2005.
- [120] E. M. Purcell, “Spontaneous emission probabilities at radio frequencies,” *Phys. Rev.*, vol. 69, no. 681, p. 37, 1946.
- [121] B.-S. Song, S. Noda, T. Asano, and Y. Akahane, “Ultra-high-Q photonic double-heterostructure nanocavity,” *Nat. Mater.*, vol. 4, no. 3, pp. 207–210, Mar. 2005.
- [122] Z. Zhang and M. Qiu, “Small-volume waveguide-section high Q microcavities in 2D photonic crystal slabs,” *Opt. Express*, vol. 12, no. 17, pp. 3988–3995, 2004.
- [123] M. Nomura, K. Tanabe, S. Iwamoto, and Y. Arakawa, “High-Q design of semiconductor-based ultrasmall photonic crystal nanocavity,” *Opt. Express*, vol. 18, no. 8, pp. 8144–8150, 2010.
- [124] U. P. Dharanipathy, M. Minkov, M. Tonin, V. Savona, and R. Houdré, “High-Q silicon photonic crystal cavity for enhanced optical nonlinearities,” *Appl. Phys. Lett.*, vol. 105, p. 101101, 2014.
- [125] H.-Y. Ryu, M. Notomi, and Y.-H. Lee, “High-quality-factor and small-mode-volume hexapole

- modes in photonic-crystal-slab nanocavities,” *Appl. Phys. Lett.*, vol. 83, no. 21, pp. 4294–4296, 2003.
- [126] H. Takagi, Y. Ota, N. Kumagai, S. Ishida, S. Iwamoto, and Y. Arakawa, “High Q H1 photonic crystal nanocavities with efficient vertical emission,” *Opt. Express*, vol. 20, no. 27, pp. 28292–28300, 2012.
- [127] Y. Akahane, T. Asano, B.-S. Song, and S. Noda, “High-Q photonic nanocavity in a two-dimensional photonic crystal,” *Nature*, vol. 425, pp. 944–947, 2003.
- [128] Y. Akahane, T. Asano, B.-S. Song, and S. Noda, “Fine-tuned high-Q photonic-crystal nanocavity,” *Opt. Express*, vol. 13, no. 4, pp. 1202–1214, 2005.
- [129] M. Minkov and V. Savona, “Automated optimization of photonic crystal slab cavities,” *Sci. Rep.*, vol. 4, p. 5124, 2014.
- [130] T. Asano, B.-S. Song, Y. Akahane, and S. Noda, “Ultrahigh-Q Nanocavities in Two-Dimensional Photonic Crystal Slabs,” *IEEE J. Sel. Top. Quantum Electron.*, vol. 12, no. 6, pp. 1123–1134, Nov. 2006.
- [131] H. Sekoguchi, Y. Takahashi, T. Asano, and S. Noda, “Photonic crystal nanocavity with a Q-factor of ~ 9 million,” *Opt. Express*, vol. 22, no. 1, pp. 916–924, 2014.
- [132] J. T. Robinson, C. Manolatu, L. Chen, and M. Lipson, “Ultrasmall Mode Volumes in Dielectric Optical Microcavities,” *Phys. Rev. Lett.*, vol. 95, p. 143901, 2005.
- [133] T. Yamamoto, M. Notomi, H. Taniyama, E. Kuramochi, Y. Yoshikawa, Y. Torii, and T. Kuga, “Design of a high-Q air-slot cavity based on a width-modulated line-defect in a photonic crystal slab,” *Opt. Express*, vol. 16, no. 18, p. 13809, Sep. 2008.
- [134] A. Di Falco, L. O’Faolain, and T. F. Krauss, “Chemical sensing in slotted photonic crystal heterostructure cavities,” *Appl. Phys. Lett.*, vol. 94, no. 6, p. 63503, Feb. 2009.
- [135] K. Li, J. Li, Y. Song, G. Fang, C. Li, Z. Feng, R. Su, B. Zeng, X. Wang, and C. Jin, “Ln Slot Photonic Crystal Microcavity for Refractive Index Gas Sensing,” *IEEE Photonics J.*, vol. 6, no. 5, p. 6802509, 2014.
- [136] J. Jágerská, H. Zhang, Z. Diao, N. Le Thomas, and R. Houdré, “Refractive index sensing with an air-slot photonic crystal nanocavity,” *Opt. Lett.*, vol. 35, no. 15, pp. 2523–2525, 2010.
- [137] K. Li, J. Li, Y. Song, G. Fang, C. Li, Z. Feng, R. Su, B. Zeng, X. Wang, and C. Jin, “Ln Slot Photonic Crystal Microcavity for Refractive Index Gas Sensing,” *IEEE Photonics J.*, vol. 6, no. 5, pp. 1–9, Oct. 2014.
- [138] A. Di Falco, L. O’faolain, and T. F. Krauss, “Chemical sensing in slotted photonic crystal heterostructure cavities,” *Appl. Phys. Lett.*, vol. 94, p. 63503, 2009.
- [139] S. Hamed Mirsadeghi, E. Schelew, and J. F. Young, “Photonic crystal slot-microcavity circuit implemented in silicon-on-insulator: High Q operation in solvent without undercutting,” *Appl. Phys. Lett.*, vol. 102, p. 131115, 2013.
- [140] H.-G. Park, S.-H. Kim, S.-H. Kwon, Y.-G. Ju, J.-K. Yang, J.-H. Baek, S.-B. Kim, and Y.-H. Lee, “Electrically Driven Single-Cell Photonic Crystal Laser,” *Science (80-.)*, vol. 305, p. 1444, 2004.
- [141] M. Nomura, S. Iwamoto, M. Nishioka, S. Ishida, and Y. Arakawa, “Highly efficient optical pumping of photonic crystal nanocavity lasers using cavity resonant excitation,” *Appl. Phys. Lett.*, vol. 89, no. 16, p. 161111, Oct. 2006.

- [142] B. Ellis, M. A. Mayer, G. Shambat, T. Sarmiento, J. Harris, E. E. Haller, and J. Vučković, “Ultralow-threshold electrically pumped quantum-dot photonic-crystal nanocavity laser,” *Nat. Photonics*, vol. 5, no. 5, pp. 297–300, May 2011.
- [143] Y. Takahashi, Y. Inui, M. Chihara, T. Asano, R. Terawaki, and S. Noda, “A micrometre-scale Raman silicon laser with a microwatt threshold,” *Nature*, vol. 498, pp. 470–474, 2013.
- [144] K. Hirose, Y. Liang, Y. Kurosaka, A. Watanabe, T. Sugiyama, and S. Noda, “Watt-class high-power, high-beam-quality photonic-crystal lasers,” *Nat. Photonics*, vol. 8, no. 5, pp. 406–411, Apr. 2014.
- [145] D. G. Angelakis, M. F. Santos, V. Yannopoulos, and A. Ekert, “A proposal for the implementation of quantum gates with photonic-crystal waveguides,” *Phys. Lett. Sect. A Gen. At. Solid State Phys.*, vol. 362, pp. 377–380, 2007.
- [146] R. H. Hadfield, “Single-photon detectors for optical quantum information applications,” *Nat. Photonics*, vol. 3, 2009.
- [147] W.-C. Lai, S. Chakravarty, Y. Zou, and R. T. Chen, “Silicon nano-membrane based photonic crystal microcavities for high sensitivity bio-sensing.”
- [148] P. E. Barclay, K. Srinivasan, and O. Painter, “Nonlinear response of silicon photonic crystal microresonators excited via an integrated waveguide and fiber taper,” *Opt. Express*, vol. 13, no. 3, pp. 801–820, 2005.
- [149] E. M. Purcell, “Spontaneous emission probabilities at radio frequencies,” *Phys. Rev.*, vol. 69, p. 681, 1946.
- [150] L. C. Andreani and G. Panzarini, “Strong-coupling regime for quantum boxes in pillar microcavities: Theory Lucio,” *Phys. Rev. B*, vol. 60, no. 19, pp. 13276–13279, 1999.
- [151] S. G. Johnson and J. D. Joannopoulos, “Block-iterative frequency-domain methods for Maxwell’s equations in a planewave basis,” *Opt. Express*, vol. 8, no. 3, pp. 173–190, 2000.
- [152] C. Caër, X. Le Roux, and E. Cassan, “High- Q silicon-on-insulator slot photonic crystal cavity infiltrated by a liquid,” *Appl. Phys. Lett.*, vol. 103, no. 25, p. 251106, Dec. 2013.
- [153] S. Shi, C. Chen, and D. W. Prather, “Plane-wave expansion method for calculating band structure of photonic crystal slabs with perfectly matched layers,” *J. Opt. Soc. Am. A*, vol. 21, no. 9, p. 1769, Sep. 2004.
- [154] A. Taflove, *Computational Electrodynamics The Finite-Difference Time-Domain Methods*. Artech house, INC., 1995.
- [155] Y. Tanaka, T. Asano, and S. Noda, “Design of Photonic Crystal Nanocavity With Q-Factor of $\sim 10^9$,” *J. Light. Technol.*, vol. 26, no. 11, pp. 1532–1539, 2008.
- [156] B.-S. Song, S.-W. Jeon, and S. Noda, “Symmetrically glass-clad photonic crystal nanocavities with ultrahigh quality factors,” *Opt. Lett.*, vol. 36, no. 1, pp. 91–93, 2010.
- [157] T. Asano, B. S. Song, Y. Tanaka, and S. Noda, “Investigation of a channel-add/drop-filtering device using acceptor-type point defects in a two-dimensional photonic-crystal slab,” *Appl. Phys. Lett.*, vol. 83, no. 3, pp. 407–409, 2003.
- [158] Z. Zhang and M. Qiu, “Compact in-plane channel drop filter design using a single cavity with two degenerate modes in 2D photonic crystal slabs,” *Opt. Express*, vol. 13, no. 7, pp. 2596–2604, 2005.

- [159] T. Tanabe, M. Notomi, S. Mitsugi, A. Shinya, and E. Kuramochi, "All-optical switches on a silicon chip realized using photonic crystal nanocavities," *Appl. Phys. Lett.*, vol. 87, no. 15, pp. 1–3, 2005.
- [160] Y. Yu, M. Heuck, H. Hu, W. Xue, C. Peucheret, Y. Chen, L. K. Oxenløwe, K. Yvind, and J. Mørk, "Fano resonance control in a photonic crystal structure and its application to ultrafast switching," *Appl. Phys. Lett.*, vol. 105, no. 6, p. 61117, Aug. 2014.
- [161] Y. Zhao, C. Qian, K. Qiu, J. Tang, Y. Sun, K. Jin, and X. Xu, "Gain enhanced Fano resonance in a coupled photonic crystal cavity-waveguide structure," *Sci. Rep.*, vol. 6, no. 1961, p. 33645, Sep. 2016.
- [162] D. Yang, H. Tian, and Y. Ji, "Nanoscale photonic crystal sensor arrays on monolithic substrates using side-coupled resonant cavity arrays," *Opt. Express*, vol. 19, no. 21, p. 20023, Oct. 2011.
- [163] E. Waks and J. Vuckovic, "Coupled mode theory for photonic crystal cavity-waveguide interaction," *Opt. Express*, vol. 13, no. 13, p. 5064, 2005.
- [164] A. Faraon, E. Waks, D. Englund, I. Fushman, and J. Vučković, "Efficient photonic crystal cavity-waveguide couplers," *Appl. Phys. Lett.*, vol. 90, no. 7, p. 73102, Feb. 2007.
- [165] D. Englund, A. Faraon, B. Zhang, Y. Yamamoto, and J. Vučković, "Generation and transfer of single photons on a photonic crystal chip," *Opt. Express*, vol. 15, no. 9, pp. 5550–5558, 2007.
- [166] M. Okano, S. Kako, and S. Noda, "Coupling between a point-defect cavity and a line-defect waveguide in three-dimensional photonic crystal," *Phys. Rev. B*, vol. 68, p. 235110, 2003.
- [167] G.-H. Kim, Y.-H. Lee, A. Shinya, and M. Notomi, "Coupling of small, low-loss hexapole mode with photonic crystal slab waveguide mode," *Opt. Express*, vol. 12, no. 26, pp. 6624–6631, 2004.
- [168] C. Manolatou, M. J. Khan, S. Fan, P. R. Villeneuve, H. A. Haus, and J. D. Joannopoulos, "Coupling of modes analysis of resonant channel add-drop filters," *IEEE J. Quantum Electron.*, vol. 35, no. 9, pp. 1322–1331, 1999.
- [169] Q. Li, T. Wang, Y. Su, M. Yan, and M. Qiu, "Coupled mode theory analysis of mode-splitting in coupled cavity system," *Opt. Commun.*, vol. 18, no. 8, pp. 8367–8382, 2010.
- [170] Y. Xu, R. K. Lee, and A. Yariv, "Scattering-theory analysis of waveguide-resonator coupling," *Phys. Rev. E - Stat. Nonlinear, Soft Matter Phys.*, vol. 62, no. 5, pp. 7389–7404, 2000.
- [171] M. Minkov and V. Savona, "Automated optimization of photonic crystal slab cavities," *Sci. Rep.*, vol. 4, p. 5124, May 2014.
- [172] S. Hughes, L. Ramunno, J. F. Young, and J. E. Sipe, "Extrinsic optical scattering loss in photonic crystal waveguides: Role of fabrication disorder and photon group velocity," *Phys. Rev. Lett.*, vol. 94, p. 33903, 2005.
- [173] S. Mazoyer, P. Lalanne, J. C. Rodier, J. P. Hugonin, M. Spasenović, L. Kuipers, D. M. Beggs, and T. F. Krauss, "Statistical fluctuations of transmission in slow light photonic-crystal waveguides," *Opt. Express*, vol. 18, no. 14, p. 14654, Jul. 2010.
- [174] Y. Zhao, C. Qian, K. Qiu, Y. Gao, and X. Xu, "Ultrafast optical switching using photonic molecules in photonic crystal waveguides," *Opt. Express*, vol. 23, no. 7, p. 9211, Apr. 2015.
- [175] T. Karle, A. Michaeli, M. Salib, and T. Krauss, "Coupled photonic crystal heterostructure nanocavities," *Opt. Express*, vol. 15, no. 3, pp. 1228–1233, 2007.
- [176] S. V Boriskina, "Spectrally engineered photonic molecules as optical sensors with enhanced

- sensitivity: a proposal and numerical analysis,” *J. Opt. Soc. Am. B*, vol. 23, no. 8, pp. 1565–1573, 2006.
- [177] N. Caselli, F. Intonti, F. Riboli, and M. Gurioli, “Engineering the mode parity of the ground state in photonic crystal molecules,” *Opt. Express*, vol. 22, no. 5, p. 4953, Mar. 2014.
- [178] K. Nozaki, A. Shinya, S. Matsuo, T. Sato, E. Kuramochi, and M. Notomi, “Ultralow-energy and high-contrast all-optical switch involving Fano resonance based on coupled photonic crystal nanocavities,” *Opt. Express*, vol. 21, no. 10, p. 11877, May 2013.
- [179] M. Notomi, E. Kuramochi, and T. Tanabe, “Large-scale arrays of ultrahigh-Q coupled nanocavities,” *Nat. Photonics*, vol. 2, no. 12, pp. 741–747, Nov. 2008.
- [180] M. Bayer, T. Gutbrod, J. P. Reithmaier, A. Forchel, T. L. Reinecke, P. A. Knipp, A. A. Dremin, and V. D. Kulakovskii, “Optical Modes in Photonic Molecules,” *Phys. Rev. Lett.*, vol. 81, no. 12, pp. 2582–2585, 1998.
- [181] C. Schmidt, A. Chipouline, T. Käsebier, E. B. Kley, A. Tünnermann, T. Pertsch, V. Shuvayev, and L. I. Deych, “Observation of optical coupling in microdisk resonators,” *Phys. Rev. A - At. Mol. Opt. Phys.*, vol. 80, p. 43841, 2009.
- [182] S. V Boriskina, “Coupling of whispering-gallery modes in size- mismatched microdisk photonic molecules,” *Opt. Lett.*, vol. 32, no. 11, pp. 1557–1559, 2007.
- [183] T. Mukaiyama, K. Takeda, H. Miyazaki, Y. Jimba, and M. Kuwata-Gonokami, “Tight-Binding Photonic Molecule Modes of Resonant Bispheres,” *Phys. Rev. Lett.*, vol. 82, no. 23, pp. 4623–4623, 1999.
- [184] B. M. Möller, U. Woggon, M. V. Artemyev, and R. Wannemacher, “Photonic molecules doped with semiconductor nanocrystals,” *Phys. Rev. B - Condens. Matter Mater. Phys.*, vol. 70, p. 115323, 2004.
- [185] L. I. Deych, C. Schmidt, A. Chipouline, T. Pertsch, and A. Tünnermann, “Optical coupling of fundamental whispering-gallery modes in bispheres,” *Phys. Rev. A - At. Mol. Opt. Phys.*, 2008.
- [186] P. T. Rakich, M. A. Popovi, M. Soljač, I. And, and E. P. Ippen, “Trapping, corralling and spectral bonding of optical resonances through optically induced potentials,” *Nat. Photonics*, vol. 1, pp. 658–665, 2007.
- [187] D. D. Smith, H. Chang, and K. A. Fuller, “Whispering-gallery mode splitting in coupled microresonators,” *J. Opt. Soc. Am. B*, vol. 20, no. 9, pp. 1967–1974, 2003.
- [188] S. A. Miller, Y. Okawachi, S. Ramelow, K. Luke, A. Dutt, A. Farsi, A. L. Gaeta, and M. Lipson, “Tunable frequency combs based on dual microring resonators,” *Opt. Express*, vol. 23, no. 16, pp. 21527–21540, 2015.
- [189] K.-K. Law, “Analysis of a coupled absorptive Fabry-Perot resonator in a passive-active configuration,” *Opt. Lett.*, vol. 19, no. 9, pp. 607–609, 1994.
- [190] A. Armitage, M. S. Skolnick, V. N. Astratov, D. M. Whittaker, G. Panzarini, L. C. Andreani, T. A. Fisher, J. S. Roberts, A. V Kavokin, M. A. Kaliteevski, and M. R. Vladimirova, “Optically induced splitting of bright excitonic states in coupled quantum microcavities,” *Phys. Rev. B*, vol. 57, no. 23, pp. 14877–14881, 1998.
- [191] S. Ishii, K. Nozaki, and T. Baba, “Photonic Molecules in Photonic Crystals,” *Jpn. J. Appl. Phys.*, vol. 45, no. 8A, pp. 6108–6111, 2006.
- [192] P. B. Deotare, M. W. Mccutcheon, I. W. Frank, M. Khan, M. Lonar, and M. Lončar, “Coupled

- photonic crystal nanobeam cavities,” *Appl. Phys. Lett.*, vol. 95, no. 96, p. 31102, 2009.
- [193] A. R. A Chalcraft, S. Lam, B. D. Jones, D. Szymanski, R. Oulton, A. C. T Thijssen, M. S. Skolnick, D. M. Whittaker, T. F. Krauss, A. M. Fox, M. Benyoucef, S. Kiravittaya, Y. F. Mei, A. Rastelli, O. G. Schmidt, M. Sahin, D. Sanvitto, M. S. Skolnick, H. Liu, M. Hopkinson, E. Gallardo, L. J. Martinez, A. K. Nowak, H. P. van der Meulen, J. M. Calleja, C. Tejedor, I. Prieto, D. Granados, A. G. Taboada, and J. M. Gar, “Mode structure of coupled L3 photonic crystal cavities,” *Opt. Express*, vol. 19, no. 6, pp. 5670–5675, 2011.
- [194] S. Haddadi, P. Hamel, G. Beaudoin, I. Sagnes, C. Sauvan, P. Lalanne, J. A. Levenson, and A. M. Yacomotti, “Photonic molecules: tailoring the coupling strength and sign,” *Opt. Express*, vol. 22, no. 10, p. 12359, May 2014.
- [195] S. Haddadi, A. M. Yacomotti, I. Sagnes, F. Raineri, G. Beaudoin, L. Le Gratiet, and J. A. Levenson, “Photonic crystal coupled cavities with increased beaming and free space coupling efficiency,” *Appl. Phys. Lett.*, vol. 102, p. 11107, 2013.
- [196] N. Caselli, F. Riboli, F. La China, A. Gerardino, L. Li, E. H. Linfield, F. Pagliano, A. Fiore, F. Intonti, and M. Gurioli, “Tailoring the Photon Hopping by Nearest-Neighbor and Next- Nearest-Neighbor Interaction in Photonic Arrays,” *ACS Photonics*, 2015.
- [197] J. Lian, S. Sokolov, E. Yüce, S. Combrié, A. De Rossi, and A. P. Mosk, “Dispersion of coupled mode-gap cavities,” *Opt. Lett.*, vol. 40, no. 19, pp. 4488–4491, 2015.
- [198] M. Alonso and E. J. Finn, *Quantum and Statistical Physics, Fundamental University Physics, Vol. 3*. Addison- Wesley, Reading, MA, 1968.
- [199] N. Caselli, F. Intonti, F. Riboli, A. Vinattieri, D. Gerace, L. Balet, L. H. Li, M. Francardi, A. Gerardino, A. Fiore, and M. Gurioli, “Antibonding ground state in photonic crystal molecules,” *Phys. Rev. B*, vol. 86, no. 35133, 2012.
- [200] N. Caselli, F. Intonti, C. Bianchi, F. Riboli, S. Vignolini, L. Balet, L. H. Li, M. Francardi, A. Gerardino, A. Fiore, and M. Gurioli, “Post-fabrication control of evanescent tunnelling in photonic crystal molecules,” *Appl. Phys. Lett.*, vol. 101, p. 211108, 2012.
- [201] W. A. Harrison, *Electronic Structure and the Properties of Solids*. Dover Publications, 1989.
- [202] A. Yariv, Y. Xu, R. K. Lee, and A. Scherer, “Coupled-resonator optical waveguide: a proposal and analysis,” *Opt. Lett.*, vol. 24, no. 11, pp. 711–713, 1999.
- [203] M. Sumetsky and B. J. Eggleton, “Modeling and optimization of complex photonic resonant cavity circuits,” *Opt. Express*, vol. 11, no. 4, pp. 381–391, 2003.
- [204] M. Fatih Yanik and S. Fan, “Stopping Light All Optically,” *Phys. Rev. Lett.*, vol. 92, no. 8, p. 83901, 2004.
- [205] P. Chak and J. E. Sipe, “Minimizing finite-size effects in artificial resonance tunneling structures,” *Opt. Lett.*, vol. 31, no. 17, pp. 2568–2570, 2006.
- [206] M. J. Hartmann, F. G. S. L. Brandão, and M. B. Plenio, “Quantum many-body phenomena in coupled cavity arrays,” *Laser Photonics Rev.*, vol. 2, no. 6, pp. 527–556, 2008.
- [207] N. Stefanou and A. Modinos, “Impurity bands in photonic insulators,” *Phys. Rev. B*, vol. 57, no. 19, pp. 12127–12133, 1998.
- [208] C. Martijn De Sterke, “Superstructure gratings in the tight-binding approximation,” *Phys. Rev. E*, vol. 57, no. 3, pp. 3502–3509, 1998.

- [209] E. Lidorikis, M. M. Sigalas, E. N. Economou, and C. M. Soukoulis, "Tight-Binding Parametrization for Photonic Band Gap Materials," *Phys. Rev. B*, vol. 81, no. 7, pp. 1405–1408, 1998.
- [210] T. Mukaiyama, K. Takeda, H. Miyazaki, Y. Jimba, and M. Kuwata-Gonokami, "Tight-Binding Photonic Molecule Modes of Resonant Bispheres," *Phys. Rev. Lett.*, vol. 82, no. 23, pp. 4623–4626, 1999.
- [211] H. Miyazaki and Y. Jimba, "Ab initio tight-binding description of morphology-dependent resonance in a bisphere," *Phys. Rev. B - Condens. Matter Mater. Phys.*, vol. 62, no. 12, pp. 7676–7997, 2000.
- [212] F. S. S. Chien, J. B. Tu, W. F. Hsieh, and S. C. Cheng, "Tight-binding theory for coupled photonic crystal waveguides," *Phys. Rev. B - Condens. Matter Mater. Phys.*, 2007.
- [213] J. P. Albert, C. Jouanin, D. Cassagne, and D. Bertho, "Generalized Wannier function method for photonic crystals," *Phys. Rev. B*, vol. 61, no. 7, pp. 4381–4384, 2000.
- [214] M. Bayindir, B. Temelkuran, and E. Ozbay, "Tight-Binding Description of the Coupled Defect Modes in Three-Dimensional Photonic Crystals," *Phys. Rev. Lett.*, vol. 84, no. 10, pp. 2140–2143, 2000.
- [215] E. Ozbay, M. Bayindir, I. Bulu, and E. Cubukcu, "Investigation of localized coupled-cavity modes in two-dimensional photonic bandgap structures," *IEEE J. Quantum Electron.*, vol. 38, no. 7, pp. 837–843, 2002.
- [216] Z. Wang, N. Zhu, Y. Tang, L. Wosinski, D. Dai, and S. He, "Ultracompact low-loss coupler between strip and slot waveguides," *Opt. Lett.*, vol. 34, no. 10, p. 1498, May 2009.
- [217] R. Palmer, L. Alloatti, D. Korn, W. Heni, P. C. Schindler, J. Bolten, M. Karl, M. Waldow, T. Wahlbrink, W. Freude, C. Koos, and J. Leuthold, "Low-Loss Silicon Strip-to-Slot Mode Converters," *IEEE Photonics J.*, vol. 5, no. 1, pp. 2200409–2200409, Feb. 2013.
- [218] X. Zhang, H. Subbaraman, A. Hosseini, and R. T. Chen, "Highly efficient mode converter for coupling light into wide slot photonic crystal waveguide," *Opt. Express*, vol. 22, no. 17, p. 20678, Aug. 2014.
- [219] T. Nishid, M. Notom, R. Iga, and T. Tamamura, "Quantum wire fabrication by e⁻beam elithography using high-resolution and high-sensitivity e⁻beam resist zep-520," *Jpn. J. Appl. Phys.*, vol. 31, no. 12 S, pp. 4508–4514, 1992.
- [220] C. Caër, S. F. Serna-Otálvaro, W. Zhang, X. Le Roux, and E. Cassan, "Liquid sensor based on high-Q slot photonic crystal cavity in silicon-on-insulator configuration," *Opt. Lett.*, vol. 39, no. 20, p. 5792, Oct. 2014.
- [221] D. Yang, H. Tian, Y. Ji, and Q. Quan, "Design of simultaneous high-Q and high-sensitivity photonic crystal refractive index sensors," *J. Opt. Soc. Am. B*, vol. 30, no. 8, pp. 2027–2031, 2013.
- [222] J. Zhou, H. Tian, D. Yang, Q. Liu, L. Huang, and Y. Ji, "Refractive index sensing utilizing parallel tapered nano-slotted photonic crystal nano-beam cavities," *J. Opt. Soc. Am. B*, vol. 31, no. 8, pp. 1746–1752, 2014.
- [223] S. Mandal and D. Erickson, "Nanoscale optofluidic sensor arrays," *Opt. Express*, vol. 12, no. 3, pp. 3169–3176, 2007.
- [224] Y. Takahashi, T. Asano, D. Yamashita, and S. Noda, "Ultra-compact 32-channel drop filter with 100 GHz spacing," *Opt. Express*, vol. 22, no. 4, pp. 4692–4698, 2014.

- [225] D. Duval, A. B. Gonzalez-Guerrero, and L. M. Lechuga, "Silicon Photonic Based Biosensors: The Future of Lab-on-a-Chip Diagnostic Devices," *IEEE Photonics Soc.*, vol. 26, no. 4, pp. 1–8, 2012.
- [226] H. Sumikura, E. Kuramochi, H. Taniyama, and M. Notomi, "Cavity-enhanced Raman scattering of single-walled carbon nanotubes," *Cit. Appl. Phys. Lett. Appl. Phys. Lett. Appl. Phys. Lett. Appl. Phys. Lett.*, vol. 102, no. 10, pp. 231110–171107, 2013.
- [227] H. Yang, V. Bezugly, J. Kunstmann, A. Filoramo, and G. Cuniberti, "Diameter-Selective Dispersion of Carbon Nanotubes via Polymers: A Competition between Adsorption and Bundling," *ACS Nano*, vol. 9, no. 9, pp. 9012–9019, 2015.
- [228] N. Izard, E. Gauffrès, X. Le Roux, S. Kazaoui, Y. Murakami, D. Marris-Morini, E. Cassan, S. Maruyama, and L. Vivien, "Electroabsorption study of index-defined semiconducting carbon nanotubes," *Eur. Phys. J. Appl. Phys.*, vol. 55, no. 2, p. 20401, Aug. 2011.
- [229] I. W. Chiang, B. E. Brinson, A. Y. Huang, P. A. Willis, M. J. Bronikowski, J. L. Margrave, R. E. Smalley, and R. H. Hauge, "Purification and Characterization of Single-Wall Carbon Nanotubes (SWNTs) Obtained from the Gas-Phase Decomposition of CO (HiPco Process)," *J. Phys. Chem. B*, vol. 105, no. 35, pp. 8297–8301, Sep. 2001.
- [230] A. Parini, P. Hamel, A. De Rossi, S. Combrié, N.-V.-Q. Tran, Y. Gottesman, R. Gabet, A. Talneau, Y. Jaouen, and G. Vadala, "Time-Wavelength Reflectance Maps of Photonic Crystal Waveguides: A New View on Disorder-Induced Scattering," *J. Light. Technol.*, vol. 26, no. 23, pp. 3794–3802, Dec. 2008.
- [231] S. Combrié, N.-V.-Q. Tran, E. Weidner, A. De Rossi, S. Cassette, P. Hamel, Y. Jaouën, R. Gabet, and A. Talneau, "Investigation of group delay, loss, and disorder in a photonic crystal waveguide by low-coherence reflectometry," *Appl. Phys. Lett.*, vol. 90, no. 23, p. 231104, 2007.
- [232] M. Patterson, S. Hughes, S. Combrié, N.-V.-Q. Tran, A. De Rossi, R. Gabet, and Y. Jaouën, "Disorder-Induced Coherent Scattering in Slow-Light Photonic Crystal Waveguides," *Phys. Rev. Lett.*, vol. 102, no. 25, p. 253903, Jun. 2009.
- [233] C. Caër, S. Combrié, X. Le Roux, E. Cassan, and A. De Rossi, "Extreme optical confinement in a slotted photonic crystal waveguide," *Appl. Phys. Lett.*, vol. 105, no. 12, p. 121111, Sep. 2014.
- [234] S. Serna, "Design and characterization of Silicon Photonic structures for third order nonlinear effects," 2016.
- [235] W. Zhang, "Hybrid integration of Er-doped materials and CNTs on silicon for light emission and amplification," University Paris-Saclay, 2016.
- [236] A. Hartschuh, "Simultaneous Fluorescence and Raman Scattering from Single Carbon Nanotubes," *Science (80-.)*, vol. 301, no. 5638, pp. 1354–1356, Sep. 2003.

Synthèse en français

RESUME EN FRANÇAIS

« Cavités à fente à cristaux photoniques pour l'intégration hybride sur silicium »

Cette thèse a pour contexte la **photonique silicium**, dont les réalisations des dernières années ont atteint des niveaux de maturité suffisants pour la réalisation de circuits photoniques complets en technologie CMOS, tel que celui décrit en **Fig. RF-1**.

Les briques élémentaires de la photonique silicium, incluant un panel large de composants passifs (guides d'ondes optiques, filtres optiques, résonateurs, etc) et de composants actifs (modulateurs électro-optiques, photodétecteurs, etc) fonctionnant dans le proche infra-rouge ($\lambda \sim 1.3\mu\text{m} - 1.55\mu\text{m}$) permettent la réalisation de circuits photoniques intégrables avec l'électronique CMOS, ou du moins réalisés par les mêmes techniques de fabrication (substrats SOI : silicium sur isolant ; lithographie, gravure). Cette approche repose sur l'utilisation de matériaux de la colonne IV (Si, Ge, et alliages).

Ces travaux ont ouverts la voie à une co-intégration de fonctions électroniques et de fonctions optiques sur les mêmes puces.

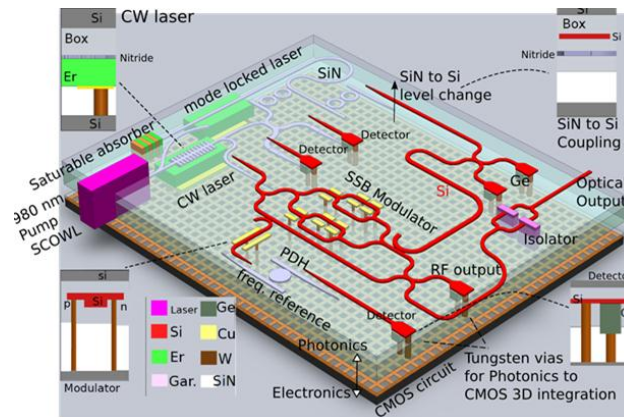


Fig. RF-1 : Circuit optique/optoélectronique en photonique sur silicium, compatible CMOS.

Simultanément, cette approche fait face à une difficulté : elle n'a pas permis à ce jour la réalisation de sources de lumière intégrées délivrant des niveaux de signaux suffisants pour l'alimentation de circuits photoniques de transmission de données, le silicium étant un matériau semiconducteur à bande interdite indirecte. Par ailleurs, elle permet d'adresser essentiellement la problématique des interconnexions optiques (et datacom) ; or, la photonique sur SOI, en tant que plateforme d'intégration optoélectronique, ouvre la voie à des applications variées incluant tout le domaine des capteurs et bio-capteurs sur puce. Pour ces raisons, l'**intégration sur silicium de matériaux actifs** (non-linéaires, luminescent, électro-optiques, biomarqueurs, etc) est une voie qui ouvre la possibilité de combiner les avantages d'une plateforme de guidage extraordinaire (guides SOI compacts, à faible pertes) et les propriétés apportées par les matériaux déposés (polymères dopés, liquides, couches minces dopées : par épitaxie, ALD ; boîtes quantiques colloïdales, etc).

Ce travail de thèse est une contribution au développement de cette **intégration hybride sur silicium**. Partant du résultat selon lequel les effets physiques exploitables dans cette approche ne sont efficaces que si un recouvrement spatial suffisant existe entre les modes optiques guidés et les matériaux rapportés, les études menées se sont focalisées sur des géométries de guides à cœur creux ('slot waveguides'). Par

ailleurs, nous avons visé immédiatement au renforcement du champ électromagnétique dans les structures photoniques et avons ainsi privilégié essentiellement des géométries de résonateurs à guides creux exploitant les propriétés de cristaux photoniques planaires bi-dimensionnels : les **cavités à guides à fentes à cristaux photoniques**.

DANS CE CONTEXTE, LES APPORTS DE CE TRAVAIL SONT LES SUIVANTS :

1) La conception par simulation numérique, la fabrication, et la caractérisation de cavités à cristaux photoniques à fentes à hétérostructure :

- Dans une approche sur silice (non-membranaire), mécaniquement robuste, avec remplissage systématique des structures par des liquides d'indice ou des couches minces (polymères PFO).
- Présentant un ajustement possible de la longueur d'onde de résonance des cavités dans une plage spectrale allant de $1.3\mu\text{m}$ à $1.6\mu\text{m}$.
- Présentant des volumes modaux effectifs de l'ordre de $0,03(\lambda/n)^3$ et simultanément des facteurs de qualité de 20 000 à 30 000 à $\lambda \sim 1.55\mu\text{m}$.

La **Fig. RF-2** présente la structure type des cavités qui ont été étudiées.

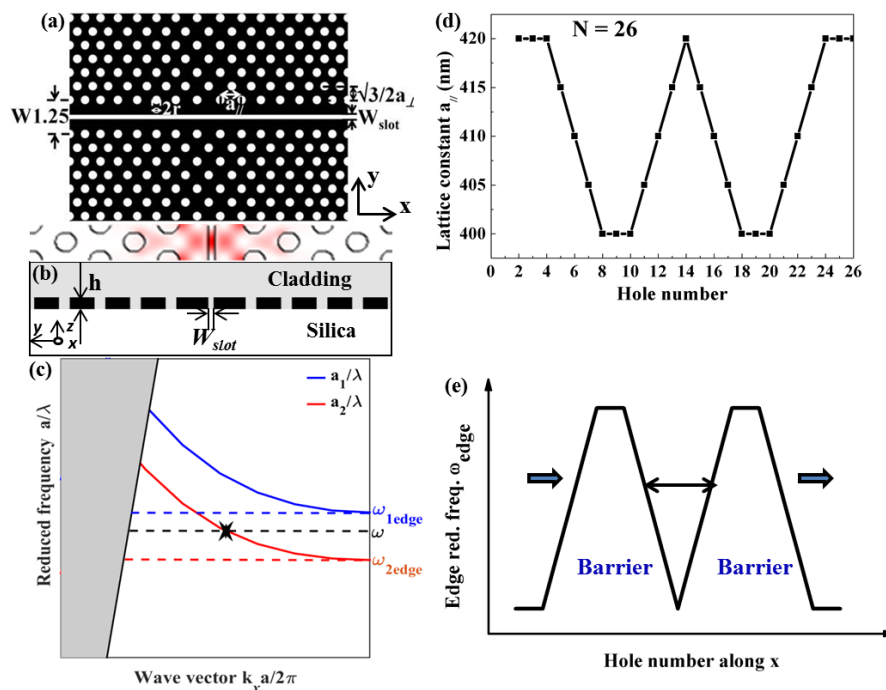


Fig. RF-2 : Description du principe conduisant à la conception des cavités à hétérostructures à cristaux photoniques (CP) étudiées dans le manuscrit : partant d'un guide CP à fente, une modulation du paramètre de maille du réseau permet d'obtenir une double barrière de l'énergie de bande interdite vue par la lumière, conduisant à une cavité Fabry-Perot de quelques μm (car $a \sim 400\text{nm}$).

La modulation du paramètre de maille du cristal photonique dans la direction de propagation de la lumière permet d'induire une double barrière du bord de bande photonique vu par la lumière, et ainsi de créer une cavité Fabry-Perot de quelques μm de longueurs.

La **Fig. RF-3(a)** montre le profil spatial de la composante majoritaire du champ électrique

du mode résonant de la structure (calcul par FDTD-3D ; FDTD : FiniteDifference Time Domain Method), tandis que la **Fig. RF-3(b)** permet d’apprécier, dans l’espace réciproque, que les pertes par diffraction hors du cône de lumière (cercle blanc en figure (b)) sont très limitées : $Q \sim 120\,000$ malgré un cône de lumière très bas induit par un matériau de remplissage – le superstrat – d’indice ~ 1.52 .

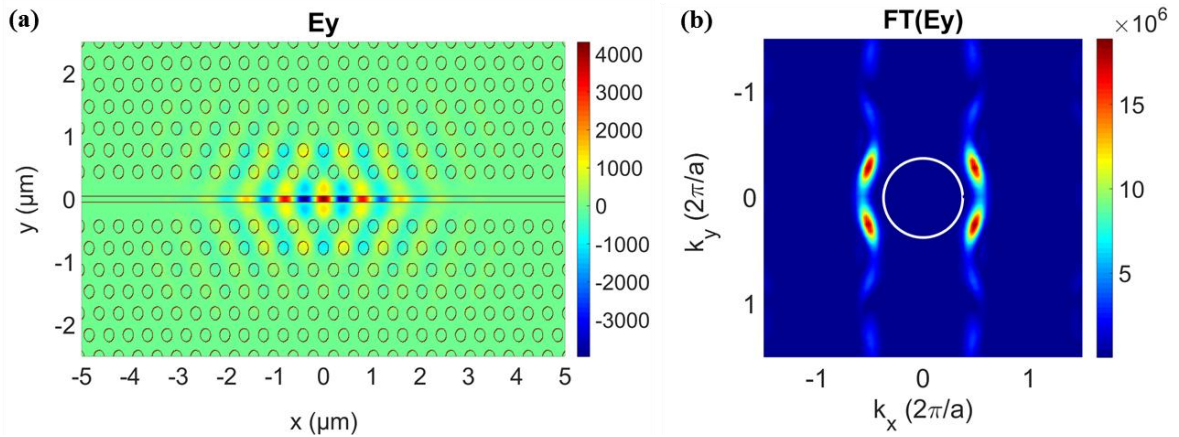


Fig. RF-3 : Caractérisation du mode de résonance de la cavité représentée en **Fig. RF-2** : (a) Profil spatial de la composante E_y du champ électrique à la longueur d’onde de la résonance ($\lambda_{res}=1.57\mu\text{m}$) ; (b) Transformée de Fourier du champ E_y pour observation de ses composantes radiatives en champ lointain (à l’intérieur du cône de lumière représenté ici par le cercle blanc).

Ces structures ont été fabriquées au sein de la salle blanche du C2N (UMR 9001), au travers de deux étapes principales : lithographie électronique et gravure ICP-RIE. La **Fig. RF-4** montre le détail d’une structure et indique le bon niveau de maîtrise technologique atteint pour la réalisation de ces cavités à cristaux photoniques.

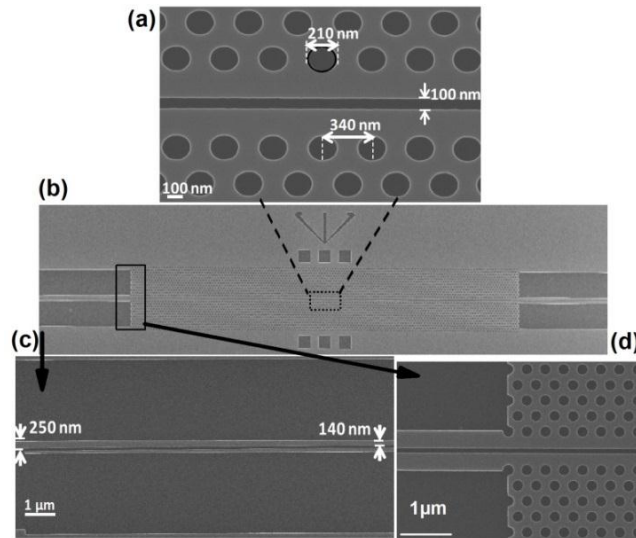


Fig. RF-4 : Images MEB (Microscopie par balayage électronique) d’une cavité à cristaux photoniques à guide à fente.

La caractérisation optique de ces structures a été conduite sur des bancs d’optique guidée, et a permis la validation expérimentale des étapes de conception et de fabrication précédentes (voir **Fig. RF-5**).

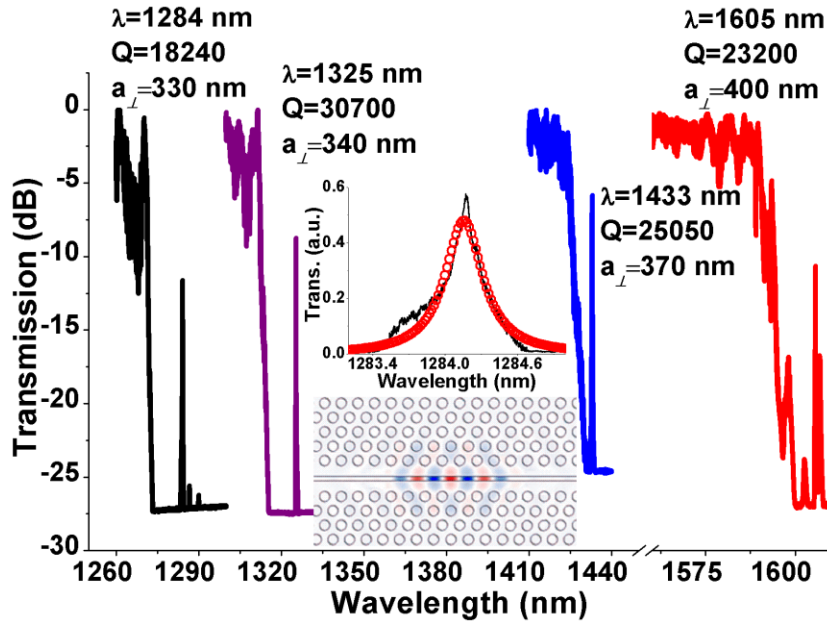


Fig. RF-5 : Résultats de la caractérisation expérimentale de cavités à cristaux photoniques à guides à fente (dans des conditions de remplissage des structures par des liquides d'indice $n \sim 1.35-1.52$).

2) Une second contribution a été l'exploration théorique (par simulation numérique) du couplage d'une cavité SOI à cristal photonique à fente : i) à un guide externe, ii) à une autre cavité.

Nous avons étudié tout particulièrement le couplage latéral d'une cavité à fente et d'un guide à fente, comme illustré en **Fig. RF-6**. Nous avons ainsi identifié les conditions de couplage et d'excitation du mode « true slot » d'une cavité à fente en terme, notamment de distance guide/cavité, et avons montré qu'une excitation proche du couplage critique de la cavité était possible à une longueur d'onde choisie autour de $1.55 \mu\text{m}$.

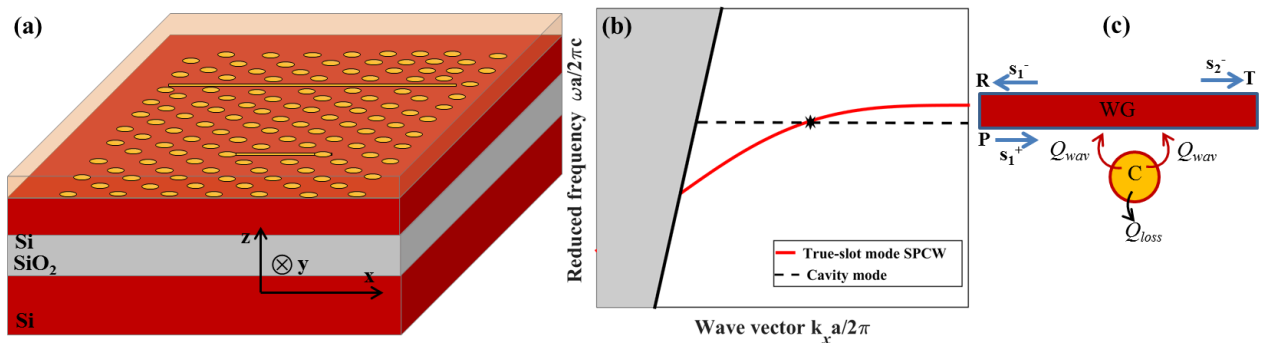


Fig. RF-6 : Schéma de principe du couplage entre une cavité CP à fente ('slot') et un guide à fente, par couplage évanescent : (a) Géométrie considérée ; (b) Diagramme de dispersion des deux entités ; (c) Schéma de principe faisant apparaître les constantes de temps impliquées.

La question du couplage entre deux cavités à fente (voir **Fig. RF-7**) a été adressée afin d'explorer les possibilités d'ingénierie des supermodes formés par l'assemblage de deux cavités 'slot'.

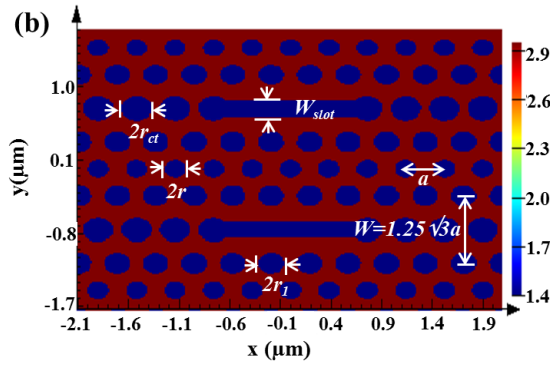


Fig. RF-7 : Géométrie typique de « molécule photonique » constituée du couplage entre deux cavités à fente.

Les questions explorées ont porté sur deux points :

- i) Le couplage entre deux cavités ‘slot’ donne-t-il lieu, comme pour des cavités non fendues, à un échange possible des longueurs d’onde de résonance des supermodes pairs (« Bonding ») et impairs (« Antibonding ») ; voir **Fig. RF-8** ?
- ii) Une méthode perturbative semi-analytique (« Tight Binding » : TB) consistant à décrire le champ total des deux cavités couplées comme la superposition du champ des deux cavités prises isolément est-elle de nature à reproduire les tendances observées par simulation numérique complète (FDTD), avec à la clef la possibilité de décrire des réseaux plus complexes de cavités couplées (3 cavités, 4 cavités, etc).

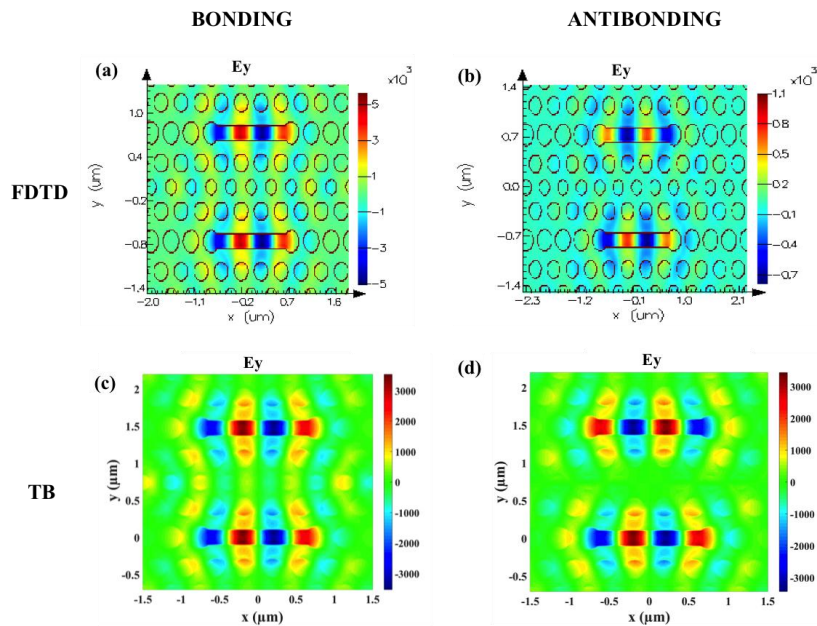


Fig. RF-8 : Composante E_y du champ électrique des deux supermodes de la molécule photonique représentée en **Fig. RF-7** : (a) Supermode pair à $\lambda_B = 1528.57$ nm (FDTD) ; (b) Supermode impair à $\lambda_{AB} = 1534.3$ nm (FDTD) ; (c) Supermode pair à $\lambda_B = 1530.47$ nm (TB) ; (d) Supermode impair à $\lambda_{AB} = 1534.4$ nm (TB).

Sur ces deux questions, les travaux menés ont conduit à des réponses positives.

3) La dernière contribution principale de ce travail a porté sur l'intégration d'un milieu actif constitué d'un matériau polymère (PFO) dopé aux nanotubes de carbone semiconducteurs.

Cette dernière partie s'est appuyée sur une collaboration interne au groupe de recherche, impliqué en tant que coordinateur dans un projet européen (FP7-CARTOON : 2013-2017). Bénéficiant d'une mise à disposition d'un matériau polymère PFO dopé aux nanotubes de carbone (CNTs), l'intégration hybride de ce matériau actif dans des cavités à cristal photonique à fente a été conduite. Le renforcement de la photoluminescence des structures photoniques a été étudié par illumination verticale des dispositifs (pompage optique à $\lambda \sim 740\text{nm}$), après caractérisation de la transmission optique par la tranche : voir Fig. RF-9.

Par cette approche, nous avons pu observer un renforcement significatif de la photoluminescence (PL) par l'effet de la cavité et collecter la lumière émise par les CNTs vers $\lambda \sim 1.28\mu\text{m}$ après plusieurs millimètres de propagation dans des guides d'onde SOI, l'ensemble de ces travaux constituant ainsi une première preuve de principe vers une source intégrée sur silicium à $\lambda = 1.3\mu\text{m}$ à base de nanotubes de carbone.

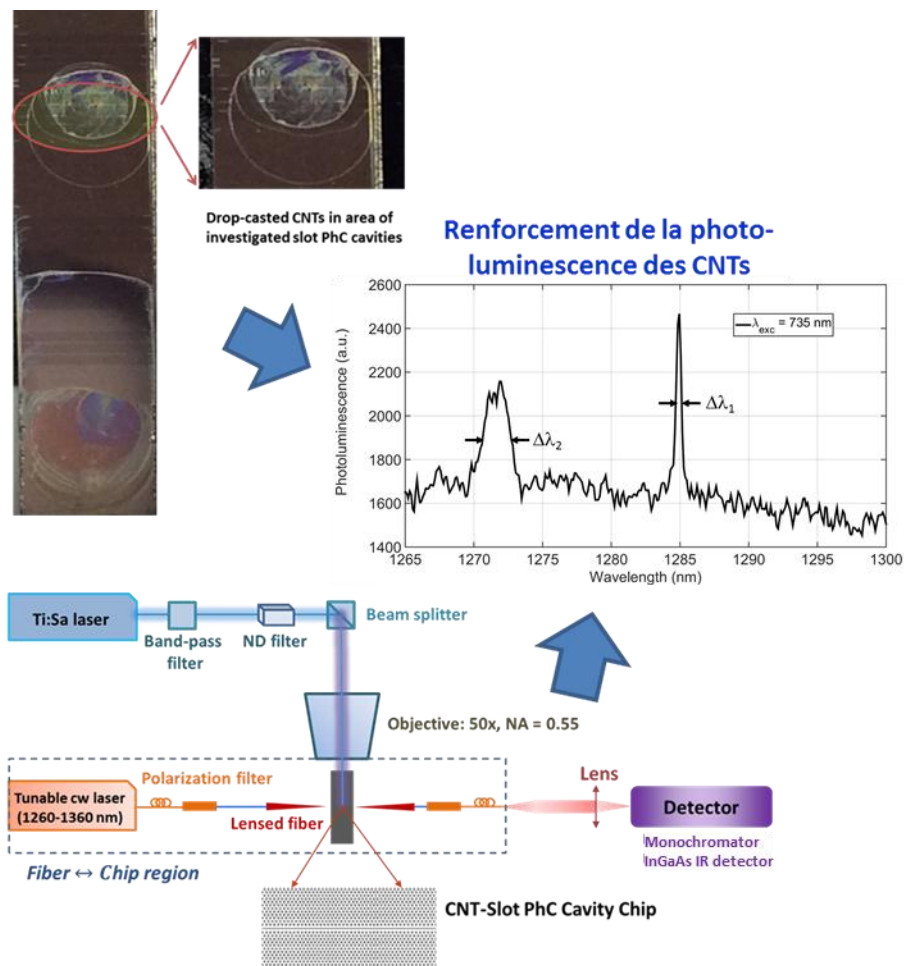


Fig. RF-9 : Intégration de nanotubes de carbone dans une cavité à cristal photonique à fente, pompage optique à $\lambda \sim 740\text{nm}$ et collection de la photoluminescence dans un guide d'onde SOI, puis propagation de la lumière sur plusieurs millimètres jusqu'à sa collection par un photodétecteur infrarouge InGaAs.

Titre : Cavités à fente à cristaux photoniques pour l'intégration hybride sur silicium

Mots clés : Photonique silicium, guide à cœur creux, cavités à cristaux photoniques, intégration hybride, nanotubes de carbone, photoluminescence

Résumé :

Cette thèse est une contribution à la modélisation et à l'étude expérimentale de cavités à cristaux photoniques à fente développées en vue d'une intégration hybride de matériaux actifs sur silicium. Parmi les travaux de conception, nous avons d'abord utilisé la méthode des ondes planes et la méthode des différences finies (FDTD) pour concevoir une série de cavités SOI à hétérostructures, mécaniquement robustes infiltrées par des liquides d'indices ($n \sim 1,5$), présentant des longueurs d'onde de résonance dans la gamme des télécommunications ($1,3 \mu\text{m} - 1,6 \mu\text{m}$), des facteurs de qualité de plusieurs dizaines de milliers, et des volumes modaux proches de $0,03 (\lambda/n)^3$. Nous avons ensuite étudié analytiquement et numériquement le couplage entre une cavité à cristaux photoniques à fente et un guide d'onde à fente par la théorie des modes couplés, complétée par des simulations FDTD, qui ont permis de confirmer la possibilité d'exciter efficacement les modes de fente des cavités à partir d'un guide externe. Enfin, nous avons étudié numériquement et semi-analytiquement des géométries de molécules photoniques constituées de deux cavités à cristaux photoniques à fentes couplées, dont l'écart fréquentiel entre les supermodes a pu être ajusté en amplitude en signe. Nous avons utilisé une méthode perturbative (« Tight binding ») pour estimer les distributions spatiales des modes des molécules photoniques et prédire leurs fréquences dans plusieurs configurations de cavités de cristaux photoniques à fentes couplées.

Ce travail exploratoire a été complété par une partie expérimentale qui a porté sur l'étude d'une famille de cavités de hétérostructure à cristaux photoniques à fente. Les cavités à cœur creux fabriquées ont montré des facteurs de qualité (Q) de plusieurs dizaines de milliers, associés à des volumes modaux de l'ordre de $V=0,03 (\lambda/n)^3$ après infiltration de la fente et des trous des structures par des liquides d'indice de réfraction proches de 1,46. Des facteurs Q/V supérieurs à 600 000 et atteignant 1 000 000 dans le meilleur des cas (vers $\lambda \approx 1,3 \mu\text{m}$) ont ainsi été observés. Cette phase expérimentale préliminaire a donné ensuite lieu à deux types de développements.

Tout d'abord, les propriétés des cavités à cristaux photoniques à fentes ont été étudiées pour des applications en détection d'indice en volume, et testées en utilisant différents liquides d'indice de réfraction compris entre 1,345 à 1,545. Les résonateurs étudiés ont présenté des sensibilités de $\sim 235 \text{nm}/\text{RIU}$ et des facteurs de mérite de détection d'indice de l'ordre de 3700, à l'état de l'art pour des résonateurs silicium intégrés à cœur creux.

Dans une autre direction, le potentiel des résonateurs diélectriques à fente a été exploré en vue d'une intégration des matériaux actifs sur silicium. Un polymère dopé aux nanotubes de carbone semiconducteurs a été déposé comme matériau de couverture en vue d'étudier le renforcement de la photoluminescence (PL) des nano-émetteurs sous pompage optique vertical à $\lambda \sim 740 \text{nm}$. Les expériences conduites ont permis de corréler le renforcement de la PL des nanotubes avec les modes de résonance des cavités et de démontrer le couplage partiel de cette PL vers des guides SOI longs de plusieurs millimètres (collection par la tranche vers $\lambda \approx 1,3 \mu\text{m}$), apportant une preuve de principe d'une possible intégration des nanotubes émetteurs en photonique sur silicium.

Title: Planar slot photonic crystal cavities for on-chip hybrid integration

Keywords: Photonic crystal cavities, silicon photonics, hybrid integration, hollow core optical waveguides, index sensing, carbon nanotubes, photoluminescence

Abstract: This Ph.D. work is a contribution to the modeling and the experimental study of slot photonic crystal cavities for hybrid on-silicon integration. Among the design works, we first have used plane wave expansion and finite-difference time-domain methods to design a series of mechanically robust (non-free membrane) SOI slot photonic crystal heterostructure cavities with resonance wavelength in the telecommunication range, *i.e.* from $1.3 \mu\text{m}$ – $1.6 \mu\text{m}$, with Q -factors of around several tens of thousands and mode volumes around $0.03(\lambda/n)^3$ after being infiltrated by cladding materials with typical index values around 1.5. We have then analytically and numerically studied the coupling between a slot photonic crystal cavity and a slot photonic crystal waveguide by using the coupled mode theory and FDTD simulation. Then we confirmed the ability to excite the cavity slot modes from a waveguide by using FDTD simulation. Finally, as a preliminary step towards the use of several coupled slotted cavities for future hybrid integration schemes, we have numerically and semi-analytically investigated photonic molecules made of two coupled slot photonic crystal cavities providing two different supermodes (bonding and antibonding ones) with controllable wavelength splitting. We successfully employed the tight-binding (TB) approach, which relies on the overlap of the two tightly confined cavity electric fields, to predict the supermodes frequencies and spatial distributions in several coupled slot photonic crystal cavity configurations.

This exploratory work was supplemented by an experimental part, which focused on the investigation of a family of slot photonic crystal heterostructure cavities. The fabricated silicon on insulator hollow core cavities showed quality factors of several tens of thousands, *i.e.* from 18,000 to 31,000 and mode volumes V_s of $\sim 0.03(\lambda/n)^3$ after being infiltrated with liquids of ~ 1.46 refractive index, yielding Q/V ratio larger than 600,000, and reaching 1,000,000 in the best case (at $\lambda \approx 1.3 \mu\text{m}$).

This preliminary experimental stage gave rise to two types of additional developments.

Firstly, the properties of the studied slot photonic crystal cavities have been investigated for index sensing applications by using different liquids with refractive index values ranging from 1.345 to 1.545. The considered photonic crystal resonators have demonstrated quality factors of several tens of thousands with sensitivities of $\sim 235 \text{ nm/RIU}$ and index sensing $FOMs$ around 3,700, *i.e.* at the state of the art considering hollow core silicon integrated resonators.

Secondly, in the view of the integration of active materials on silicon, the potential of these hollow core nanoresonators has been considered to enhance the photo-luminescence (PL) of semiconducting single-walled carbon nanotubes (s-SWNTs) integrated in thin films deposited on top of silicon. We have brought the first experimental demonstration of s-SWNTs PL collection (at $\lambda \sim 1.28 \mu\text{m}$) under vertical pumping at short wavelength ($\sim 740 \text{ nm}$) from a slotted resonator into millimeter long integrated silicon waveguides, providing a first proof-of-concept step towards nanotube/Si-PhC integration as an active photonic platform. The reported works demonstrate the feasibility of integrating telecommunication wavelength nanotube emitters in silicon photonics as well as emphasize the role of slot photonic crystal cavities for on-chip hybrid integration.